Abstract

Building energy and indoor air quality (IAQ) are of great importance to climate change and people's health and wellbeing. They also play a key role in mitigating the risk of transmissions of infectious diseases such as COVID-19. Building design with high performance in energy efficiency and IAQ improvement can save energy, reduce carbon emissions, and improve human health. High-performance building (HPB) design at the early design stage is critical to building's real performance during operation. Fast and reliable prediction of building performance is, therefore, required for HPB design during the early design iterations. A modular-based method to analyze building performance on energy efficiency, thermal comfort, IAQ, health impacts, and infection risks was developed, implemented, and demonstrated in this study. The modular approach groups the building technologies and systems to modules that can be analyzed at multi-scale building environments, from urban scale, to building, room, and personal scale. The proposed approach was implemented as a plugin on Rhino Grasshopper, a 3D architectural geometry modeling tool. The design and simulation platform was named Green Design Studio. Reduced-order physics-based models were used to simulate thermal, air, and mass transfer and storage in the buildings. Three cases were used as the study case to demonstrate the module-based approach and develop the simulation platform. Optimization algorithms were applied to optimize the design and settings of the building modules beyond the reference case. The case study shows that the optimal design of the small office determined by the developed platform can save up to 27.8% energy use while mitigating more than 99% infection risk compared to the reference case. It reveals that the optimization of green building design using the proposed approach has high potential of energy saving and IAQ improvement. In support of the application of the Green Design Studio platform, a database of green building technology modules for energy efficiency and IAQ

improvement was created. Two selected emerging IAQ strategies were studied using the proposed approach and the developed tool, including the in-duct needlepoint bipolar ionizer and the combination of displacement ventilation and partitions. The in-duct ionization system can provide an equivalent single pass removal efficiency (SPRE) of 3.8-13.6% on particle removal without significant ozone and volatile organic compounds (VOCs) removal and generation with minimal energy use. The combined application of displacement ventilation and desk partitions can also effectively mitigate potential virus transmission through coughing or talking. The abundant performance data from experiments and detailed simulations for the studied technologies will be used by the database of the green building technologies and systems. It will allow these two technologies to be applied through the Green Design Studio approach during the early-design stage for a high-performance building. This can potentially help to address IAQ issues, particularly the airborne transmission of respiratory diseases, while maintaining high energy efficiency.

GREEN DESIGN STUDIO: A MODULAR-BASED APPROACH FOR HIGH-PERFORMANCE BUILDING DESIGN

by

Jialei Shen

B.S., Xi'an Jiaotong University, 2015
M.S., Nanjing University, 2018

Dissertation
Submitted in partial fulfillment of the requirements for the degree of
Doctor of Philosophy in Mechanical and Aerospace Engineering

Syracuse University
August 2023

Acknowledgements

First, I would like to express my deepest appreciation to my advisor Prof. Jianshun Zhang, for his continuous and selfless support to my PhD research and my life. He has been an invaluable source of knowledge and inspiration, and I am truly fortunate to have him as a mentor. He is not only an expert in research, but also a kind, patient, and humble person, who treats his students, colleagues, friends, and family with the utmost respect and kindness. I am truly grateful for his support and encouragement.

I would like to extend my appreciation to all my colleagues in BEES Lab, Ms. Beverly Guo, Zhenlei Liu, Dr. Meng Kong, Dr. Rui Zhang, Xin Guo, Shayan Mirzabeigi, and Sameeraa Soltanian-Zadeh. Without their help and friendship, I would not have been able to complete this journey. They have always been willing to lend a helping hand and provide me with guidance and support.

I also sincerely appreciate other colleagues who have provided invaluable help on this dissertation and my research. Prof. Bess Krietemeyer and Prof. Amber Bartosh, who were the first two colleagues I worked with since starting this project, have provided persistent support and inspiration over these years. Prof. Bing Dong has broadened my knowledge and provided inspiration with his innovative research topics. I very much appreciate Prof. Peng Gao for serving on my defense committee on the dissertation. I also appreciate Prof. Bing Dong for serving on the defense committee and Prof. Bess Krietemeyer for chairing the defense committee. I also

appreciate Prof. Ed Boguzc and Prof. Thong Dang for providing help and guidance on the dissertation during my PhD proposal defense.

I would also like to express appreciation to my industrial collaborators, Dr. Michael Birnkrant, Dr. Peter McKinney, and Mr. Dan Love, for their support in providing exciting and valuable research opportunities in addressing IAQ and COVID-19 issues during the pandemic. I also appreciate all other collaborators who have worked together with me, including Prof. Zhi Gao, Mr. Mingjie Zhang, Ms. Yibing Hu, and Mr. Fusuo Xu from Nanjing University.

Last but not least, I would like to thank all my family and friends. Special thanks to Rui Tian and my parents. They have always believed in me and encouraged me to pursue my dreams. I am grateful for their love and support.

Jialei Shen

Rockville, MD, March 2023

Table of Contents

List of Figures

List of Table

1. Introduction

1.1 Background and challenges

Climate change already inflicts serious damage on the world. In recent years, we have seen more frequent and severe droughts, heatwaves, wildfires, storms, and flooding across the world (Cappucci and Kornfield 2022; Hoffman 2022; Office of Climate Change and Health Equity 2022; U.S. Census Burean 2021). The ongoing extreme heatwaves in this summer are threatening millions of people on this planet (Cappucci and Kornfield 2022; NASA 2022; Office of Climate Change and Health Equity 2022). Experts have warned that these extreme weather events will worsen and become more frequent in the coming decades because of climate change (Hoffman 2022). In the meantime, the unprecedented COVID-19 pandemic brings more challenges to the world. Climate and health have become two major global crises, leading to devastating loss of life and economy. Many efforts have been made worldwide to address the global climate crisis and health issues, such as setting up carbon neutrality goals (European Parliament 2021; White House 2021b). But we are still facing many challenges to implement actions to achieve these goals.

Buildings play a significant role in energy consumption and climate change as the building sector is the largest energy consumer across other sectors, accounting for 35% of global energy use and 38% of carbon dioxide (CO2) emission (Figure 1-1) (United Nations Environment Programme 2020). As the carbon neutrality goal set up by the Intergovernmental Panel on Climate Change (IPCC), global net human-caused emissions of carbon dioxide would need to fall by about 45% from 2010 levels by 2030, reaching ‘net zero’ around 2050 (IPCC 2018). Therefore, the potential of carbon emission reduction in buildings is huge, but the challenges are also great. Building indoor environmental quality (IEQ) is closely associated with occupant health and comfort as people

spend nearly 90% of their time indoors (deCastro et al. 2007). Occupant exposure to indoor air pollutants, such as volatile organic compounds (VOCs), ozone, and particulate matters (PM), may cause short- or long-term adverse health effects, including increasing in respiratory-related morbidity, cardiovascular morbidity and premature mortality (Bell et al. 2004; Day et al. 2017; Gan et al. 2011; Tagiyeva and Sheikh 2014). The COVID-19 pandemic also highlighted the significance of indoor air quality (IAQ) as most outbreaks occurred in building indoor scenarios and airborne transmission plays a key role in virus spreading (H. Qian et al. 2020; Shen, Kong, Dong, et al. 2021b). Efforts to improve IAQ and comfort can improve people's health, well-being, and productivity. The increasing demand for healthier and more comfortable indoor environments is usually contradictory to building energy saving as increased energy use is typically required for space conditioning, ventilation, and air cleaning. Hence, it is essential for high-performance building design to achieve the trade-off between energy efficiency, and improved IAQ and thermal comfort.

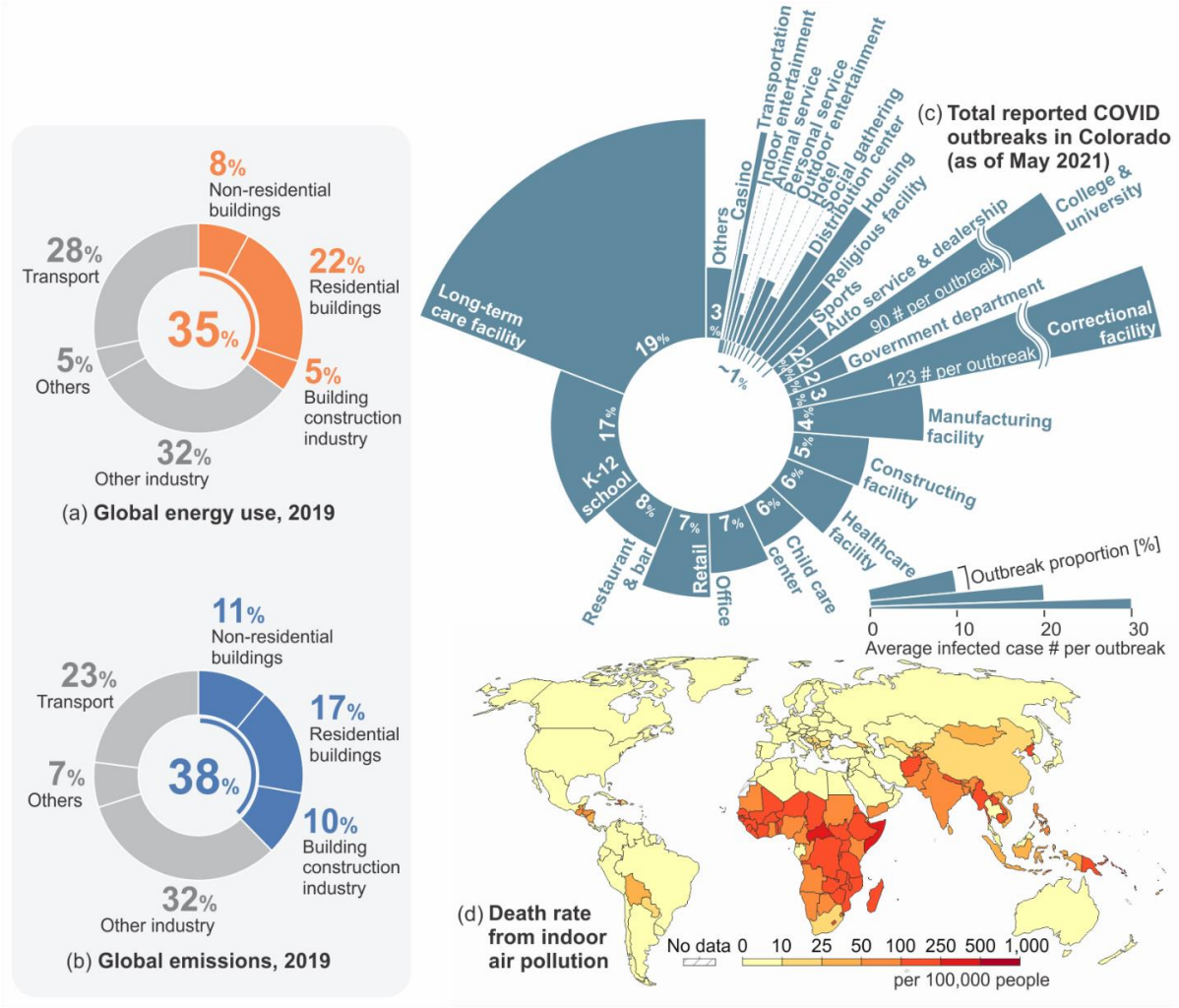

Figure 1-1. (a) Global energy consumption and (b) CO2 emission by buildings in 2019 (adapted from (United Nations Environment Programme 2020)), (c) COVID-19 outbreaks in different scenarios (data in Colorado, U.S. as of May 26th, 2021 (CDPHE 2020)), and (d) death rate from indoor air pollution (as of 2018) (Max Roser and Hannah Ritchie 2022).

The last two decades has seen rapid growth in high-performance building (HPB) design (also known as green building design or sustainable building design) with the emergence of many worldwide green building standards or certification/rating systems to minimize or optimize

consumption of natural resources and control pollution. It is estimated that there are approximately 600 HPB certification systems globally (Doan et al. 2017; Vierra 2018), including the most widely used ones such as LEED rating system (USGBC 2013), ASHRAE standard 189.1 (ASHRAE 2017c), BREEAM standard (BRE 2018), and WELL building standard (IWBI 2018). The LEED Rating System (USGBC 2013) is an internationally recognized green building certification system aimed at improving performance across all the metrics including energy savings, water efficiency, CO2 emission reduction and IEQ improvement. It has become one of the most common green building certification systems in the world (USGBC 2022). Currently, more than 90 thousand building projects have been certified by the LEED system in more than 167 countries [13,19]. The BREEAM System (BRE 2018) is the first and another leading green certification system. It evaluates performance across the building lifecycle, from new construction to in-use and refurbishment. Nearly 600 thousand buildings have been certified by the BREEAM system in 90 counties (BRE 2019). The WELL Building System (IWBI 2018) is a more recent international certification system that aims to improve human health and wellbeing through the built environment. Over 9 thousand buildings have been certified by the WELL system globally (IWBI 2019). The U.S. has a large market for green buildings. Figure 1-2 shows top 10 countries and regions in terms of total LEED-certified floor area (square feet) in 2021 (U.S. Green Building Council 2022). The U.S. is the world's largest market for LEED, with more than 280 million square feet certified to LEED in 2021.

Although better performance is expected for the certified green buildings, the practical performance of green buildings may not always be consistent with the target rating level. A study analyzed the energy use from 100 LEED-certified buildings and found that around 30% of them

consumed more energy than their conventional counterparts, although on average, LEED-certified buildings saved 18-39% of energy use (Newsham et al. 2009). A recent study revealed that LEED-certified buildings consume only 10% less site energy than similar buildings that are not LEED-certified (Scofield and Doane 2018). Some green buildings may perform well on energy saving, water saving, carbon emission reduction, and operation cost reduction, but have poor performance on IAQ and thermal comfort. A more recent study reported average 25% less energy use, 11% less water use, 34% reduced CO2 emission, and 19% lower operation cost for 22 LEED-certified green buildings compared to conventional buildings (Fowler et al. 2010). But the IAQ and thermal comfort in these green buildings were worse than conventional buildings (Fowler et al. 2010). Even the buildings that certified by the WELL standard, that aims to promote IAQ and occupant health, may exhibit higher measured concentrations for some VOCs and TVOC relative to non-WELL-certified buildings (Licina and Langer 2021).

Figure 1-2. Top 10 countries and regions in terms of total LEED-certified floor area (square feet) in 2021 (data from (U.S. Green Building Council 2022)).

Green technologies, strategies, facilities, or building components that perform better on energy efficiency, IAQ and comfort improvement, have been developed and widely implemented in buildings to achieve higher performance across multiple scales (from urban scale, to building and room scales, to personal microenvironment), e.g. green roof, superinsulation building envelope, low-emission building materials, and personalized ventilation system (Cao et al. 2016; Kong et al. 2015; Pétigny et al. 2021; Sadineni et al. 2011; Shen, Kong, Dong, et al. 2021b, 2021a; Tomson et al. 2021; J. J. Zhang et al. 2022). Different building systems can have completely different or even contradictory performance on energy efficiency and IAQ and thermal comfort. Even the same technology may perform differently under various conditions. For example, in-duct filters with higher efficiencies are usually suggested for removing indoor particles or mitigating the airborne transmission risk, but higher energy consumptions by the driving fan are usually required to

compensate the increased pressure drop through the filter (Risbeck et al. 2021; Shen, Kong, Dong, et al. 2021b, 2021a). Natural ventilation can enhance indoor ventilation, mitigate indoor air pollution and reduce the energy use by mechanical ventilation, but when the ambient air is not clean enough, it will likely introduce contaminants from the outdoor air like ozone and nitrogen oxides (NOx) into indoor air (Shen et al. 2020; Shen, Kong, Dong, et al. 2021a). To mitigate the airborne transmission risk of SARS-CoV-2, a higher fraction of outdoor air in the supply air of the heating, ventilation, and air conditioning (HVAC) system (e.g. 100% outdoor air) is usually recommended to improve the indoor ventilation, although it will consume more energy to condition the additional outdoor air (Shen et al. 2020; Shen, Kong, Dong, et al. 2021a). Enhanced ventilation can also break the equilibrium near the surfaces of building materials. It can lead to release of pollutants, which are primarily emitted by materials (intrinsic emissions) and also those that adsorb on surfaces and are absorbed in the building structures (Steinemann et al. 2017). Therefore, the selection and combination of various building technologies are significant to building performance. Inappropriate selection and use of some systems in green buildings may impair building performance. Hence, it is essential to address these issues at the design stage of green buildings.

Figure 1-3 illustrates a typical building design process. To aid decision-making of a HPB design, building simulation is widely used in the late design stages, but its application is still limited in the early stages in which design decisions have a major impact on final building performance and costs (Attia et al. 2012; Hygh et al. 2012; Konis et al. 2016; Larsson 2009). Predicting the consequences of early decisions is particularly difficult, but crucial, since adverse design decisions will reduce the remaining design space and make it more strenuous and expensive to meet high

performance goals (Østergård et al. 2016). Research shows that during early design phases, 20% of the design decisions taken subsequently influence around 80% of all design decisions (Bogenstätter 2010). The early integration of simulation programs faces several challenges, including time-consuming modeling, rapid change of the design, conflicting requirements, input uncertainties, and large design variability (Østergård et al. 2016). In addition, building design is a multi-collaborator discipline, where design decisions are influenced by architects, engineers, and clients (building owners) (Østergård et al. 2016). Several studies have shown that current design and decision support tools are inadequate, user hostile and too incomplete to be used by architects to support and inform the HPB design, particularly during the early design phase (Attia et al. 2009, 2012; Riether and Butler 2008; Stine 2022). Per the building performance simulation (BPS) tools originally listed by the U.S. DOE, out of the total 392 tools listed on the DOE website in 2011, less than 40 tools are targeting architects during the early design phases (Attia et al. 2012; BESTD 2022). To address these challenges for early-phase HPB design, two approaches can be implemented. One is developing a program that can provide real-time or near-real-time and reliable feedback of building performance simulation results to meet the rapid changes of the design. Another possible approach is to establish a comprehensive database of various building features/technologies/systems with pre-defined parameters and pre-calculated/pre-measured performance metrics embedded. During the early design stage, the pre-calculated/pre-measured information can provide direct guidance on the selection and configurations of different building features in HPB designs.

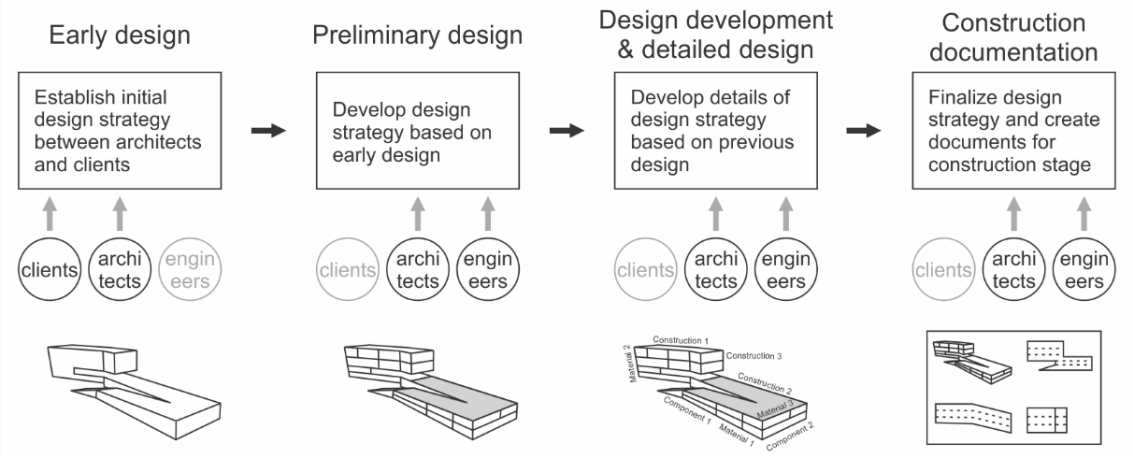

Figure 1-3. Schematic of a typical building design process.

Both approaches require quantitative analyses on various building performance metrics. Therefore, quantitative and comprehensive analyses on the performance and cost of different green building technologies in realistic scenarios are important for building design to achieve the performance goal, which can provide useful supports and reference to designers for making decisions on selecting green technologies and systems in the design. Building performance simulation can support decision making in early design of high-performance building as they can provide quantitative analysis to designers (Østergård et al. 2016). Multiple simulation tools have been developed and applied to evaluate various building performance, including EnergyPlus (DOE 2017), eQuest (JJH 2018) (based on DOE-2 (Hirsch 2016)), ESP-r (ESRU 2018), and TRNSYS (TRNSYS 2019) for building energy efficiency modelling, Radiance (LBNL 2017) for lighting simulation, CONTAM (NIST 2018) and CHAMPS-Multizone (Feng et al. 2012) for multizone IAQ and ventilation analysis, and computational fluid dynamics (CFD) tools (e.g. ANSYS Fluent (ANSYS 2021) and OpenFOAM (OpenFOAM Ltd 2023)) for room air distribution simulation. These tools are usually developed based on physical equations of thermal and mass (air and

contaminants) models in building physics, which likely include some complicated equations and advanced algorithms for solving the coupling of different variants in the equations. These equations and algorithms can provide more accurate and reliable simulation results, but also require very detailed and complicated inputs such as detailed building envelope properties or HVAC system parameters. However, some of these detailed input parameters may not be available yet at the early stage of a building design. Failure to provide accurate input can result in poor prediction performance. In the meanwhile, it may consume considerable processing and simulation time for models with large and complex inputs, which is unfavorable for early-phase building design as there are always rapid changes to the building design at this phase, so real-time or near-real-time feedback of building performance estimation is required (Shen et al. 2020). Besides, most of these building physics modeling tools are specific to a certain task, e.g. EnergyPlus on energy simulation and CONTAM on IAQ simulation. It is not quite convenient and straightforward to run multidisciplinary modeling with these tools. External platforms or tools (e.g. Building Controls Virtual Test Bed (BCVTB) (LBNL 2016)) are usually needed to run the coupling simulations (or co-simulations) with these tools. Therefore, a tool that can perform multidisciplinary building performance simulations for early design stage that requires minimal inputs and fast response is necessary.

A database of green building technologies on various performance metrics (including energy efficiency, IAQ, comfort, and cost) will be beneficial for HPB design but is still lacking. Many studies have analyzed the performance for certain technologies, but a systematic analysis for them under various conditions is scarce. A comprehensive review of the performance analyses for different green building technologies is thus required.

To optimize the application of various building technologies/systems in HPB design, performance simulation tools can also collaborate with some optimization algorithms to determine their optimal configurations (Kheiri 2018; Nguyen et al. 2014). Multi-objective optimization (MOO) is widely used to optimize the building features to achieve the trade-off between different performance criteria, e.g. energy efficiency, IAQ, thermal comfort, and cost (Chegari et al. 2021; Diakaki et al. 2008; Ghaderian and Veysi 2021; W. Li et al. 2021; Hongbin Liu et al. 2013; Shaikh et al. 2018; N. Wang et al. 2014; X. Wei et al. 2015; B. Wu et al. 2021). However, building performance optimization (BPO) usually requires numerous iterations to meet certain criteria, which will consume considerable time and is less likely to give a fast response for early design. Hence, fast and reliable performance simulation and optimization models are required for early-phase HPB design.

Therefore, the main challenges for early-phase HPB design include:

a) Current green building design standards and rating systems cannot provide quantitative and comprehensive support for high-performance building design, which may result in the actual building performance not achieving the target green level.

b) Most building design and performance analysis platforms require complicated inputs and considerable processing time and cannot provide fast responses for building performance simulation and optimization at early design stage and in operation.

c) A database that contains comprehensive analysis for green building technologies and systems, can provide support to designers for early-stage high-performance building design but is not available.

Hence, a building design and analysis platform that can provide fast and reliable responses for building performance simulation and optimization, is required. A green building technology/system database with comprehensive and systematic analysis on building performance also needs to be established in support of the design and analysis platform.

1.2 Research gaps

Based on the review on existing building performance databases, the main *research gaps* of the existing building performance databases include: (1) Existing whole building performance databases usually only provide very limited building characteristics information, typically including floor area, built year, and floor number. Building components or systems with design features were usually not provided; (2) Most databases focused on one performance aspect, either energy or IAQ. Datasets with metrics of multiple performance aspects (energy and IAQ) are still scarce; (3) Databases of building components or systems usually do not provide performance metrics like energy use or carbon emissions for each component/system. Therefore, a database of building technologies, components, or systems with design features and performance metrics is required for the development of a BPS program for early-phase design (adopting design features as inputs for physics-based modellings and developing data-driven models to predict performance metrics).

1.3 Goals and objectives

The research goal of this dissertation is to develop an approach for designing buildings with improved performance at the early design phase through 1) a framework for high-performance building design, 2) advanced algorithms for building performance simulation that can provide fast and reliable response, 3) a database of green building technologies and systems from real and validated practices, and 4) an optimization model that can coordinate different green features to achieve an optimal performance. The performance metrics that the proposed approach aims to improve include energy efficiency, IAQ, thermal comfort, and airborne infection risk for respiratory diseases, with the consideration of costs. The key scientific contributions will stem from a framework used for representing building components/systems and quantifying building performance metrics, a high-performance building design and optimization program with advanced simulation and optimization algorithms, and the comprehensive green building technology/system datasets. The proposed framework regularizes the parameters of various types of building components/systems and simplifies the inputs for performance analyses at the early building design phase. It also proposes a quantitative assessment approach for comprehensively analyzing the performance of buildings and building components/systems. It works for different scales of building systems, from community, site, building, floor, room, to personal microenvironment. The program with advanced simulation models can provide fast and reliable response of performance metrics, which is required for early-phase building design. The database of green building technologies and systems can provide supporting data for building design and be used to improve the data-driven simulation models. The performance optimization models can be used to find the design with optimal configurations of building technologies and systems.

Therefore, the proposed approach and platform can be used as a decision tool at the early design stage for the use of various green building technologies and systems in high-performance building design. Since the platform considers the infection risk of respiratory diseases through airborne transmission, it can also be used to estimate the infection risk in different scenarios, and evaluate the effectiveness of various mitigation strategies, which can provide helpful supports for selecting favorable control strategies in addressing respiratory diseases such as COVID-19. The platform is also well-suited for controlling the operation of different green building technologies and systems as control parameters and feedback metrics are defined and readily to be implemented in operation with the application of Internet of Things (IOTs). The hypothesis of the proposed research is that innovative and optimized high-performance building design has a great potential for significant energy saving, and occupant health and well-being improvement, and an approach with fast and reliable performance prediction models can significantly improve the building design and operation.

1.4 Research scope and roadmap

The research aims to develop an approach for designing green buildings at the early design phase. The present work is limited to the following research scope:

(1) Developing an approach that can be used to design green buildings and predict performance metrics.

(2) Developing an approach to establishing a database of green building technologies or components with design features and performance metrics that can be further used by data-driven models.

(3) Focusing on the performance modelling for early-phase building designs that require simplified modelling inputs and real-time or near-real-time response.

(4) Demonstrating building performance modelling and green building design with some representative study cases.

To simplify the inputs for building performance modelling and establish the database of green building technologies, building technologies, components, or systems can be defined as building modules with both design features and performance metrics. Therefore, the modular approach is applied to modularize and regularize building technologies, components, and systems in this study. The research will be performed through 1) a framework for high-performance building design, 2) advanced algorithms for building performance simulation that can provide fast and reliable response, 3) a database of green building technologies and systems from real and validated practices, and 4) an optimization model that can coordinate different green features to achieve an optimal performance. Figure 1-4 shows the roadmap of accomplishing this research. The key scientific contributions will stem from the comprehensive green building technology/system datasets, a modular framework used for representing building components and systems, and a module-based high-performance building design and optimization platform with advanced simulation and optimization models. The proposed modular framework regularizes the parameters

of various types of building components and systems and simplifies the inputs for performance analyses at the early building design phase. It works for different scales of building systems, from community, site, building, floor, room, to personal microenvironment. The module-based platform with advanced simulation models can provide (near) real-time and reliable response of performance metrics prediction, which is required for early-phase building design. It also enables members of a multidisciplinary design team (architects, engineers, and clients) to provide inputs from different perspectives concurrently and therefore develop building designs and analyses easily and quickly through the same platform. The database of green building technologies and systems can provide supporting data for building design and be used to improve the data-driven simulation models. The performance optimization models can be used to find the design with optimal building technologies and systems. Hence, the proposed platform can be used as a decision tool at the early design stage for the use of various green building technologies and systems in high-performance building design. As the platform considers the infection risk of respiratory diseases through airborne transmission, it can also be used to estimate the infection risk in different scenarios, and evaluate the effectiveness of various mitigation strategies, which can provide helpful supports for selecting favorable control strategies, particularly during the COVID-19 pandemic. The platform is also well-suited for controlling the operation of different green building technologies and systems as control parameters and feedback metrics are defined in modules, which is readily to be implemented in operation with the application of IOTs. The hypothesis of the proposed research is that innovative and optimized high-performance building design has a great potential for significant energy saving, and occupant health and well-being improvement, and a modular based approach with fast and reliable performance prediction models can significantly improve the building design and operation.

The proposed research was accomplished through the following subtasks:

(1) Module-based building design and analysis platform (R1): A module-based design and analysis platform called Green Design Studio (GDS) is proposed. The proposed modular approach is applied to modularize and regularize building components and systems with building parameters and performance attributes embedded. A database containing a bunch of building modules is established and used by the platform to enhance the simulation algorithms and provide supporting data to building design. Reduced-order physics-based models and data-driven models are established and used to provide fast and reliable response on performance simulation. The database of green modules is used to improve the data-driven models. Expected outcomes include: (1) a modular framework and procedure to modularize and regularize building components and systems; (2) a module-based platform that requires simplified inputs and provides fast and reliable performance simulation response; and (3) advanced building performance simulation models, including reduced-order models and data-driven models.

(2) Database of green building technologies and systems (R2): A database of building modules with green features from real building practices is developed. The green building technologies and systems implemented in existing buildings will be modularized using the proposed modular framework to collect their configuration parameters. The performance attributes of each module are analyzed by detailed physics-based simulation models or verified and reliable reduced-order physics-based models. The performance attributes can also be originated from the measured data

when they are available in the studied building. The measured data can also be used for improving the reduced-order models cooperating with certain optimization algorithms. The established database will be used to improve the data-driven models for performance simulations. It can also provide information of how each module work in practice in different conditions and scenarios through certain statistical analyses, which can be used to provide supporting reference to designers for selecting green modules that corporate better with the building design. The expected outcome is the database of green building modules.

(3) Building performance optimization models coordinating various building modules (R3):

Simulation-based building performance optimization models are developed to integrate and coordinate building modules to find out the design with optimal performance. Multi-objective optimization models will be developed to optimize the design and operation of building modules to achieve the tradeoff between energy efficiency, IAQ, thermal comfort, airborne infection risk mitigation and cost with certain constraints. The expected outcome is the building performance optimization models.

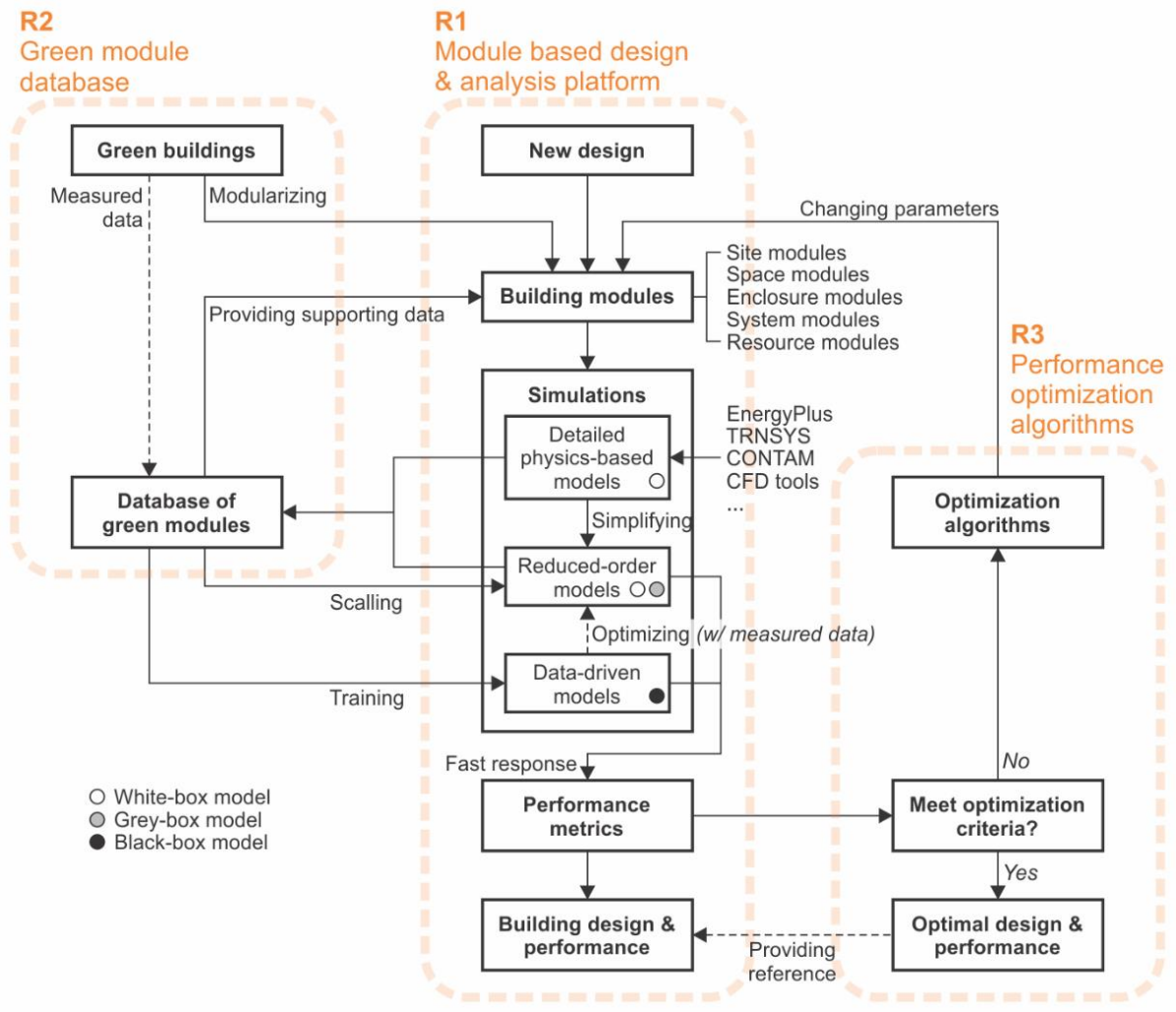

Figure 1-4. Roadmap of the proposed research.

2. Platform development for energy and IAQ analyses

2.1 Review of state-of-the-art research

2.1.1 Performance analysis tools/models in building designs

There have been numerous programs developed for simulating various building performance metrics including energy efficiency, IAQ, thermal comfort, and infection risk. Many of these BPS tools have been widely applied in building designs. Simulation models in BPS tools can be roughly

categorized into three types, i.e. physical/engineering models, statistical methods, and hybrid approaches (Foucquier et al. 2013; Fumo 2014).

2.1.1.1 Physics-based models

Physics-based models ("white box") usually can be implemented through different approaches, including the CFD approach for detailed thermal/air/mass distribution modelling in a space (treating the space as a 3-D problem), the zonal method that divides a space into multiple zones (treating the space as a 2-D problem), and the nodal method that assumes uniform state variables in the space (treating the space as a 1-D problem) (Foucquier et al. 2013). The CFD and zonal methods can provide spatial and time distribution of local state variables (e.g., air temperature or pollutant concentration) in the target space, while the nodal approach can just present the uniform values for the entire space. However, considering that a building usually consists of multiple rooms, CFD and zonal models for the whole building simulation usually require huge computation time with high complexity of the model implementation (especially CFD models). Therefore, the nodal method is widely applied in many building energy and IAQ simulation tools. The application of nodal models in buildings with multiple spaces can provide multizone simulations for energy and IAQ analyses. Most available building energy and IAQ programs are based on the nodal/multizone analyses, most typically EnergyPlus and CONTAM. For multizone models, the state variables can be estimated by a series of governing equations for calculating the thermal or mass balance in the space. Some simulation programs apply more comprehensive models to calculate the detailed thermal or mass distributions, e.g., the detailed construction layers in EnergyPlus, and the detailed HVAC systems in EnergyPlus, ESP-r, eQuest, and TRNSYS. The complexity of these detailed models will determine the accuracy and simulation time of applying these programs. Detailed

physics-based BPS tools like EnergyPlus and CONTAM have been widely applied in various research to evaluate the performance of different design features or novel technologies/systems (Al-Janabi and Kavgic 2019; Attia et al. 2012; Ng et al. 2013, 2021; Persily et al. 2010; S. Shi et al. 2015; Soares et al. 2014; Zhu et al. 2013).

These BPS programs can provide reliable and accurate predictions on different aspects of building performance, but the integration/coupling of various BPS programs is not very convenient or straightforward. External platforms or tools are usually required to run the co-simulations with these tools. BCVTB is a software environment that allows users to couple different simulation programs for co-simulation (e.g. EnergyPlus, Radiance, and TRNSYS), and to couple simulation programs with actual hardware (e.g. the BACnet system of a building) (LBNL 2016). It allows expert users of building simulation to expand the capabilities of individual simulation tools by linking them to other tools. It has been widely used by researchers and engineers to run co-simulations of building physics and control systems. Other tools that can export simulation programs as Functional Mock-up Units (FMU) using the Functional Mock-up Interface (FMI) standard (an interface to exchange dynamic models) also have the potential to perform co-simulations (FMI-standard 2022). For example, the EnergyPlusToFMU package is a package in Python that can export EnergyPlus as FMU for dynamic co-simulation or control (LBNL 2021). Simulations between EnergyPlus and CONTAM can be coupled through the CONTAM 3D Exporter that supports FMU (NIST 2022). Another significant approach for building physics co-simulation is programming in Modelica using the Building Library, which is an open-source library with dynamic simulation models for building and district energy and control systems (LBNL 2022). It is a more open platform/environment for building physics modeling, but usually

requires expert backgrounds on building physics and control systems. The co-simulation of building energy and IAQ performance is a widely studied topic since they are the major tasks of building performance. The co-simulation of energy and IAQ is usually performed through the coupling between EnergyPlus and airflow simulation programs like CONTAM for multizone airflow estimation (Dols et al. 2021; Justo Alonso et al. 2022; Ng et al. 2021) and CFD tools (e.g. ANSYS Fluent and OpenFOAM) for detailed airflow patterns in certain spaces (W. Guo et al. 2022; Xiong and Chen 2021). In general, the co-simulation of building energy, IAQ and other performance tasks is usually complicated and requires expert knowledge and experience in building physics modelling or programming.

Some simplified physics-based models have also been applied to simulate energy and IAQ performance with certain assumptions and simplifications (Rahman 2019; Xu and Wang 2007). Reduced-order resistance-capacitance (RC) thermal or air network models have been applied to simulate the thermal, air and mass transfer and balance in buildings (Braun and Chaturvedi 2002; Hao 2019; D. W. Kim et al. 2013; Z. Li et al. 2021; Mirakhorli and Dong 2016; O'Neill et al. 2010; O'Neill and Narayanan 2014; Ogunsola et al. 2014; Rahman 2019; S. Wang and Xu 2006; Xu and Wang 2007; K. Zheng et al. 2016). The RC network (including 3R2C and 2R2C models) is used to derive a set of first order differential equations representing the building thermal, air, and mass transfer and balance. Based on the RC thermal network, the energy balance equation for building envelopes has been applied to get the state-space model. In general, the resistances in the RC network cover outside convection resistances, wall conduction resistances, inside convection resistances, and window thermal resistance. The thermal mass effects are represented by the capacitances in the RC model. The network also includes the external and internal heat gains/losses

that apply on external or internal thermal nodes. For the airflow network based on the RC approach, the room air infiltration, natural ventilation, mechanical ventilation, contaminant sources and removals are considered. Research has shown that the RC network can describe the building heat transfer and a model with higher quality can give a better estimation accuracy (Hao 2019; D. W. Kim et al. 2013). The RC thermal/airflow network models have also been applied to integrate advanced control strategies such as model predictive control (MPC) in buildings (Boodi et al. 2019; Mirakhorli and Dong 2016) or work with other statistical methods such as genetic algorithm (GA) to establish hybrid models based on measurements or other datasets for better predicting building performance (Hao 2019; Xu and Wang 2007). In general, the reduced-order RC network models can provide fast and relatively accurate estimations on building performance with simplified inputs. Therefore, it is probably more suitable to apply reduced-order models in the early design phase as many physical information of buildings or systems required by detailed physics-based models/tools is unavailable at early design phase, which may result in poor prediction performance if failed to provide accurate inputs. Besides, the detailed physics-based models/tools usually consume more processing and simulation time, which is unfavorable for early-phase building design as there are always rapid changes to the building design at this phase, so real-time or near-real-time feedback of building performance estimation is required.

2.1.1.2 Data-driven models

Statistical methods using machine learning (ML) models ("black box") have been used to estimate building performance more and more frequently in recent years. Compared to the physics-based models, the statistical models usually do not require physical information about the building or systems but estimate performance metrics based on existing datasets from measurements or

validated simulations (i.e., data-driven modelling). Based on the historical data, with suitable model and algorithms, statistical methods could "learn" the non-linear relationship between the independent variables and target variables (Zhijian Liu et al. 2019). This approach typically includes regression models such as multiple linear regression (MLR) and ordinary least squares regression (OLS), models based on decision trees, artificial neural network (ANN), and classifier models like support vector machine (SVM) (Foucquier et al. 2013; Seyedzadeh et al. 2018; W. Wei et al. 2019). Numerous data-driven studies have been conducted to predict and optimize building energy and IAQ performance (Foucquier et al. 2013; Seyedzadeh et al. 2018; W. Wei et al. 2019). According to a literature review on data-driven building energy consumption predictions published in 2018 (Amasyali and El-Gohary 2018), most studies, i.e., 47% and 25% of the studies, utilized ANN and SVM, respectively, to train their models. Only 4% of the studies utilized decision trees and 24% of the studies utilized other statistical algorithms such as MLR and OLS. These algorithms are also widely used in IAQ-related predictions (W. Wei et al. 2019). The accuracy of energy and IAQ predictions using ML methods usually depend on the suitability of training datasets and the selection of input variables/features, as well as the algorithms used to train the model. For energy simulations using data-driven models, building energy use/demand and heating/cooling loads are usually the target variables as outputs. Input variables of training datasets usually include meteorological and climate data (e.g. outdoor temperature, humidity, solar radiation, pressure, wind speed and direction), time information that associated with meteorological and occupant information (e.g. predicted season and date), building characteristics (e.g. stories, room features, construction year, orientation, geometry information such as area, height, and shape, window-to-wall ratio, glazing features, envelope characteristics, and shading characteristics, etc.), occupant information (e.g. number, density, and behavior), and active system

characteristics (e.g. HVAC, lighting, and ventilation system features and operations). Some studies also used historical data of the target/studied variables (i.e. energy use or heating/cooling loads) to predict the variables at the "current" moment (Amasyali and El-Gohary 2018; Seyedzadeh et al. 2018). For IAQ-related predictions, the output variables (or target variables) that were studied mainly include indoor concentrations of various pollutants (e.g. PM2.5, PM10, CO, CO2, NO2, airborne bacteria, total VOCs) or some IAQ indices consisting of multiple IAQ parameters (e.g. air quality index (AQI)), of which the PM concentration in indoor air is the most frequently studied parameter (W. Wei et al. 2019). Input variables of data-driven models for IAQ predictions are usually like the input features of models for energy predictions, including meteorological and climate parameters, time information, building characteristics, occupant information, and active system characteristics. Outdoor pollutant concentrations of the studied or other pollutant(s) are also commonly used as the input variables to predict the indoor concentrations of target pollutant(s). Besides, previous/historical indoor concentrations of the studied pollutant(s) can also be used to the indoor pollutant concentrations at the "current" moment (W. Wei et al. 2019). Research revealed that occupant behavior plays a crucially important role in building energy consumption and IAQ performance due to its high variability (Amasyali and El-Gohary 2021; W. Wei et al. 2019). A study presented that occupant behavior can make a difference up to over 7 times in energy consumption (Amasyali and El-Gohary 2021).

In general, data-driven models usually use more general parameters of building, meteorological, system, and occupant characteristics or historical data as inputs in their models, compared to the detailed and comprehensive parameters required by physics-based models. Therefore, the quality of training datasets can greatly affect the prediction accuracy of the data-driven models. Training

datasets are usually obtained through real measurements from sensors or simulated results from validated cases (e.g., validated CFD or EnergyPlus cases). To evaluate the performance of different building design features, datasets with building and system characteristics are required. However, many available public databases for building energy/IAQ predictions do not provide datasets with these features. In addition, to provide more accurate predictions, a large scale of datasets is usually required, which needs great efforts to generate and collect this number of datasets with studied features if no available databases existed.

Many studies have compared the performance of different data-driven algorithms on predicting energy and IAQ performance, which can vary greatly depending on the model nature (e.g., SVM vs ANN) and model features like hidden layer number for ANN models. Thus, the accuracy and speed of a specific data-driven model will vary from case to case. For example, many studies review by Amasyali and El-Gohary (Amasyali and El-Gohary 2018) revealed that SVM models perform higher accuracy than ANN models but some other studies observed the opposite. Many models can achieve high accuracy with the coefficient of variation (CV) below 5%, while others exhibited lower accuracy with very high CV (even greater than 100% for some cases) (Amasyali and El-Gohary 2018). According to the ASHRAE Guideline 14 (ASHRAE 2014), an hourly prediction model is considered calibrated if its hourly CV values fall below 30%. It indicates that the performance of using a data-driven model for prediction can vary significantly. For the same type of models, more layers or features usually result in higher accuracy, but also require greater training time. But prediction time of utilizing a pre-trained data-driven model is usually very fast, normally faster than detailed physics-based models. The choice of the algorithm to use, therefore,

depends on the application requirements (e.g., needed accuracy) and constraints (e.g., data availability) (Amasyali and El-Gohary 2021).

Even though data-driven models can provide fast and relatively reliable estimation of energy and IAQ performance, there may still be some limitations with the use of data-driven models. The models may not perform well outside of their training range, therefore, may not be reliable to be used beyond the training range (or beyond the studied building cases). For example, a model that was trained by learning from a limited dataset (e.g., data collected from a small set of buildings) may not perform well outside of the training data (e.g., different types of buildings in terms of physical properties, operation strategies, weather conditions, occupant behavior, etc.) (Amasyali and El-Gohary 2018). The dataset used for training must, thus, be representative of the range of application and contain sufficient variety. Collecting such sufficiently representative and wide-ranging data may be difficult, costly, and/or time consuming. Besides, data-driven models are black-box models, meaning that their internals are unknown for users. A black-box model may provide sufficient estimation accuracy but may be limited in providing a detailed understanding of the different parameters and its behavior in terms of energy and IAQ prediction compared to a white-box physical model.

2.1.1.3 Hybrid models

Hybrid methods ("grey box"), that offer a combination of physics-based and data-driven prediction models, thereby have been proposed and applied to leverage the advantages and minimize the disadvantages of both methods. In black-box data-driven models, a large amount of input

variables/features are usually required by the statistical algorithms to increase the predictive accuracy, of which some parameters and equations are physically interpretable and can be better described through physical models (Amasyali and El-Gohary 2018). It retains a part of physical meaning for the prediction. The advantages of one method remove the drawbacks of the other one. There are several strategies to apply hybrid models in energy and IAQ estimation. The hybrid methods can be used to estimate some physical parameters (based on statistical methods from available datasets), which are sometimes unavailable or less reliable in conventional physics-based models (Foucquier et al. 2013). RC network models with genetic algorithms are usually used to implement this strategy. Another common strategy is to utilize statistics to implement a learning model describing the building/occupant behavior as it is the most variable and determinant factor for predicting building energy use or IAQ (Foucquier et al. 2013). This learning model is designed from a learning basis built from a physical approach. A third strategy consists in using data-driven methods in fields where physics-based models are not effective and accurate enough (Foucquier et al. 2013).

Many studies have attempted to couple the data-driven models with the physics-based models (usually reduced-order physical models such as RC thermal network models). For example, Dong et al. (B. Dong et al. 2016) developed a hybrid model that coupled a data-driven model and a RC thermal network model for predicting the energy consumption in residential buildings and compared its prediction performance to other statistical models. Ouaret et al. (Ouaret et al. 2018) developed a hybrid model of using the historical formaldehyde concentration data as the only input of the model and integrating with the physical airflow models to forecast the indoor formaldehyde

concentrations in an office. Studies revealed that hybrid models can usually perform better than conventional physical models or data-driven models (Amasyali and El-Gohary 2018).

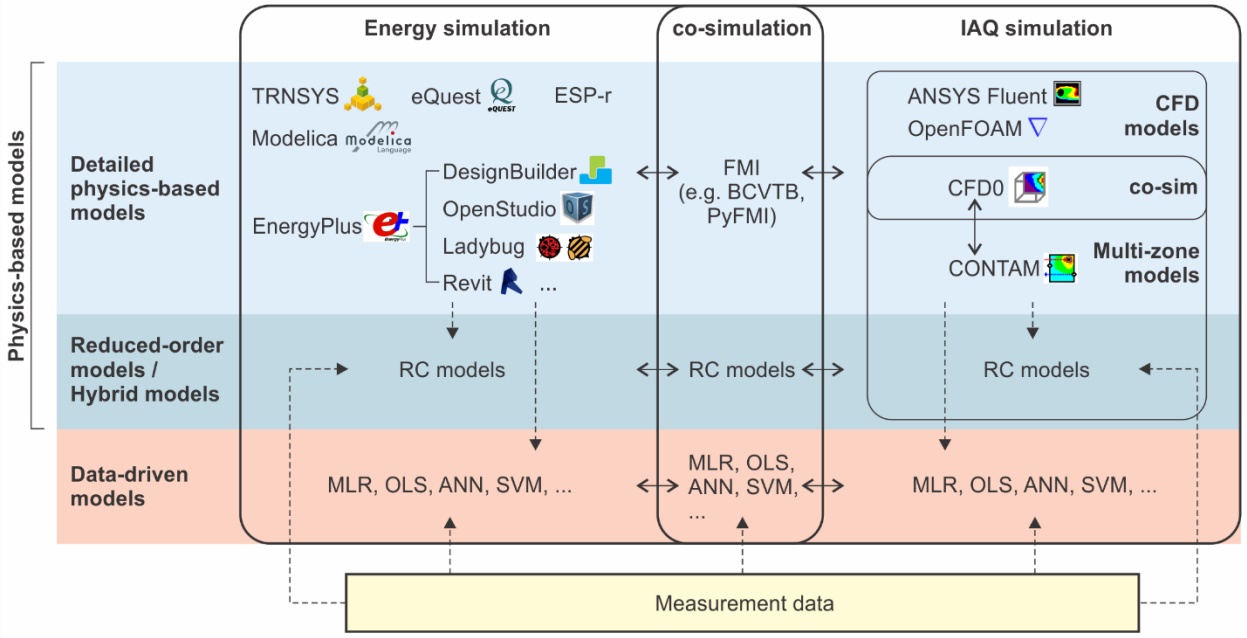

Figure 2-1. Schematic of existing BPS tools/models (S. Wang and Xu 2006).

2.1.1.4 Thermal comfort assessment models

Thermal comfort and infection risk in buildings can be calculated based on the thermal and IAQ variables estimated by BPS tools/models. Some building energy simulation programs such as EnergyPlus can directly generate and export thermal comfort metrics as its outputs. Thermal comfort is usually quantified through metrics like predicted mean vote (PMV) and predicted percentage of dissatisfied (PPD), depending on the operative temperature, relative humidity, air speed, occupant's metabolic rate and clothing level. They can be calculated through methods introduced in ASHRAE Standard 55 (ASHRAE 2020a). The standard regulates the recommended

thermal comfort level in indoor spaces. To comply ASHRAE 55, the recommended thermal limit on the 7-point scale of PMV is between -0.5 and +0.5. PPD varies depending on where the occupant is in the space, and it should not exceed 20% per standard. Another standard, ISO Standard 7730 (ISO 2005), expands on this limit, giving different indoor environments ranges. It defines the hard limit as ranging between -2 and +2, for existing buildings between -0.7 and +0.7, and new buildings ranging between -0.5 and +0.5. An online thermal comfort estimation tool (CBE Thermal Comfort Tool (Tartarini et al. 2020)) has been developed by the Center for the Built Environment (CBE) of the Lawrence Berkeley National Laboratory (LBNL). It incorporates the major thermal comfort models, including the PMV, PPD, standard effective temperature (SET), adaptive models, local discomfort models, SolarCal, and dynamic predictive clothing insulation (Tartarini et al. 2020). The tool also provides dynamic and interactive visualizations of thermal comfort zones. It has several practical applications, and each year is used by more than 49,000 users worldwide, including engineers, architects, researchers, educators, facility managers and policymakers (Tartarini et al. 2020).

2.1.1.5 Infection risk estimation models

Some IAQ simulation tools such as CONTAM have the capability for simulating multizone particle transmission in indoor spaces, which has the possibility to be applied for modelling the multizone airborne transmission of viable particles. But most available IAQ performance simulation tools cannot directly perform estimations of infection risks of respiratory diseases. To address the challenges of COVID-19, many tools for estimating infection risks through airborne transmission in a single zone have been developed based on the Wells-Riley model, which is a widely used equation determining infection risks through the susceptible individual's inhalation

exposure to the suspended viable pathogen generated by the infectors (Riley et al. 1978; Stephens 2013; Sze To and Chao 2010; Wells 1955). For example, Kasibhatla et al. (Kasibhatla et al. 2020) developed a web-based tool COVID Exposure Modeler for estimating the COVID-19 infection risk from airborne transmission during classroom teaching incorporating a Monte Carlo approach. Allen et al. (Allen et al. 2020) developed a Google sheet to calculate the risk reduction by using portable air cleaners. Corsi et al. (Corsi et al. 2020) established a web-based platform named SafeAirSpaces COVID-19 Aerosol Relative Risk Estimator for evaluating the airborne infection risk and tracking the infectious particles. Dols et al. (Dols et al. 2020; William S. Dols et al. 2020) developed the web-based Fate and Transport of Indoor Microbiological Aerosols (FaTIMA) tool, which allows for single-zone analysis of airborne transmission of SARS-CoV-2 using a simplified user interface that implements CONTAM as its simulation engine.

Other tools include the Indoor Scenario Simulator developed by Riediker and Monn (Riediker and Monn 2020) for estimating virus concentration and inhaled dose in the room, the COVID-19 Ventilation Calculator created by REHVA (REHVA 2020) for estimating the effect of ventilation on COVID-19 airborne transmission, and the COVID-19 Aerosol Transmission Estimator established by Jimenez and Peng (Jimenez and Peng 2020) to evaluate infection risks in various indoor scenarios such as classrooms, supermarkets, and stadiums. Bazant et al. (Bazant 2021) developed a web-based application COVID-19 Indoor Safety Guideline that can estimate the infection risk using the Wells-Riley model and indicate the safe level of occupancy or duration time based on the input configurations. It can also assess the risk based on indoor carbon dioxide concentrations. Shen et al. (Shen, Kong, Birnkrant, et al. 2021; Shen, Kong, Dong, et al. 2021a) developed a spreadsheet-based calculator for estimating the infection risk in several space types

including ballrooms, conference rooms, bistro/cafeteria, hotel guest rooms, offices, and classrooms. The calculator can perform steady-state and stochastic simulations to evaluate the effectiveness of various mitigation strategies in reducing infection risks from baseline conditions established by ASHRAE 62.1 (ASHRAE 2019a).

However, these tools all rely on the assumption of well-mixing in a single space. Multizone airflow analysis tools, such as CONTAM, can perform viable particle transmission simulations but are unable to provide direct calculations of infection risks. As a result, currently available BPS programs cannot estimate infection risks associated with respiratory diseases in cases of multizone transmission.

2.1.1.6 Research gaps

Based on the review on existing building performance simulation tools and models, most of the reviewed tools and models are developed for engineers or researchers, which usually requires deep knowledges of building physics modelling or data science programming. These tools and models have been well applied by engineers and researchers for studying the performance of certain technologies or developing advanced strategies for energy saving and/or enhanced IAQ. However, they are inadequate, user hostile and too incomplete to be used by architects to support and inform the green building design, particularly during the early design phase (Attia et al. 2009, 2012; Riether and Butler 2008; Stine 2022). Besides, the implementation of these building performance simulation and optimization tools/models in building design tools/platforms (that are widely used by architects) is still limited. Table 2-1 shows the typical simulation and optimization tools that

were integrated in the most used architecture design software, including SketchUp, Rhino, and Revit. Most of these embedded analysis tools are established based on detailed physics-based models, e.g., EnergyPlus, Radiance, CONTAM, and OpenFOAM, while less tools rely on reduced-order physics-based models and data-driven models. Although attempts have been made to integrate building design with performance analysis, owing to the limitations and challenges of various building performance simulation tools and models mentioned earlier, barriers to integrating and practicing building performance analysis at early design phase remain high. The major research gaps of performing building performance analysis at early design phase: (1) Detailed physics-based models usually require comprehensive inputs which are likely unavailable at early design stage; (2) Performance analyses at early design phase require real-time or near-real-time responses while the simulation process of current detailed tools can be very time-consuming. (3) The performance of simulations using data-driven models relies on the selection of datasets and training variables, which may result in inaccurate estimations; (4) The co-simulation of different programs for estimating various performance metrics (e.g. energy efficiency, IAQ, thermal comfort, and infection risks) can be complicated and usually require expert background; (5) The estimation of infection risk has not been implemented in available multizone airflow simulation programs integrated with energy and IAQ assessments. Therefore, the performance analyses at early building design phase require real-time or near-real-time responses on multidisciplinary performance tasks with simplified inputs, easy-to-use user interface for architects.

Table 2-1. Common building design and performance analysis platforms and tools.

Platform	**Design tools**	**BPS tools**	**BPO tools**
SketchUp	SketchUp	OpenStudio (*EnergyPlus*, *Radiance*)	Sefaira (*parameter analysis*)
		Sefaira (*EnergyPlus*, *Radiance*)	MOOSAS (*multi-objective optimization*)
		designPH (s*implified energy models*)	
Rhino	Rhino/Grasshopper	Ladybug (*EnergyPlus*, *Radiance*)	Octopus (*multi-objective optimization*)
		Honeybee (*EnergyPlus*, *Radiance*)	Galapagos (*multi-objective optimization*)
		ArchSim (*EnergyPlus*)	
		DIVA (*Daysim*)	
		Butterfly (*OpenFOAM*)	
		Dragonfly (*UWG*, *CitySim*)	
Revit	Revit	Energy Analysis (*EnergyPlus*)	Insight 360 (*data-driven optimization*)
		Insight 360 (*EnergyPlus, data-driven lighting & solar models*)	

2.2 Methodology

A module-based green building design and analysis platform is proposed to achieve the research goals. The platform estimates performance metrics based on the analyses on building modules with advanced models and algorithms. The platform is implemented in the Rhino Grasshopper. Some representative study cases are also introduced to be applied by the developed platform.

2.2.1 Building modules

Every building contains a very complex set of interdependent systems comprising multiple subsystems such as the building enclosure, internal spaces/zones, and environmental service systems, which in turn consist of many components made of substantial elements. Each element has many physical parameters such as dimensions, density, specific heat, and heat conductivity for each material of a wall assembly; location, supply air temperature and flow rate of a room terminal unit of an internal space/zone; and airflow rate and pressure rise of a fan of an air handling unit of an HVAC system. A modular framework to configure these building elements can simplify and regularize various building components and systems, and provide performance metrics for data-driven modelling. Hence, building modules are defined based on building systems, subsystems, components, and elements at multiple levels, and are embedded with physical parameters and performance metrics. Building modules are like functional LEGO blocks with design features and performance attributes. These functional "LEGO blocks" can be selected, organized and integrated into a whole building of higher performance with certain algorithms. A hierarchical structure is adopted to organize the building modules that allow bottom to top aggregation across different levels (Figure 2-2). They are classified into five different types: site modules, space modules, enclosure modules, service system modules and sustainable resource modules. Site modules are

those site features related to the surrounding physical context which may affect the building performance, including local climate and weather (e.g., air temperature and solar radiance), traffic emission, surrounding vegetation (greening), and proximity to adjacent structures and building density (neighborhood). Space modules represent the building interior spaces including whole building, floors, and zones. Enclosure modules represent interior and exterior building enclosures, such as wall assembly (including window units and shading systems), ceiling and floor, which are the interfaces between zones. Service system modules include HVAC systems, lighting systems, water systems and other appliances. The service systems may consist of other specific subsystems or features. Sustainable resource modules include active renewable energy systems such as photovoltaic solar panels or active solar thermal systems, and water recycle systems.

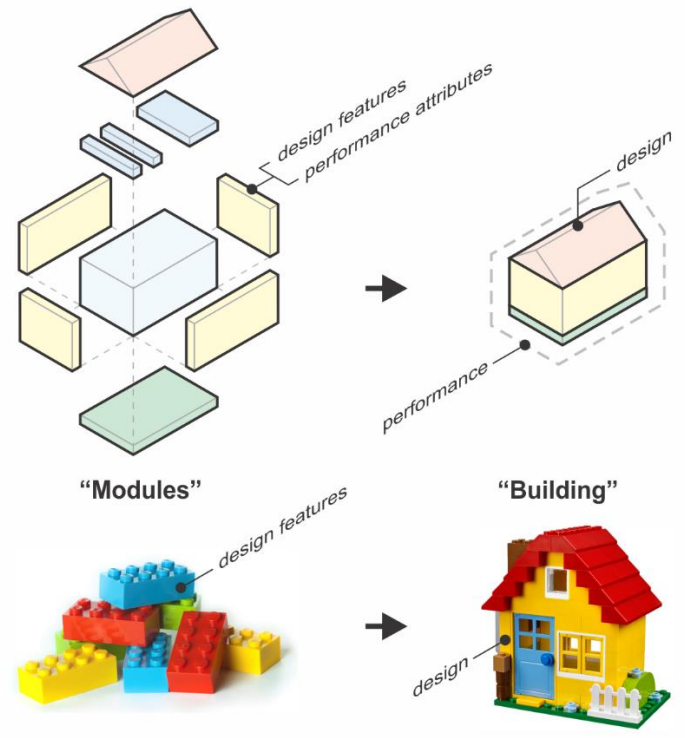

(a) Schematic of building modules and process from modules to a building.

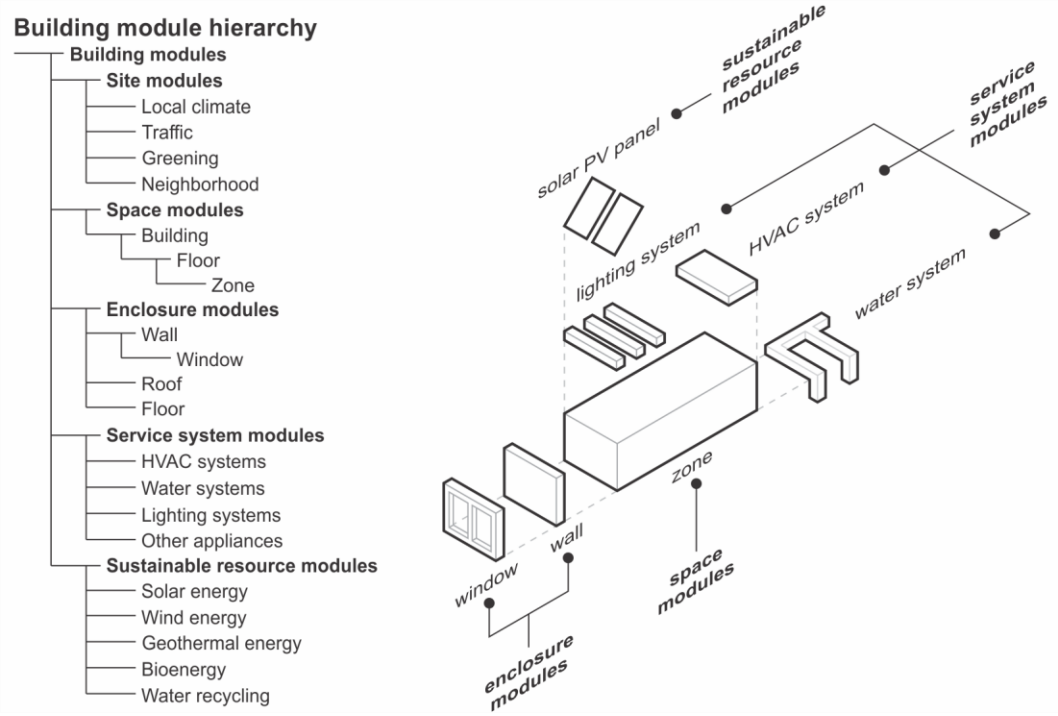

(b) Building module hierarchy and an example of building modules.

Figure 2-2. Building module hierarchy and schematics of building modules.

A building module is defined as an autonomous functional building block containing design and control parameters that determine its physical state and performance. It is represented as an object consisting of module parameters, state variables, interface variables, performance indicators and methods (Figure 2-3). Module parameters are further divided into design parameters and control parameters. The design parameters are those parameters determining the module's composition, geometry, and physical properties, which vary with the module types. For example, the design parameters for an enclosure wall module include the geometric dimensions, window-to-wall ratio, R-value, specific heat, and radiant absorption coefficients. Control parameters are parameters that can be adjusted during operation, such as the percent of shading for the window, and the setpoint

temperature of the HVAC system. The definition of these parameters is ready for system control and optimization. The state variables are those representing the physical state of the module, e.g., temperatures at selected locations across the wall, and the indoor concentration of a certain pollutant. The interface variables are the boundary conditions subjecting to which the module would operate. They can be either the values of the state variables at the module's boundaries or the flux related to the gradient of the state variables at the boundary, e.g., the temperature and heat flux at the boundary for building enclosure modules. The design features are usually used as the inputs for physics-based modelling.

Performance indicators are used to quantify the performance metrics of the module, such as energy saving, IAQ, thermal comfort, and risk mitigation effectiveness, in terms of its improvement potential over a reference building module per local standard or best practice. The performance metrics directly calculated through simulation, such as energy consumption, pollutant concentration and PMV/PPD, can be used to quantify the building performance. For energy analysis, the energy saving percentage relative to the reference case is used as the performance indicator. For IAQ analysis, the change of disability-adjusted life years (DALYs) to typical indoor air pollutants of a certain technology to the reference case is calculated to quantify the IAQ improvement of the studied technology. For thermal comfort analysis, the change of PMV compared to the reference case is estimated. For infection risk analysis, the infection probability changes of using a specific technology compared to the reference case is calculated as the performance indicator. The detailed definition and calculation of different performance metrics are introduced in Section 2.1.3.

The performance of a green building module or whole building may vary across regions under different climate and weather conditions. Therefore, the green performance of each building module of the target building can be evaluated by comparing its performance metrics to a local reference building. A local reference building is defined as a building, with its construction complying with the local standards/codes or adopting the local best practice. The local best practice of building design can be accessed through the local building documents, reports, cases, or available datasets, e.g., the Building Performance Database (LBNL 2011). When the local best practice is unavailable or does not meet the local building standards and codes, then the local standards and codes will be adopted to define the reference building. Many standards or codes have developed reference criteria for various types of buildings. For example, DOE (U.S. DOE 2020) has developed commercial reference buildings of 16 building types that represent approximately 70% of the commercial buildings in the U.S., according to a report published by the National Renewable Energy Laboratory (NREL) (Deru et al. 2011). The reference buildings provide complete descriptions for whole building energy analysis using EnergyPlus. The Pacific Northwest National Laboratory (PNNL) modified the DOE commercial prototype building models (U.S. DOE 2013) to accommodate the ASHRAE Standard 90.1 (ASHRAE 2019c) and International Energy Conservation Code (IECC) (ICC 2009). The PNNL commercial prototype buildings (U.S. DOE 2013) cover all DOE reference building types (with the exception of supermarkets), and also an additional prototype representing high-rise apartment buildings, resulting in 16 commercial building types in 19 climate locations. For residential buildings, PNNL uses two base prototypes to simulate single-family detached houses and multi-family low-rise apartment buildings (U.S. DOE 2013). These prototypes are then modified to accommodate four different heating system types and four foundation types typically found in new residential

construction. For single-family houses in the U.S., NREL has developed the benchmark building for each climate zone (i.e. Building America B10 Benchmark (Wilson et al. 2014)), which is consistent with the 2009 IECC (ICC 2009). Besides, ASHRAE standards (ASHRAE 2018, 2019b) defined the design criteria like envelope construction and ventilation requirement for single-family house in each climate zone, which should also be satisfied by the local reference house. The IEA Annex 68 project developed a detailed procedure along with an example for defining a local reference building for both IAQ and energy performance evaluation (Zhenlei Liu et al. 2017; Qin and Zhang 2020). Baseline settings of public buildings in terms of airborne infection risk estimation and IAQ evaluation were also presented recently (Shen, Kong, Dong, et al. 2021a). For a module's performance, the percentage of improvement over the local reference building due to the application of the green technology used in the module will be calculated. The definition of building modules, particularly the module parameters, is like the building components defined in the EnergyPlus input data files (IDFs). But the building modules defined by this study contain performance indicators and can provide interactive performance feedback, which is a big difference from IDFs. All the building systems, components or elements at any level can be modularized following this modular framework and structure. The improvement of building performance compared to the reference case will be calculated as the metrics to indicate the performance and effectiveness of certain building module.

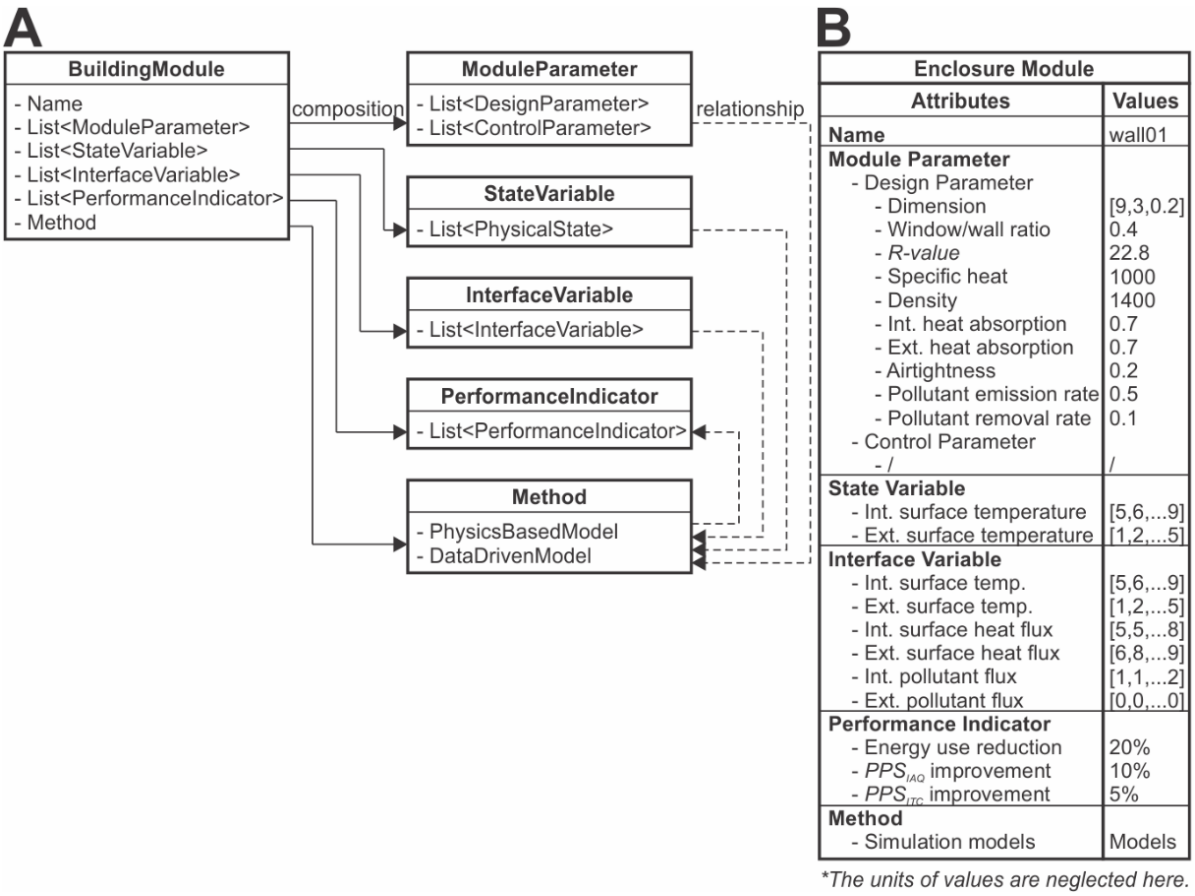

Figure 2-3. (a) Structure and composition of a building module and (b) an example of an enclosure module (wall module).

2.2.2 Reduced-order physics-based models

Physics-based modeling has been adequately developed over the past decades and it uses elaborated physical functions of thermodynamics, fluid dynamics and mass transfer to perform calculation precisely, and usually includes simplified modeling and detailed comprehensive modeling (ANSYS 2021; DOE 2017; NIST 2018). Due to lack of comprehensive parameters of building characteristics in early design phase and the considerable simulation process time, comprehensive/detailed physics-based modelling is usually not practical and unfavorable for

early-phase building design and performance analysis. Reduced-order physics-based models of energy and IAQ equations with certain assumptions and simplifications are more suitable for early-phase building performance analysis, which can simplify inputs through the modular approach and get (near) real-time modelling response (Rahman 2019; Xu and Wang 2007). Reduced-order resistance-capacitance (RC) thermal or air network models have been applied to simulate the thermal, air and mass transfer and balance in buildings, which are also used in this study (Braun and Chaturvedi 2002; Hao 2019; D. W. Kim et al. 2013; Z. Li et al. 2021; Mirakhorli and Dong 2016; O'Neill et al. 2010; O'Neill and Narayanan 2014; Ogunsola et al. 2014; Rahman 2019; S. Wang and Xu 2006; Xu and Wang 2007; K. Zheng et al. 2016). The RC networks, including 3R2C and 2R2C models, are used to derive a set of first order differential equations representing the building thermal, air, and mass transfer and balance. An example of RC network model for simulating thermal balance is shown in Figure 2-4. Previous studies have shown that the RC network can describe building physics in good accuracies (Hao 2019; D. W. Kim et al. 2013). Therefore, the RC network is applied to describe the thermal, air, and mass transfer and balance in this study. The used physical models in this study include thermal balance models, air balance models, and pollutant mass balance models, as well as the equations for determining the heating and cooling load, energy use, thermal comfort, occupant exposure to pollutants and health impact metrics, infection risk through airborne transmission, and cost assessment. The models are usually called nodal models or multi-zone models or lumped models, which only uses one node to represent a space or component. For example, in IAQ and pollutant transmission simulation, the indoor air is typically assumed to be well-mixed.

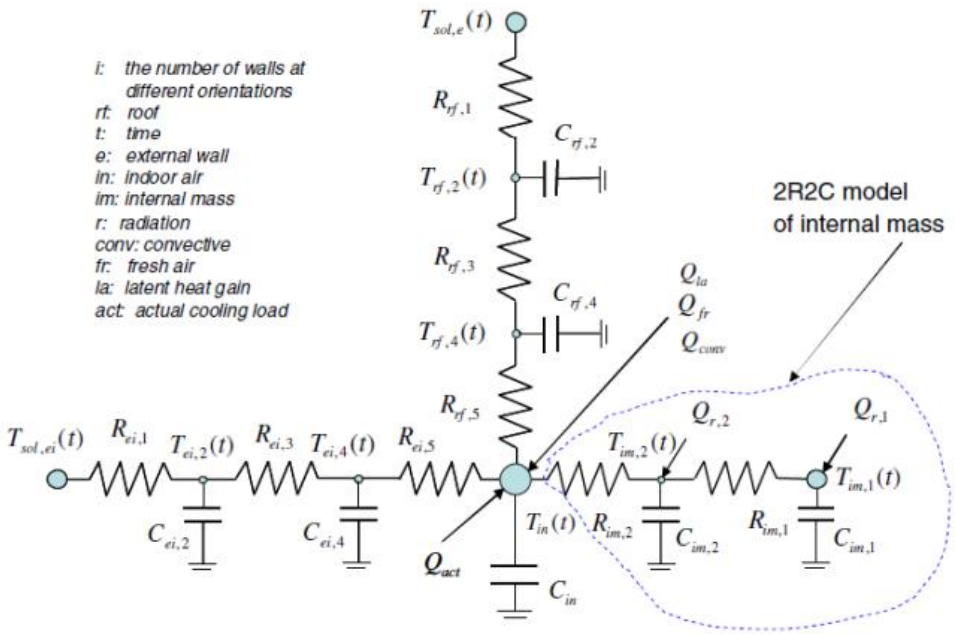

Figure 2-4. An example of RC network model for thermal modelling (S. Wang and Xu 2006).

2.2.2.1 Thermal models

Heat transfer in a building can be illustrated by Figure 2-5. Based on the RC thermal network, the energy balance equation for building envelopes has been applied to get the state-space model. The values of resistance and capacitance in the model represent the thermal resistance and thermal capacitance of the building, which depend on the building thermal properties. The RC network for thermal transfer and balance modelling is illustrated in Figure 2-6. In general, the resistances in the RC network cover outside convection resistances, wall conduction resistances, inside convection resistances, and window thermal resistance. The thermal mass effects are represented by the capacitances in the RC model. The network also includes the external and internal heat gains/losses that apply on external or internal thermal nodes. The R_s, C_s, and heat gain or loss on each node (q_s) are input parameters that are known for modelling, while air temperatures and

surface temperatures are the state variables that need to be calculated. Outdoor air temperature and ground temperature are the boundary conditions for the thermal network. In the present work, the Energyplus weather (EPW) files are adopted to use the dry air temperature and ground temperature as the boundary for modelling.

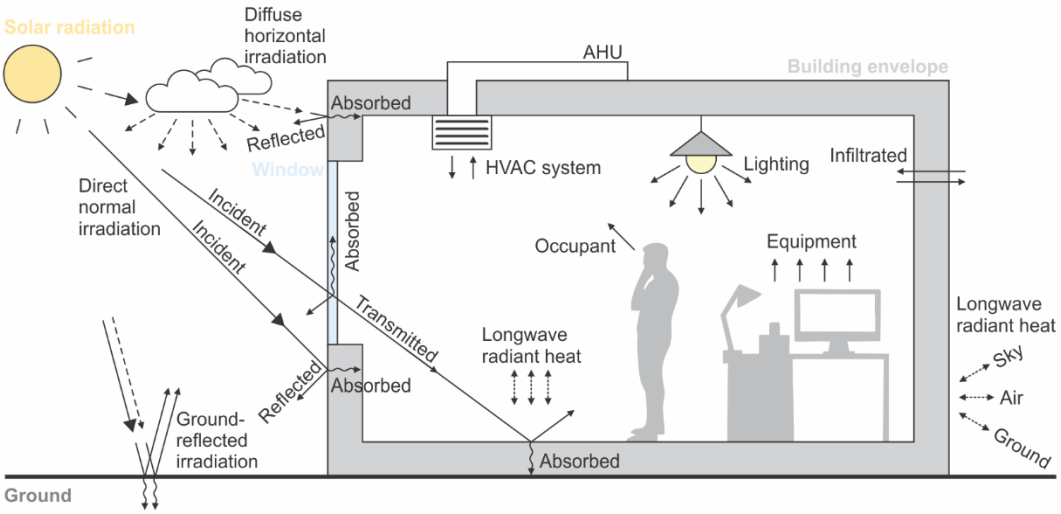

Figure 2-5. Schematic of heat transfer in a building.

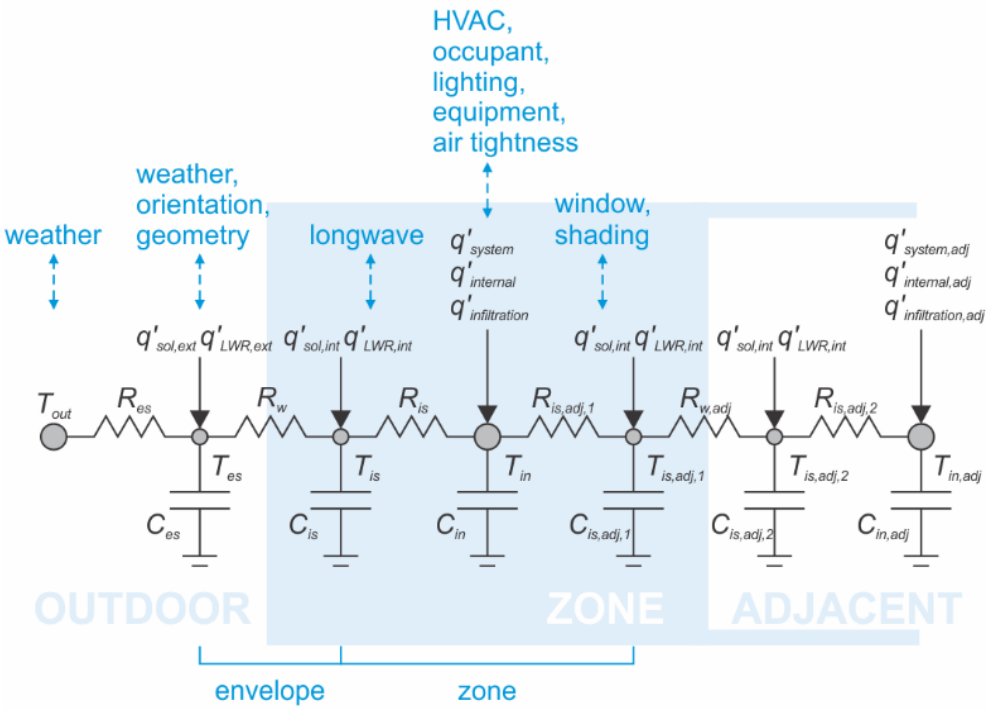

Figure 2-6. Schematic of the simplified thermal balance models in RC network.

As shown in Figure 2-7, the air temperature in each zone (room) of the network can be represented as a space node, and each envelope (external/internal wall/window) can be represented by two surface nodes (one for each side). Each envelope module can be represented by 3 Rs and 2 Cs, including the resistance of envelope (R_w), the resistance between internal surface and interior air (R_{is}), and resistance between external surface and exterior air (R_{es}), and two equivalent capacitances that equally represent the half of the thermal mass of the envelope (C_{is} and C_{es}). For each envelope, a 3R2C model is established. For an individual room, a bunch of 3R2C models are constructed and connected with each other through the space node (room air). For a building with multiple rooms, the 3R2C models of different rooms are connected by identical space nodes. Therefore, the complexity of the RC network increases with the increase of zones/rooms and

envelopes of the building. For a single room with 6 walls and no windows or other openings, the RC network typically contains 6 3R2C models connected by the space node, resulting in 1 indoor air node, 5 outdoor air nodes, 1 ground node, and 12 envelope surface nodes, which means 13 Cs (12 surface Cs and 1 indoor air C) and 18 Rs in total. Figure 2-7 shows a schematic of the RC network for a simplified two-floor building with 6 rooms (no windows). A total of 6 space nodes, 3 ground nodes, 19 outdoor air nodes, and 58 envelope surface nodes are presented. For transient thermal modelling, three types of models can be established, including the thermal models on exterior surface nodes (Eq. 2-1), the models on interior surface nodes (Eq. 2-2), and the models on space/air nodes (Eq. 2-3):

$$C_{es}\frac{dT_{es}}{dt} = \frac{T_{out}-T_{es}}{R_{es}} - \frac{T_{es}-T_{is}}{R_w} + q'_{sol,out} + q'_{rad,out} \tag{2-1}$$

$$C_{is}\frac{dT_{is}}{dt} = \frac{T_{es}-T_{is}}{R_w} - \frac{T_{is}-T_{in}}{R_{is}} + q'_{sol,in} + q'_{rad,in} \tag{2-2}$$

$$C_{in}\frac{dT_{in}}{dt} = \frac{T_{is}-T_{in}}{R_{is}} - \frac{T_{in}-T_{is,adj,1}}{R_{is,adj,1}} + q'_{system} + q'_{internal} + q'_{infiltration} \tag{2-3}$$

where *T* is temperature, *C* is thermal capacity (for thermal balance models), *R* is thermal resistance (for thermal balance models), *q'* is heat flow, and *t* is time. For subscripts, *es* is exterior surface, *is* is interior surface, *w* is wall, *out* is outdoor or outside, *in* is indoor or inside, *adj* is adjacent zone, *sol* is solar heat, and *rad* is longwave radiant heat.

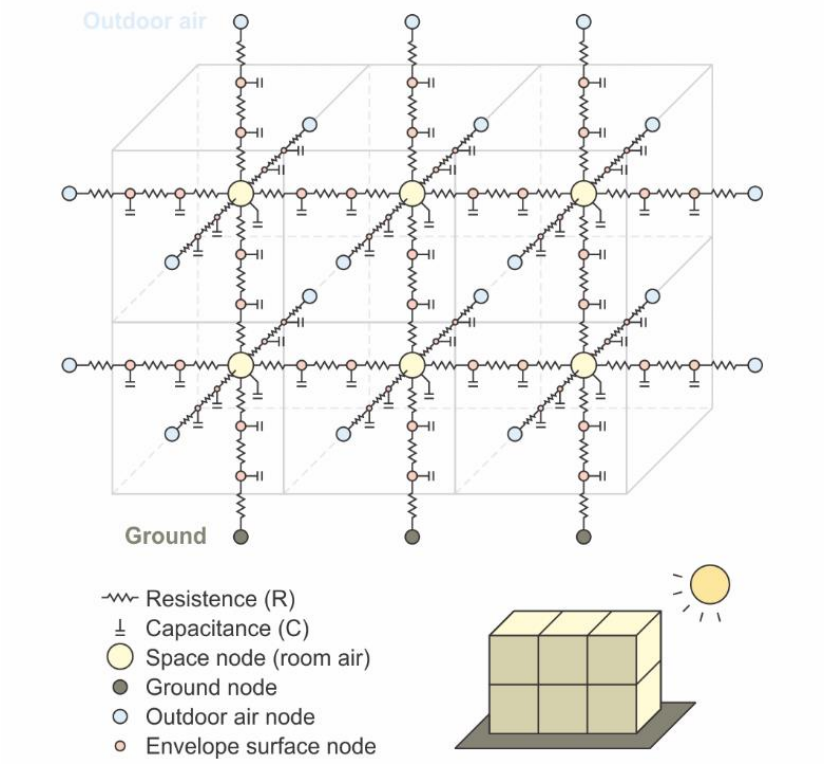

Figure 2-7. A schematic of the RC network for a two-floor building.

The thermal resistance of the building envelope module in the model is related to but not identical to the R-value of the wall assembly. It depends on the building geometry (thickness and area) and the thermal conductivity:

$$R_w = \frac{R-value}{A} = \frac{L}{k_w \cdot A} \tag{2-4}$$

where L is thickness of envelope, k_w is thermal conductivity. The thermal resistance near the envelope surfaces (interior and exterior) determines the thermal transfer between the envelope surface and the indoor or ambient air. It depends on the thermal convection near the surface as given by

$$R_{is} = h_{is}A \tag{2-5}$$

$$R_{es} = h_{es}A \tag{2-6}$$

where h_{is} is the convective heat transfer coefficient on the interior surface, h_{es} is the convective heat transfer coefficient on the exterior surface. The convective heat transfer coefficient is related to the airflow velocity near the surface. Substantial research has gone into the formulation of models for estimating the convection coefficient on building surfaces, such as the simple combined model, the TARP approach, and the MoWiTT approach (EnergyPlus 2022b). In this study, the simple combined model is applied. The simple algorithm uses surface roughness and local surface windspeed to calculate the heat transfer coefficient (EnergyPlus 2022b). The basic equation used is:

$$h = D + E \cdot v_z + F \cdot {v_z}^2 \tag{2-7}$$

where h is heat transfer coefficient, v_z is local wind speed calculated at the height above ground of the surface centroid, D, E, and F are material roughness coefficients as shown in Table 2-2.

The local wind speed is dependent on the meteorological data and local environments like the surrounding terrain. It is usually calculated by Eq. (2-8). The wind speed profile coefficients α_{wind}, δ, α_{met}, and δ_{met}, are variables that depend on the roughness characteristics of the surrounding terrain. Typical values for α_{wind} and δ are shown in Table 2-3. The default value for z_{met} for wind speed measurement is 10 m above ground. The default values for α_{met} and δ_{met} are 0.14 and 270 m, respectively, because most meteorological stations are located in an open field.

$$v_z = v_{met}\left(\frac{\delta_{met}}{z_{met}}\right)^{\alpha_{met}}\left(\frac{z}{\delta}\right)^{\alpha_{wind}} \tag{2-8}$$

where z is altitude or height above ground, v_z is wind speed at altitude z, α_{wind} is wind speed profile exponent at the site, δ is wind speed profile boundary layer thickness at the site, z_{met} is height above ground of the wind speed sensor at the meteorological station, v_{met} is wind speed measured at the meteorological station, α_{met} is wind speed profile exponent at the meteorological station, and δ_{met} is wind speed profile boundary layer thickness at the meteorological station.

Table 2-2. Coefficients to calculate material heat transfer properties.

Roughness index	***D***	***E***	***F***	**Example material**
1 (Very Rough)	11.58	5.894	0.0	Stucco
2 (Rough)	12.49	4.065	0.028	Brick
3 (Medium Rough)	10.79	4.192	0.0	Concrete
4 (Medium Smooth)	8.23	4.0	-0.057	Clear pine
5 (Smooth)	10.22	3.1	0.0	Smooth Plaster
6 (Very Smooth)	8.23	3.33	-0.036	Glass

Table 2-3. Coefficients to determine local wind speed.

Terrain description	**Exponent, α_{wind}**	**Boundary layer thickness, δ [m]**
Flat, open country	0.14	270
Rough, wooded country	0.22	370
Towns and cities	0.33	460
Ocean	0.10	210
Urban, industrial, forest	0.22	370

The thermal capacitance is related to the specific heat of the material. For each envelope, two identical thermal capacitances are defined in this model. For indoor air, the capacitance depends on the specific heat of air and the room volume. They can be calculated as given by

$$C_{es} = C_{is} = \frac{\rho_w C_{p,w} AL}{2} \tag{2-9}$$

$$C_{in} = \rho_{air} C_{p,air} V \tag{2-10}$$

where C_{es} is the thermal capacitance on the exterior surface, C_{is} is the thermal capacitance on the interior surface, C_{in} is the thermal capacitance of indoor air, ρ_w is the density of wall material, C_p is the specific heat of the wall material, A is the wall surface area, L is the wall thickness, ρ_{air} is the air density, $C_{p,air}$ is the specific heat of indoor air, and V is the room volume.

The external heat exchange between the exterior surfaces and the surrounding environment mainly includes solar radiation (or shortwave radiation) and longwave radiant heat exchange. Solar radiation is a key factor affecting building thermal environment. The incident solar radiation on a specific building envelope (exterior or interior) depends on the solar intensity and the geometry of the envelope. Some studies used the clear sky solar radiation model to estimate, which determines the angle of inclination on the surface based on the geographical location and the time of the day and of the year. In this study, the ambient solar intensity is obtained from the solar radiation data

in EPW files, including direct normal irradiation (DNI) and diffuse horizontal irradiation (DHI). Direct normal irradiation is the amount of solar radiation received directly from the solar disk on a surface perpendicular to the sun's rays, which means the incident DNI on building surfaces also depends on the angle of incidence θ_{in} (between sun's rays and normal to the surface). Diffuse horizontal irradiation is the terrestrial radiation received by a horizontal surface which has been scattered or diffused by the atmosphere. The heat flux on the exterior envelope from the diffuse solar radiation is also dependent on the angle between the surface and the sky ($\theta_{s\text{-}sky}$). Partial of DNI and DHI incident on the ground are reflected to the building envelope. The incident solar radiation (direct, diffuse, and ground-reflected) on the opaque building envelope is either reflected or absorbed by the exterior of the envelope, depending on the surface absorptance of the envelope. The incident solar radiation on the transparent building envelope (e.g., windows) can be reflected, absorbed, or transmitted, depending on the glazing characteristics. Eq. 2-11 determines the relationship of absorptance (α), reflectance (ρ), and transmittance (τ) of the envelope. The transmitted solar radiation enters the indoor space and strikes interior surfaces (walls, floor, furniture, etc.). Therefore, the total heat flux of solar radiation on the exterior envelope is the summation of incident DNI ($q'_{DNI,ext}$), DHI ($q'_{DHI,ext}$), and the ground-reflected solar radiation ($q'_{sol\text{-}reflected,ext}$), which can be determined by Eqs. 2-12 to 2-15 (DesignBuilder Software Ltd 2017a, 2017b; EnergyPlus 2022d). If the heat flux of DNI on the exterior surface calculated by Eq. 2-13 is negative, meaning that the direct solar irradiation does not strike on the exterior surface, the heat flux equals zero. The ground-reflected solar radiation depends on the ground reflectance (ρ_{gnd}), the sun's zenith angle (θ_z), and the envelope surface angle ($\theta_{s\text{-}sky}$). Ground reflectance is a factor between 0 and 1 that characterizes the fraction of solar radiation reflected by the ground. Some typical ground reflectance values are shown for various surface types in Table 2-4. The default

ground reflectance in this study is 0.2, representing typical ground types in urban or suburban areas (ASHRAE 2017a). For the ground with snow covered, a modifier is usually multiplied by the ground reflectance. The snow-covered ground usually has higher reflectance. Table 2-4 also shows the typical reflectance for snow-covered ground types. The heat flux on the exterior surface from reflected solar radiation also depends on the angle between the surface and the ground ($\theta_{s\text{-}gnd}$).

$$\rho + \tau + \alpha = 1 \tag{2-11}$$

$$q'_{sol,ext} = q'_{DNI,ext} + q'_{DHI,ext} + q'_{sol-reflected,ext} \tag{2-12}$$

$$q'_{DNI,ext} = \alpha \cdot I_{DNI} \cdot \cos(\theta_{in}) \tag{2-13}$$

$$q'_{DHI,ext} = \alpha \cdot I_{DHI} \cdot \frac{1+\cos(\theta_{s-sky})}{2} \tag{2-14}$$

$$q'_{sol-reflected,ext} = \alpha \cdot (I_{DNI} \cdot \cos(\theta_z) + I_{DHI}) \cdot \rho_{gnd} \cdot \frac{1-\cos(\theta_{s-gnd})}{2} \tag{2-15}$$

Table 2-4. Reflectance of typical ground types (DesignBuilder Software Ltd 2017a).

Surface Type	**Surface Reflectance**
Water (large angle of incidences)	0.07
Coniferous forest (winter)	0.07
Bituminous and gravel roof	0.13
Dry bare ground	0.20
Weathered concrete	0.22
Green grass	0.26
Dry grassland	0.2 to 0.3
Desert sand	0.4
Light building surfaces	0.6
Snow-covered typical city center	0.2
Snow-covered typical urban site	0.4
Snow-covered typical rural site	0.5
Snow-covered isolated rural site	0.7

The radiant heat on exterior surfaces represents the longwave infrared radiation exchange between the surface, the ambient air, the ground, and the sky. The longwave heat exchange is a potential approach for building passive cooling during the nighttime (Craig et al. 2008; Hu et al. 2022; Okoronkwo et al. 2014). The radiation heat flux is calculated from the surface emittance (= absorptivity), surface temperature, sky, air and ground temperatures, and sky and ground view factors. It is assumed that each surface emits or reflects diffusely and is gray and opaque, meaning that the emittance is assumed to be equal to the absorptance. Besides, each surface is assumed to be at a uniform temperature and the heat flux is evenly distributed across the surface (EnergyPlus 2022b). The total longwave radiative heat flux ($q'_{LWR,ext}$) is the sum of components due to radiation exchange with the ground ($q'_{LWR,s-gnd}$), sky ($q'_{LWR,s-sky}$), and air ($q'_{LWR,s-air}$) as given by

$$q'_{LWR,ext} = q'_{LWR,s-gnd} + q'_{LWR,s-sky} + q'_{LWR,s-air} \tag{2-16}$$

Applying the Stefan-Boltzmann Law to each component yields, the calculation is represented as (EnergyPlus 2022b)

$$q'_{LWR,ext} = \varepsilon\sigma F_{gnd}\left(T_{gnd}^4 - T_{es}^4\right) + \varepsilon\sigma F_{sky}\left(T_{sky}^4 - T_{es}^4\right) + \varepsilon\sigma F_{air}\left(T_{out}^4 - T_{es}^4\right) \tag{2-17}$$

where ε is longwave emittance of the surface, σ is Stefan-Boltzmann constant, F_{gnd} is view factor of wall surface to ground surface temperature, F_{sky} is view factor of wall surface to sky temperature, F_{air} is view factor of wall surface to air temperature, T_{es} is outside surface temperature, T_{gnd} is

ground surface temperature, T_{sky} is sky temperature, and T_{out} is outdoor air temperature. Linearized radiative heat transfer coefficients are introduced to render the above equation more compatible with the heat balance formulation (EnergyPlus 2022b),

$$q'_{LWR,ext} = h_{r,gnd}(T_{gnd} - T_s) + h_{r,sky}(T_{sky} - T_s) + h_{r,air}(T_{air} - T_s) \quad (2\text{-}18)$$

where $h_{r,gnd}$ is equivalent radiative heat transfer coefficient between envelope surface and ground, $h_{r,sky}$ is equivalent radiative heat transfer coefficient between envelope surface and sky, $h_{r,air}$ is equivalent radiative heat transfer coefficient between envelope surface and air. They can be determined through

$$h_{r,gnd} = \frac{\varepsilon\sigma F_{gnd}\left(T_{gnd}^4 - T_s^4\right)}{T_{gnd} - T_s} \quad (2\text{-}19)$$

$$h_{r,sky} = \frac{\varepsilon\sigma F_{sky}\left(T_{sky}^4 - T_s^4\right)}{T_{sky} - T_s} \quad (2\text{-}20)$$

$$h_{r,air} = \frac{\varepsilon\sigma F_{air}\left(T_{air}^4 - T_s^4\right)}{T_{air} - T_s} \quad (2\text{-}21)$$

The longwave view factors to ground and sky are calculated with the following expressions (Walton 1983):

$$F_{gnd} = \frac{1-cos\Phi}{2} \tag{2-22}$$

$$F_{sky} = \frac{1+cos\Phi}{2} \tag{2-23}$$

where Φ is the tilt angle of the surface. The view factor to the sky is further split between sky and air radiation by a factor β:

$$\beta = \sqrt{\frac{1+cos\Phi}{2}} \tag{2-24}$$

The ground surface temperature is assumed to be the same as the air temperature. The final forms of the radiative heat transfer coefficients are shown here.

$$h_{r,gnd} = \frac{\varepsilon\sigma F_{gnd}\left(T_{air}^4 - T_s^4\right)}{T_{air} - T_s} \tag{2-25}$$

$$h_{r,sky} = \frac{\varepsilon\sigma F_{sky}\beta\left(T_{sky}^4 - T_s^4\right)}{T_{sky} - T_s} \quad (2\text{-}26)$$

$$h_{r,air} = \frac{\varepsilon\sigma F_{sky}(1-\beta)\left(T_{air}^4 - T_s^4\right)}{T_{air} - T_s} \quad (2\text{-}27)$$

The air temperature can be obtained from the weather data (EPW file). The sky temperature (T_{sky}) is calculated from the horizontal infrared radiation intensity (IR_H), which represents the rate of infrared radiation emitted from the sky falling on a horizontal upward-facing surface, and is usually available in the weather data (EPW file) as well (EnergyPlus 2022a). It can be calculated through

$$T_{sky} = (IR_H/\sigma)^{0.25} - 273.15 \quad (2\text{-}28)$$

where T_{sky} is effective mean sky temperature, or sky radiative temperature, °C, IR_H is rate of infrared radiation emitted from the sky falling on a horizontal upward-facing surface, W/m^2.

The solar irradiation on windows consists of three parts, including the reflected, the absorbed, and the transmitted parts. Solar heat gain coefficient (SHGC) is a measure of how much solar radiation is absorbed and transmitted through the glass. It is a commonly used metric for quantifying the shading effectiveness of a glazing material, depending on the glazing material and structure properties. The lower the SHGC, the less solar heat it transmits and the greater its shading ability. The absorbed solar heat by the glass will eventually be transferred to indoor air and other interior

surfaces and occupants through conduction, convection or longwave radiation. Windows will likely work with shading components such as blinds or curtains. The heat balance on shading devices can be very complicated (EnergyPlus 2022e). For example, the solar radiation that is reflected by a venetian blind depends on the slat angle and reflectance of the venetian blind, which is time-varying. In this study, the effectiveness of the window shading devices is simplified and integrated with the SHGC of the window. Therefore, the shading effectiveness will be represented by the equivalent SHGC of the window system. A window system with a more effective shading device has a lower SHGC factor than a window system without or with less effective shading units. The solar radiation transmitted through the window system (including glazing and shading) will be received by various interior surfaces like floor, walls, furniture and occupants. In this study, it is assumed that the transmitted radiation is evenly distributed on each interior surface.

Other internal heat gains include heat generated by electric lights, equipment, and occupants. The total radiant gains from lights must be divided into visible and thermal portions. In this study, the visible part is not calculated as the internal heat gain while the thermal part is added as the heat gain in the equation. For example, the total electric input to typical incandescent lights is converted to 10% visible radiation, 80% thermal radiation, and 10% convective gain. In contrast, the electric input to typical fluorescent lights is converted to 20% visible radiation, 20% thermal radiation, and 60% convective gain. In this study, it is assumed that 20% of lighting input energy is converted to visible part. The rest 80% of input energy is calculated as the internal heat gain. The lighting power in the indoor space can be estimated through ASHRAE 90.1 and 90.2 for different types of indoor spaces (ASHRAE 2018, 2019c). For example, the lighting power density is assumed to be 1 W/ft^2 (10.8 W/m^2) for office spaces. For indoor equipment including computers, the internal heat gain

can be directly set up by the users. For portable air cleaners, it is assumed that 30% of the input energy is converted to the convective heat while 70% of the input energy is consumed to drive the fan. A survey showed that the median electric power of portable air cleaners is around 56W, which is applied in this study.

Table 2-5. The distribution of performance and price for 100 best-selling air purifiers in China (adapted from (B. Zhao et al. 2020a)).

	P5	**P25**	**Median**	**P75**	**P95**
Clean air delivery rate (CADR) [m^3/h]	170	250	361	455	800
Electric power [W]	22	44	56	70	145
Electric power per CADR [$W/(m^3/h)$]	0.10	0.12	0.15	0.19	0.28

Heat is generated in the human body by metabolic activities. The heat is dissipated from the body surface and respiratory tract by a combination of radiation, convection (sensible heat), and evaporation (latent heat) (EnergyPlus 2022f). Latent heat is not considered in this study. The heat released by the occupants depends on the metabolic rate, which equals 0.7 MET for sleeping, 1.0 MET for quietly seated, 1.2 MET for relaxed standing, 1.7-3.8 MET for walking/running at different speeds, and 4.0 MET and higher for heavy works (Tartarini et al. 2020). Therefore, metabolic rates in typical indoor scenarios are around 104-125W (1.0-1.2 MET) assuming a body

surface area of 1.8 m^2 (Figure 2-8), in which the convective heat loss was approximately 40% of the total heat loss (Murakami et al. 2000; Y. Yan et al. 2016).

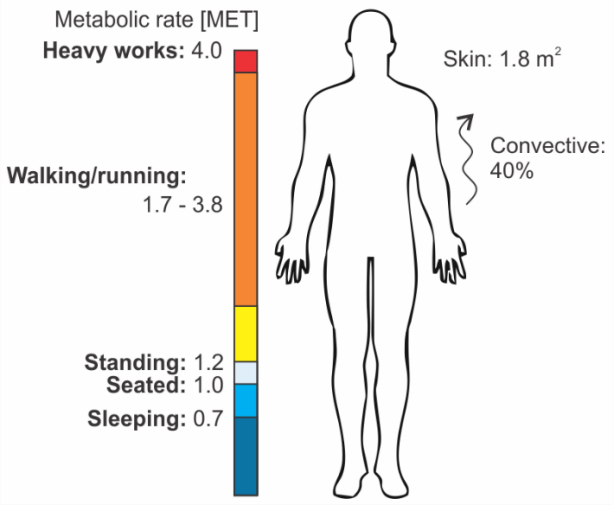

Figure 2-8. Occupant activity settings.

The actual internal heat gains from lights, equipment, and occupants also rely on their schedules and activities, which can vary greatly in different scenarios. Figure 2-9 (a) illustrates the simplified schedule of occupancy in office scenarios during weekdays and weekends. Occupant densities in different scenarios are determined by ASHRAE 62.1 (ASHRAE 2019a). The occupant density during weekends and holidays is maintained at zero. Figure 2-9 (b-c) shows the lighting and equipment schedules in office scenarios during weekdays and weekends, which are from the default settings in EnergyPlus (DOE 2017). In this study, simplified schedules are adopted to demonstrate the platform. More complicated and realistic schedules can always be input to the program to increase the representation of simulations. For example, the occupant schedules in the ASHRAE occupant behavior database (ASHRAE 2022) can be applied in the model.

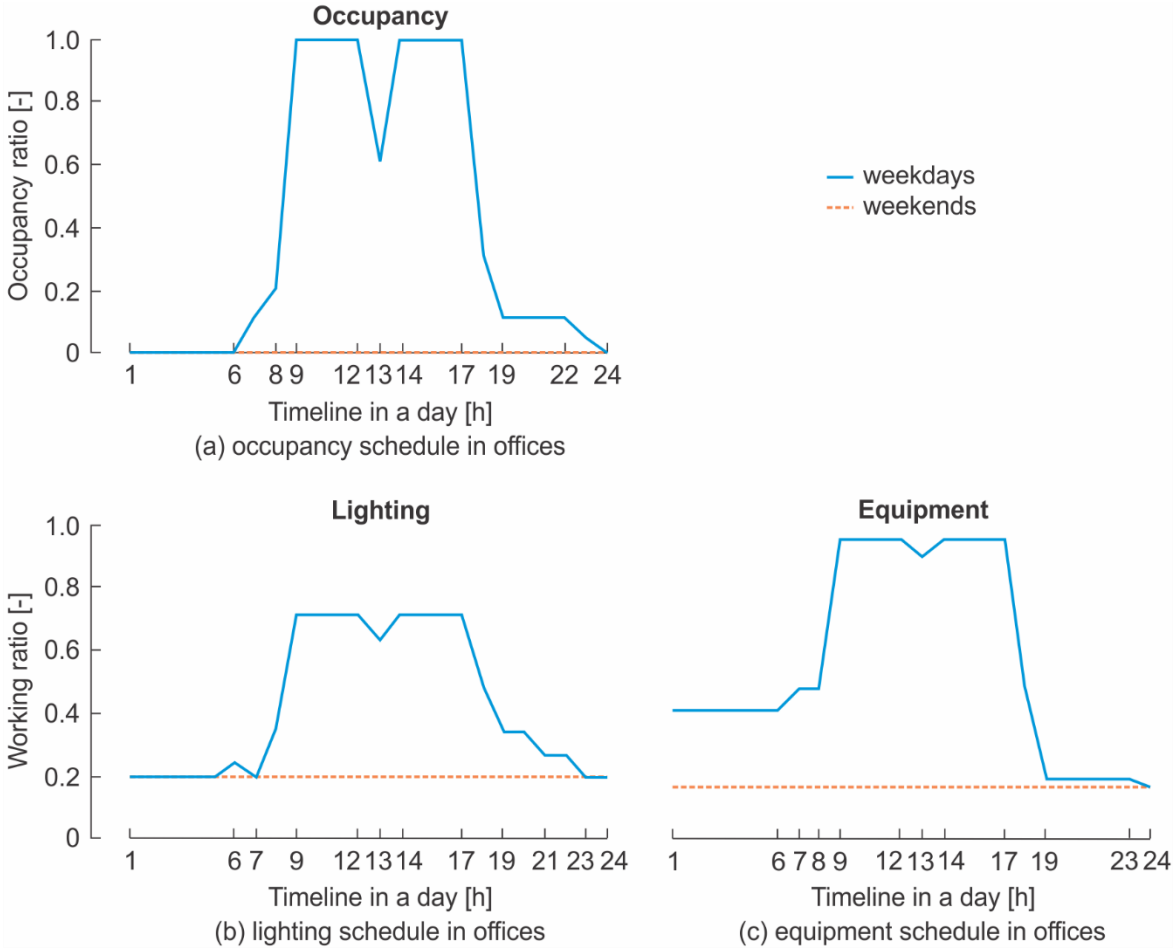

Figure 2-9. (a) Occupancy schedule, (b) lighting schedule, and (c) equipment schedule in office scenarios during weekdays and weekends.

Air infiltration through building enclosure can contribute greatly to indoor heat gain/loss as well as indoor air quality, therefore, is very significant for indoor thermal and air quality control (Crowe 2015). Eq. 2-29 represents the heat transfer through air infiltration between indoor and outdoor air. The infiltration rate can be estrimated based on the pressurization tests under a specific pressure difference, usually 50 or 75 Pa, and the enclosure area. Many building standards have proposed

the suggested or mandatory baseline/reference of building enclosure air tightness (Table 2-6). ASHRAE 90.1 (ASHRAE 2019c) and IECC standards indicate that the measured air leakage through the building enclosure shall not exceed 2 L/s/m^2 (0.4 CFM/ft^2) at 75 Pa. The 2021 International Green Construction Code (IgCC) requires the measured air leakage through enclosure shall not exceed 1.25 L/s/m^2 (0.25 CFM/ft^2) enclosure area (at 75 Pa). The PHIUS standard requires the highest air tightness with the measured air leakage through enclosure below 0.5 L/s/m^2 (0.1 CFM/ft^2) or 0.4 L/s/m^2 (0.08 CFM/ft^2) at 75 Pa pressure difference. In this study, the ASHRAE baseline (2 L/s/m^2 or 0.4 CFM/ft^2) is used as the reference air tightness level for building enclosure. The total air infiltration rate of the space equals the summation of the air infiltration rate though each exterior envelope.

$$q'_{infiltration} = C_{p,air} \cdot m'_{inf} \cdot (T_{out} - T_{in}) \tag{2-29}$$

Table 2-6. Air tightness requirements in different standards.

Standard	**Building type**	**Air tightness target**
ASHRAE 90.1 (ASHRAE 2019c)	All buildings except low-rise residential buildings	2 L/s/m^2 (0.4 CFM/ft^2) @ 75 Pa
IECC 2021 (International Code Council (ICC) 2021)	Commercial buildings	2 L/s/m^2 (0.4 CFM/ft^2) @ 75 Pa
	Residential buildings	3.0 ACH_{50}

IgCC 2021 (ICC and ASHRAE 2021)	All buildings	1.25 L/s/m^2 (0.25 CFM/ft^2) @ 75 Pa
LEED BD+C (USGBC 2013)	Residential buildings	Varies
Net Zero Energy	All buildings	1.0 ACH_{50}
Passive house (Passivhaus Institute 2023)	All buildings	0.6 ACH_{50}
PHIUS+ 2015 (Salonvaara et al. 2015)	Buildings with 5+ storeys	0.5 L/s/m² (0.1 CFM/ft^2) @ 75 Pa
	All other buildings	0.4 L/s/m² (0.08 CFM/ft^2) @ 75 Pa

HVAC systems are used to condition the supply air to meet certain heating or cooling loads in the space/building. Heating and cooling loads can be estimated through the proposed models. An ideal HVAC system was set up to meet the heating/cooling loads. In this study, the energy consumption by the HVAC system mainly includes the energy use by the heating/cooling coils for conditioning the air, and the fan used to drive the air in the duct. Other energy end-use sectors also include the lighting energy use, equipment energy use, and energy uses by other facilities (e.g. portable air cleaners).

Renewable energy technologies can utilize renewable resources such as solar radiation, geothermal, and wind energy, to produce energy and reduce the net energy consumption. Typical renewable energy generation technologies are presented in later sections. Solar energy is typically the most utilized energy in buildings, through either passive (e.g., solar chimney) or active (e.g., photovoltaics panel or PV panel) utilizations. In this study, a simple PV panel example is presented. The physical model for the simple PV panel example is:

$$P_{PV} = A_{PV} \cdot f_{activ} \cdot G_T \cdot \eta_{cell} \cdot \eta_{invert} \tag{2-30}$$

where P_{PV} is the electrical power produced by photovoltaics, A_{PV} is the net area of PV surface, f_{activ} is the fraction of surface area with active solar cells, G_T is the total solar radiation incident on PV array, η_{cell} is the module conversion efficiency, η_{invert} is the DC to AC conversion efficiency. Net energy use can be estimated by considering both energy consumption and energy generation.

2.2.2.2 Air and mass transfer models

For the airflow network based on the RC approach, the room air infiltration, natural ventilation, mechanical ventilation, contaminant sources and removals are considered. Research has shown that the RC network can describe the building heat transfer and a model with higher quality can give a better estimation accuracy (Hao 2019; D. W. Kim et al. 2013). The RC thermal/airflow network models have also been applied to integrate advanced control strategies such as model predictive control (MPC) in buildings (Boodi et al. 2019; Mirakhorli and Dong 2016), or work with other statistical methods such as genetic algorithm (GA) to establish hybrid models based on

measurements or other datasets for better predicting building performance (Hao 2019; Xu and Wang 2007). In general, the reduced-order RC network models can provide fast and relatively accurate estimations on building performance with simplified inputs. Therefore, it is probably more suitable to apply reduced-order models in the early design phase as many physical information of buildings or systems required by detailed physics-based models/tools is unavailable at early design phase, which may result in poor prediction performance if failed to provide accurate inputs. Besides, the detailed physics-based models/tools usually consume more processing and simulation time, which is unfavorable for early-phase building design as there are always rapid changes to the building design at this phase, so real-time or near-real-time feedback of building performance estimation is required.

The transfer of indoor air pollutants and pathogens is illustrated in Figure 2-10. Indoor air pollutants can be originated from the outdoor air and indoor emission sources. Outdoor pollutants enter the indoor environment through infiltration or national ventilation, as well as the air duct system. Indoor emission sources can be from interior materials, furniture, equipment, and occupant activities, depending on the nature of the pollutant species. Indoor pollutants can be removed by natural deposition on material surfaces, chemical reactions with materials and gaseous compounds, and filtered/removed by indoor air cleaning devices (e.g. portable air cleaners). Chemical reactions between compounds may also generate secondary emissions of pollutants. Pollutants can also be transmitted between different rooms or spaces. Respiratory airborne pathogens (e.g. virus-laden aerosols) are generated by respiratory activities of the infectors.

Air duct system plays an important role in pollutant and infection risk control, depending on the system design and pollutant/pathogen nature. Pollutants can be transmitted between rooms or spaces through the central HVAC system. Return air from each room gets mixed in the return air duct. A part of the return air gets recirculated and mixed with the outdoor air, filtrated or cleaned by the air cleaning equipment or filters and then supplied to the rooms/spaces again. Therefore, air pollutants may get cross-contaminated between rooms.

The mass balance equation for a specific indoor air pollutant can be presented as Eq. 2-31.

$$\frac{dC_i}{dt} = \frac{m'_{inf,i}}{V_i}(P_i C_{out} - C_i) + \frac{m'_{hvac,i}}{V_i} C_{hvac,s} - \frac{m'_{hvac,i}}{V_i} C_i + \sum(\frac{m'_{adj,j}}{V_i} C_{adj,j}) - \frac{m'_{PAC,i}}{V_i} \eta_{PAC,i} C_i - k_{d,i} C_i - k_{a,i} C_i + k_{b,i} C_i + \frac{E_i}{V_i} - \frac{R_i}{V_i} \quad (2\text{-}31)$$

where,

$$C_{hvac,r} = \frac{\sum(m'_{hvac,i} \times C_i)}{\sum m'_{hvac,i}} \quad (2\text{-}32)$$

$$C_{hvac,s} = (1 - \eta_{ACD})(1 - \eta_{filter})\left[\varepsilon_{hvac,rec} C_{hvac,r} + (1 - \varepsilon_{hvac,rec}) C_{out}\right] \quad (2\text{-}33)$$

where, C_i is the indoor concentration of the specific pollutant in room i, C_{out} is the outdoor concentration of the specific pollutant, P_i is the penetration factor of the pollutant through infiltration or natural ventilation, $m'_{inf,i}$ is the air flow rate of air infiltration or natural ventilation between the outdoor air and the indoor air of room i, $C_{hvac,s}$ is the pollutant concentration of the supply air of the HVAC system, $m'_{hvac,i}$ is the supply and return air flow rate of the HVAC system to room i, $m'_{adj,j}$ represents the air flow rate between room i and the adjacent room j, $C_{adj,j}$ is the pollutant concentration of the adjacent room j, $m'_{PAC,i}$ is the air flow rate of the portable air cleaners (PAC) in room i, $\eta_{PAC,i}$ is the pollutant removal efficiency of the PAC in room i, $k_{d,i}$ is the deposition rate of the pollutant in room i, $k_{a,i}$ is the first-order reaction rate of the pollutant with other gaseous compounds in room i, $k_{b,i}$ is the first-order generation rate of the pollutant due to reactions in room i, E_i is the total concentration-independent emission rate of the pollutant in room i, R_i represents the total concentration-independent removal rate of the pollutant in room i, V_i is the volume of room i. $C_{hvac,s}$ depends on the pollutant concentration of the system return air ($C_{hvac,r}$), which is the mixture of the return air from all rooms, the recirculated air ratio of the system ($\varepsilon_{hvac,rec}$), and also the outdoor pollutant concentration (C_{out}). The pollutant in the supply air duct is also filtered and cleaned by the air cleaning equipment in the system duct, including filters and other air cleaning devices (ACD). $C_{hvac,s}$ and $C_{hvac,r}$ can be calculated through Eqs. 2-32 and 2-33. Although many pollutants may react with each other and produce other compounds, the coupled simulation of the chemical reactions between multiple pollutants are neglected in this study.

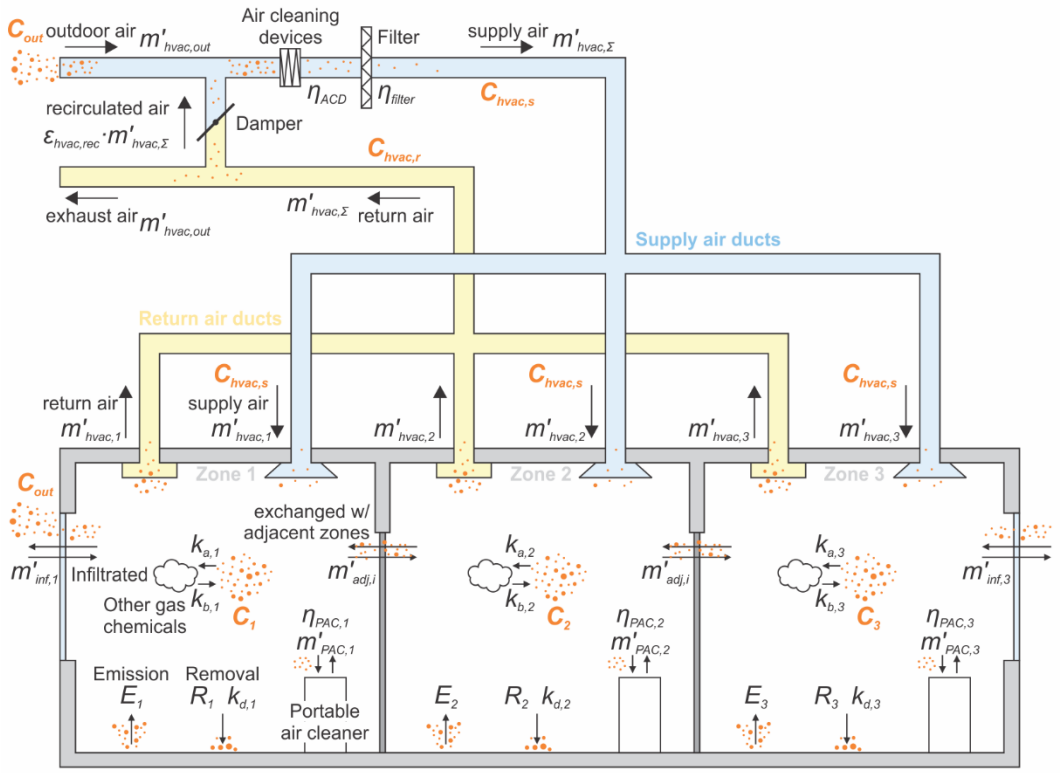

Figure 2-10. Schematic of air and mass (pollutant) flow in a building and its system.

Indoor pollutant generation can vary greatly in different scenarios. Occupant activities and indoor materials, furniture, and decorations, and specific equipment are usually the major indoor emission sources. Occupant activities can generate particles through respiratory activities and other behaviors like walking, vacuuming, cooking, smoking, and burning incense. Research (J. Qian et al. 2014) has revealed that occupant activities can contribute significantly to indoor particles. Occupant respiratory activities can also generate CO2, depending on occupant metabolic rate and age group (Eq. 2-34 and Table 2-7).

$$V'_{CO2} = BMR \times M \times 0.000484 \quad (2\text{-}34)$$

where V'_{CO2} is the volumetric emission rate of CO2, BMR is the basal metabolic rate (BMR), M is the metabolic rate. Ozone is usually generated by laser printer, photocopier, UV lights, ionizer, and specific air cleaners with UV or ionization units (C. Guo et al. 2019). Particle removal can be due to natural deposition or removal by air cleaners or in-duct air cleaning devices like filters. Ozone is very reactive and can be easily deposit on building materials or reacted with other chemicals (Shen and Gao 2018). Typical indoor emission sources and removals of PM2.5 and ozone are shown in Table 2-8.

Table 2-7. BMR of adult age group.

Age	**BMR (MJ/day)**
21 to <30	8.24
30 to <40	7.83
40 to <50	8.00

Table 2-8. Typical emission sources and removal sinks and their rates for common indoor pollutants.

Pollutant	**Emission**		**Removal**	
	Source	**Rate**	**Sink**	**Rate**
PM2.5	Occupant activities (vacuuming) (PM0.5-20) (J. Qian et al. 2014)	300 mg/h	MERV 8 filter (Shen, Kong, Dong, et al. 2021a)	43-54% (removal efficiency)
	Occupant activities (frying) (PM0.01-1) (J. Qian et al. 2014)	540 mg/h	MERV 11 filter (Shen, Kong, Dong, et al. 2021a)	66-74% (removal efficiency)
	Occupant activities (candle burning) (PM0.01-1) (J. Qian et al. 2014)	1560 mg/h	MERV 13 filter (Shen, Kong, Dong, et al. 2021a)	82-86% (removal efficiency)
	Occupant activities (smoking) (PM0.01-1) (J. Qian et al. 2014)	600 mg/h	HEPA filter (Shen, Kong, Dong, et al. 2021a)	99.9% (removal efficiency)
	Occupant activities (incense burning) (PM0.01-1) (J. Qian et al. 2014)	240 mg/h	Natural deposition	0.25 h^{-1} indoors (Shen, Kong, Dong, et al. 2021a)

	Occupant activities (walking) (PM0.8-10) (J. Qian et al. 2014)	480 mg/h		
	Occupant activities (walking) (PM0.4-10) (J. Qian et al. 2014)	54 mg/h		
	Occupant activities (walking) (PM2.5) (J. Qian et al. 2014)	7 mg/h		
	Occupant activities (walking) (PM5) (J. Qian et al. 2014)	24 mg/h		
Ozone	In-duct air cleaners (e.g. ionizer, UV unit) (C. Guo et al. 2019)	62.8 mg/h	Activated carbon filter (Weschler et al. 1994)	90-95% (removal efficiency)
	Ozone generator (C. Guo et al. 2019)	76.3 mg/h	Natural deposition on carpet (Shen et al. 2017; Shen and Gao 2018)	0.07 cm/s (deposition velocity)

Room air cleaners (e.g. ionization-based, UV-based) (C. Guo et al. 2019)	4.6 mg/h	Natural deposition on wooden floor (Shen et al. 2017; Shen and Gao 2018)	0.02 cm/s (deposition velocity)
Photocopier (C. Guo et al. 2019)	3.3 mg/h	Natural deposition on wallpaper (Shen et al. 2017; Shen and Gao 2018)	0.03 cm/s (deposition velocity)
Laser printer (C. Guo et al. 2019)	0.8 mg/h	Natural deposition on painted wall (Shen et al. 2017; Shen and Gao 2018)	0.01-0.07 cm/s (deposition velocity)
Other small devices (C. Guo et al. 2019)	0.4 mg/h	Natural deposition on perlite ceiling tile (Shen et al. 2017; Shen and Gao 2018)	0.05 cm/s (deposition velocity)

2.2.3 Performance metrics

2.2.3.1 Energy consumption

HVAC systems are used to condition the supply air to meet certain heating or cooling loads in the space/building. Heating and cooling loads can be estimated through the proposed models. An ideal HVAC system (variable air volume system, VAV system) was set up to meet the heating/cooling loads. In this study, the energy consumption by the HVAC system mainly includes the energy use by the heating/cooling coils for conditioning the air, and the fan used to drive the air in the duct (E_{fan}). The energy used in the heating/cooling coil (E_{htg} and E_{clg}) is applied to condition the intake air (the mixture of outdoor air and the recirculated air) to the temperature set up for the supply air ($T_{hvac,s}$). The media fluid (refrigerant) in the refrigerator is compressed and driven by the compressor. Electric energy is used to drive the compressor and other compounds in the system. In this study, the refrigeration cycle is simplified by multiplying a conversion factor (η_{coil}) to the energy use to meet the conditioning requirement by the heating/cooling coil (Eqs. 2-35 and 2-36). In this study, the conversion efficiency is assumed to be 0.9.

$$E_{htg} = C_{p,air} \cdot m'_{hvac,s} \cdot \left(T_{hvac,s} - T_{hvac,intake}\right)/\eta_{coil} \quad (2\text{-}35)$$

$$E_{clg} = C_{p,air} \cdot m'_{hvac,s} \cdot \left(T_{hvac,intake} - T_{hvac,s}\right)/\eta_{coil} \quad (2\text{-}36)$$

The fan in the air duct is used to compensate for the pressure drop along the duct and across the filter and other in-duct equipment, to provide sufficient air flow supplied to the space. The fan

power depends on the total pressure drop in the duct system, air flow rate of the duct system, and the conversion factor of the fan, which can be estimated through Eq. 2-37. The total pressure drops in the HVAC system (ΔP_{hvac}) include the pressure drop by the return grille ($\Delta P_{return\ grille}$), return duct ($\Delta P_{return\ duct}$), filter ($\Delta P_{filter}$), heating/cooling coil (ΔP_{coil}), supply duct ($\Delta P_{supply\ duct}$), and diffuser ($\Delta P_{diffuser}$). The actual pressure drop along the duct is actually related to the duct length. In this study, the impact of the duct length on the pressure drop is not considered. The pressure drop of each HVAC part is presented in Table 2-9.

$$E_{fan} = m'_{hvac,s} \cdot \Delta P_{hvac} \tag{2-37}$$

$$\Delta P_{hvac} = \Delta P_{return\ grille} + \Delta P_{return\ duct} + \Delta P_{filter} + \Delta P_{coil} + \Delta P_{supply\ duct} + \Delta P_{diffuser} \tag{2-38}$$

Table 2-9. Pressure drops by different parts in the HVAC system.

Part	**Pressure drops, ΔP**	
	in wg	**Pa**
Return grille	0.04	10.0
Return duct	0.08	19.9
Filter	0.12 (1 inch MERV 8 @ 1000CFM)	29.9

	0.25 (1 inch MERV 13 @ 1000CFM)	62.2
	0.50 (1 inch HEPA @ 1000CFM)	124.4
Heating/cooling coil	0.23	57.2
Supply air	0.14	34.8
Diffuser	0.03	7.5

The pressure drop across the filter relies on the filter geometry, filter level (removal efficiency), and airflow rate. It can be estimated through Eq. 2-39 (EnergyPlus 2022c), where K_{filter} is the filter pressure drop coefficient. It varies with the filter levels. For example, the K_{filter} for MERV 8, 13 and HEPA filters are 7.18×10^{-5}, 3.59×10^{-5}, and 1.72×10^{-5}.

$$\Delta P_{filter} = \left[K_{filter} + f\left(\frac{L}{D}\right)\right]\frac{\left(m'_{hvac,s}\right)^2}{2\cdot\rho_{air}} \quad (2\text{-}39)$$

Other energy end-use sectors also include the lighting energy use, equipment energy use, and energy uses by other facilities (e.g. portable air cleaners). The total energy consumption, therefore, include the HVAC use (heating, cooling and fan), lighting use (E_{lgt}), equipment use (E_{eqm}), and other facility use (E_{fac}). The net energy use (E_{net}) for building needs to consider the generation of any renewable or sustainable energy production (E_{pro}). The net energy use then can be calculated through

$$E_{net} = (E_{htg} + E_{clg} + E_{fan}) + E_{lgt} + E_{eqm} + E_{fac} - E_{pro} \quad (2\text{-}40)$$

2.2.3.2 IAQ metrics

As people spend nearly 90% of their time indoors (Klepeis et al. 2001; Schweizer et al. 2007), indoor air quality (IAQ) plays a crucial role for occupant health, e.g. the indoor ozone exposure accounts for 59% (95% confidence interval: 26%-79%) of the total ozone exposure for humans (Xiang et al. 2019). IAQ is a complex problem largely because it involves many types of pollutants (Figure 2-11): (1) inorganic compounds (e.g., CO, SO2, NOx, and O3); (2) organic compounds including volatile organic compounds (VOCs, e.g. acetaldehyde, acetone, benzene, formaldehyde, naphthalene, phenol, xylenes, etc.) and semi-volatile organic compounds (SVOCs, e.g. polycyclic aromatic hydrocarbons or PAHs, din-butyl phthalate or DnBP, butyl benzyl phthalate or BBP, and di(2-ethylhexyl), Phthalate or DEHP); (3) radioactive gases (e.g., radon); (4) particulate matters (PM10, PM2.5, and ultrafine particles); and (5) bio-aerosols derived from virus, bacteria, fungi, protozoa, dust mites, and pollen (J. J. Zhang et al. 2022). Ozone-initiated oxidation products are also significant air contaminants including many VOCs and SVOCs, e.g. methacrolein, methyl vinyl ketone, nitrogen dioxide, acetone, 6-MHO, geranyl acetone, 4-OPA, formaldehyde, nonanal, decanal, 9-oxo-nonanoic acid, azelaic acid, and nonanoic acid.

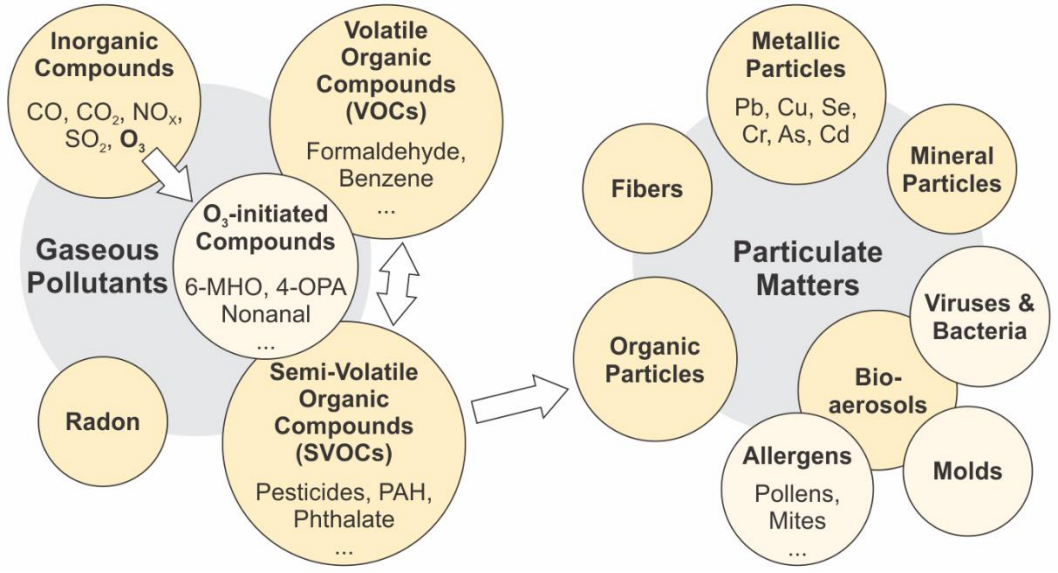

Figure 2-11. Classification of indoor pollutants (J. J. Zhang et al. 2022).

Various indoor air pollutants usually have quite different indoor sources, concentration levels, and health impacts. Inorganic gaseous compounds, such as NOx, CO and SO2, mainly originate from the ambient air that are released by traffic and industrial exhausts (U.S. EPA 2022c), and can enter buildings in the process of ventilating or by air infiltration through the building envelope (M. O. Abadie and Wargocki 2017). Ground-level ozone is a secondary pollutant and formed through chemical reactions of other compounds, specifically NOx and VOCs through photochemical reactions under certain ultraviolet (UV) light (Minnesota Pollution Control Agency 2022). Some of these compounds can also be directly emitted in indoor environments by combustion processes performed indoors, such as smoking, heaters, burning incense, cooking, etc. in the case of NOx and CO, and by printers and copiers or other ozone sources in case of ozone (M. O. Abadie and Wargocki 2017; C. Guo et al. 2019; U.S. EPA 2021a). The VOC family consists of hundreds of compounds for which emission sources are multiple and have not been completely characterized

to date. The major sources of indoor VOCs include ambient air, building materials and decoration products, occupant activities such as cleaning, cooking and combustion, and some electronic equipment like computers.

Various indoor air pollutants may have different indoor levels in different scenarios. Indoor ozone concentrations are usually below 20 ppb (Nazaroff and Weschler 2021). Measurements in approximately 2000 indoor environments show an average indoor ozone concentration of 4-6 ppb and the interquartile range of about 2-11 ppb in homes, schools, and offices (Nazaroff and Weschler 2021). In some regions with worse ambient air quality, the indoor ozone concentrations can be higher. Indoor concentrations of fine particles vary considerably, from less than 10 $\mu g/m^3$ up to thousands of $\mu g/m^3$, greatly depending on the indoor generation or resuspension due to occupant activities (Z. Zhou et al. 2016). The total volatile organic compounds (TVOC) levels in buildings are typically around 300 $\mu g/m^3$ (M. O. Abadie and Wargocki 2017; Logue et al. 2012). Figure 2-12 shows concentration distributions of typical air contaminants measured in the residential buildings based on a review of multiple studies in U.S., Europe, Asia, and Australia including over 20 thousand residential building cases in total (M. Abadie et al. 2019; M. O. Abadie and Wargocki 2017). Some studies revealed the most significant VOCs in offices include formaldehyde, xylene, d-limonene, hexanal, acetaldehyde, 2-ethyhexanol, and α-pinene, with concentrations from as low as 0.5 $\mu g/m^3$ to over 100 $\mu g/m^3$ (M. Abadie et al. 2019; M. O. Abadie and Wargocki 2017; Logue et al. 2012).

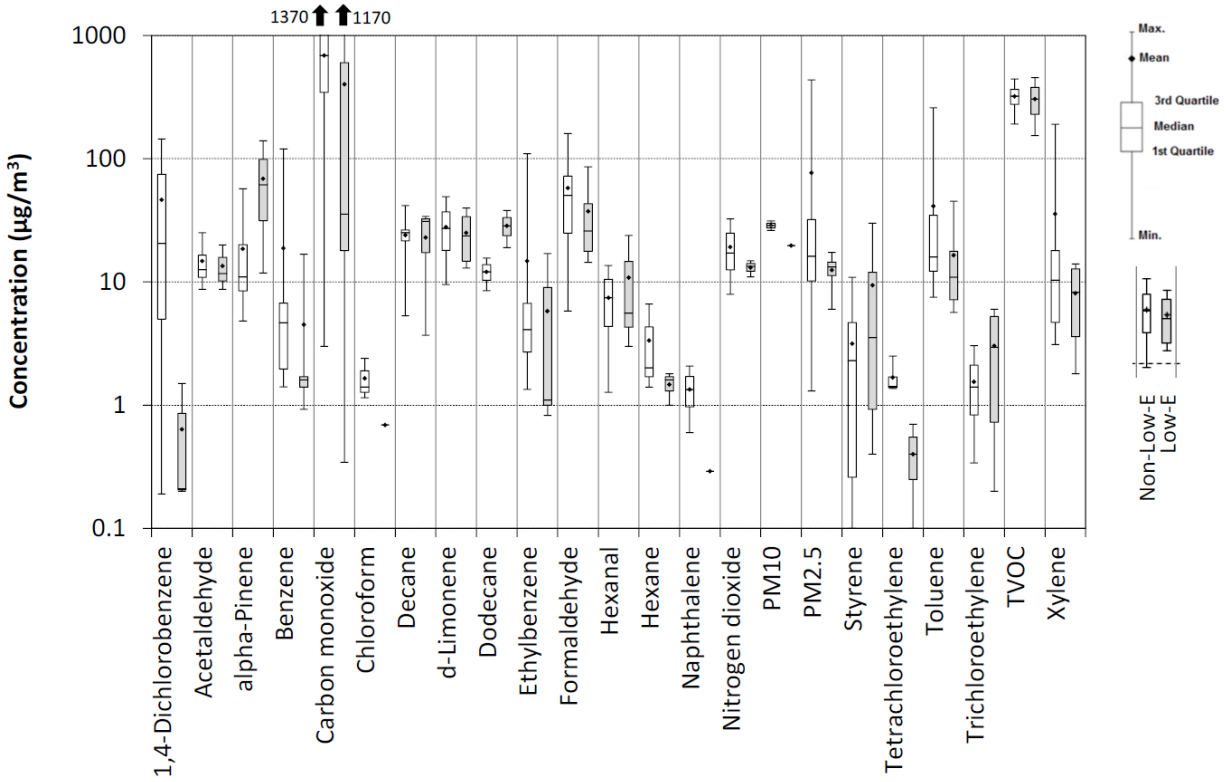

Figure 2-12. Concentration distributions of typical air contaminants measured in the residential buildings based on a review of multiple studies in U.S., Europe, Asia, and Australia (totally over 20 thousand residential buildings studied) (M. Abadie et al. 2019; M. O. Abadie and Wargocki 2017). For each pollutant, left unshaded symbols are for non-low-energy buildings and right shaded symbols correspond to low-energy residential buildings.

Most indoor air pollutants can have acute or chronic adverse health effects on people's respiratory, cardiovascular and/or reproductive systems, etc. (WHO 2022a). They can increase the morbidity and mortality associated with these diseases, reduce life quality and cause disability or even pre-mature deaths. Some of these air pollutants are believed to be carcinogens (WHO 2022b). It has been revealed that household air pollution is responsible for an estimated 3.2 million deaths per

year in 2020 (WHO 2022a). Table 2-10 shows the health impacts of some common indoor air pollutants of concerns. Therefore, many agencies have documented standards or guidelines for indoor air pollutants, including WHO, OEHHA, and ATSDR. But the concentration limits for various pollutants are usually very different based on their typical levels and health impacts. Table 2-11 shows the concentration limits for different indoor air pollutants in standards and guidelines. Some researchers believe that there is no safe level of exposure that can be recommended for some compounds, particularly carcinogens. The indoor concentrations of them need to be maintained as low as possible. Therefore, it is not easy to quantitatively evaluate indoor air pollutants merely based on their concentrations as their indoor levels and limits may vary greatly.

Table 2-10. Health impacts of indoor air pollutants of concerns

Classification	**Compounds**	**CAS No.**	**IARC Classification [a] (WHO 2022b)**	**Chronic target organs [b] (OEHHA 2019, 2022)**
Inorganic gaseous compounds	CO	630-08-0		Brain (Townsend and Maynard 2002)
	SO2	9/5/7446		Respiratory system (ATSDR 2020)
	NO2	10102-44-0	/	Respiratory system (U.S. EPA 2021b)

	O3	10028-15-6		Respiratory system; Cardiovascular system (Shen and Gao 2018)
	Radon	10043-92-2	1 (Radon-222)	Respiratory system (lung cancer) (U.S. EPA 2022b; Virginia Department of Health 2022)
VOCs	Acetaldehyde	75-07-0	2B	Respiratory system
	Acetone	67-64-1		Reproductive system; Skin; Alimentary system (liver); Kidney; Nervous system (New Jersey Department of Health 2015)
	Acrolein	107-02-8	2A	Respiratory system

	Benzene	71-43-2	1	Hematologic system; Nervous system; Development
	1,3-butadiene	106-99-0	1	Reproductive system
	1,4-Dichlorobenzene	106-46-7	2B	Nervous system; Respiratory system; Alimentary system (liver); Kidney
	Dichloromethane	75-09-2	2A	Cardiovascular system; Nervous system
	Ethylene glycol	107-21-1		Respiratory system; Kidney; Development
	Formaldehyde	50-00-0	1	Respiratory system
	n-Hexane	110-54-3		Nervous system
	Naphthalene	91-20-3	2B	Respiratory system
	Phenol	108-95-2	3	Alimentary system (liver); Cardiovascular

				system; Kidney; Nervous system
	Propylene	115-07-1	3	Respiratory system
	Tetrachloroethylene	127-18-4	2A	Alimentary system (liver); Kidney
	Toluene	108-88-3	3	Acquired color vision impairment (dyschromatopsia)
	1,1,1-trichloroethane	71-55-6	2A	Nervous system
	Trichloroethylene	79-01-6	1	Nervous system; Eyes
	Xylene, total	108-83-3 (m) 95-47-6 (o) 106-42-3 (p) (mixture: 1330-20-7)	3	Nervous system; Respiratory system; Eyes
SVOCs	PAH (Benzo[a]pyrene)	50-32-8	1	Skin; Respiratory system; Alimentary

			system (liver); Kidney; Stomach; Reproductive system (New Jersey Department of Health 2017)
Particles	PM2.5	/	Respiratory system; Cardiovascular system (U.S. EPA 2022a)
	PM10	/	Respiratory system; Cardiovascular system (U.S. EPA 2022a)

[a] IARC: GROUP 1: the agent may be a carcinogenic mixture for humans (proven carcinogen or certainly carcinogenic); GROUP 2A: The mentioned agents are probably carcinogenic for human beings; GROUP 2B: 272 agents appear on this list of agents probably carcinogenic to humans; GROUP 3: 508 agents appear on this list and are not classifiable as to their carcinogenicity to humans; GROUP 4: to indicate agents which are probably not carcinogenic for human beings.

[b] Data collected from (OEHHA 2019, 2022) except the ones indicated separately.

Table 2-11. Concentration limits for different indoor air pollutants in standards and guidelines [μg/m^3] (except for Radon [Bq/m^3])

Categories	**Compounds**	**CAS No.**	**OEHHA (Cal EPA) RELs (OEHHA 2019, 2022)**			**WHO (WHO 2005, 2010)**	**ANNEX 68 ELV (M. O. Abadie and Wargocki 2017)**	
			Acute	**8-hour**	**Chronic**		**Long-term**	**Short-term**
Inorganic gaseous compounds	CO	630-08-0	23000					
	SO2	9/5/7446	660			20 (24-hour) 500 (10-min)		
	NO2	10102-44-0	470			200 (1-hour) 40 (annual)	20	470
	O3	10028-15-6	180			100 (8-hour)		
	Radon	10043-92-2					200	400
VOCs	Acetaldehyde	75-07-0	470	300	140		48	/
	Acetone	67-64-1						

Acrolein	107-02-8	2.5	0.7	0.35		0.35	6.9
Benzene	71-43-2	27	3	3	No SL [a]	0.2	/
1,3-butadiene	106-99-0	660	9	2			
1,4-Dichlorobenzene	106-46-7			800			400
Dichloromethane	75-09-2	14,000		400			
Ethylene glycol	107-21-1			400			
Formaldehyde	50-00-0	55	9	9	100 (30-min)	9	123
n-Hexane	110-54-3			7000			
Naphthalene	91-20-3			9	10 (annual)	2	/
Phenol	108-95-2	5,800		200			
Propylene	115-07-1				3000		
Tetrachloroethylene	127-18-4	20,000		35	250		

	Toluene	108-88-3	5,000	830	420		250	/
	1,1,1-trichloroethane	71-55-6	68,000		1,000			
	Trichloroethylene	79-01-6			600		2	/
	Xylene, total	108-83-3 (m) 95-47-6 (o) 106-42-3 (p) 1330-20-7 [c]	22,000		700			
	TVOC							400
SVOCs	PAH (Benzo[a]pyrene)	50-32-8				No SL		
Particles	PM2.5					10 (annual) 25 (24-hour)	10	25
	PM10					20 (annual)	20	50

				50 (24-hour)		

(continued)

Categories	**Compounds**	**CAS No.**	**BIFMA M7.1-2010 (CDGS 2008) (ANSI/BIFMA 2007)**	**ATSDR [b] (ATSDR 2022)**		
				Acute	**Int.**	**Chronic**
Inorganic gaseous compounds	CO	630-08-0				
	SO2	9/5/7446				
	NO2	10102-44-0				
	O3	10028-15-6				
	Radon	10043-92-2				
VOCs	Acetaldehyde	75-07-0	9			

Acetone	67-64-1		71,000		
Acrolein	107-02-8		6.9	0.09	
Benzene	71-43-2	30	28.8	19.2	9.6
1,3-butadiene	106-99-0				
1,4-Dichlorobenzene	106-46-7	400	12024.6	1202.5	60.1
Dichloromethane	75-09-2	200			
Ethylene glycol	107-21-1	200	5077.3		
Formaldehyde	50-00-0	16.5	49.1	36.8	9.8
n-Hexane	110-54-3	3500			2114.9
Naphthalene	91-20-3	4.5			3.7

	Phenol	108-95-2	100			
	Propylene	115-07-1				
	Tetrachloroethylene	127-18-4	17.5	40.7	40.7	40.7
	Toluene	108-88-3	150	7537.1		3768.5
	1,1,1-trichloroethane	71-55-6	500	10912.1	3819.2	
	Trichloroethylene	79-01-6	300		2.1	2.1
	Xylene, total	108-83-3 (m) 95-47-6 (o) 106-42-3 (p) 1330-20-7 [c]	350	8683.9	2605.2	217.1
	TVOC					
SVOCs	PAH (Benzo[a]pyrene)	50-32-8				

Particles	PM2.5				
	PM10				

(continued)

Categories	**Compounds**	**CAS No.**	**Health Canada (Health Canada 2018, 2022)**		**WELL (Air Feature 01) (IWBI 2018)**
			Long-term (24-hour)	**Short-term (1-hour)**	
Inorganic gaseous compounds	CO	630-08-0	11.5	28.6	11250
	SO2	9/5/7446			
	NO2	10102-44-0	20	170	
	O3	10028-15-6	40 (8-hour)		100
	Radon	10043-92-2	200		148

VOCs	Acetaldehyde	75-07-0	280	1420	
	Acetone	67-64-1	70,000		
	Acrolein	107-02-8	0.44 (IARL=0.35)	38	
	Benzene	71-43-2	No SL		
	1,3-butadiene	106-99-0	1.7		
	1,4-Dichlorobenzene	106-46-7	60		
	Dichloromethane	75-09-2	600		
	Ethylene glycol	107-21-1			
	Formaldehyde	50-00-0	50	123	22
	n-Hexane	110-54-3			
	Naphthalene	91-20-3	10		
	Phenol	108-95-2			

	Propylene	115-07-1			
	Tetrachloroethylene	127-18-4	40		
	Toluene	108-88-3	2300	15000	
	1,1,1-trichloroethane	71-55-6			
	Trichloroethylene	79-01-6			
	Xylene, total	108-83-3 (m) 95-47-6 (o) 106-42-3 (p) 1330-20-7 [c]	100		
	TVOC				500
SVOCs	PAH (Benzo[a]pyrene)	50-32-8			
Particles	PM2.5		No SL		15

PM10	50

[a] No SL: No safe level of exposure can be recommended (pollutant concentration should be maintained as low as possible).

[b] For Duration, Acute = 1 to 14 days, Intermediate = 15 to 364 days, and Chronic = 1 year or longer.

[c] Mixture of various xylenes.

One approach to evaluate indoor air pollutants is assessing the IAQ satisfaction on health thresholds regulated in standards and guidelines, which was proposed by this study earlier (Shen et al. 2020). However, for most pollutants, any slight increase in pollutant concentration will cause certain health effects and raise the morbidity/mortality rate, even below the threshold level. For example, it is considered to be safe by the WHO standard if PM2.5 levels are below 35 μg/m^3 within a day and the 8-hour ozone levels are below 35 ppb (WHO 2005). But every 10 μg/m^3 increase in daily PM2.5 exposure will lead to 1% increased daily mortality rate among adults 65 years and older, and every 1ppb increase in daily ozone concentration raises the daily mortality rate by 0.5% (WHO 2005). Therefore, it is preferred to evaluate IAQ per health impacts directly. The DALY metric quantifies Disability-Adjusted Life Years (DALYs) due to exposure to a chemical substance and has been widely used to evaluate IAQ in recent years (T. Gao et al. 2014; K. K. Lee et al. 2020; Logue et al. 2012; Nurchis et al. 2022; Z Wang et al. 2009; Wysocka 2018). As defined by WHO (WHO 2020b), one DALY can be thought of as one lost year of "healthy" life. The sum of these DALYs across the population, or the burden of disease, can be thought of as a measurement of the gap between current health status and an ideal health situation where the entire population lives to an advanced age, free of disease and disability. The DALY method allows quantifying and comparing the health impact from various pollutants, including the various types of disease induced. The DALYs lost per incidence can be calculated by (Logue et al. 2012):

$$DALY_{disease} = YLL_{disease} + YLD_{disease} \quad (2\text{-}41)$$

where $YLL_{disease}$ are years of life lost (YLL) due to premature death from the disease and $YLD_{disease}$ are years of life disability (YLD), weighted from 0 to 1 depending on disease severity. The equation can be rewritten as:

$$DALYs = \frac{\partial \text{DALY}}{\partial \text{disease incidence}} \times disease\ incidence = DALY\ factor \times disease\ incidence \quad (2\text{-}42)$$

According to Logue et al. (Logue et al. 2012), there are two different ways of estimating DALYs lost for indoor air pollutants health impact. An intake-incidence-DALY (IND) approach is based on epidemiological data and epidemiology-based concentration-response (C-R) functions to quantify disease incidence. If the epidemiological data are not available, it is yet possible to use animal toxicity literature in order to calculate health impact via an intake-DALY (ID) method. Both ID and IND methods are accepted health impact models and, for both of them, only the annual average value of pollutant concentration is needed to estimate the population long-term impact. For criteria pollutants, including ozone, NO2, PM2.5, SO2, and CO, the IND method is usually applied. For other non-criteria pollutants (e.g. VOCs) the ID approach is usually used to calculate health impact associated with intake of non-criteria pollutants based on animal toxicity literature as shown in the work of Huijbregts et al. (Huijbregts et al. 2005). The IND approach is usually preferred as it provides more accurate estimations. But the IND approach can be used merely for pollutants with data on C-R functions in humans. Ozone was the only pollutant for which both the IND and ID approaches could be applied.

The IND approach calculates disease incidence using the C-R function (Eq. 2-43). The DALYs then are determined by disease incidence and DALY factor using Eq. 2-42. The exposure-related concentration is calculated by considering the inhalation of indoor polluted air of mean concentration C_{in} relative to a pollutant-free indoor air. Logue et al. (Logue et al. 2012) considered that, in the U.S., people spend 70% of their time in residential buildings so that the chronic exposure-relevant concentration contributed from indoor exposure was set to 70% of the indoor concentration (Eq. 2-44). Some other studies have suggested that the average time people spent indoors can exceed 80% (nearly 90%). Thus, people's exposure to indoor air pollutants may be higher than the estimation by Eq. 2-44. But in this study, the equation is still used for calculation.

$$\Delta incidence = population \times y_0 \times \left(1 - e^{-\beta_{exp} \times \Delta C_{exposure}}\right) \quad (2\text{-}43)$$

where y_0 is the baseline prevalence of illness per year, β_{exp} is the coefficient of the concentration change, $C_{exposure}$ is the exposure-related concentration, and population is the number of persons exposed (it is often set to 100,000 to obtain a DALY lost per 100,000 persons). For each pollutant and outcome, $y0$ and β_{exp} vary. Table 2-12 summarizes the health end points selected and DALY loss per incidence of disease (adapted from (Fazli and Stephens 2018; Logue et al. 2012; Lvovsky et al. 2000)). Many studies performed Monte-Carlo simulations based on the statistical distribution (95% confidence interval, CI) of β_{exp} and DALY factor (Logue et al. 2012). It can be observed that the coefficients for PM2.5 are relatively higher than the coefficients for other pollutants, especially the DALY factors (DALY per incidence) for diseases due to PM2.5 exposure. Therefore, it

suggests that the exposure to PM2.5 has stronger adverse effects on people's health compared to other compounds.

$$\Delta C_{exposure} = 0.7 C_{in} \tag{2-44}$$

Table 2-12. Criteria pollutant C-R function outcomes and DALYs lost per incidence (Fazli and Stephens 2018; Logue et al. 2012; Lvovsky et al. 2000).

Pollutants	**Outcome**	**β_{exp} (95% CI)**	**y_0**	**DALY factor, ∂DALYs/∂incidence (95% CI)**
PM2.5	Total mortality	0.058 (0.002, 0.010)	7.40×10^{-3}	1.4 (0.14, 14)
	Chronic bronchitis	0.091 (0.078, 0.105)	4.00×10^{-4}	1.2 (0.12, 12)
	Nontatal stroke	0.025 (0.002, 0.048)	2.00×10^{-4}	9.5 (9.25, 9.75), 0 complication 11.7 (11.1, 12.4), 1 complication 13.1 (12.2, 14.0), >1 complication
CO	Asthma	0.033 (0.016, 0.050)	1.80×10^{-3}	2.64×10^{-2} (Fazli and Stephens 2018; Lvovsky et al. 2000)
	Lung disease	0.025 (0.000, 0.057)	2.10×10^{-3}	2.64×10^{-2} (Fazli and Stephens 2018; Lvovsky et al. 2000)

	Dysrhythmias	0.058 (0.012, 0.102)	2.40×10^{-3}	2.64×10^{-2} (Fazli and Stephens 2018; Lvovsky et al. 2000)
	Heart failure	0.034 (0.002, 0.066)	3.40×10^{-3}	2.64×10^{-2} (Fazli and Stephens 2018; Lvovsky et al. 2000)
NO2	Respiratory issues	0.004 (0.000, 0.008)	9.50×10^{-3}	2.64×10^{-2} (Fazli and Stephens 2018; Lvovsky et al. 2000)
	Congestive heart failure	0.003 (0.001, 0.004)	3.40×10^{-3}	2.64×10^{-2} (Fazli and Stephens 2018; Lvovsky et al. 2000)
	Ischemic heart disease	0.003 (0.002, 0.004)	8.00×10^{-3}	2.64×10^{-2} (Fazli and Stephens 2018; Lvovsky et al. 2000)
	Respiratory illness, indicated by symptoms	0.028 (0.002, 0.053)	N/A	2.64×10^{-2} (Fazli and Stephens 2018; Lvovsky et al. 2000)
Ozone	Mortality	0.001 (0.000, 0.002)	7.70×10^{-3}	1 (0.1, 10)

	Asthma	0.003 (0.001, 0.004)	1.80×10^{-3}	2.64×10^{-2} (Fazli and Stephens 2018; Lvovsky et al. 2000)
	Lung disease	0.003 (0.001, 0.005)	2.10×10^{-3}	2.64×10^{-2} (Fazli and Stephens 2018; Lvovsky et al. 2000)
	Respiratory infection	0.002 (0.001, 0.003)	5.80×10^{-3}	2.64×10^{-2} (Fazli and Stephens 2018; Lvovsky et al. 2000)
	Dysrhythmias	0.002 (0.000, 0.004)	2.40×10^{-3}	2.64×10^{-2} (Fazli and Stephens 2018; Lvovsky et al. 2000)
SO2	Hospital admissions	0.002 (0.000, 0.003)	8.00×10^{-3}	2.64×10^{-2} (Fazli and Stephens 2018; Lvovsky et al. 2000)

The ID approach extrapolated directly from indoor concentrations to total DALYs lost due to intake of specific pollutants. The DALYs equation is rewritten as

$$DALYs = \frac{\partial \text{DALY}}{\partial \text{intake}} \times intake \tag{2-45}$$

where $intake$ is the mass of pollutant that an individual inhales over a given time period. The DALYs per intake of the pollutant in Equation 16 consists of two categories for cancer and non-cancer effects and can be calculated by

$$\frac{\partial \text{DALY}}{\partial \text{intake}} = \left(\frac{\partial \text{DALY}}{\partial \text{intake}}\right)_{cancer} \times ADAF + \left(\frac{\partial \text{DALY}}{\partial \text{intake}}\right)_{non-cancer} \tag{2-46}$$

where $(\partial DALY/\partial intake)_{cancer}$ and $(\partial DALY/\partial intake)_{non-cancer}$ are DALYs lost per unit of intake from carcinogenic and non-carcinogenic causes for each pollutant (year/kg) and ADAF is the age-dependent adjustment factor. The DALYs per intake from carcinogenic and non-carcinogenic causes for various pollutants are available in Huijbregts et al. (Huijbregts et al. 2005). Table 2-13 shows the data for some selected indoor pollutants of concern adapted from (Huijbregts et al. 2005), including ozone, some VOCs and SVOCs. The full table can be found in (Huijbregts et al. 2005). The age at which carcinogens are inhaled has an appreciable effect on total toxicity, and the U.S. EPA has developed ADAFs to calculate cancer health impact as a function of exposure age (U.S. EPA 2005). To align with U.S. EPA-recommended ADAFs, Logue et al. (Logue et al. 2012)

considered three age groups: < 2, 2–16, and > 16 years of age. A population-weighted average annual air intake volume and ADAF were calculated by combining age distribution of the U.S. population, age-specific inhalation rates, and time spent at home as shown in Table 2-14. The average ADAF is 1.6 for population in the U.S. Based on the estimated ADAF, the combined DALYs per intake can be determined and is shown in Table 2-14. The mass of pollutant that an occupant inhales over a given period in an indoor space can be evaluated by:

$$intake = Q_{intake} \times C_{in} \times \Delta t \tag{2-47}$$

where Q_{intake} is the volume rate of air intake (m^3/day), C_{in} is indoor concentration (μg/m^3), Δt is the exposure time (day), usually taken to 365 to estimate the DALYs lost per year. The ID approach also usually works with Monte-Carlo sampling to account for confidence intervals of coefficients. But this study only performs calculations using the selected median or mean values. Earlier studies have performed both approaches with Monte-Carlo sampling method, and their results revealed that there is still a large uncertainty in the number of DALY losses estimated for each pollutant by the IND and ID methods but it is the only scientifically-based method available to evaluate and compare the health impacts of the exposure to different pollutants (M. O. Abadie and Wargocki 2017; Logue et al. 2012).

Table 2-13. DALYs per intake for selected compounds (adapted from (Huijbregts et al. 2005)).

CAS No.	Substance	Cancer ∂DALYs/∂intake [year/kg]	Non-cancer ∂DALYs/∂intake [year/kg]	Combined ∂DALYs/∂intake [year/kg]
10028-15-6	Ozone	9.20×10^{-1}		1.47×10^{0}
100-41-4	Ethylbenzene	2.20×10^{-4}	3.30×10^{-4}	6.82×10^{-4}
100-42-5	Styrene	3.30×10^{-2}	8.30×10^{-3}	6.11×10^{-2}
106-46-7	1,4-Dichlorobenzene	1.20×10^{-3}	1.90×10^{-3}	3.82×10^{-3}
106-99-0	1,3-Butadiene	3.00×10^{-3}	7.10×10^{-2}	7.58×10^{-2}
0107-02-08	Acrolein		5.00×10^{1}	5.00×10^{1}
108-88-3	Toluene	2.20×10^{-4}	4.70×10^{-3}	5.05×10^{-3}
108-95-2	Phenol			
110-54-3	Hexane		7.70×10^{-3}	7.70×10^{-3}
50-00-0	Formaldehyde	7.60×10^{-1}		1.22×10^{0}
50-32-8	Benzo(a)pyrene	1.10×10^{1}		1.76×10^{1}
71-43-2	Benzene	5.80×10^{-3}	3.10×10^{-3}	1.24×10^{-2}
75-07-0	Acetaldehyde	6.40×10^{-3}	3.20×10^{-2}	4.22×10^{-2}

75-09-2	Methylene chloride	1.10×10^{-3}		1.76×10^{-3}
79-01-6	Trichloroethylene	1.20×10^{-3}		1.92×10^{-3}
91-20-3	Naphthalene	1.10×10^{-2}	6.10×10^{-2}	7.86×10^{-2}

Table 2-14. Residential occupancy characteristics in the U.S. (Logue et al. 2012).

Age [years]	**Percent of population [%]**	**Cancer ADAF**	**Percent of time indoors [%]**	**Air intake [m3/day]**
<2	3	10	75	7
2-16	19	3	75	13
>16	78	1	69	15
Population average	/	1.6	70	14.4

The platform developed in this study uses both approaches for estimating DALYs for different air pollutants. An online tool for DALY estimation is also developed and can be accessed through (Shen 2022). Table 2-15 shows the typical indoor air pollutants in offices and their concentrations. DALYs for these pollutants are calculated using the present method. Figure 2-13 shows the DALYs per year per 100,000 population in office scenario. It suggests that PM2.5, acrolein, formaldehyde, ozone, and NO2 are the significant pollutants that have stronger adverse health

effects on occupants in offices. Figure 2-14 illustrates the global DALYs per year per 100,000 population due to cardiovascular and respiratory diseases based on the data between 2000 and 2019 (WHO 2020a).

Table 2-15. Typical air pollutants in offices (concentrations are adapted from (Campagnolo et al. 2017)).

Pollutant	**Concentration [μg/m^3]**	**DALYs per year per 100,000 population**
PM2.5 (Jones et al. 2021)	18	621
Ozone (Nazaroff and Weschler 2021)	12	7.06
NO2 (Salonen et al. 2019)	23	2.98
Benzene	1.8	0.0117
Toluene	4.5	0.0119
Ethylbenzene	1.2	0.00043
n-Hexane	1.5	0.00607
Limonene	12	0.0394
2-Butoxyethanol	2.5	0.0088
2-Ethylhexanol	4	0.00259

Styrene	0.8	0.0257
Formaldehyde	14	8.95
Acetaldehyde	6	0.0133
Acrolein	2.5	65.7
Benzaldehyde	1	0.00109

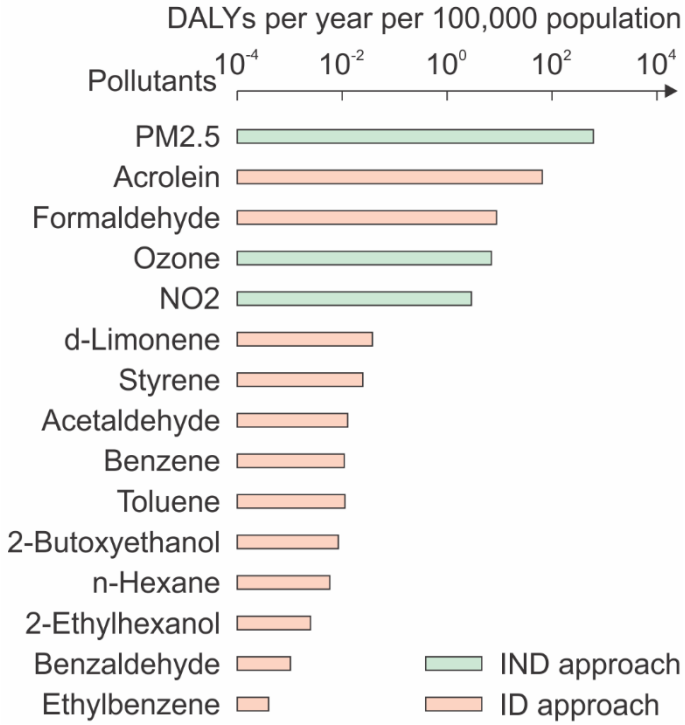

Figure 2-13. DALYs per year per 100,000 population in office scenario.

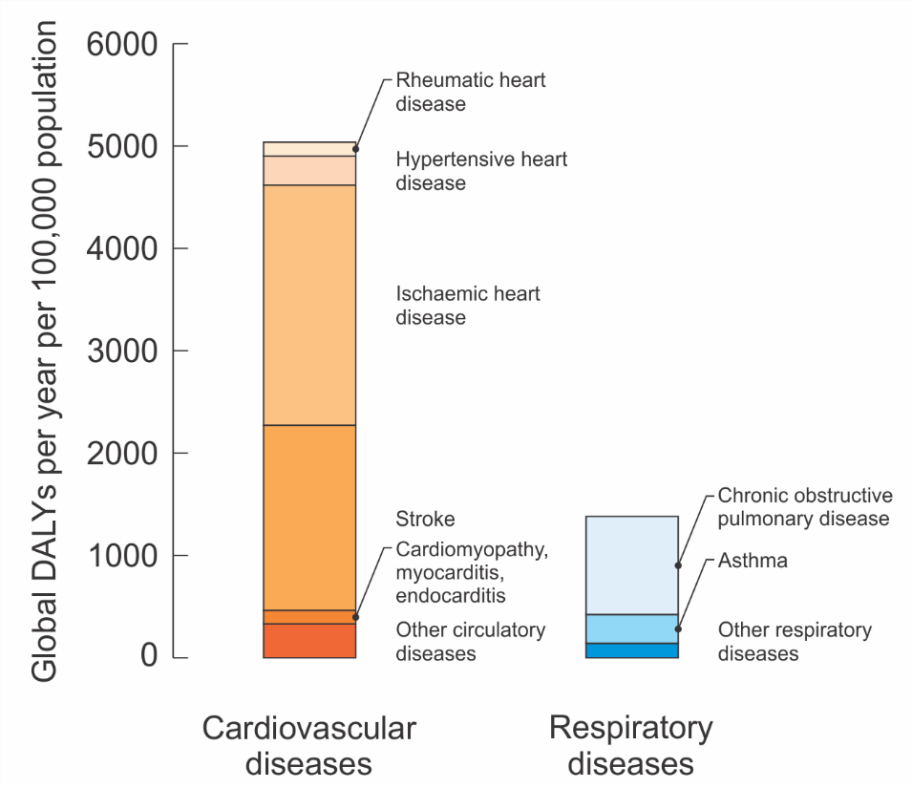

Figure 2-14. Global DALYs per year per 100,000 population due to cardiovascular and respiratory diseases (data as of 2000 to 2019 by WHO (WHO 2020a)).

2.2.3.3 Thermal comfort

Thermal environment is one of the main factors that influence occupants' comfort, health, work productivity and study performance (Jiang et al. 2018; Kaushik et al. 2020; Rupp et al. 2015; Tham et al. 2020). Research has revealed the strong relationship between thermal comfort and work productivity or study performance (Bueno et al. 2021; Jiang et al. 2018; Kaushik et al. 2020; Zomorodian et al. 2016). As almost a third of the workday is connected to work-related activities for adults or study-related activities for students, thermal comfort can be a key factor affecting people’s work productivity and study performance (Bueno et al. 2021). Thermal environment also

influences occupant health. Exposure to both low and high indoor temperatures can increase the mortality and disorder risk relevant to respiratory and cardiovascular systems, and even morbidity under certain circumstance, particularly to the susceptible individuals like the elderly (Collins 1986; Ormandy and Ezratty 2012; Tham et al. 2020). For example, research suggests that high indoor temperatures affect aspects of human health, with the strongest evidence for respiratory health, diabetes management and core schizophrenia and dementia symptoms (Tham et al. 2020). Cold extremities and slight lowering of core temperature can induce short-term increases in blood pressure, which may be important causal factors in the increased winter morbidity and mortality due to heart attacks and strokes (Collins 1986). Symptoms of mental health disorders are also exacerbated by extreme indoor temperatures (Tham et al. 2020).

Therefore, it is essential to evaluate and control indoor thermal comfort. It is known that thermal comfort is influenced by a range of environmental and individual factors (ASHRAE 2020a; Ormandy and Ezratty 2012). The environmental factors include the air temperature, the temperature of the surrounding surfaces, the airflow velocity, the relative humidity, and the rate of air exchange (ventilation). Thermal comfort also depends on occupant activity (that varies with age, health status, and gender) and clothing. Other factors such as room crowding and body exposure to sun radiation also have influences on thermal comfort.

PMV and PPD are the most used metrics for evaluating indoor thermal comfort, which can be calculated through methods introduced in ASHRAE Standard 55 (ASHRAE 2020a). The methods in ASHRAE Standard 55 are used in this study to estimate PMV and PPD. The PMV is determined

by the heat generation and losses of the human body and the thermal sensation transfer coefficient (Eq. 2-48). Heat production on the skin surface equals metabolic heat minus the heat input from external work (q'_{WME}, which is normally around 0). Metabolic rate (*MET*) is the energy produced per unit skin surface area by metabolic activities of a person, and 1 met equals 58.15 W/m^2 energy produced per unit skin surface area of an average person seated at rest. Thus, the equivalent heat generation by the individual (q'_{MW}) can be determined by Eq. 2-49. Table 2-16 shows the metabolic rates for typical indoor activities relevant to this study (selected from ASHRAE 55 (ASHRAE 2020a)). The thermal sensation transfer coefficient (*ts*) is dependent on the metabolic rate (in W/m^2) and can be calculated by Eq. 2-50.

$$PMV = ts \cdot (q'_{MW} - q'_{HL}) \tag{2-48}$$

$$q'_{MW} = q'_{M} - q'_{W} = (q'_{MET} - q'_{WME}) \cdot 58.15 \approx q'_{MET} \cdot 58.15 \tag{2-49}$$

$$ts = 0.303 \cdot e^{-0.036 \cdot q'_{M}} + 0.028 \tag{2-50}$$

Table 2-16. Metabolic rates for typical indoor activities relevant to this study (selected from ASHRAE 55 (ASHRAE 2020a)).

Activity	**Metabolic rate**	
	met	**W/m^2**

Sleeping	0.7	40
Seated (quite/reading/writing)	1.0	60
Standing, relaxed	1.2	70
Walking (0.9, 1.2, 1.8 m/s)	2.0, 2.6, 3.8	115, 150, 220
Typing	1.1	65
Lifting/packing	2.1	120
Cooking	1.6 – 2.0	95 – 115
House cleaning	2.0 – 3.4	115 – 200
Exercise	3.0 – 4.0	175 – 230

Heat losses on the skin surface include heat loss through skin ($q'_{HL,1}$), heat loss by sweating ($q'_{HL,2}$), latent respiratory heat loss ($q'_{HL,3}$), dry respiratory heat loss ($q'_{HL,4}$), heat loss by radiation ($q'_{HL,5}$), and heat loss by convection ($q'_{HL,6}$), which can be calculated by Eq. 2-51. Eq. 2-52 represents the heat loss through skin, depending on the body heat generation (q'_{MW}) and water vapor pressure of indoor air (p_a). Indoor air water vapor pressure can be determined through Eq. 2-53.

$$q'_{HL} = q'_{HL,1} + q'_{HL,2} + q'_{HL,3} + q'_{HL,4} + q'_{HL,5} + q'_{HL,6} \quad (2\text{-}51)$$

$$q'_{HL,1} = 3.05 \times 10^{-3} \cdot (5733 - 6.99 \cdot q'_{MW} - p_a) \quad (2\text{-}52)$$

$$p_a = 10 \times RH \cdot \left(16.6536 - \frac{4030.183}{T_a + 235}\right) \quad (2\text{-}53)$$

Heat loss by sweating ($q'_{HL,2}$) is determined by the sweating level of occupant under certain behaviors or activities. It is assumed that people sweat when > 1 MET, which means if the metabolic rate is less than 1 met, people will not sweat and no heat will be removed by sweating ($q'_{HL,2} = 0$). The heat loss by sweating when > 1 MET can be calculated by:

$$q'_{HL,2} = 0.42 \cdot (q'_{MW} - 58.15) \quad (2\text{-}54)$$

Respiratory heat losses include latent heat loss ($q'_{HL,3}$) and dry heat loss ($q'_{HL,4}$), representing the heat removed through respiratory activities, which are affected by occupant metabolic activity and water vapor pressure (Eq. 2-55) or dry air temperature (Eq. 2-56).

$$q'_{HL,3} = 1.7 \times 10^{-5} \cdot q'_M \cdot (5867 - p_a) \quad (2\text{-}55)$$

$$q'_{HL,4} = 0.0014 \cdot q'_M \cdot (34 - T_a) \quad (2\text{-}56)$$

Heat loss by radiation ($q'_{HL,5}$) and convection ($q'_{HL,6}$) are through the heat transfer between outer surface temperature of the clothed body and the mean radiant temperature of surrounding surfaces or surrounding air temperature, which are calculated by Eqs. 2-57 and 2-58. The mean radiant temperature of surrounding surfaces can be determined by the surface temperature of interior surfaces and the angle factors between the individual and the surfaces. The outer surface temperature of the clothed body can be calculated as Eq. 2-59, depending on the surrounding air temperature and the clothing vapor permeation efficiency ratio (I_{cl}).

$$q'_{HL,5} = 3.96 \times 10^{-8} \cdot f_{cl} \cdot ((T_{cl} + 273)^4 - (T_{mrt} + 273)^4) \quad (2\text{-}57)$$

$$q'_{HL,6} = f_{cl} \cdot h_c \cdot (T_{cl} - T_{in}) \quad (2\text{-}58)$$

$$T_{cl} = T_{in} + \frac{35.5 - T_{in}}{3.5 \cdot (6.45 \cdot I_{cl} + 1)} \quad (2\text{-}59)$$

I_{cl} is the clothing vapor permeation efficiency ratio of actual evaporative heat flow capability through clothing to sensible heat flow capability, which is an empirical quantity and can be derived from the clothing insulation value (1 clo = 0.155 $m^2 \cdot °C/W$). Table 2-17 shows the clothing insulation I_{cl} values for typical indoor ensembles (selected from ASHRAE 55 (ASHRAE 2020a)). However, the clothing level can be very subjective, which is difficult to determine for simulation. In this study, it is assumed that the clothing insulations in offices, schools, or other commercial/public buildings are 0.65 clo in summer and 1.00 clo in winter, and clothing

insulations in residential units are 0.55 clo in summer and 0.70 clo in winter. f_{cl} is the clothing area factor and dimensionless, depending on the clothing insulation, and can be determined by Eq. 2-60. h_c is the overall convective heat transfer coefficient between body (including clothing) and the surrounding air. The calculation of h_c is expressed as Eq. 2-61.

$$f_{cl} = \begin{cases} 1 + 1.29 \cdot I_{cl} & I_{cl} < 0.078 \\ 1.05 + 0.645 \cdot I_{cl} & I_{cl} \geq 0.078 \end{cases} \quad (2\text{-}60)$$

$$h_c = Max\left(2.38(T_{cl} - T_a)^{0.25}, 12.1\sqrt{v}\right) \quad (2\text{-}61)$$

Table 2-17. Clothing insulation I_{cl} values for typical indoor ensembles (selected from ASHRAE 55 (ASHRAE 2020a)).

Clothing description	**Garments included**	$\boldsymbol{I_{cl}}$ **[clo]**
Trousers	Trousers, short-sleeve shirt	0.57
	Trousers, long-sleeve shirt	0.61
	Trousers, short-sleeve shirt, suit jacket	0.96
Skirts/dresses	Knee-length skirt, short-sleeve shirt	0.54
	Knee-length skirt, long-sleeve shirt, full slip	0.67
	Knee-length skirt, long-sleeve shirt, half slip, suit jacket	1.04

Shorts	Walking shorts, short-sleeve shirt	0.36
Sleepwear	Long-sleeve pajama tops, long pajama trousers	0.96

Some variables in the calculation of PMV are not calculated by the thermal balance models, e.g., the RH of indoor air and local airflow velocity in the indoor air. It is assumed in this study that indoor RH is maintained at 50%, which is the typical and controlled RH in indoor environments. The airflow velocity around the occupant is difficult to determine, depending on the detailed air distribution that is dependent on the ventilation unit, furniture, occupant location, and other facilities like air cleaners. The detailed air distribution and airflow velocity around the occupant usually require field measurements or CFD simulations to determine. In this study, still air is assumed in the indoor environment with the velocity of 0.1 m/s when the ventilation system is off, while the airflow velocity equals 0.5 m/s when the ventilation system is working.

After the PMV is determined, the PPD can be calculated by Eq. 2-62. The satisfied ratio is then calculated by 1 – PPD. The ASHRAE 55 standard regulates the recommended thermal comfort level in indoor spaces. To comply it, the recommended thermal limit on the 7-point scale of PMV is between -0.5 and +0.5. PPD varies depending on where the occupant is in the space, and it should not exceed 20% per standard. The performance of a building module on thermal comfort satisfaction ratio is calculated compared to the reference case.

$$PPD = 100 - 95 \cdot e^{-(0.03353PMV^4 + 0.2179PMV^2)} \quad (2\text{-}62)$$

2.2.3.4 Infection risk

Estimating the risk of airborne transmission in indoor environments is essential for designing control strategies to reduce infection risk and improve people's health, particularly for those diseases like COVID-19 that can cause enormous life and economic losses. The most commonly used model for estimating the airborne transmission risk in a confined space is the Wells-Riley model, which assumes the air in the space is well-mixed in steady-state (RILEY et al. 1978; Wells 1955). The model has also been extended by some researchers to include unsteady exposure (Gammaitoni and Nucci 1997) and imperfect mixing (Ko et al. 2001, 2004), and incorporate with stochastic modeling (Noakes and Sleigh 2009). The infection risk determined by the Wells-Riley model depends on the susceptible individual's inhalation exposure to the viral suspended pathogen generated by the infectors (Stephens 2013; Sze To and Chao 2010).

The model has been widely adopted to estimate the airborne transmission risk of many respiratory diseases, such as influenza, tuberculosis, middle east respiratory syndrome, and measles (S. C. Chen and Liao 2008; H. Qian et al. 2009; Stephens 2013; Yates et al. 2016; Zemouri et al. 2020). Recent studies also applied the Wells-Riley model in estimating the airborne transmission risk in addressing the challenges of SARS-CoV-2 (Dai and Zhao 2020; Harrichandra et al. 2020; Pavilonis et al. 2021; Peng and Jimenez 2021; Shen, Kong, Dong, et al. 2021a; Stabile et al. 2021). The Wells-Riley model applies the C-R model for estimating the infection probability. In earlier studies, the infection possibility (P), which can be used to estimate the new infection cases (N_C) based on the susceptible cases (N_S), is calculated as a function of the inhalation exposure dose

(RILEY et al. 1978), which depends on the number of infectors (I), the emission rate of infectious quanta per infector (ER), the equivalent fraction of infectious particle penetration through the face mask (η'_{mask}, including the masks by susceptible and infectious subjects), inhalation rate (Q_{inhale}), exposure time (Δt), the equivalent room air change rate (Λ) and room volume (V) as shown in Eq. 2-63. If the indoor concentration of viral particles is known, the inhalation of viral particles can be determined first based on the inhalation rate, indoor viral particle concentration, exposure time, and susceptible subjects' mask efficiency, while the equivalent indoor viral particle concentration depends on the virus emission rate and equivalent ventilation rate that is related to the ventilation effectiveness and inactivation efficiency. Then the infection probability can be determined by the C-R model. In this study, the concentration of viral particles (C_{vir}) is first simulated using the air and mass balance models defined in above sections and the infection probability is then determined.

$$P = \frac{N_C}{N_S} = 1 - e^{-inhalation} = 1 - e^{-\eta_{mask} \cdot Q_{inhale} \cdot C_{vir} \cdot \Delta t} = 1 - e^{-\eta'_{mask} \cdot \frac{I \cdot ER \cdot Q_{inhale} \cdot \Delta t}{V\Lambda}} \quad (2\text{-}63)$$

The equivalent air change rate (Λ) represents the equivalent supply flow rate of fresh air per unit volume of the room space. It depends on the equivalent ventilation air change rate (λ_{vent}), pathogen inactivation rate by ultraviolet germicidal irradiation (UVGI) system (k_{UV}), infectious particle deposition rate ($k_{deposition}$) and pathogen natural inactivation rate in the air ($k_{inactivation}$):

$$\Lambda = \lambda_{vent} + f_{UV} k_{UV} + k_{deposition} + k_{inactivation} \quad (2\text{-}64)$$

The equivalent ventilation rate (λ_{vent}) includes the fresh air supply rate by the HVAC system (λ_{HVAC})

and standalone portable air cleaners ($k_{AirCleaner}$). The original Wells-Riley model is based on the perfect-mixing assumption. However, indoor airflow patterns and mixing level are highly dependent on room configurations and air distributions. In order to evaluate the infection risk in imperfect-mixed scenarios, an additional ventilation factor (ε_{vent}) is multiplied by the ventilation rate in the model, representing the dilution efficiency in a particular location compared to the perfect mixing ventilation. It can be estimated by comparing the tracer gas concentration in the target location (C_i) and the concentration in the exhaust air ($C_{exhaust}$) through Eq. 2-65, which is similar to the zone air distribution effectiveness in ASHRAE 62.1 [22]. Some other studies performed CFD simulations to figure out the spatial concentration distribution of viruses and incorporated them with the Wells-Riley model to estimate the spatial exposure risk distribution in the space (N. P. Gao et al. 2008; H. Qian et al. 2009; Tung and Hu 2008). CFD simulations have been performed in scenarios like restaurant, classroom, grocery store, bus, car, elevator, hospital ward, and underground parking space for estimating the spatial risk distribution of SARS-CoV-2 (Dbouk and Drikakis 2021; Y. Guo et al. 2021; Y. Li et al. 2020; Han Liu et al. 2021; Mathai et al. 2021; Nazari et al. 2021; Shao et al. 2021; X. Yang et al. 2020; Z. Zhang et al. 2021). The ventilation effectiveness equals one for the perfect mixing condition. Spaces with more efficient air distribution (such as displacement ventilation) have a ventilation factor greater than one. Table 2-18 shows the ventilation effectiveness for some typical ventilation strategies (Shen, Kong, Dong, et al. 2021a; J. Zhang 2020). A similar ventilation factor was also applied incorporating with the Wells-Riley model by Sun and Zhai (Sun and Zhai 2020). The equivalent ventilation rate (λ_{vent}) can be calculated by Eq. 2-66.

$$\varepsilon_{vent} = \frac{C_{exhaust}}{C_i} \tag{2-65}$$

$$\lambda_{vent} = f_{HVAC}\lambda_{HVAC}\varepsilon_{vent} + f_{AirCleaner}k_{AirCleaner} \quad (2\text{-}66)$$

Table 2-18. Ventilation effectiveness of some ventilation strategies (Shen, Kong, Dong, et al. 2021a; J. Zhang 2020).

Ventilation strategy	**Ventilation effectiveness**
Mixing ventilation	1
Displacement ventilation	1.2 – 2
Semi-open space with partitions installed	2 – 3
Displacement ventilation with partitions installed	14 – 100
Personal ventilation	1.4 – 10

The fresh air supplied by the HVAC system (λ_{HVAC}) includes the outdoor part and the recirculated part. The recirculated fresh air supply rate (Eq. 2-67) depends on the recirculated airflow rate ($\lambda_{recirculated}$) and the infectious particles filtration efficiency by the filters (η_{filter}).

$$\lambda_{HVAC} = \lambda_{outdoor} + \lambda_{recirculated}\eta_{filter} \quad (2\text{-}67)$$

The total supply airflow rate of the ventilation system equals to the summary of outdoor airflow rate and the recirculated airflow rate, which can be calculated by

$$\lambda_{supply} = \lambda_{outdoor} + \lambda_{recirculated} = \frac{\lambda_{outdoor}}{1-f_{recirculated}} \quad (2\text{-}68)$$

A portable air cleaner can supply additional fresh air. The infectious particle removal rate by air cleaners ($k_{AirCleaner}$) can be estimated by its airflow rate ($\lambda_{AirCleaner}$) and filter efficiency ($\eta_{AirCleaner}$), or based on its clean air delivery rate (CADR) and room volume (V):

$$k_{AirCleaner} = \lambda_{AirCleaner}\eta_{AirCleaner} = \frac{CADR}{V} \quad (2\text{-}69)$$

The pathogen removal rate by the UVGI system depends on the fraction of UVGI operation time (f_{UV}) and the pathogen inactivation rate due to ultrafine (UV) irradiation (k_{UV}). The infectious particle deposition rate ($k_{deposition}$) relies on an approximate estimate of gravitational settling (Eq. 2-70) (Nicas et al. 2005), which depends on the particle diameter (d_p) and room height (H). The possible impacts of environmental conditions on particle deposition (L. Zhao et al. 2020) are not considered in this study.

$$k_{deposition} = \frac{0.108{d_p}^2(1+\frac{0.166}{d_p})}{H} \quad (2\text{-}70)$$

Virus-carrying aerosols expelled by the COVID-19 patients have been detected to be infectious in some hospital settings (Lednicky et al. 2020; Santarpia et al. 2020). However, the field data are not designed to determine how long the virus can survive. Some experimental studies have also been conducted in laboratory environments to study the viability of virus-laden aerosols in the air

under different environmental conditions. The infectivity of viral aerosols can typically remain for up to hours in the air under typical indoor environment conditions. But a rapid decay was observed when the aerosols were exposed to sunlight (Dabisch et al. 2020; Schuit et al. 2020). Temperature and humidity may also influence the persistence of viable SARS-CoV-2 in aerosols. van Doremalen et al. (van Doremalen et al. 2020) observed an inactivation rate of $0.63h^{-1}$ for SARS-CoV-2. Fears et al. (Fears et al. 2020) measured a nearly zero decay rate. Schuit et al. (Schuit et al. 2020) revealed a mean decay rate of $0.48h^{-1}$ without sunlight. Smither et al. (Smither et al. 2020) suggested a decay rate of $0.95h^{-1}$ in aerosols at medium humidity condition and $0.24h^{-1}$ at high humidity condition. Dabisch et al. (Dabisch et al. 2020) observed decay rates of $0.36h^{-1}$ and $1.02h^{-1}$ in the environment with room temperature and no sunlight. Therefore, the typical inactivation rate of SARS-CoV-2 aerosols at typical indoor temperature and humidity is generally between 0 and $1h^{-1}$. Sunlight can possibly contribute greatly to the inactivation of SARS-CoV-2 (Dabisch et al. 2020; Schuit et al. 2020), but is not considered in this study. In this study, the inactivation rate of $0.63h^{-1}$ is adopted as the natural inactivation rate for estimation.

Another significant factor that affects infection risk is the emission rate of viral particles. Quantum generation rate per infector (*ER*) is a critical parameter in the Wells-Riley model. The magnitude of *ER* depends on disease species, infector activities (e.g. breathing, coughing) and interventions (e.g. wearing masks), and may vary significantly case by case (Buonanno, Stabile, et al. 2020; Stephens 2012). The value of *ER* of a COVID-19 infector is currently not well established. It is believed to be close to the *ER* of influenza and SARS-CoV-1 because their basic reproduction numbers (R_0) are close (Dai and Zhao 2020; Imai et al. 2020; Khalili et al. 2020; Q. Li et al. 2020; Majumder and Mandl 2020; Read et al. 2020; S. Zhao et al. 2020). One quantum in the model

represents an infectious dose that would infect 63% of the population with the exposure per the Wells-Riley model (Riley et al. 1978). It describes the number of infectious particles in a way that implicitly includes both the number and the infectivity of virus particles (which also inherently captures particle size effects and probability of deposition in appropriate regions of the respiratory system) (Stephens 2012). The quanta emission rate has a unit of quanta per hour (h^{-1}), and the magnitude relies on disease species, infector activities (e.g. breathing, coughing) and interventions, and may vary significantly case by case (Buonanno, Stabile, et al. 2020; Stephens 2012). The quantum generation rate can be estimated from retrospective analysis on real outbreak events if sufficient epidemiological data are available for the disease. However, the epidemiological data for emerging respiratory diseases like COVID-19 are likely insufficient especially at the early stage of outbreaks.

The viral load of the particles exhaled by the infector is closely associated with the infection risk of airborne transmission. However, it is still difficult to directly determine the viral load of the exhaled particles. Considering that exhaled particles are formed in the respiratory tract and released through respiratory activities, it is possible to derive the exhaled viral load based on the viral load in the respiratory tract, which can be detected more easily (Buonanno, Stabile, et al. 2020). A viral load model has been proposed (Eq. 2-71) to estimate the viral load emitted by a contagious subject based on the viral load in the mouth (or sputum), the type of respiratory activity (e.g., breathing, speaking, or coughing) and activity level (e.g., resting, standing, light exercise) (Buonanno, Stabile, et al. 2020). The emission rate of virus quanta (ER) can be determined by the viral load in the sputum (c_v), the conversion factor (c_i), inhalation rate (IR), and total particle volume (relies on particle number N_D and volume V_D of each size in diameter D).

$$ER = c_v \cdot c_i \cdot IR \cdot \int (N_D \cdot dV_D) \quad (2\text{-}71)$$

The viral load in sputum has been measured in some studies. Fajnzylber et al. (2020) measured 1.8-9.0 $\log_{10}$ RNA copies/mL in sputum with a median level of 4.4 $\log_{10}$ RNA copies/mL. Wölfel et al. (2020) measured the average viral load in sputum of 6.85 $\log_{10}$ RNA copies/mL, with a maximum of 9.37 $\log_{10}$ RNA copies/mL. Yoon et al. (2020) reported the viral load in the sputum of two patients between 4.86 and 8.22 $\log_{10}$ RNA copies/mL. Kim et al. (2020) detected the viral load in the sputum of the first two patients in South Korea roughly between 5 and 9 $\log_{10}$ RNA copies/mL. Pan et al. (2020) collected sputum samples from 80 patients and observed a median viral load of 5.88 $\log_{10}$ RNA copies/mL with a maximum of 11.13 $\log_{10}$ RNA copies/mL. Zheng et al. (2020) collected 1846 respiratory samples (including sputum and saliva samples) and detected the viral load approximately between 3 and 8 $\log_{10}$ RNA copies/mL. To et al. (2020) measured the peak viral load in the respiratory tract between 3.91 and 7.56 $\log_{10}$ RNA copies/mL with a median of 5.29 $\log_{10}$ RNA copies/mL for patients with mild disease, and the peak viral load between 4.27 and 7.40 $\log_{10}$ RNA copies/mL with a median of 6.91 $\log_{10}$ RNA copies/mL for patients with severe disease. Han et al. (2020) detected the viral load in the sputum of a patient roughly between 4 and 6 $\log_{10}$ RNA copies/mL. It can be observed that the viral load in sputum can reach a level as high as 11 $\log_{10}$ RNA copies/mL, while most of the existing data is approximately below 9 $\log_{10}$ RNA copies/mL. A recent study (J. Li et al. 2021) reviewed and analyzed the existing data of viral load in sputum in literature (397 samples) and observed a normal distribution of viral load with a mean value of 4.87 $\log_{10}$ RNA copies/mL and a standard deviation of 1.90, indicating 99% of the viral load in sputum is below 9.30 $\log_{10}$ RNA copies/mL. Some

variants may have higher viral loads than the original strain. A study reported over 1000 times greater viral loads in oropharyngeal swabs for the Delta variant than the original viral lineage (B. Li et al. 2021).

Some studies have conducted measurements of virus distribution in indoor environments rather than directly on exhaled droplets. Stephens (2013) reviewed such studies for influenza and estimated the size-resolved distribution of pathogen using the data in the literature (W G Lindsley et al. 2010), i.e. 15% of pathogens in the 0.3-1μm size range, 25% in the 1-3μm size range, and 60% in the 3-10μm size range. A report from CDPH (2020) suggested the distribution of 20%, 30%, and 50% for infectious particles of SARS-CoV-2 in 0.3-1μm, 1-3μm and 3-10μm, respectively. It was assumed that those indoor measurements account for a combination of all human respiratory activities that occur indoors (Stephens 2013). In this study, it is assumed that 15% of virus-laden particles are in the 0.3-1μm size range, 25% in the 1-3μm size range, and 60% in the 3-10μm size range.

Table 2-19 shows the quantum generation rate of SARS-CoV-2 from retrospective analysis and through the viral load model in literature. In this study, the infectious quantum generation rate is estimated based on the viral load model (Eq. 2-71). Previous studies measured the viral load of COVID-19 patients and suggested that the viral load can typically reach 10^9 RNA copies/mL (Buonanno, Stabile, et al. 2020; Dubert et al. 2020; Han et al. 2020; J. Y. Kim et al. 2020; Pan et al. 2020; Rothe et al. 2020; Wölfel et al. 2020), which is used in this study. A reported average value of 0.02 is applied as the c_i in the model (Buonanno, Stabile, et al. 2020). The highest droplet number concentration in (Buonanno, Stabile, et al. 2020) is adopted. The droplet volume

calculation uses the geometric mean diameters for each particle size bin (i.e., 0.55μm, 1.7μm, and 5.5μm for particles of 0.3-1μm, 1-3μm, and 3-10μm, respectively [98]). Three different activity levels are considered: sedentary and light-intensity (breathing or whispering while seated or standing), moderate-intensity (speaking while seated or standing) and high-intensity (breathing or speaking while running or doing exercises).

Table 2-19. Quanta emission rates (*ER*) of SARS-CoV-2 particles in different studies.

Activity	***ER*** **[h^{-1}]**	**Introduction**	**Reference**
Estimated from retrospective analysis on real outbreak events			
Standing + singing	970±390	Skagit Valley Chorale superspreading event	Miller et al. (2020)
Standing + singing	341	Skagit Valley Chorale superspreading event	Buonanno et al. (2020)
Standing + singing	870	Skagit Valley Chorale superspreading event	Bazant et al. (2021)
Seated + vocalization	61	Guangzhou restaurant outbreak event	Buonanno et al. (2020)
Resting + breathing	45	Zhejiang tour coach outbreak event	Bazant et al. (2021)
Resting + breathing	30	Diamond Princess cruise ship outbreak event	Bazant et al. (2021)
Resting + breathing	29	Wuhan city outbreaks	Bazant et al. (2021)
Resting + breathing	185.63	Diamond Princess cruise ship outbreak event	Chen et al. (2021)
Estimated using the viral load model			
Resting	<1		Buonanno et al. (2020)
Intermediate	≤100	Estimated based on the viral load in the sputum	
Light activity + vocalization	>100		
Resting + breathing/whispering[a]	3	Estimated based on $c_v = 10^9$ RNA copies/mL and	Buonanno et al. (2020)

Standing + breathing/whispering	3	c_i = 0.02	
Light activity + breathing/whispering	9		
Resting + speaking[b]	50		
Standing + speaking	56		
Light activity + speaking	142[c]		
Estimated using statistical methods			
Sedentary state	14-48	Estimated based on the fitting curve between *ER* and R_0 from the data of other respiratory diseases (e.g., influenza and SARS-CoV-1)	Dai and Zhao (2020b)

[a] Breathing/whispering represents the mean value between whispering and breathing (Buonanno, Stabile, et al. 2020).

[b] Speaking is considered as the mean value between unmodulated vocalization and voiced counting (Buonanno, Stabile, et al. 2020).

[c] This value was adopted by many studies (Harrichandra et al. 2020; S. Zhang and Lin 2020).

Genetic variants of SARS-CoV-2 have been emerging and circulating around the world throughout the COVID-19 pandemic (U.S. CDC 2021d). Evidence has shown that some variants are associated with an increase in transmissibility and more severe disease, e.g. increased hospitalizations or deaths, and may also reduce the effectiveness of previous treatment measurements (U.S. CDC 2021d). At the current stage, the main SARS-CoV-2 variants of concern (VOCs) include the Alpha variant (B.1.1.7, first detected in the U.K.), the Beta variant (B.1.351, first detected in South Africa), the Gamma variant (P.1, first detected in Brazil), the Epsilon variant (B.1.427 and B.1.429, first detected in California) and the Delta variant (B.1.617.2, first detected in India). Studies have revealed that these variants generally have higher transmissibility than the original lineage, therefore, cause even more concerns about their spreading. The Alpha variant was observed 43 to 90% more transmissible than the predecessor lineage (N. Davies et al. 2021). The Beta variant was estimated to be 1.56 (95% CI 1.50-1.74) times transmissible as previously circulating lineages (Pearson et al. 2020). The Epsilon variant was detected and estimated to have an 18.6-24% increase in transmissibility (Deng et al. 2021). The latest and prevailing variant so far, the Delta variant, is responsible for over 83% of new infections in the U.S. as of July 2021 (Fry and Rapp 2021). It is highly contagious, nearly twice as transmissible as the original strain or previous variants (with an odds ratio of 1.88 (95% CI 0.95-3.76) compared with the original type (Ong et al. 2021) or an odds ratio of 1.64 (95% CI 1.26-2.13) compared to the Alpha variant (Hester Allen et al. 2021)). A recent report indicated that the viral loads of Delta infections were on average around 1000 times greater compared to the original strain of COVID-19 (B. Li et al. 2021). In many countries, the Omicron variant has become the major challenge of COVID-19. Thus, the transmission of the airborne route for the Omicron variant requires certain attention and studies. In this study, the virus generation rate is assumed to be 200 quanta/h.

Face masks provide air filtration at a personal level for wearers, which is a critical strategy for mitigating infection risk. Face masks can reduce the average emission rate by approximately 30%, 50% and 95% with cloth, surgical and N95 masks, respectively (Mueller et al. 2020). Konda et al. (Konda et al. 2020) measured the mask filtration efficiency for particles in different diameters (Table 2-20). The particle-size weighted removal efficiencies of different masks can be estimated based on the assumed infectious particle size distribution. The particle-size-weighted efficiency is around 32%, 44% and 95% for cloth, surgical and N95 masks, respectively. This study uses the present Wells-Riley model for estimating the infection risk in indoor spaces. An online tool is also developed based on the proposed model and can be accessed through: (Shen, Kong, Birnkrant, et al. 2021).

Table 2-20. Mask filtration efficiency for particles with different sizes.

Mask	**Particle removal efficiency η_{filter} [%]**			
	0.3-1μm	**1-3μm**	**3-10μm**	**Particle-size-weighted[c]**
Cloth (cotton/silk, with gap)[a]	27	33	34	32-33
Surgical (with gap)[a]	41	44	45	44
N95[b]	95	95	95	95

[a] Average value of the data measured in (Konda et al. 2020).

[b] Assuming 95% for all size ranges.

[c] Monte Carlo approach is implemented that adopts uniform probability distribution of particle sizes, i.e. 10-20% in 0.3-1μm, 20-30% in 1-3μm, and remaining 50-70% in 3-10μm.

2.2.4 Simulation methods and implementation

2.2.4.1 Model linearization

State-space matrices (SSM) are created to solve the RC network models of thermal and mass balance equations, respectively. The SSM representation is a mathematical model of a physical system as a set of input, output and state variables related by first-order linear differential equations, which is widely used for solving control problems (X. Chen et al. 2015; Fontenot et al. 2021; Tang and Wang 2019). Therefore, the SSM approach is suitable for solving the problems presented in this study. The SSM for thermal and mass balance models with p inputs (p_1, p_2, and p_3), q outputs and n state variables can be represented as Eq. 2-72. x is the state vector representing the state variables in this study such as air and surface temperatures and pollutant concentrations, $x \in R^n$. u, v, and w are the input (or control) vectors and are usually represented as a single vector as u in other studies. In this study, to better describe and distinguish different parameters, the input vector is divided into three vectors, $u \in R^{p1}$, $v \in R^{p2}$, $w \in R^{p3}$. In this study, u represents the input vector such as heat gains for thermal modelling and pollutant production for mass modelling. v and w are control vectors only available in thermal modelling, representing the HVAC inputs and heating/cooling setpoints, respectively. y is the output vector, representing the heating and cooling loads for thermal modelling, $y \in R^q$. A is the state (or system) matrix with a dimension of $n \times n$. B, E, and F are the input matrices with a dimension of $n \times p_1$, $n \times p_2$, and $n \times p_3$ respectively. C is the output matrix with a dimension of $q \times n$. D, G, and H are the feedthrough (or feedforward) matrices with a dimension of $q \times p_1$, $q \times p_2$, and $q \times p_3$ respectively. For thermal modelling in this study, G is a zero matrix. $\dot{x}$ is the time derivative of the state variable.

$$\dot{x} = A \cdot x + B \cdot u + E \cdot v + F \cdot w \tag{2-72}$$

$$y = C \cdot x + D \cdot u + G \cdot v + H \cdot w \quad (2\text{-}73)$$

For thermal models, the state variables in x include surface temperatures of an envelope (interior and exterior) and the space temperature. Therefore, for a building case with f surfaces and s spaces, the dimension of x for annual hourly simulation (8760 hours annually) is $(2f+s)\times 8760$. u contains thermal boundary conditions (ambient air temperature and ground temperature) and heat gains on each surface and space (including solar heat gain, longwave radiative heat gain, and other internal heat gains such as infiltrated, lighting, occupant, equipment heat gains). So the dimension of u is $(2+4f+4s)\times 8760$. w is the heating or cooling energy input in the space with a dimension of $s\times 8760$. v is the heating and cooling setpoint (or setback) temperature of the space and its dimension is $2s\times 8760$. For mass modelling, the state variables in x represents the concentration of a specific pollutant in the space, with a dimension of $s\times 8760$. u includes the pollutant boundary condition (ambient pollutant concentration) and pollutant removals and generations in each space (internal pollutant sources and sinks). The dimension of the input matrix u is $(2s+1)\times 8760$.

2.2.4.2 Model discretization

The SSM models are discretized to transfer continuous functions, models, variables, and equations into discrete counterparts. The discretization of the SSM models in this study is performed using Eqs. 2-74 to 2-81. The matrices with subscript of d are the discretized forms, where t_s is the sampling time.

$$A_d = e^{A \cdot t_s} \quad (2\text{-}74)$$

$$B_d = A^{-1}(A_d - I)B \tag{2-75}$$

$$E_d = A^{-1}(A_d - I)E \tag{2-76}$$

$$F_d = A^{-1}(A_d - I)F \tag{2-77}$$

$$C_d = C \tag{2-78}$$

$$D_d = D \tag{2-79}$$

$$G_d = G \tag{2-80}$$

$$H_d = H \tag{2-81}$$

2.2.4.3 Model solving

Thermal and mass state variables are solved through the iteration of the SSM models established. Closed-loop simulations will be performed considering the operation of HVAC systems to address heating/cooling demand by the occupants indoors. The operation of HVAC systems is determined by the setpoint and setback temperatures. The schedule depends on either preset operation schedules or the occupancy of the room (occupancy-based control) or other control strategies. The

operations of other building modules (such as air cleaners and shading system) also depend on the control/operation strategies user set up, either fixed schedule, occupancy-based schedule, or other control strategies (e.g. CO2-level-based control or solar-radiation-based control). For building modules with variant schedules, the operation of the module is determined within each time-step iteration. Besides, for calculations considering the longwave radiant heat transfer between surfaces, during each time-step iteration, the thermal transfer between surfaces is calculated and applied as the heat gain/loss at the next time step. As the weather data and ambient pollutant data is usually collected hourly. In this study, the iteration is performed hourly. In this study, annual simulation is performed.

2.2.5 Optimization

To optimize the application of various building technologies/systems in green building design, performance simulation models can also collaborate with optimization algorithms to determine their optimal configurations (Kheiri 2018; Nguyen et al. 2014). Multi-objective optimization (MOO) is widely used to optimize the building features to achieve the trade-off between different performance criteria, e.g. energy efficiency, IAQ, thermal comfort, and cost (Chegari et al. 2021; Diakaki et al. 2008; Ghaderian and Veysi 2021; W. Li et al. 2021; Hongbin Liu et al. 2013; Shaikh et al. 2018; N. Wang et al. 2014; X. Wei et al. 2015; B. Wu et al. 2021). MOO refers to finding the optimal solution values of more than one desired goal. The motivation for using MOO is because it does not require complicated equations, which consequently simplifies the problem. MOO has emerged as the preferable approach to tackling sustainability problems. The process of optimization is to minimize the objective cost functions (e.g. energy consumption and infection risk). The solution of MOO models is generally expressed as a set of Pareto optima, representing

optimal trade-offs between given criteria. In this study, a multi-objective genetic algorithm (MOGA) is applied, which is based on the process of the genetic algorithm; the population-based property of the genetic algorithm is well applied in MOGAs (Long et al. 2015).

2.3 Modeling and simulation platform (A plugin in Rhino Grasshopper)

The algorithms and models of performance simulation and optimization are developed and tested by Matlab or Python (Shen et al. 2020; Shen and Zhang 2019). To better demonstrate the green building design process using the proposed module-based GDS platform, a graphic user interface (GUI) is built as a plugin in Rhino Grasshopper, which is a widely used programmable building design platform as introduced earlier in this paper. Grasshopper is a parametric and algorithmic modelling tool created by David Rutten at Robert McNeel & Associates (Robert McNeel and Associates 2009), which works with Rhino to allow a powerful and efficient new way of designing. It allows different types of algorithms in design including numeric, textual, audio-visual and haptic applications. Currently, numerous developers have contributed to the development of a variety of applications in Grasshopper, such as parametric geometry modelling, optimization algorithms, machine learning methods, and environmental calculations (Robert McNeel & Associates 2022a). As reviewed in Chapter 1, the BPS tools developed in Grasshopper include Ladybug, Honeybee and ArchSim that estimate energy use and/or solar radiation based on EnergyPlus and/or Radiance, CFD-based building or urban airflow simulation tools such as Butterfly, Eddy, and RhinoCFD, and urban energy simulation and optimization tools like Dragonfly (based on UWG and CitySim) (Robert McNeel & Associates 2022a). Rhino and Grasshopper provide powerful software development kits (SDKs) for developers, which allow developers to program applications through C#, Python or VB.

RhinoCommon is the cross-platform .NET plugin SDK for Rhino development, while Grasshopper SDK is the SDK for Grasshopper development (Robert McNeel & Associates 2022b; Robert McNeel and Associates 2009). Figure 2-15 shows the hierarchy of RhinoCommon API and Grasshopper API. Except the classes shown in Figure 2-15, functions in System and MathNet.Numerics packages are also used in this study that deal with systematic issues and numeric calculations as shown in Figure 2-6. The general logic of the development of a Grasshopper plugin is taking the geometric models created in Rhino as inputs, connecting the components developed in Grasshopper with the geometries from Rhino, performing algorithms/models within each component of Grasshopper, and exporting and/or visualizing modelling results. Therefore, the programming of the plugin in this study is roughly divided into three categories, including the functions/classes defining the components in Grasshopper (GH Components, i.e., representation of GDS modules), the functions/classes used for calculations through different algorithms (GDS Functions), and the functions/classes for developing the panels in Rhino (GDS Panels) for information inputs as illustrated in the schematic in Figure 2-16.

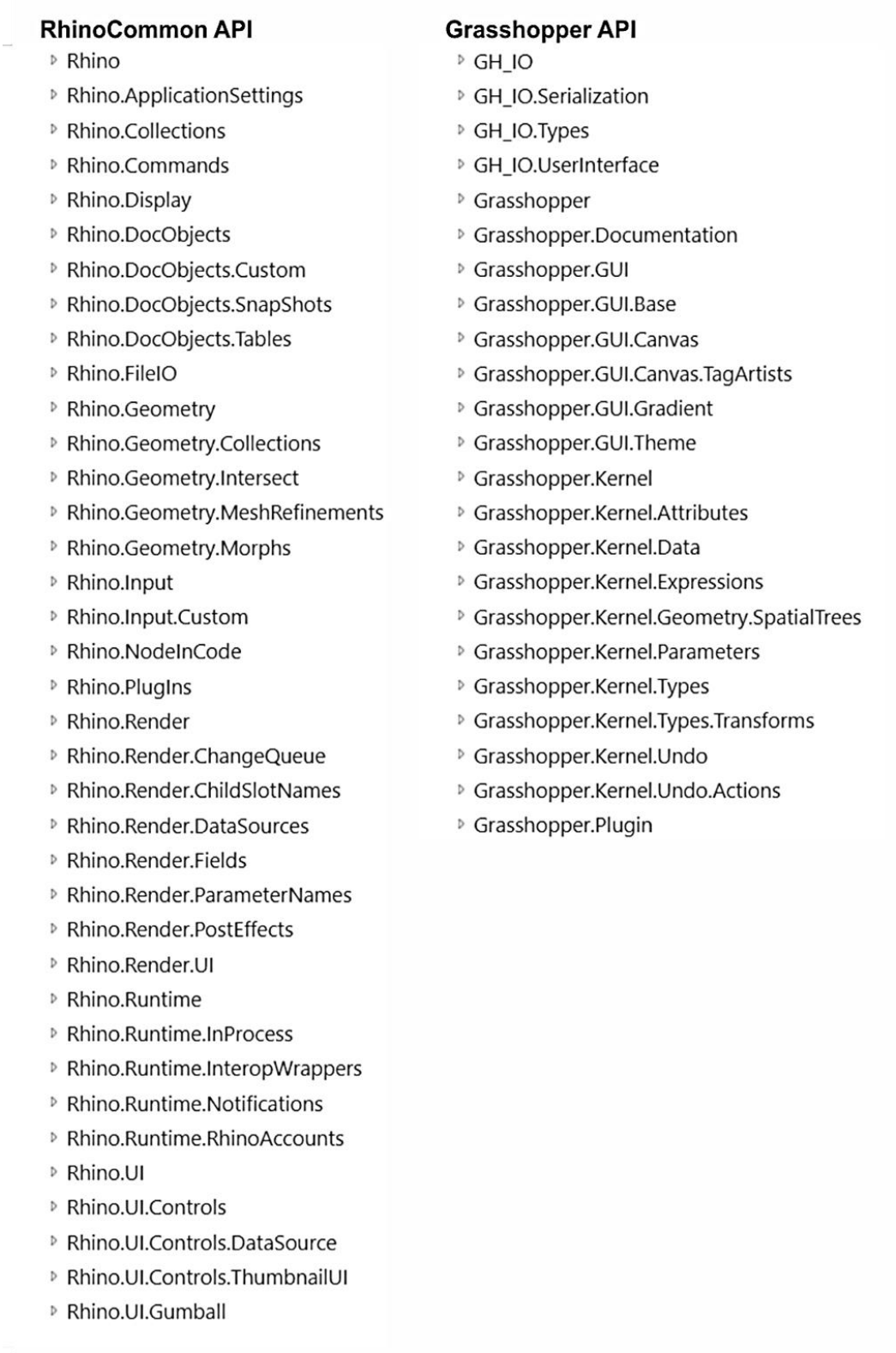

Figure 2-15. Structure of RhinoCommon API and Grasshopper API.

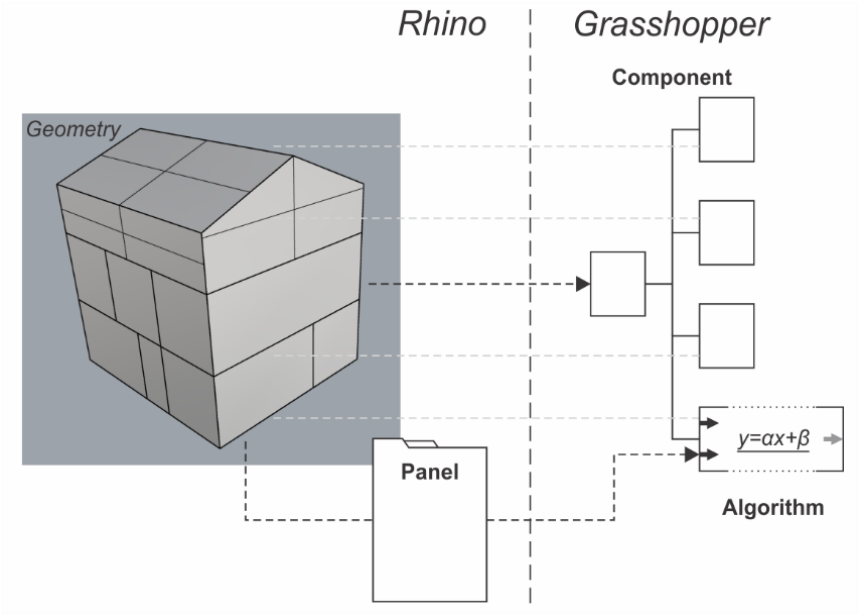

Figure 2-16. Schematic of workflow of Grasshopper components with Rhino geometries.

The components in Grasshopper are inherited from the GH_Component class from Grasshopper.Kernal. The component needs to be initialized first to define its name, description, category, and the father plugin's name. In this study, all components are registered under the GreenDesignStudio plugin. Then developers should register all input parameters and output parameters, with a variety of categories such as geometry (e.g. point, surface, box, etc.), number, Boolean, matrix, mesh, text parameters, etc. The geometry inputs are usually collected from the selections in Rhino UI, and the other inputs can be the outputs from other components or manual inputs by users. The structure of input and output parameters can be an item, a list, or a tree. The method of the component is defined in the SolveInstance property to perform and solve calculation using the data collected from the inputs and export the results to outputs. It is also necessary to

provide an icon for the component. The Exposure property controls where in the panel a component icon will appear. Besides the mandatory properties, developers can also override properties such as BeforeSolveInstance or define their own properties to add advanced functions before or after the method of the component.

The development of general algorithms has less restrictions than the development of components. Properties such as classes and functions can be defined for backend calculations. They are used for advanced processing or calculations that work with components. The development of panels in Rhino is based on the Rhino.PlugIns.PlugIn property in RhinoCommon. Commands can also be defined to perform certain commands by certain operations in Rhino. The development of panels is optional in this study. The main purpose of them is to provide a more straightforward approach to define some features to the geometry created in Rhino. In this study, building and room functional types can be defined through the GreenDesignStudio panel, e.g., bedroom, living room, and kitchen for residential buildings, conference room, open plan office, and lobby for offices. This information can also be assigned in Grasshopper through the developed components. But it is more straightforward to be defined through the panel in Rhino. More panels that can assign inputs or change parameters can be developed in future. But in this study, the development of panel is just for demonstration and is only used for representing building/room types. The hierarchy of the properties developed in this study is shown in Table 2-21. A brief description of each function/class is also presented.

Table 2-21. Functions and classes defined in the GreenDesignStudio plugin.

Category	**Property**	**Description**
GH Components (GDS modules)	GHCommunity	Component that defines a community module (a bunch of building modules) from the selection of geometries in Rhino
	GHBuilding	Component that defines a building module from the selection of geometries in Rhino
	GHBuildingInfo	Component that can edit/update detailed building information
	GHSpace	Component that defines a space module
	GHEnvelope	Component that defines an envelope module
	GHEnvelopeInfo	Component that can edit/update detailed envelope information
	GHConstruction	Component that defines a construction
	GHMaterial	Component that defines a material
	GHOccupancy	Component that defines an occupancy module

GHSchedule	Component that defines and contains schedules
GHHVAC	Component that defines a HVAC system with certain settings (e.g., airflow rate, set point temperature, etc.)
GHLight	Component that defines a lighting system
GHEquipment	Component that defines an equipment
GHAirCleaner	Component that defines an air cleaner
GHRenewableEnergy	Component that defines a renewable energy generation system
GHGreenModules	Component that contains green modules
GHDBConstruction	Component that contains datasets of construction in the systematical database
GHDBMaterial	Component that contains datasets of materials in the systematical database
GHFFD	Component that performs fast fluid dynamics (FFD) (not completed)

	GHSimulation	Component that performs BPS
	GHResults	Component that processes simulation results
	GHComparison	Component that compares simulation results from multiple cases
GDS Functions	GDSModules	Functions/classes that define building modules
	GDSSimulation	Functions/classes that perform BPS
	GDSGreenModules	Functions/classes that contain green modules
	GDSReference	Definitions of data structures for key classes/variables
	GDSExtensions	Library of factors, materials, schedules, etc.
GDS Panels	GDSPanelPlugIn	Panel instance
	GDSPanelCommand	Commands to the actions from the panel

Figure 2-17 shows the detailed inputs and outputs for major GH components of the GDS plug-in, and Figure 2-18 illustrates the rational of connections between different components of a simple example. Building component creates the GDS_Building instance that contains detailed settings for building, zone, envelope, construction, occupancy, HVAC, lighting, equipment, and other facilities. The default settings are generated based on the reference settings for a specific type of building/space from standards or practices. The GDS_Building instance is generated from the geometries (Boundary REPresentation, or BREP) created in Rhino. Each BREP block is created to represent a single space/zone/room. The combination of multiple BREP blocks forms a building model. The connection between different BREP blocks is processed by determining whether two adjacent blocks are intersected by the same surface. The surface is marked as an interior surface, and set up by specific characteristics for a certain type of interior surface (e.g. interior wall, ceiling, floor, or interior window).

The generated GDS_Building instance then exports to the building information component to change its settings such as HVAC system, envelope settings, lighting, and equipment settings, if necessary. Envelope information components can be used to change the settings of a specific type of envelope of the building. For that selected type of envelope, the construction, infiltration coefficient, and window and shading settings will be set up. Special features of the envelope can also be added, e.g., solar chimney. HVAC components are created to change the HVAC settings for the whole building. Users can set up the HVAC variables like mode (e.g., ideal system), airflow rate, recirculated fraction, filter efficiency, other in-duct air cleaning efficiency, setpoint/setback temperature control and settings, and air delivery method (e.g., mixing ventilation, displacement ventilation), and occupancy sensing feature. Lighting and equipment components can set up the

power, working schedule, control method, and pollutant emission rate. Air cleaner components are used to set up the power, pollutant removal efficiency, secondary emission (if it exists), and working schedule and control method. Renewable energy generation component can change the settings for a specific type of renewable energy generation technology. For example, for a PV panel, the conversion coefficient and delivery coefficient of the energy generation, PV panel area, activated fraction of the area, and PV panel direction (Azimuth and Zenith angles), and the control method, can be set up. Simulation component imports the generated and update GDS_Building instance as the input, and run the simulation with certain weather and air quality conditions collected and parsed from the EPW file (for thermal modelling) and the data provided by U.S. EPA (AQS API (U.S. EPA 2023)). Result component can import the simulation results, generate export files containing state variables (surface and air temperatures, pollutant concentrations), and visualize the result in Rhino Grasshopper. The result data visualization can also be performed by incorporating the components in other plug-ins, e.g., the data visualization components in Ladybug. The performance of a certain green building technology can be presented by comparing the case with proposed green technologies and the reference without green features.

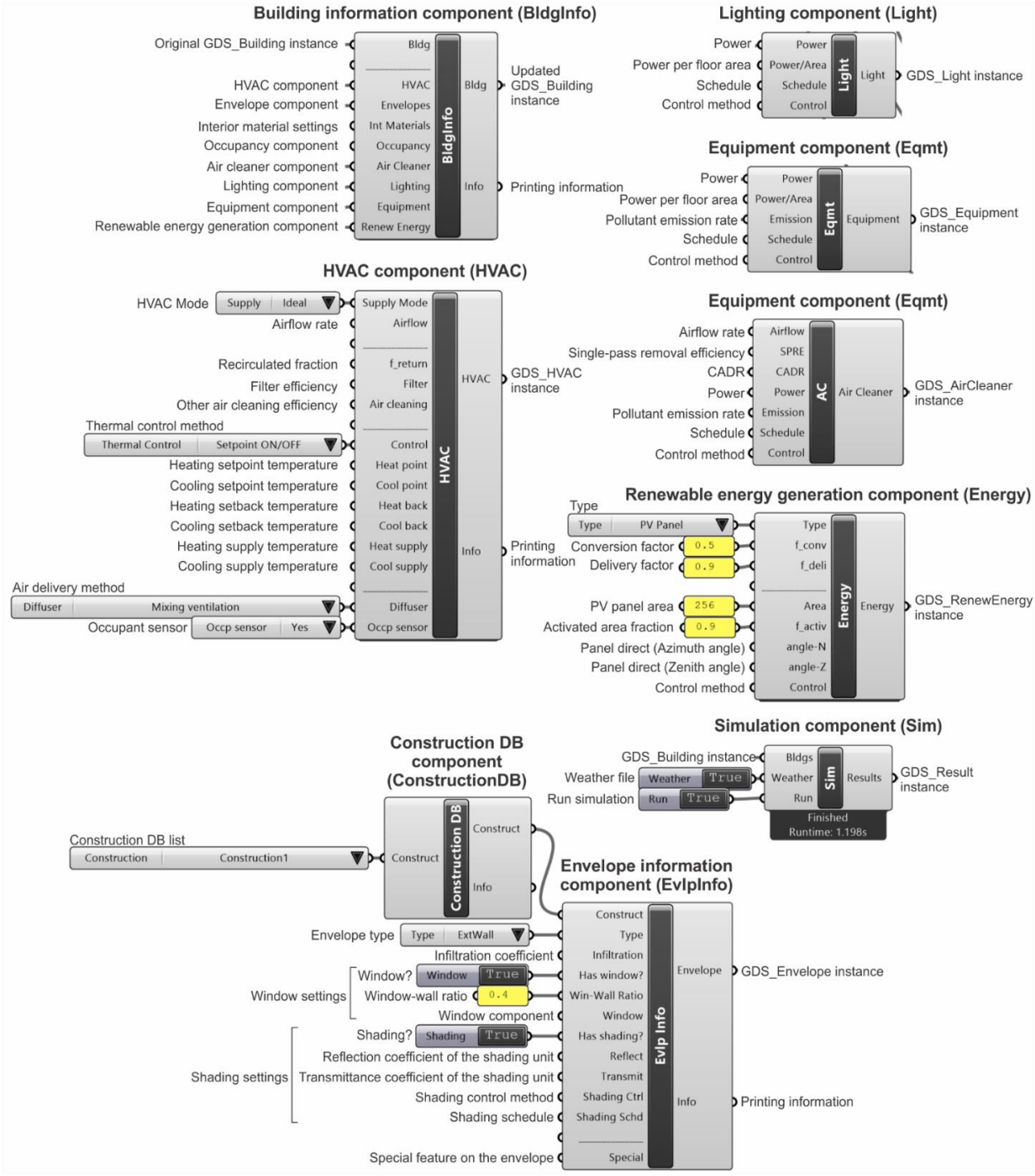

Figure 2-17. Major GH compounds (GDS modules) of the GDS plug-in.

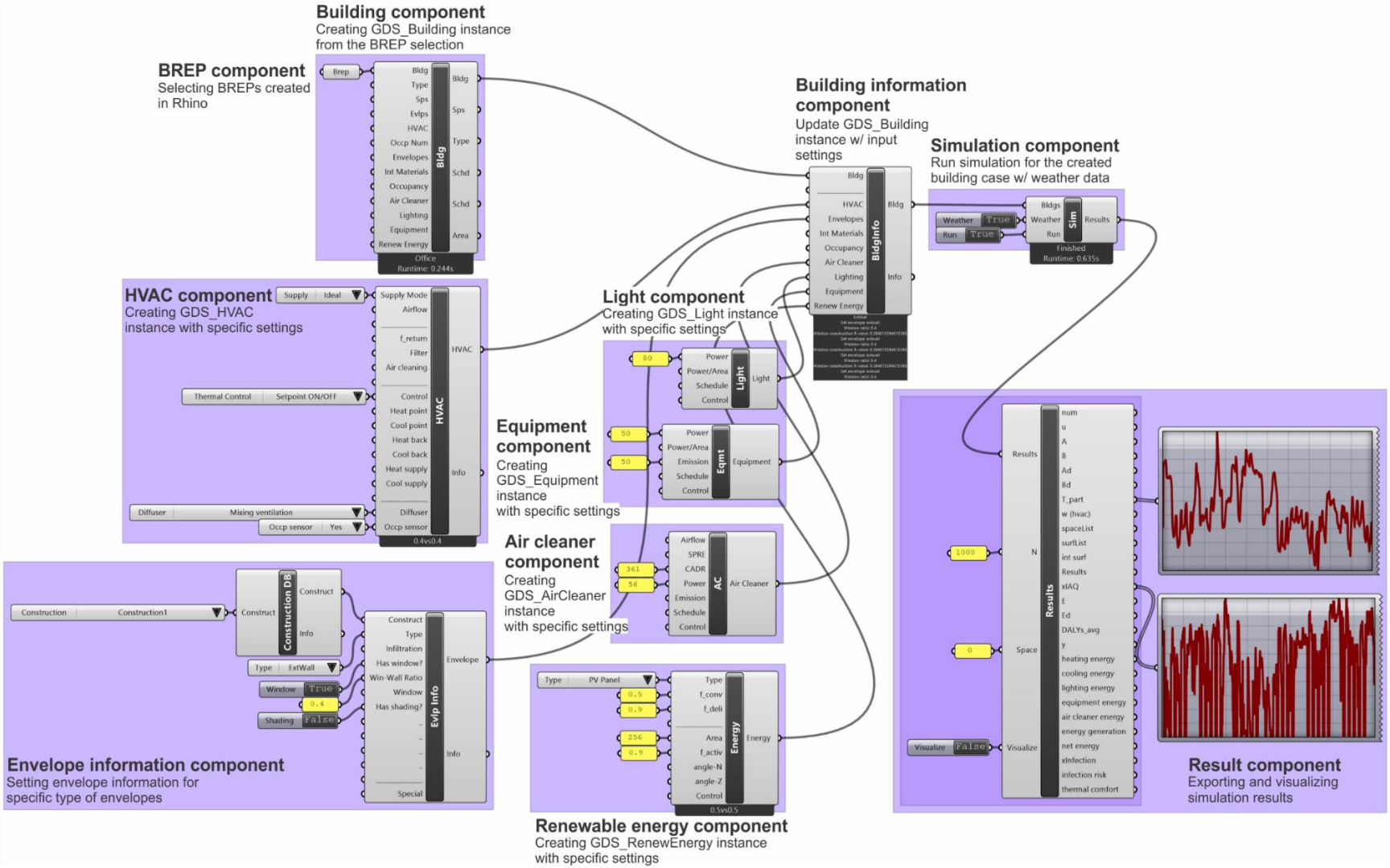

Figure 2-18. An example of the application of GDS plugin.

2.4 Case study

Case study is conducted to demonstrate the application of the developed GDS plug-in for building performance analysis and green building design. Two study cases are presented, including a DOE prototype building (small office) and the Syracuse COE headquarter building.

2.4.1 DOE prototype building - Small office case

2.4.1.1 Case description

DOE prototype buildings were created by U.S. DOE, which cover 75% of the commercial building floor area in the U.S. for new construction, including both commercial buildings and mid- to high-rise residential buildings, and across all U.S. climate zones (U.S. DOE 2013). The case files were generated for EnergyPlus modelling (IDF files), comply with the ASHRAE 90.1 and IECC standard. The small office prototype building is a one-floor building with an unconditioned attic underneath the pitch roof (Figure 2-19). The building has four perimeter zones and one central zone used for office scenario. The room settings are shown in Table 2-22.

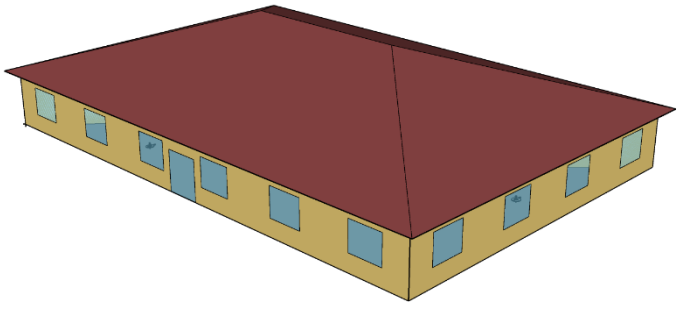

Figure 2-19. DOE prototype building of small office (U.S. DOE 2013).

The building has a total of 510 m^2 of conditioning area. The window-wall ratio on exterior walls was set as 0.4. Each window has a U-value of U-0.45 and a SHGC of 0.38. Exterior walls with R-20, interior walls with R-5, floor with R-15, ceiling with R-45, and exterior roof with R-30 were set up in the simulation. Envelope thermal properties were derived from the IDF file of the original prototype case and align with the ASHRAE 90.1 Standard. The maximum air infiltration on each exterior surface is 1.8 $m^3/h \cdot m^2$, while during the simulation operation a 0.25 ratio of the maximum infiltration was applied on the surface. Lighting and equipment were operated with the typical office schedules (Figure 2-9). The heat generation from lighting and equipment aligned with the EnergyPlus setting. The occupant density defined in ASHRAE 62.1 Standard was used to estimate the occupancy number in offices (0.05 person/m^2), resulting in 29 occupants in total. The occupancy schedules in Figure 2-8 were used. Occupants were seated or walking with 1 MET activity level when presented in the building. Heat generation from occupancy activities was 104 W with 40% convective heat that considered by the simulation. The clothing condition by occupants was assumed to be 1 clo in winter and 0.5 clo in other seasons.

The study case was simulated with the climate in Syracuse, NY. EnergyPlus weather (EPW) file of Syracuse was applied to the case. Building energy consumption, thermal comfort, IAQ (4 typical indoor contaminants, i.e. PM2.5, ozone, CO2, formaldehyde), health impacts and infection risks of COVID-19 were simulated. Ambient PM2.5 and ozone concentrations were collected from EPA Air Quality System (AQS) database. Ambient CO2 level was assumed to be 400 ppm while outdoor formaldehyde was assumed to be 7.2 $\mu g/m^3$, which was suggested by the WHO report (WHO 2010). Data collected from Brazil, Canada, Germany, Italy, Mexico, Netherlands, and U.S., provided ambient concentrations of 1.5-16.4 $\mu g/m^3$ with a mean value of 7.2 $\mu g/m^3$ (SD = 5.1

μg/m^3). Outdoor concentration variations of ambient CO2 and formaldehyde were not considered in this study. Indoor pollutant emission sources included occupant activities and building materials, furniture, and decorations. Each occupant was assumed to generate PM2.5 in 10 mg/h, 13.9 L/h CO2 (based on estimation using Eq. 2-34 (M. Li et al. 2022; Persily and de Jonge 2017)). Indoor materials generate 500 μg/h formaldehyde in each zone. Natural decay of PM2.5 in indoor environments was assumed to be 0.25 h^{-1} (Shen, Kong, Dong, et al. 2021a) and natural decay of ozone was 4 h^{-1} (Yao and Zhao 2018). Infection risks were simulated with the assumption of one infector was presented in each zone during the occupied period of the zone. Each infector produced 100 quanta/h virus-laden aerosols to the space (Shen, Kong, Dong, et al. 2021a, 2021b). Natural decay of virus-laden aerosols included particle natural deposition of 0.25 h^{-1} and natural virus inactivation of 0.63 h^{-1} in the air (Shen, Kong, Dong, et al. 2021a, 2021b).

An ideal HVAC system was used to provide conditioned air to meet the heating and cooling requirements of the building. Air volume was variable depending on the requirement. A simple ON/OFF control was applied to control the operation of the system. When the indoor air meets the heating/cooling setpoint/setback temperature, the system was off. Otherwise, the system would be operated to provide conditioned air to the space until the temperature meets the criteria again. The system was assumed to provide 25% outdoor air as the reference. A MERV 8 filter was used to filtrate the intake air.

Table 2-22. Simulation settings.

Zones	Type	Zone south (ZS): Office Zone north (ZN): Office Zone east (ZE): Office Zone west (ZW): Office Zone central (ZC): Office Attic: Unconditioned zone
Geometry	Dimensions	Zone south (ZS): 113 m^2 × 3.05 m = 345 m^3 Zone north (ZN): 113 m^2 × 3.05 m = 345 m^3 Zone east (ZE): 67 m^2 × 3.05 m = 204 m^3 Zone west (ZW): 67 m^2 × 3.05 m = 204 m^3 Zone central (ZC): 150 m^2 × 3.05 m = 458 m^3 Attic: 568 m^2 with 3.28 m height, 720 m^3 in volume (pitched roof)
Envelope	Window setting	Window-wall ratio on exterior walls: 0.4 U-value: U-0.45 SHGC: 0.38
	Surface thermal properties	Exterior wall: R-20, Cp = 1090 J/kg·K, ρ = 800 kg/m^3, θ = 0.1 m Interior wall: R-5, Cp = 1090 J/kg·K, ρ = 800 kg/m^3, θ = 0.05 m Floor: R-15, Cp = 1500 J/kg·K, ρ = 2000 kg/m^3, θ = 0.2 m

		Ceiling: R-45, Cp = 1090 J/kg·K, ρ = 800 kg/m^3, θ = 0.1 m Exterior roof: R-30, Cp = 1090 J/kg·K, ρ = 800 kg/m^3, θ = 0.1 m
	Infiltration	1.8 m^3/h·m^2 maximum on exterior surfaces (schedule ratio: 0.25)
Lighting	Intensity	6.89W/m^2 (10% convective heat)
	Schedule	See Figure 2-9
Equipment	Intensity	6.78W/m^2 (convective heat)
	Schedule	See Figure 2-9
Occupancy	Density	0.05 person/m^2 per ASHRAE 62.1 Standard (29 occupants in total)
	Schedule	See Figure 2-8.
	Activity	Seated when occupied (1 MET) Skin area: 1.8 m^2 Heat generation per person: 104 W (40% convective heat) Clothing: 1 clo in winter and 0.5 clo in other seasons
Indoor pollutant emissions	Pollutant generations	PM2.5: 10 mg/h·person [a] Ozone: 0 (5 μg/h if an upper-room UVGI system used) CO2: 13.9 L/h·person (1 MET, BMR = 8) (M. Li et al. 2022; Persily and de Jonge 2017)

		Virus quanta: 100 quanta/h·infector (1 infector assumed in each zone) Formaldehyde: 500 μg/h from materials, furniture and decorations in each room
Indoor pollutant removal	Pollutant removals	PM2.5: 0.25 h^{-1} (Shen, Kong, Dong, et al. 2021a) Ozone: 4 h^{-1} (Yao and Zhao 2018) CO2: 0 Virus quanta: 0.25 h^{-1} (natural deposition) + 0.63 h^{-1} (natural inactivation) (Shen, Kong, Dong, et al. 2021a, 2021b) Formaldehyde: 0
HVAC	Setpoint	Heating: 23 °C Cooling: 26 °C
	Setback	Heating: 12 °C Cooling: 28 °C
	Supply temperature	Heating: 38 °C Cooling: 13 °C
	Airflow rate	Variable air volume to meet the thermal requirement

	Outdoor air fraction	0.25
	Filter efficiency	MERV 8 filter: 50% for PM2.5 and virus-laden aerosols, 0% for removing ozone, CO2 and formaldehyde.

[a] Walking-induced particle emission and resuspension was around 60 mg/h per room (Practice et al. 2016). Assuming 6 occupants in each room (similar to the proposed case), each occupant generated 10 mg/h particles.

2.4.1.2 Building performance simulation

Annual energy and IAQ performance of the reference office building were performed. The simulation was performed on an Intel Core i7-8750H CPU on a Windows laptop with a 16 GB memory. The simulation finished in 36.6 seconds. Figure 2-20 shows the indoor air temperature change over the simulated period in Zone South. Indoor air temperature can be maintained at either setpoint or setback temperatures very well. Heating and cooling energy accounts for the majority part of the total energy consumption by the building. Energy used by lighting and equipment systems also make a great contribution to the total energy use, while energy consumed by the fan system of the HVAC system is very limited.

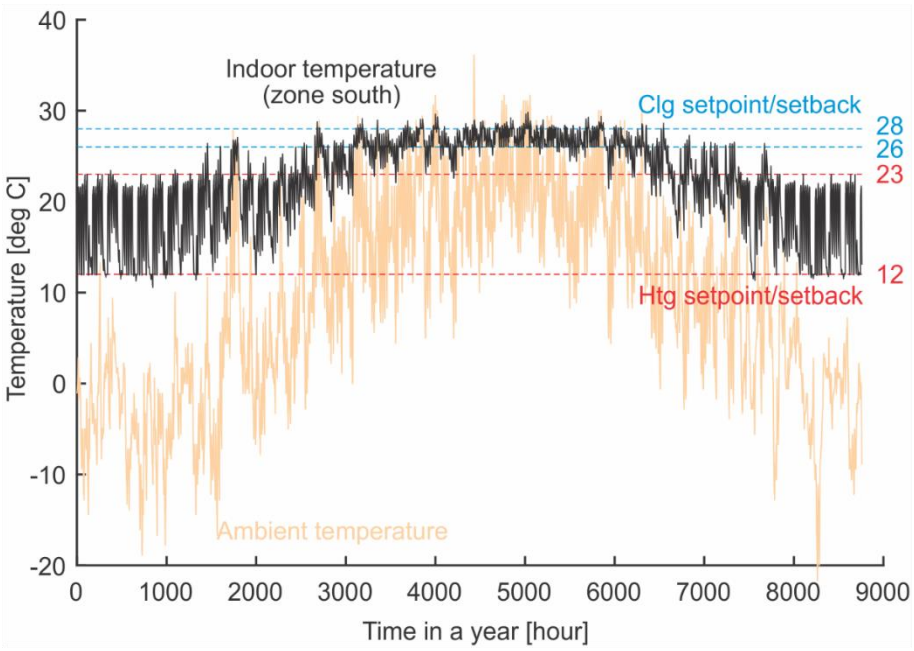

Figure 2-20. Indoor air temperature in Zone South of the simulated period.

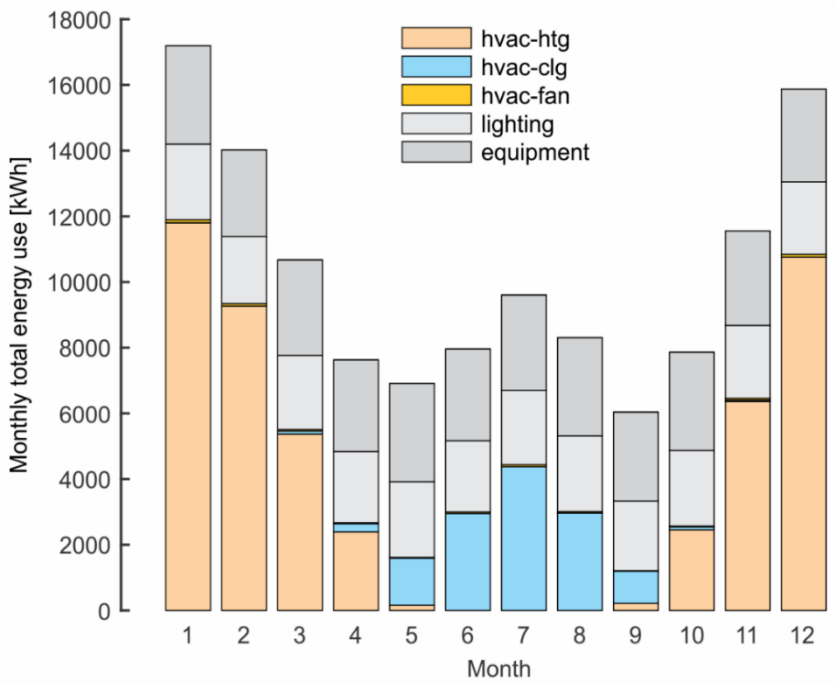

Figure 2-21. Monthly energy use by each category of the whole building.

Total energy use by the HVAC system (heating/cooling energy and fan power), lighting system, and equipment consumption is 123,636.4 kWh, with an average of 242.4 kWh per m^2 conditioned area (compared to 171.15 kWh/m^2 for offices from the EIA CBECS survey (U.S. EIA 2020b)). The average thermal comfort during the occupied period in each space is 66.1%. Average indoor concentrations of PM2.5, ozone, CO2 and formaldehyde are 4.0 mg/m^3, 5.9 ppb, 585.6 ppm, and 9.1 μg/m^3, respectively. Formaldehyde has the greatest health impact with average DALYs of 1089.6 years. PM2.5 caused DALYs of 39.8 years and ozone caused almost 0 years due to the lower indoor level. The average daily infection risk in the building is around 33.6% assuming an average exposure duration of 8 h a day. Therefore, the reference case has certain potential of energy saving and IAQ improvement to reach a better performance on IAQ and energy efficiency.

Table 2-23. Building performance of the small office prototype.

Energy use	Annual energy use [kWh]	123,636.4
	Annual energy use per conditioned area [kWh/m^2]	242.4
Thermal comfort	Average thermal comfort during occupied periods [%]	66.1
Pollutant concentrations	Average PM2.5 concentrations during occupied periods [mg/m^3]	4.0
	Average ozone concentrations during occupied periods [ppb]	5.9
	Average CO2 concentrations during occupied periods [ppm]	585.6

	Average formaldehyde concentrations during occupied periods [$\mu g/m^3$]	9.1
Health impacts	DALYs due to PM2.5 exposure [yrs]	39.8
	DALYs due to ozone exposure [yrs]	0.0007
	DALYs due to formaldehyde exposure [yrs]	1089.6
Infection risks	Average virus quanta during occupied periods [quanta]	0.17
	Average daily infection probability due to exposure to virus quanta [%]	33.6

2.4.1.3 Evaluation of potential performance of green building technology

To improve the energy and IAQ performance of the tested building, six categories of green building technologies were applied to the reference case, including advanced envelope technologies (higher insulation, thermal mass, high-reflective envelope, window technologies, and better airtightness), HVAC technologies (return air ratio, and higher-efficiency filters), portable air cleaners, upper-room UVGI system, green indoor materials with less emissions, and personal protective equipment (PPE). The proposed case with green technologies was analyzed through the GDS approach. The performance improvement (%) of each technology is presented in Table 2-24.

Higher insulation envelopes can improve the building energy efficiency, thermal comfort, and health impacts due to exposure to indoor pollutants, while impairing infection risk mitigation efficiency. However, the improvement is very limited, probably due to the fact that the reference case already used very high insulation materials. It makes thermal insulation not the critical factor influencing energy consumption. Health impacts were affected by changing thermal insulation of the building envelope because the proposed HVAC system provided variable air volume to meet the change of heating/cooling load. When the heating/cooling load changes, supply air flow rate by the HVAC system will be changed. Then the ventilation supplied by the HVAC system will be changed as well. Thermal mass and window technologies do not affect the building performance very significantly either. But air infiltration through exterior walls has considerable impacts on energy and IAQ performance. If lower infiltration envelopes were applied, health impacts due to indoor pollutants will be impaired due to the accumulation of indoor pollutants. Introducing more outdoor air is good for diluting indoor contaminants, but will cause higher energy consumption. Increasing outdoor air ratio of the HVAC system will increase the energy consumption to conditioned the outdoor air and may introduced outdoor pollutant PM2.5 and ozone and affect health impacts, but it can help to mitigate indoor emissions including formaldehyde and virus quanta. Using HEPA filter also benefit indoor health effects and infection risk mitigation efficiency. Adding carbon filter that removes ozone and formaldehyde readily will benefit indoor health impacts.

Although portable air cleaners may increase building energy use, but the penalty can be neglected compared to its considerable improvement on health impacts and risk mitigation effectiveness. The upper-room UVGI system is highly effective for removing virus quanta and mitigate infection

risk. But it also requires elevated energy consumption. Green materials with less pollutant (i.e. formaldehyde in this study) emissions is very effective for health improvement. Wearing masks is very efficient for mitigating infection risks.

Table 2-24. Performance of green building technologies.

Technology		**Performance improvement (compared to the reference case) [%]**			
		Thermal comfort	**Energy efficiency**	**DALYs**	**Risk mitigation**
Envelope	R-25 exterior wall	0.14	0.10	0.07	-0.03
	R-30 exterior wall	0.26	0.15	0.17	-0.03
	R-35 exterior wall	0.31	0.22	0.23	-0.04
	R-40 exterior wall	0.35	0.27	0.32	-0.05
	Thermal mass for exterior wall (Cp = 2000 J/kg-K)	0.06	0.05	0.09	-0.04
	High-reflective envelope (reflectance = 0.7)	-0.03	0.09	-0.24	-0.03
	Low U-value window (U-0.3)	0.46	0.31	0.69	-0.03

	High SHGC window (SHGC = 0.82)	0.50	-1.36	4.44	0.37
	High infiltration exterior wall (9 $m^3/h \cdot m^2$)	-2.81	-2.56	42.51	3.42
	Low infiltration exterior wall (0.18 $m^3/h \cdot m^2$)	0.79	0.52	-464.61	-1.16
HVAC	Return fraction = 0.5	0	-5.41	-0.61	0.89
	Return fraction = 0.25	0	-10.96	-1.09	1.68
	Return fraction = 0	0	-16.74	-1.48	2.41
	HEPA filter	0	0	0.11	2.40
	Activated carbon filter (90% on ozone removal and 50% on formaldehyde removal)	0	0	6.86	0
Air cleaner	1 air cleaner with 361 m^3/h CADR for particles; 56W power	0.30	-1.30	0.30	46.18
	2 air cleaners	0.51	-2.55	0.40	62.73
	1 air cleaner with 361 m^3/h CADR for particles and	0.30	-1.30	34.02	46.18

	carbon filter for 90% ozone and 50% formaldehyde removal; 56W power				
Upper-room UVGI system	UVGI system for inactivating virus (12 h^{-1} equivalent ACH provided during the occupied period)	0	-3.75	0	88.41
Green material	Less emission materials (50% less emission of formaldehyde)	0	0	30.05	0
PPE	Cloth masks (50% on particles)	0	0	0	68.68
	Surgical masks (75% on particles)	0	0	0	91.69
	N95 masks (95% on particles)	0	0	0	99.66

2.4.1.4 Optimization of energy and IAQ strategies

The above analysis can provide the individual performance of each building module. However, it remains unknown how different building modules interact with others. During the pandemic, many IAQ improvement strategies have been proposed or implemented to minimize the infection risk. However, many of these strategies require considerable extra costs including energy use. Therefore, it is essential to find a tradeoff between risk mitigation and energy efficiency, especially considering longer term applications of these technologies. In this study, a MOO was performed to achieve the optimal design of building modules in terms of both energy efficiency and infection risk mitigation. A MOGA with a population size of 100 and a generation size of 20 was constructed to minimize energy use per area and infection risk. Parameters including envelope R-value, specific heat, absorption, infiltration coefficient, return air ratio, filter efficiency, air cleaner efficiency, material emissions, UVGI system, and air distribution.

Figure 2-22 shows the Pareto front of the optimization, indicating the optimal design features and objective outputs of the case. It can be found that under certain restraints, energy use of the building can be as low as 171 kWh/m^2, while infection probability can be below 0.017%. If we assume the energy use per area has to be below 175 kWh/m^2, the marked point at the Pareto front will be the optimal design of the building under the current settings. Then the parameter settings in Table 2-25 are the optimal settings for the current target. Compared to the reference case, the optimal design can save up to 27.8% energy use while mitigate more than 99% infection risk.

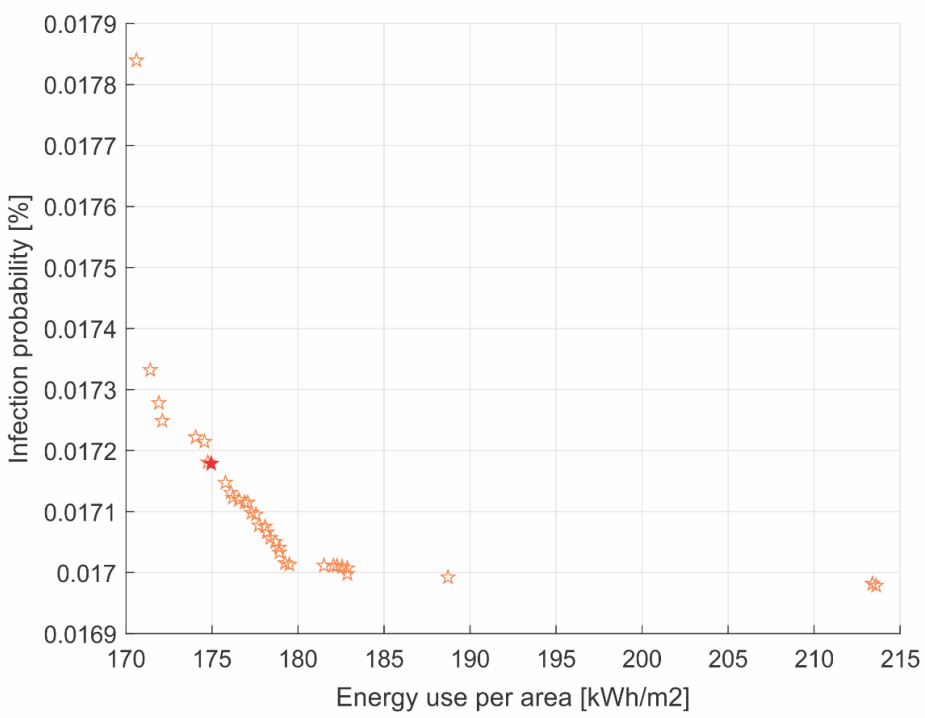

Figure 2-22. Pareto front of the optimization study.

Table 2-25. Optimal settings regarding energy efficiency and risk mitigation.

Parameter	Value
Exterior wall R-value	R-29
Exterior wall Cp [J/kgK]	1264
Exterior wall absorptance	0.39
Exterior roof R-value	R-26
Exterior roof Cp [J/kgK]	1433
Exterior roof absorptance	0.66

Window U-value	U-0.28
Window SHGC	0.69
Exterior wall infiltration coefficient	0.16
Return air ratio	0.71
Air distribution efficiency	2 (displacement ventilation)
Filter	HEPA
Air cleaner	HEPA, on
Air cleaner heat [W]	103
Air cleaner airflow rate [m^3/h]	502
UVGI system	On
UVGI efficiency [h^{-1}]	9
PPE	N95 mask (95% removal)

2.4.2 Energy and IAQ analysis in a section of Syracuse COE headquarter building

The Syracuse Center of Excellence (COE) headquarters office and laboratory building is utilized as the case study building, which is located in Syracuse, New York, US. The focus of the pilot study is on a section of the COE building, which includes a conference room (Room 203) and the affiliated south-facing corridor (Figure 2-23). The conference room is adjacent to the north side

and is connected to a part of a south-facing corridor. The south façade comprises full-height glazing and the interior walls separating the corridor and conference room utilize glass partitions for access to daylighting. The north façade is a steel-framed wall assembly with minimal glazing (window ratio around 0.4). The ceilings, floors and lateral walls/surfaces connect to adjacent rooms and corridor sections, and are therefore all interior partitions. In this study, the adiabatic boundary condition is adopted for these surfaces. Dimensions for the corridor and conference room are 3×9×3m and 15×9×3 m high, respectively (Figure 2-23).

According to the proposed modular method, the case study can be modularized following the structure in Figure 2-23, including the definition of zone modules, service system modules and enclosure modules. Some key module parameters of the study case are shown in Table 2-26. Five typical "green" strategies are applied in the building modules, including higher airtightness for building enclosure, super insulation for enclosure, thermal mass, controlled artificial lighting system and controlled shading system. The design parameters adopted for the reference case are defined based on the typical practices for conference rooms and corridors of an office building.

The airtightness of the reference case is 0.7 air changes per hour (ACH) for exterior windows. More airtight enclosures are applied to reduce heat loss or gain through infiltration in the target case, i.e. 0.5 ACH for exterior windows. Higher thermal insulation (R-value = 2.0K·m^2/W) is used for the exterior glazing surfaces on south and north façade compared to a reference R-value of 1.0K·m^2/W. Thermal mass is applied to the north wall with an elevated heat capacity of 2000J/kg·K. An intelligently controlled shading system is added to the south glazing façade of the

target case and it works when the solar irradiation on the south façade is higher than 100W/m^2 during summer (between June and August). The shading system is assumed to be able to reduce overall 70% of solar irradiation on the south façade, while the reference building does not have any shading system. The electric lighting schedule of the reference case follows the occupant schedule, which means the light is on when the corridor/room is occupied. The lighting intensity is 100lux (5W/m^2·100lux) for the corridor and 400lux (5W/m^2·100lux) for the conference room. In the target case, the lighting system is controlled depending on the daylighting intensity as well. The lighting system works following the same schedule as the reference case, but it will stop working when the daylighting can provide enough indoor illumination (100lux for corridor and 400lux for conference room).

To compare the performance of the proposed RC models in GDS and the conventional simulation model, an EnergyPlus model was developed to perform the energy and thermal simulation. Same settings of the RC models as introduced above were applied to the EnergyPlus model. Both GDS and EnergyPlus simulations were performed on the same computer (a Windows laptop with the Intel Core i7-8750H CPU and a 16 GB memory).

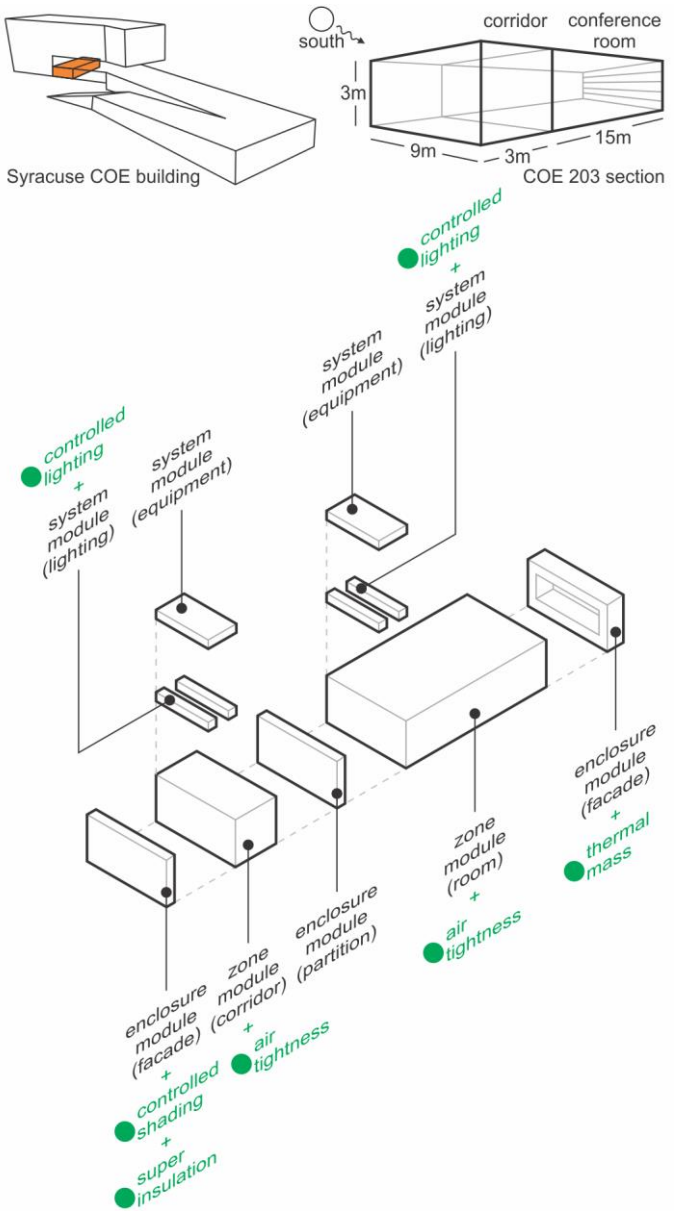

Figure 2-23. Schematic of the study case, COE building Room 203 section.

Table 2-26. Key parameters of building modules for the study case.

Module type	**Name**	**Module parameters**	**Values**	
			Target design	**Reference design[i]**
Zone	Corridor	Occupancy[a]	0.117/m^2; 140W/person;	
		Set point[a,b]	clg: 26/28°C; htg: 23/12°C;	
		R-value (int. conv.)[e]	0.3K·m^2/W	
		Air properties	1.225kg/m^3; 1005J/kg·K;	
Zone	Room	Occupancy[a]	0.111/m^2; 123W/person;	
		Set point[a,b]	clg: 25/28°C; htg: 24/12°C;	
		R-value (int. conv.)[e]	1.2K·m^2/W	
		Air properties	1.225kg/m^3; 1005J/kg·K;	
Service system (HVAC)	CorridorHVAC	Fresh air rate	1.0ACH	

		Filtration rate	100%	
		Heating Efficiency	0.5	
		Cooling COP	3.0	
Service system (HVAC)	RoomHVAC	Fresh air rate	1.0ACH	
		Filtration rate	100%	
		Heating Efficiency	0.5	
		Cooling COP	3.0	
Service system (lighting)	CorridorLighting	Illuminance[a]	Controlled lighting[c]	100lux; 5W/m^2·100lux;
Service system (lighting)	RoomLighting	Illuminance[a]	Controlled lighting[c]	400lux; 5W/m^2·100lux;
Service system (equipment)	CorridorEquipment	Heat gain[a]	1.85W/m^2	
Service system (equipment)	RoomEquipment	Heat gain[a]	11.77W/m^2	

Enclosure	SouthGlazingFacade	*R-value*	2.0K·m^2/W[g]	1.0K·m^2/W
		Cp	840J/kg·K	
		Density	2500kg/m^3	
		Thickness	0.005m	
		SHGC	0.819	
		Airtightness	0.5ACH[f]	0.7ACH
		Shading	Controlled shading[d]	No shading
		Pollutant removal[j]	0.0108h^{-1}	
Enclosure	GlazingPartition	*R-value*	1.5K·m^2/W	
		Cp	840J/kg·K	
		Density	2500kg/m^3	
		Thickness	0.005m	

		SHGC	0.768	
		Airtightness	0	0
		Shading	No shading	
		Pollutant removal	$0.0108h^{-1}$	
Enclosure	NorthFacade	*R-value*	$22.8K \cdot m^2/W$	
		Cp	$2000J/kg \cdot K^h$	$1000J/kg \cdot K$
		Density	$1400kg/m^3$	
		Thickness	0.2m	
		Thermal absorption	0.7	
		Airtightness	0ACH	
		Pollutant removal	$0.1058h^{-1}$	
Enclosure	NorthWindow	*R-value*	$2.0K \cdot m^2/W^g$	$1.0K \cdot m^2/W$

	Cp	840J/kg·K	
	Density	2500kg/m^3	
	Thickness	0.005m	
	SHGC	0.819	
	Airtightness	0.5ACH[f]	0.7ACH
	Shading	No shading	
	Pollutant removal	0.0009h^{-1}	

[a] These occupant parameters depend on specific schedules.

[b] clg means cooling and htg means heating. 25/28°C presents the set point temperature is 25°C while the setback temperature is 28°C. The set point temperature works between 6am and 7pm, while the setback temperature works for the other hours.

[c] The lighting system works following the same schedule as the reference case, but it will stop working when the daylighting can provide enough indoor illumination (100lux for corridor and 400lux for conference room).

[d] The shading system for south glazing façade will work when the solar irradiation on the south façade is higher than 100W/m^2 during summer (between June and August). When the shading system applied, the solar heat gain on the south façade need to be multiplied by a factor of 0.3.

[e] Convective *R-value* between the interior surface and air.

[f] Higher airtightness of building enclosure.

[g] Super insulation for exterior glazing façade.

[h] Thermal mass.

[i] Same as target building unless indicated otherwise.

[j] The ozone removal rate on building surface is estimated from literature (Shen and Gao 2018).

Performance metrics of energy consumption, percent of people satisfied with IAQ, thermal comfort and lighting quality are evaluated. The predicted annual performance metrics of the reference and target building by the RC model are shown in Table 2-27. The heating and cooling energy consumption is predicted assuming that the heating efficiency is 0.5 while the cooling COP is three. The target building can save considerable energy using these "green" strategies compared to the reference. People in the target building are more satisfied with the indoor air quality with more than 80% satisfaction when the indoor ozone limit is 35ppb (WHO 2005). The percent of people satisfied on indoor lighting quality is predicted when the recommended illuminance range for corridor is 50 to 150lux and the range for conference room is 300 to 500lux (IESNA 2011). The indoor illuminance is assumed to be uniformly distributed and the unevenness is not considered. The calculated lighting satisfied percent is almost zero because the indoor illuminance is far away from the recommended range due to the high-illuminance daylight transmitted through extensive glazing surfaces on façade. A more efficient shading strategy for south glazing façade is supposed to be used.

To evaluate the performance of different "green" strategies applied in the target building so as to find its best design strategy, the performance improvement potentials to the reference case are calculated based on different metrics (Figure 2-24). The table in Figure 2-24 is color-mapped by the magnitude of performance improvement potentials. A red cell means a positive potential, while a blue cell represents a negative effect. The tested five green strategies perform variably on the study case. According to the result, elevated airtightness for building enclosure can save considerable heating energy by reducing the heat loss through infiltration. But it will consume more energy for cooling due to the trapped internal heat from occupants, lighting, and incident

solar irradiation. An overall improvement for total energy use (i.e. combined heating, cooling, and lighting energy) is observed by applying higher airtightness in building enclosure. It will also improve the PPS on thermal comfort and IAQ. Lower infiltration results in the reduced ozone infiltrated from the outdoor air. Like the elevated airtightness, the higher insulation for exterior windows can save heating energy but consume more energy for cooling because of the trapped internal heat. A slight improvement is observed for the total energy efficiency. Higher insulation can slightly improve indoor thermal comfort in the corridor as well, but does not really work for improving thermal comfort in the conference room (almost 0%). It is probably because of the limited area of glazing surface on the north façade. Thermal mass does not appear to significantly affect the energy use or IEQ of the building (less than 0.5%) since the thermal mass material (concrete in this study) contributes limited to the whole building envelope. The controlled shading system can decrease the cooling energy consumption by reducing the solar heat gain in summer, while it does not work for reducing heating energy use. It has a limited improvement for total energy use for the whole building. At the same time, the controlled shading strategy will inversely impact the indoor thermal comfort, particularly for the corridor. The controlled lighting strategy can save massive lighting energy use (around 70%) since the daylight can provide considerable lighting to meet the illuminance requirement. Due to the reduced heat released from the electric lighting system, the heating energy use will increase while the cooling energy will decrease. Overall, the controlled lighting strategy will improve the total energy efficiency. However, an overall inverse impact on thermal comfort is observed, particularly for the room, which is mainly affected by the reduced internal heat gain during winter.

When applying all five strategies in the target building, the combined effect shows it will considerably reduce energy use and improve IAQ. But thermal comfort will not be improved due to the insufficient internal heat gain caused by the controlled shading and lighting strategy. Besides, neither of these strategies will affect the indoor lighting quality, likely because the incident illuminance is much higher than the recommended level. Considering that the thermal mass does not offer major improvement to the building performance in this study, and the controlled shading strategy cannot significantly improve energy efficiency and will even deteriorate the indoor thermal comfort. These two strategies are not recommended to be applied in the studied case. The other three strategies, i.e. higher airtightness, super insulation and controlled lighting, can be integrated in the building to better improve the energy efficiency but avoid the deterioration in IEQ. It can save around 14% of total energy use and elevate over 3% of people satisfied with the thermal comfort in corridor but have a slight decrease in the thermal comfort in room. People satisfied with IAQ will be improved by more than 6%. Therefore, in order to achieve a better performance and save the building cost, higher airtightness, elevated insulation, and controlled lighting strategy are recommended to be used in the design.

Table 2-27. Annual performance metrics of the reference and target building simulated by the RC model.

Case	**Space**	**Energy use[a]**				**IEQ**		
		Heating [kWh]	**Cooling [kWh]**	**Lighting [kWh]**	**Total energy use [kWh]**	**PPS_{IAQ}[b] [%]**	**PPS_{ITC} [%]**	**PPS_{ILQ} [%]**
Reference	Corridor	14427	985	591	16004	74.1	46.0	0
	Conference room	30603	2313	11826	44742	79.5	33.3	0
	Total	45030	3298	12417	60746	/	/	/
Target (with 5 strategies)	Corridor	13626	385	58	14069	79.9	42.5	0
	Conference room	32660	1125	3561	37346	84.4	32.2	0
	Total	46286	1510	3619	51415	/	/	/

[a] The total annual energy consumption is predicted assuming that the heating efficiency is 0.5 while the cooling COP is three.

[b] The indoor ozone concentration limit is assumed to be 35ppb based on the WHO baseline (WHO 2005).

[c] The illuminance limit for corridor is assumed to be in the range of 50 to 150lux, while the limit for conference room is between 300 and 500lux (IESNA 2011).

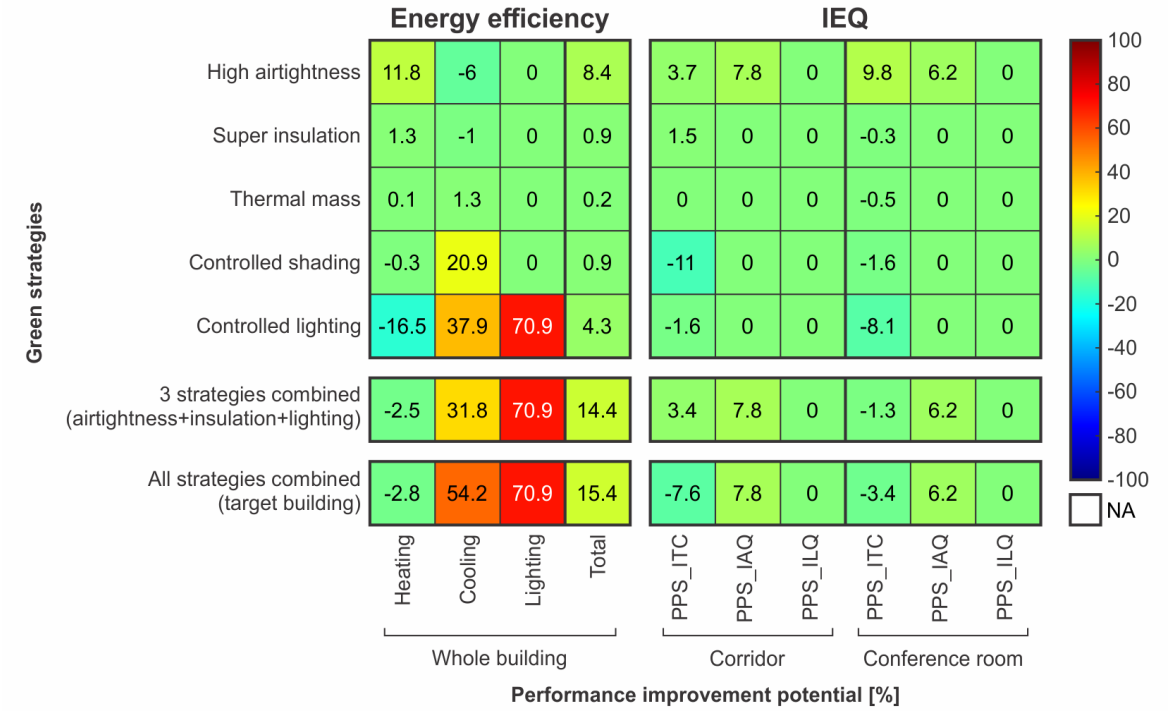

Figure 2-24. Performance improvement potentials of different green strategies.

The EnergyPlus simulation illustrates similar results. The comparison of predicted hourly air temperatures in the conference room and the corridor section of the reference case by RC model and EnergyPlus (EP) model are shown in Figure 2-25. The corresponding root mean squared errors (RMSE) of hourly air temperature between two models are 2.3 °C and 2.0 °C for the conference room and the corridor section, respectively. The runtime of the EnergyPlus model is 14.0 seconds while the runtime of the RC model is 3.6 seconds, which is significantly faster than the EnergyPlus model. The preparation process of the simulation is hard to quantify as it largely depends on users' experience and proficiency. But the application of GDS should be faster than the EnegyPlus simulation as the GDS model contains a lot of default settings, which can largely save time during the model establish process. However, the present example is a very simple case with only two

zones. When the model has a higher complexity (with more zones or surfaces), the simulation time using the RC model will increase accordingly.

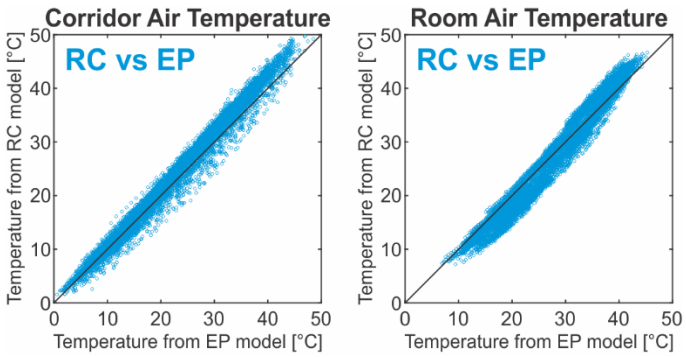

Figure 2-25. Comparison of predicted corridor and conference room air temperature from the RC model and EnergyPlus (EP) model.

2.4.3 Analysis and visualization of energy and thermal environment for the whole building of Syracuse COE headquarter

The whole building of Syracuse COE headquarter is also simulated to analyze its energy and IAQ performance. The Syracuse COE building is a 5-floor complex including both office and laboratory spaces (Figure 2-26). Figure 2-27 is a schematic of the 3D geometry model of the building in simulation. The building geometry model is simplified in certain content to simplify the simulation. The office space of the model has 56 zones across 5 floors, including open offices, small offices, conference rooms, lobbies, lounges, restrooms, dining spaces, and circulation spaces. The laboratory space of the model is simplified to 2 zones on 2 floors (1 zone per floor) as we focus on the office spaces in this study. The office space has a total area of 3113.2 m^2 (i.e., 310.3 m^2, 659.7 m^2, 665.3 m^2, 732.6 m^2, and 745.3 m^2 of floor 1 to 5, respectively). The laboratory space

has a total area of 3165.6 m^2 (1570.3 m^2 of floor 1 and 1595.3 m^2 of floor 2). The building has a total of 1051.7 m^2 window area, of which 723.2 m^2 on the south façade, 103.5 m^2 on the east façade, and 225.0 m^2 on the north façade. Energy and thermal environment simulation is performed in this example case.

Figure 2-26. Pictures of Syracuse COE building (from Toshiko Mori Architect).

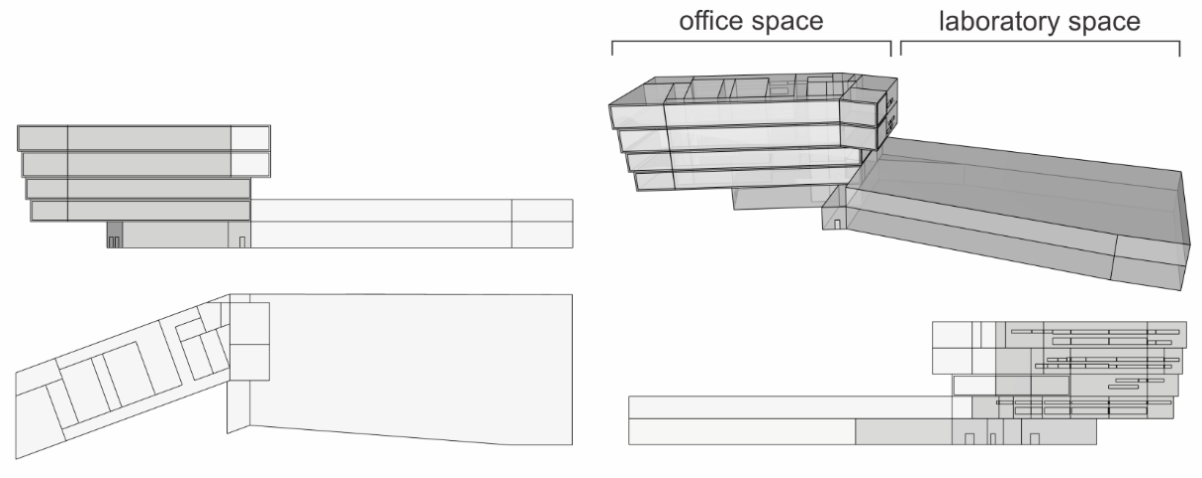

Figure 2-27. Schematic of the simulation 3D model of the building.

The same settings for Section 203 example of the building in Table 2-26 that is applied in the last section (Section 2.4.2) are applied to the whole building case here. The total energy use by the building during the whole simulation year is around 1,252,542 kWh. The average thermal comfort metrics across all zones of the building is around 82.2%. Monthly energy use for different types of applications (including heating, cooling, and fan energy of the HVAC system, lighting energy and equipment energy) is shown in Figure 2-28. Cooling energy consumption is higher than heating energy use. This is likely due to the high internal heat sources in the building, including occupant, lighting and equipment heat, as well as the higher heat gain from solar radiation through the large area of windows on the south façade. It means the design of glazing south façade can help to save considerable heating energy during the cold winter in Syracuse.

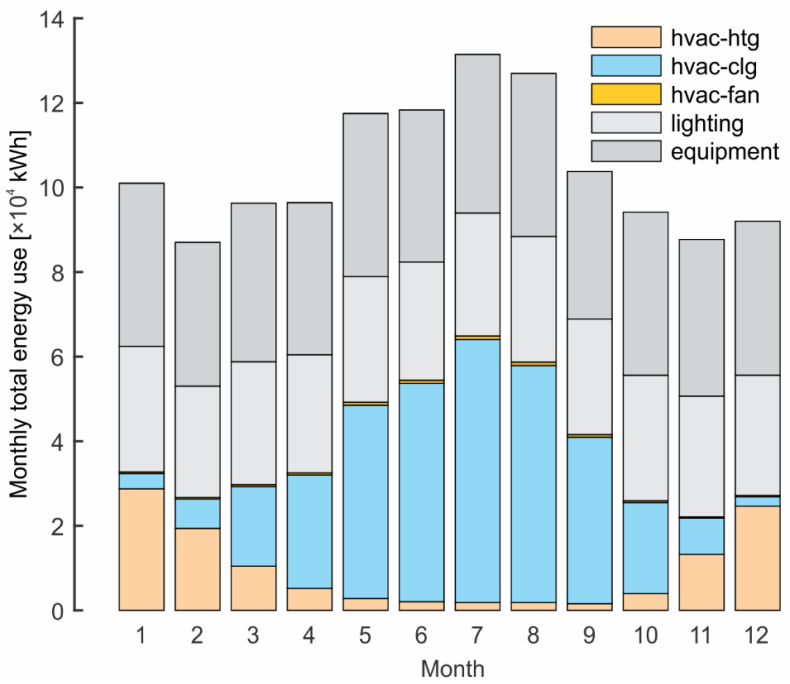

Figure 2-28. Monthly energy use for different types of applications by the building.

Room temperatures in different zones of the building are controlled by the ideal HVAC system. Figure 2-29 shows an example of the indoor room air temperature of the open office on the 3rd floor. The indoor temperatures are maintained well under the control of the ideal HVAC system. The distribution of room temperatures can be visualized by the GDS plugin in Rhino. Figure 2-30 demonstrates the room temperature distribution for the whole building on a typical summer day (June 21st) and a typical winter day (December 21st).

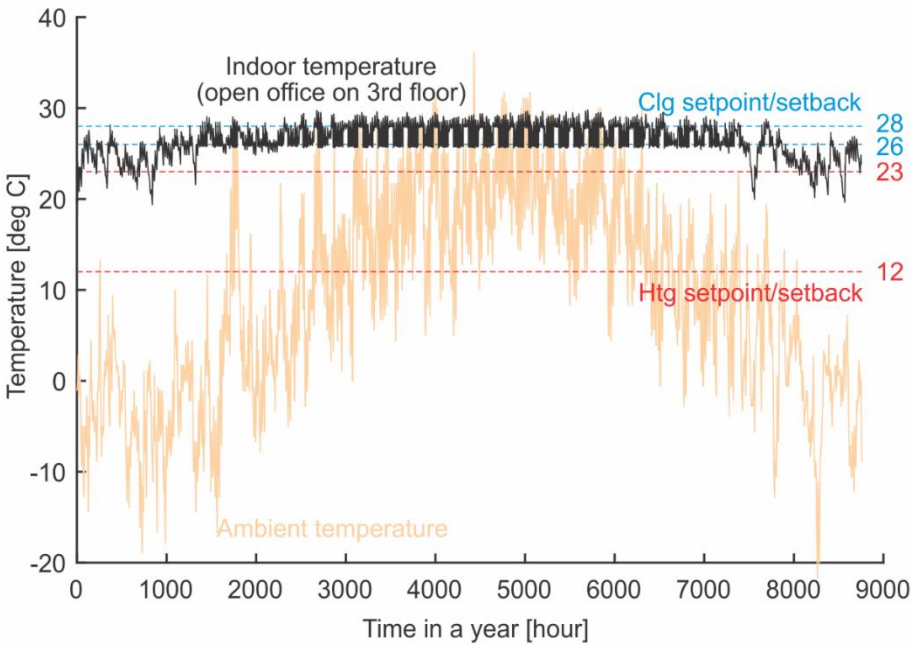

Figure 2-29. Whole-year indoor temperature of the open office on 3rd floor of the building.

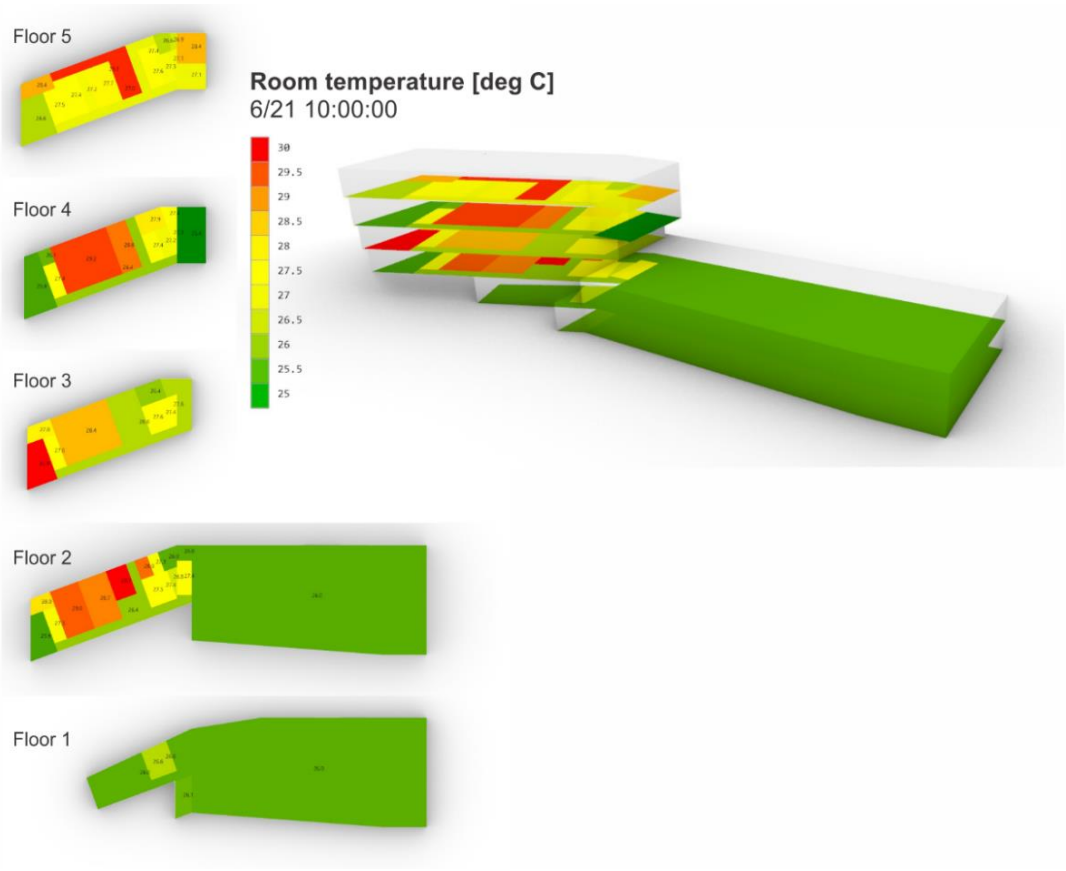

(a) Room temperature distribution at 10AM on June 21st.

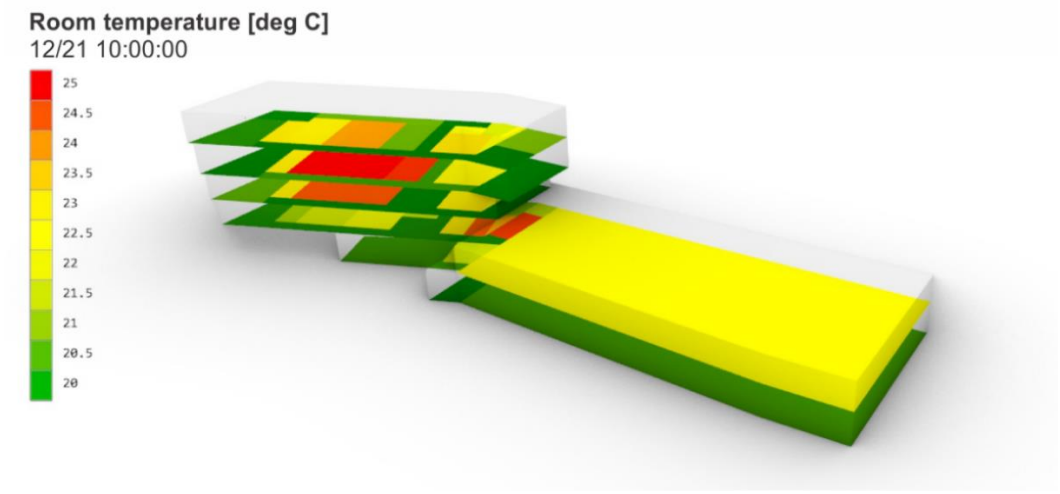

(b) Room temperature distribution at 10AM on December 21st.

Figure 2-30. Room temperature distribution of the whole building on Jun 21st and Dec 21st.

2.4.4 Energy saving analysis for an integrated building retrofitting approach - a case study in cold/very cold climates

Innovative building retrofitting strategies have been developed and implemented to achieve national goals of net-zero greenhouse gas emissions (White House 2021b, 2021a). Due to high heating demands in cold/very cold climates (McCabe et al. 2016), energy efficiency retrofits are desperately needed to reduce energy use. A whole-building retrofit solution with an envelope-HVAC integrated system has been developed to address this issue. The solution contains a novel highly-insulated exterior building envelope system that can be modularly attached to existing building enclosures, which includes a flashing solution for windows, doors, and penetrations for mechanical services, and an envelope-integrated HVAC solution that connects to an optimally-sized modular mechanical pod. Prototypes for the proposed retrofit solution have been developed and tested using facilities at Syracuse University including the Building Energy and Environmental Systems Laboratory (BEESL) and the Building Envelope Systems Testbed (BEST) (Krietemeyer et al. 2020). A diagram of the solution is shown in Figure 2-31.

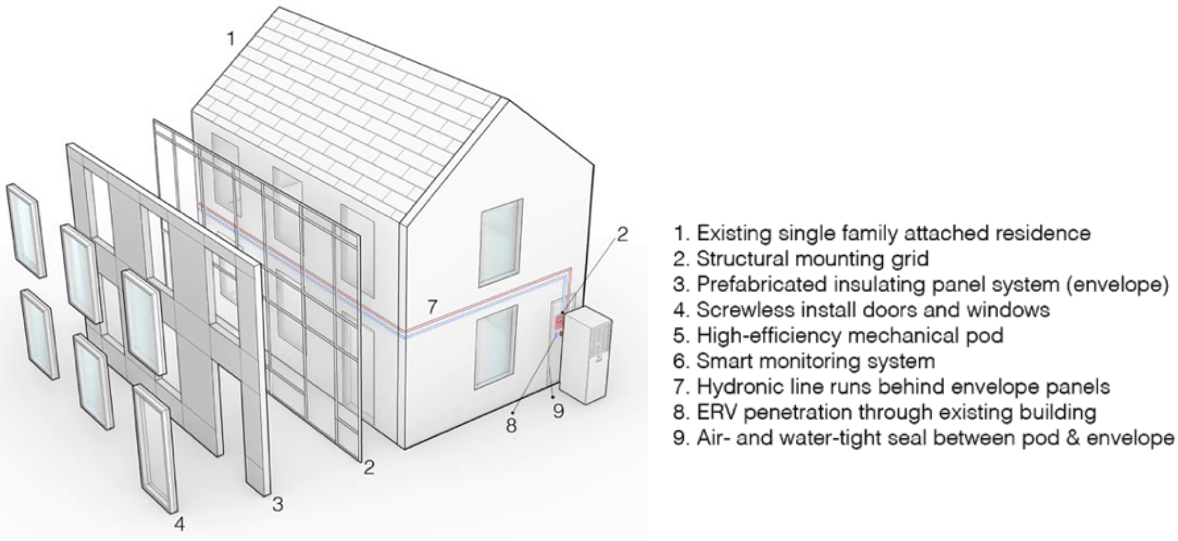

Figure 2-31. A diagram of the whole-building retrofit solution with integrated envelope-HVAC system (Krietemeyer et al. 2020).

Prefabricated retrofit envelope modules were developed in collaboration with Syracuse University, tkFabricate LLC, and Cocoon Construct Co. The envelope retrofit module consists of a 6-inch-thick lightweight sandwich panel that includes an expanded polystyrene (EPS) foam core, internal light-gauge galvanized steel members, and glass fiber reinforced cementitious lamina on all sides. The panel module assembly contains integrated structural studs and connection components that employ a "labyrinth" strategy to prevent air and water leakage. Additionally, an envelope-integrated HVAC system has been developed that enables intelligent monitoring and direct connections to a compatible modular mechanical pod for HVAC and DHW. The high-efficiency mechanical pod consists of an energy recovery ventilator (ERV) that uses smart occupancy-based control logic to ensure IAQ by maintaining CO2 levels of less than 800ppm in buildings with airtightness of less than 1.0 $L/s \cdot m^2$ exterior wall surface area at 50 Pa pressure differential. The mechanical pod offers various configurations that replace common heating, cooling, and DHW

appliances, such as fossil-fuel-driven forced air and hydronic systems, electric resistance heating, and window air conditioners, with a single high-efficiency air-to-water cold-climate heat pump and ERV. This heat pump and ERV have a core recovery efficiency of 88%. Therefore, the proposed retrofit solution can provide higher thermal insulation, better airtightness, and higher heating/cooling/DHW efficiency.

The energy performance of the retrofit solution was originally tested in EnergyPlus. In this study, the GDS approach is used to evaluate its energy performance. The solution is applied to the BEST house at Syracuse University, which is a two-floor house with replaceable envelope panels (Figure 2-32). In the field experiment, a small test room in the southeast corner of the first floor was built up with the retrofit solution implemented. Prefabricated envelope panels were mounted on the exterior walls of the test room. The mechanical pod was integrated to provide air conditioning and DHW supply to the test room. In this study, the retrofit solution is applied to the whole building to simulate its performance on a realistic-scale building. The retrofit envelope panels were mounted outside the existing exterior walls with a window on the east side of the test room. The energy-efficiency mechanical pod was used to provide heating and cooling demand. DHW is not simulated in this study. A reference building is created according to the median thermal EUI of the single-family attached building type from Building America House Simulation Protocols developed by NREL (Wilson et al. 2014). Some key settings of the reference case and the proposed case related to the retrofit strategy are shown in Table 2-28. Other settings are adapted from the study cases in the above sections. Energy use due to DHW is not simulated in the present study. The air conditioning efficiency of the retrofit module (mechanical pod) is assumed to be 3.75 times more efficient than the conventional unit based on the efficiency in Table 2-28.

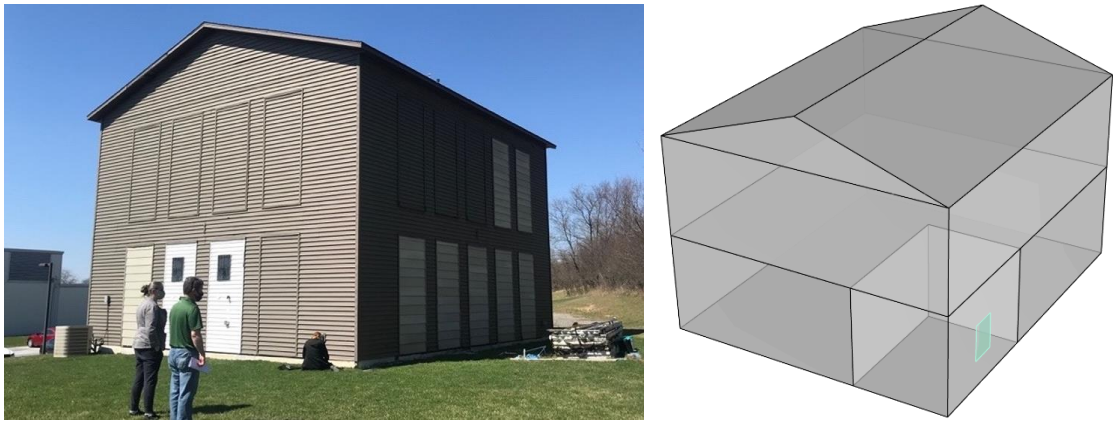

Figure 2-32. A picture and brief illustration of the BEST house.

Table 2-28. Summary of simulated conditions of the reference case and the proposed case.

Retrofit strategies	**Pre-retrofit reference**	**Post-retrofit case**
Airtightness	2.2 ACH_{50}	1.05 ACH_{50} [b]
Insulation - Exterior Wall	R-17 [a]	R-30
Insulation - Roof	R-9 [a]	-
Heating Equipment Efficiency	80 AFUE [a]	3 COP [c]
Cooling Equipment Efficiency	9.1 EER [a]	23 EER [c]
DHW Efficiency	0.56 EF [a]	2.43 COP [c] (not simulated)

[a] 2014 Building America House Simulation Protocols by NREL (Wilson et al. 2014).

[b] Based on the target airtightness level for the retrofitting system.

[c] Estimated per the Energy POD design specifications (Krietemeyer et al. 2020).

The simulation was performed on the same computer as presented in Section 2.4.1. The simulation finished in 18.4 seconds. The simulation results show that the unit energy use after retrofitting is around 173.7 kWh/m^2 per floor area compared to 314.4 kWh/m^2 before retrofitting. A 44.8% improvement in energy efficiency is achieved. The earlier work by EnergyPlus suggested an improvement of 52.2% in energy efficiency for heating and cooling, which is comparable to the result here. Therefore, the proposed retrofit solution has a significant potential of energy efficiency improvement.

2.5 Conclusions

This Chapter presented the major part of this work. A review of main BPS models was performed. Considering the requirement of modeling response and reliability for early-stage green building design, reduced-order physics-based models were applied in the GDS tool. Albeit not applied in the present work, reduced-order models have potential to integrate with measurement data to build hybrid models for improving simulation accuracy for buildings in actual scenarios. RC-structured physical models that represent building thermal, air and mass balance equations were created. Building modules were formatted to represent building systems and strategies across different scales. Building performance, including energy efficiency, thermal comfort, DALYs due to indoor contaminant exposure, and infection risks due to airborne transmission of respiratory diseases, were calculated. The simulation models were implemented in Matlab first and developed as a usable tool in Rhino Grasshopper. A plugin was developed in C# to integrate proposed BPS models

and geometry modelling functions in Rhino/Grasshopper. Multiple components were created in Rhino Grasshopper to comply with proposed building modules. The developed plugin is the main platform of the GDS approach.

Three study cases were performed using the developed platform, including a DOE prototype of small office building, a section of a realistic green building, Syracuse COE headquarter building, and a retrofitting case of an innovative integrated envelope-HVAC solution. A variety of energy-efficiency and IAQ improvement strategies were applied in the small office prototype building to estimate their performance. Building strategies usually have very variable impacts on energy and IAQ performance. Some strategies may improve certain aspects of building performance while impairing others. Therefore, it is important to find out the relatively better or optimal combination of the application of green building strategies. A simple application of building performance optimization was conducted and found that under the simulated conditions, the optimal design of the proposed small office prototype can save up to 27.8% energy use while mitigate more than 99% infection risk compared to the reference case. Therefore, it reveals that the optimization of green building design using the proposed approach has high potential of energy and IAQ improvement.

A similar analysis was performed to the Syracuse COE case. It analyzed the performance of some HPB strategies in an existing green building. It suggested that it is not recommended to implement all proposed technologies in the target building as that would impair thermal comfort in some scenarios. In order to achieve a better performance and save the building cost for the study case, higher airtightness, elevated insulation, and controlled lighting strategy are recommended to be

used in the design. It can save around 14% of total energy use and elevate over 3% of people satisfied with the thermal comfort in corridor but have a slight decrease in the thermal comfort in room.

The retrofitting case analyzed the performance of an innovative retrofitting strategy in cold/very cold climates. The solution contains a prefabricated envelope with higher thermal insulation and better airtightness. An energy-efficiency mechanical pod is integrated with the envelope system. It shows that a 44.8% improvement in energy efficiency can be achieved using the proposed solution compared to a reference case.

3. Database of green building technologies

3.1 Review of state-of-the-art research

3.1.1 Whole-building energy and IAQ database

Many public databases in the building sector have been established. Table 3-1 shows some major building performance databases associated with the research in this work. Some of these databases contain building parameters and performance metrics like energy use, while others only have general information for whole buildings or building components such as envelope materials without performance metrics data. The datasets from these databases are usually used to extract the information of different buildings or building components (e.g., understanding the geometry information of a certain type of building), and train data-driven models for building performance estimation and optimization. The U.S. DOE funded Building Performance Database (LBNL 2011) is likely the most widely used database for building energy analysis, which contains 1,115,196

datasets from residential and commercial buildings. The datasets contain information including climate and location, building parameters (e.g., built year, operating hours, floor area), building systems (e.g. lighting, cooling/heating system, glazing, wall insulation, air flow control), occupant features (e.g. number, density), green certifications (e.g. LEED score, Energy Star Rating), energy use intensity, and carbon emission. It also has a web-based tool that can be used for statistical analyses and demonstrations. The datasets were obtained from various sources, including public sectors (e.g. California Energy Commission, New York City, EPA Energy Star, EIA CBECS and RECS databases, and DOE Better Buildings Challenge) and private sectors (e.g. USAA Real Estate Company, and Dayton Residential) (Mathew et al. 2015).

U.S. Energy Information Administration (EIA) has performed periodic surveys on energy consumption for residential and commercial buildings. The obtained datasets are included in the DOE Building Performance Database. The Residential Energy Consumption Survey (RECS) (U.S. EIA 2020a) provides detailed information about energy usage in U.S. homes. RECS is a multiyear effort consisting of a household survey, data collection from household energy suppliers, and end-use consumption and expenditures estimation. The housing characteristics in the latest survey were collected in late 2020 and early 2021 (released in July 2022) from nearly 18,500 households to represent the 123.5 million housing units that are occupied as a primary residence (U.S. EIA 2020a). The datasets include building characteristics such as structural and geographic characteristics, square footage, appliances, electronics, lighting, space heating, air conditioning, water heating, household demographics, and energy use. The Commercial Building Energy Consumption Survey (CBECS) (U.S. EIA 2020b) focuses on commercial buildings in U.S. The latest CBECS contains 6,436 records of commercial buildings that represent an estimated 5.9

million total commercial buildings in the U.S. (as of 2018). Building characteristics data tables of CBECS include number of workers, ownership and occupancy, structural characteristics, energy sources and uses, energy related building features, and more (U.S. EIA 2020b). For both surveys, full datasets and comprehensive reports that contain statistical tables representing the distribution of collected data are released. Similar building energy surveys have been performed by many agencies across countries. For example, the National Energy Use Database (NEUD) (NRCan 2021) is established by the Natural Resources Canada (NRCan) through several nationwide surveys including the Survey of Household Energy Use (SHEU), the Survey of Commercial and Institutional Energy Use (SCIEU), the Survey of Energy Consumption of Multi Unit Residential Buildings (SECMURBs), the Survey of Energy Consumption of Arenas (SECA), and the Industrial Consumption of Energy (ICE) Survey. The database contains building characteristics and energy use.

The Building Energy Benchmarking Data was obtained through the Building Energy Benchmarking Program hosted by local governments, which requires owners of non-residential and multifamily buildings to track energy performance and annually report to the local agency. The program has been performed in more than 100 cities in the U.S. (ACEEE 2022). Data of some cities has been posted and can be accessed online, e.g. 3,628 datasets in Seattle, 3,939 datasets in New York City, and 17,389 datasets in California (as of 2020) (California Energy Commission 2022; Department of Finance of New York City 2022; Office of Sustainability & Environment of Seattle 2022). The datasets usually contain location, building characteristics (e.g. primary use, floor number, and built year), neighborhood information, energy use, carbon emission, and green certification information.

The Building Data Genome Project 2 Database (C. Miller et al. 2020) an open database of 3,053 energy meters from 1,636 non-residential buildings with a range of two full years (2016 and 2017) at an hourly frequency (17,544 measurements per meter resulting in approximately 53.6 million measurements). These meters were collected from 19 sites across North America and Europe, with one or more meters per building measuring whole building electrical, heating and cooling water, steam, and solar energy as well as water and irrigation meters. Part of this data was used in the Great Energy Predictor III (GEPIII) competition hosted by ASHRAE on Kaggle. The datasets include information like climate and location, weather data, building characteristics (e.g., floor area, built year, floor number, etc.), occupant number, energy use, and green certification of buildings.

The energy performance certificates (EPCs) are a rating scheme to summarize the energy efficiency of buildings (Energy Saving Trust 2022). The Energy Performance of Buildings Data (DLUHC 2022) provides datasets of EPCs in the U.K. issued up to March 2022, including data from 22,710,206 domestic and 1,059,491 non-domestic EPCs. The datasets include climate and location, building characteristics (e.g., floor area), energy use, carbon emission, and green certification. The Low Energy Building (LEB) Database (LEB 2010) is a repository of green building information created by AECB (U.K.) to help inform the planning and development of new build and refurbishment of green buildings. The repository contains 500 green building projects in the U.K. with detailed project descriptions (e.g. location, occupation date, construction type, and floor area), building service systems (e.g. lighting, heating/cooling, ventilation, and other appliances), building construction characteristics (e.g. roof, wall, floor, glazing descriptions and U-values), green design strategies (e.g. heating/cooling, ventilation, renewable energy, insulation,

daylighting, and airtightness strategies), energy use and renewable energy generation by measurement or modelling, and green certification. Some green building certification/rating systems such as LEED, also have repositories that contain green building projects with basic building information and green certification/rating levels. For example, the LEED database contains over 86,000 certified residential and commercial projects across the world, each of which provides basic project descriptions (e.g., project type, location, and floor area) and the score that project earned in different evaluation aspects including sustainable site, water efficiency, energy and atmosphere, material and resources, indoor environmental quality, innovation, and reginal priority credits. However, some key performance metrics like energy use or thermal comfort are not provided, therefore, are less commonly used by quantitative analyses. But some individual studies have performed surveys, field measurements, or modellings to obtain quantitative metrics regarding actual building performance for some LEED-certified projects (Newsham et al. 2009; Scofield and Doane 2018; Turner et al. 2008; P. Wu et al. 2016), which can be adopted to establish a LEED-certified project database with more quantitative features.

The ASHRAE Global Thermal Comfort Database II (Földváry Ličina et al. 2018; Parkinson et al. 2022) is comprised of field studies of thermal comfort from around the world, containing a total of 109,033 entries. The datasets are collected through instrumental measurements and subjective surveys, consisting of information of climate and location, season and date, building characteristics (e.g. building type, window, door), system configurations (e.g. fan, heating/cooling systems), occupant information (e.g. gender, activity level, clothing), indoor variables (e.g. temperature, humidity), and thermal comfort metrics (e.g. PMV, PPD, thermal and air movement acceptability, and thermal and air movement preference). The ASHRAE Global Occupant Behavior Database

(B. Dong et al. 2022) is a comprehensive global database about building occupant behavior. The database contains 34 field-measured building occupant behavior sources collected from 15 countries and 39 institutions across 10 climatic zones covering various building types in both commercial and residential sectors. The database includes occupancy patterns (i.e., presence and people count), occupant behaviors (i.e., interactions with devices, equipment, and systems such as door, window, fan, lighting, shading systems), indoor variables (e.g., temperature, humidity, and thermal comfort metrics such as PMV), and measurement technology (i.e. sensor information).

The Global Household Air Pollution (HAP) Database (Shupler et al. 2018), commissioned by the WHO and sponsored by the Natural Sciences and Engineering Research Council (NSERC) of Canada, provides an organized summary of data reported in the literature describing HAP microenvironments, methods and measurements associated with kitchen activities. The database contains 1290 datasets of field measurements from 196 studies published across 43 countries through 2016. The database includes general information of the studied household (e.g. location, building design, ventilation, kitchen location and type, primary cooking fuel, heating fuel, and stove type), occupant characteristics (e.g. occupant number, age, gender, and activities), field measurement data of PM2.5 and CO, simulated levels of PM2.5 and CO, health assessments evaluated by measurement data, and other health metrics derived from measurement or modelling. Many other studies, particularly literature reviews, have collected similar IAQ datasets of field measurements or modellings, including quantitative metrics of indoor pollutant concentrations such as particles, CO2, ozone and VOCs, and health effect metrics (K. K. Lee et al. 2020; M. Lee et al. 2021; Lim et al. 2022; Puttaswamy et al. 2021; Shupler et al. 2020, 2022; Z. Yang et al. 2018). However, most of these studies do not provide datasets as detailed/comprehensive as the

WHO Global HAP Database. Some key variables like building characteristics are not included as their studies focus on pollutant exposure or health effect assessments. Therefore, those studies are not considered by the present work.

Numerous datasets of COVID-19 outbreaks have been reported around the world. However, most of these datasets did not take building characteristics into consideration. Colorado Department of Public Health and Environment (CDPHE) has released COVID-19 outbreak data reported in public agencies with information of location, outbreak date, agency name (building name), building function (e.g. office, school, or healthcare), infection and death number (CDPHE 2020; Shen, Kong, Dong, et al. 2021b). The database includes data of 9,093 resolved outbreaks in Colorado. Although detailed building characteristics such as floor area and building construction are still missing, some of this information can be obtained based on online searching since the agency name of each outbreak is reported and thus can be found online. A database with more comprehensive information is therefore potential to be established. But the current database is still useful for data analyses (Shen, Kong, Dong, et al. 2021b).

3.1.2 Building component/system database

Some databases or libraries of building components and systems have been established (Table 3-2). These databases or libraries are usually developed to be used by BPS programs (energy and IAQ). Performance metrics are usually not included as a part of the building component or system. The Building Component Library (NREL 2021) is a collection of building data used to create building energy models without performance metrics included. The data are broken down into

components that represent parts of a building and measures that describe changes made to a building. The datasets are structured following the format of EnergyPlus input data file (IDF) or OpenStudio model file (OSM). The information is from real practices, which are contributed by multiple individuals or agencies. The IEA Annex 68 compiled a VOC emission database of some common building products with measured data (Qin et al. 2020), including information such as in-material diffusion coefficient, partition coefficient, and initial concentration. Similar databases with VOC emission parameters include the PANDORA database (M. Abadie and Blondeau 2011) and building material emission library in CHAMPS-BES (Grunewald and Nicolai 2005). The reaction probabilities of common building materials with ozone have also been compiled as a database that can be used for indoor ozone chemistry modelling (Shen et al. 2017; Shen and Gao 2018).

Table 3-1. Representative building performance databases associated with this study (as of 2022).

Database	Sponsor	Description	Key variables
Building Performance Database (BPD) (LBNL 2011)	DOE	Dataset size: 1,115,196 datasets Building type: Residential and commercial Scale: Whole building Performance metrics: green certifications, energy use intensity, carbon emission (annual total) Data acquisition: survey	Climate and location, building parameters (e.g. built year, operating hours, floor area), building systems (e.g. lighting, cooling/heating system, glazing, wall insulation, air flow control), occupant features (e.g. number, density), green certifications (e.g. LEED score, Energy Start Rating), energy use intensity, and carbon emission
Residential Energy Consumption Survey	EIA	Dataset size: 18,496 datasets Building type: Household Scale: Whole building	Structural and geographic characteristics, square footage, appliances, electronics, lighting,

(RECS) datasets (U.S. EIA 2020a)		Performance metrics: energy use (annual total) Data acquisition: survey	space heating, air conditioning, water heating, household demographics, and energy use
Commercial Building Energy Consumption Survey (CBECS) datasets (U.S. EIA 2020b)	EIA	Dataset size: 6,436 datasets Building type: Commercial Scale: Whole building Performance metrics: energy use (annual total) Data acquisition: survey	Number of workers, ownership and occupancy, structural characteristics, energy sources and uses, energy related building features, etc.
Building Energy Benchmarking Program Data (California Energy Commission 2022; Department of Finance	Local governments	Dataset size: City/state-dependent (e.g. 3,628 datasets for Seattle, 3,939 datasets for New York City, and 17,389 datasets for California, as of 2020)	Location, building characteristics (e.g. primary use, floor number, and built year), neighborhood information, energy use, carbon

of New York City 2022; Office of Sustainability & Environment of Seattle 2022)		Building type: Large commercial and multifamily buildings Scale: Whole building Performance metrics: Energy use, green certification (annual) Data acquisition: survey	emission, and green certification information
Building Data Genome Project 2 Database (C. Miller et al. 2020)	ASHRAE	Dataset size: 53.6 million measurements from 1,636 commercial buildings Building type: Commercial Scale: Whole building Performance metrics: Energy use (time-sequence), green certification Data acquisition: survey, field measurement	Climate and location, weather data, building characteristics (e.g. floor area, built year, floor number, etc.), occupant number, energy use, and green certification

Energy Performance of Buildings Data (DLUHC 2022)	DLUHC (U.K.)	Dataset size: Data from 22,710,206 domestic and 1,059,491 non-domestic EPCs Building type: Residential and commercial Scale: Whole building Performance metrics: Energy use, carbon emission, green certification (annual) Data acquisition: survey	Climate and location, building characteristics (e.g. floor area), energy use, carbon emission, and green certification
Low Energy Building (LEB) Database (LEB 2010)	AECB (U.K.)	Dataset size: 500 building projects Building type: Residential and commercial Scale: Whole building Performance metrics: Energy use, renewable energy generation, carbon emission, green certification (annual) Data acquisition: survey, modelling	Detailed project descriptions (e.g. location, occupation date, construction type, and floor area), building service systems (e.g. lighting, heating/cooling, ventilation, and other appliances), building construction characteristics (e.g. roof, wall, floor, glazing descriptions

			and U-values), green design strategies (e.g. heating/cooling, ventilation, renewable energy, insulation, daylighting, and airtightness strategies), energy use, renewable energy generation, and green certification
LEED certificated building datasets (USGBC 2022)	USGBC	Dataset size: 86,193 datasets Building type: Residential and commercial Scale: Whole building Performance metrics: Green certification (LEED scores) Data acquisition: survey	Basic project descriptions (e.g. project type, location, and floor area), and LEED rating scores for various evaluation aspects, including sustainable site, water efficiency, energy and atmosphere, material and resources, indoor environmental quality, innovation, and reginal priority credits

ASHRAE Global Thermal Comfort Database II (Földváry Ličina et al. 2018; Parkinson et al. 2022)	ASHRAE	Dataset size: 109,033 datasets Building type: Residential and commercial Scale: Whole building Performance metrics: Thermal comfort (daily) Data acquisition: field measurement (real scenarios), subjective survey (questionnaire)	Climate and location, season and date, building characteristics (e.g. building type, window, door), system configurations (e.g. fan, heating/cooling systems), occupant information (e.g. gender, activity level, clothing), indoor variables (e.g. temperature, humidity), thermal comfort metrics based on instrumental measurements or subjective surveys (e.g. PMV, PPD, thermal and air movement acceptability, and thermal and air movement preference)
ASHRAE Global Occupant Behavior	ASHRAE	Dataset size: Datasets from 34 sources Building type: Residential and commercial	Occupancy patterns (i.e., presence and people count), occupant

Database (B. Dong et al. 2022)		Scale: Whole building Performance metrics: Thermal comfort (time-sequence) Data acquisition: field measurement	behaviors (i.e., interactions with devices, equipment, and systems such as door, window, fan, lighting, shading systems), indoor variables (e.g. temperature, humidity, and thermal comfort metrics such as PMV and thermal sensation vote), and measurement technology (i.e. sensor information)
Global household air pollution database (Shupler et al. 2018)	WHO, NSERC	Dataset size: 1,290 datasets from 196 sources Building type: Residential Scale: Whole building	General information of the studied household (e.g. location, building design, ventilation, kitchen location and type, primary cooking fuel, heating fuel, and stove type), occupant characteristics (e.g. occupant number, age, gender, and

		Performance metrics: PM2.5 and CO concentration and health assessments (average over the test period) Data acquisition: field measurement, modelling	activities), field measurement data of PM2.5 and CO, simulated levels of PM2.5 and CO, health assessments evaluated by measurement data, and other health metrics derived from measurement or modelling
COVID-19 indoor outbreak database (CDPHE 2020; Shen, Kong, Dong, et al. 2021b)	CDPHE	Dataset size: 9,093 datasets (resolved cases) Building type: Residential and commercial Scale: Whole building Performance metrics: Infection and death number Data acquisition: Survey	Location, outbreak date, agency name (building name), building function (e.g. office, school, or healthcare), infection and death number

Table 3-2. Building component and system database.

Database	Sponsor	Description	Key variables
Building Component Library (BCL) (NREL 2021)	DOE	Dataset size: 34,096 datasets Building type: Residential and commercial Scale: Building component or system Performance metrics: NA Data acquisition: Survey, practice	Detailed characteristics of building components and systems in IDF (for EnergyPlus) or OSM (for OpenStudio) formats
Material VOC emission database (Qin et al. 2020)	IEA	Dataset size: Data of 5 common materials Building type: Residential and commercial Scale: Building material Performance metrics: NA Data acquisition: Laboratory measurement	VOC emission parameters of materials (including in-material diffusion coefficient, partition coefficient, and initial concentration)

Material ozone deposition rate database (Shen et al. 2017; Shen and Gao 2018)	/	Dataset size: Data of 54 common materials Building type: Residential and commercial Scale: Building material Performance metrics: NA Data acquisition: Laboratory measurement	Reaction probability of the material with ozone

3.2 Database of green building technologies

3.2.1 Green building technology definition and collection

There have been numerous green building technologies developed to address building energy and IAQ issues, so that the technologies can be divided into two categories regarding their major purposes, i.e. energy-efficiency technologies and IAQ-enhance technologies (Cao et al. 2016; Shen, Kong, Dong, et al. 2021a, 2021b). Some technologies are designed to save energy use and improve IAQ simultaneously, thus can be included in both categories. Green building technologies can also be categorized based on their energy use condition. Passive strategies are the building technologies that do not require or require minimal active energy inputs, which are usually more energy-efficient for application in buildings. Active technologies are the technologies that require energy consumption. Those passive technologies actually have a much longer history associated with their use in buildings than active strategies, before electricity was utilized by human beings (X. Li et al. 2017). Early passive technologies, such as cave dwellings (utilizing thermal insulation and thermal mass of the cave), kang (a domestic heating system used in rural northern China) (S. Yan et al. 2020; Zhuang et al. 2009), wind catcher (a system introduces cooled outdoor air to indoor space in Middle East) (Masrour et al. 2012; Montazeri et al. 2010), etc. have existed for hundreds or thousands of years for improving indoor thermal or air quality environments, and some of them are still being utilized in many modern buildings. Although passive technologies usually consume minimal energy, their efficiencies are sometimes limited and insufficient for modern buildings. Active systems, conversely, consume a certain quantity of energy use, but can condition the indoor air more efficiently.

For IAQ improvement technologies, typical IAQ improvement technologies include three categories, i.e., source control, ventilation, and air cleaning. IAQ technologies at different scales can have very different characteristics and efficiencies. Figure 3-1 shows the typical IAQ strategies at different scales of building/urban environment, from urban scale, building scale, room scale to personal microenvironment (J. J. Zhang et al. 2022). During COVID-19 pandemic, many of these IAQ strategies have been applied to mitigate the airborne transmission of SARS-CoV-2. Some emerging technologies were also proposed or utilized, such as the needlepoint bipolar ionization technology. An earlier study evaluated the effectiveness of different IAQ strategies in mitigating airborne transmission of COVID-19 (Shen, Kong, Dong, et al. 2021a).

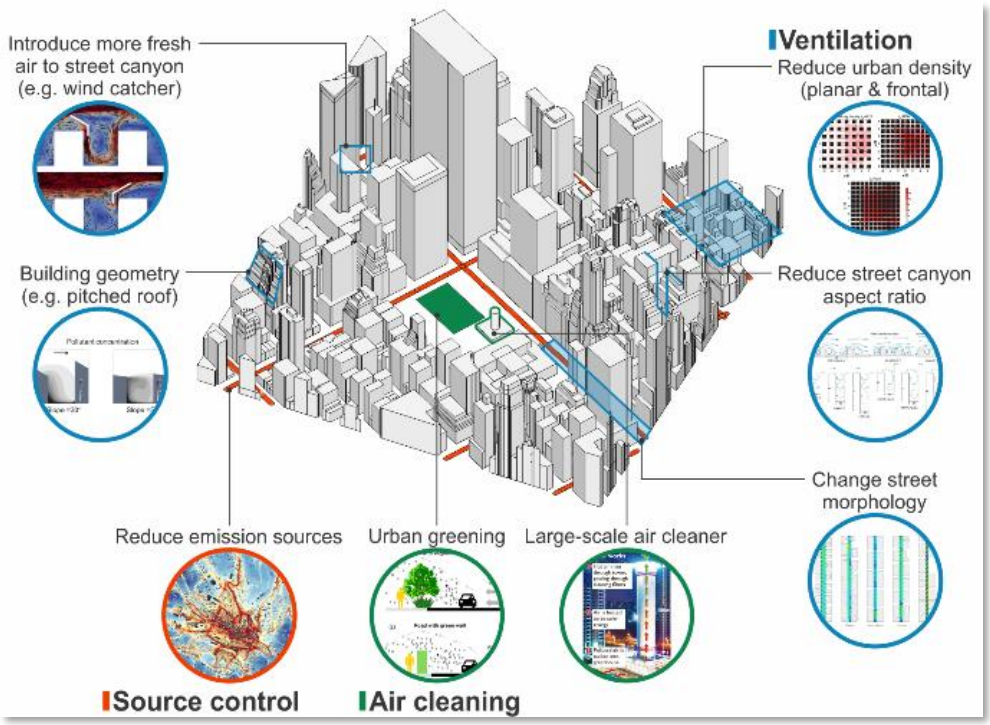

(a) Urban-scale strategies.

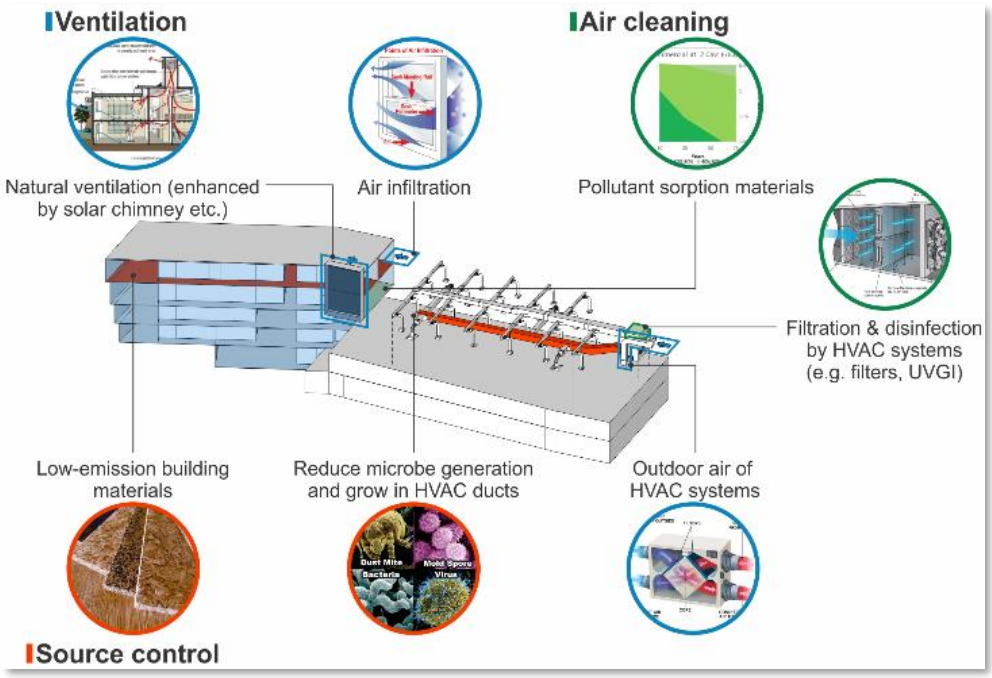

(b) Building-scale strategies.

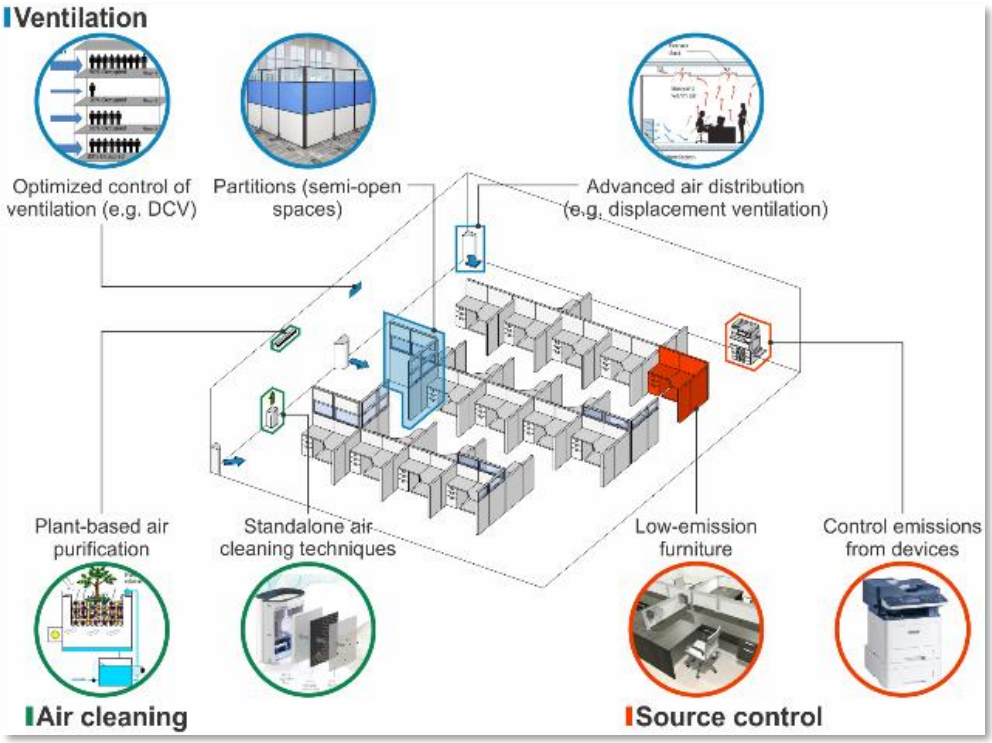

(c) Room-scale strategies.

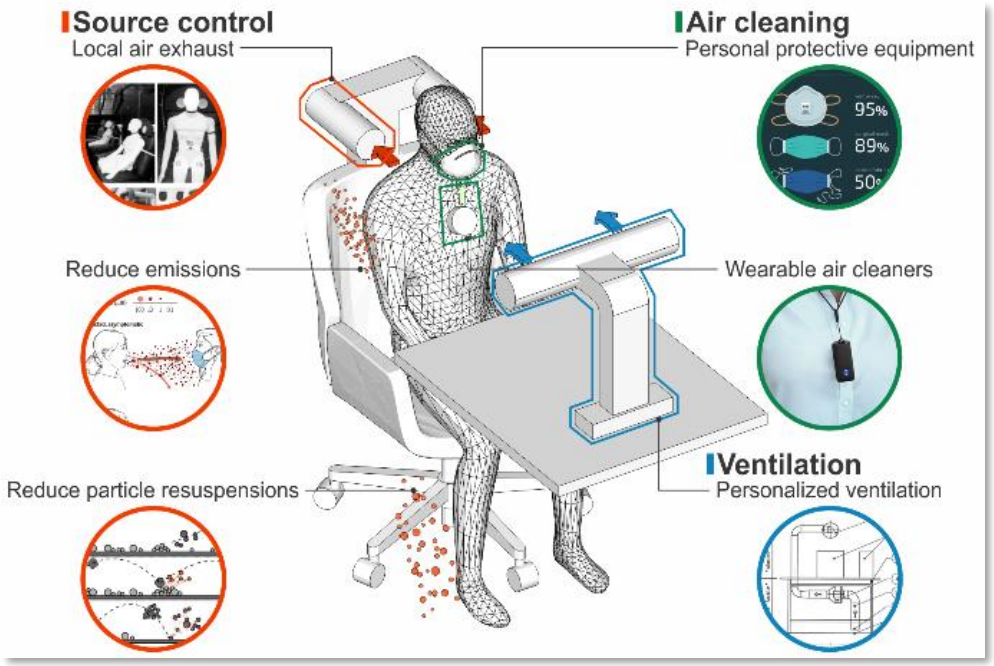

(d) Microenvironment-scale strategies.

Figure 3-1. IAQ control strategies at multiple scales (adapted from (J. J. Zhang et al. 2022)).

3.2.2 Baseline case definition

In order to evaluate the effectiveness of various energy efficiency and IAQ strategies, it is necessary to define a baseline case as a reference. A local reference building is defined as a building, with its construction complying with the local standards/codes or adopting the local best practice. The local best practice of building design can be accessed through the local building documents, reports, cases, or available datasets, e.g. the Building Performance Database (LBNL 2011). When the local best practice is unavailable or does not meet the local building standards and codes, then the local standards and codes will be adopted to define the reference building. Many standards or codes have developed reference criteria for various types of buildings. For

example, DOE (U.S. DOE 2020) has developed commercial reference buildings of 16 building types that represent approximately 70% of the commercial buildings in the U.S., according to a report published by the National Renewable Energy Laboratory (NREL) (Deru et al. 2011). The reference buildings provide complete descriptions for whole building energy analysis using EnergyPlus. The Pacific Northwest National Laboratory (PNNL) modified the DOE commercial prototype building models (U.S. DOE 2013) to accommodate the ASHRAE Standard 90.1 (ASHRAE 2019c) and International Energy Conservation Code (IECC) (ICC 2009). The PNNL commercial prototype buildings (U.S. DOE 2013) cover all DOE reference building types (with the exception of supermarkets), and also an additional prototype representing high-rise apartment buildings, resulting in 16 commercial building types in 19 climate locations. For residential buildings, PNNL uses two base prototypes to simulate single-family detached houses and multi-family low-rise apartment buildings (U.S. DOE 2013). These prototypes are then modified to accommodate four different heating system types and four foundation types typically found in new residential construction. For single-family houses in the U.S., NREL has developed the benchmark building for each climate zone (i.e. Building America B10 Benchmark (Wilson et al. 2014)), which is consistent with the 2009 IECC (ICC 2009). Besides, ASHRAE standards (ASHRAE 2018, 2019b) defined the design criteria like envelope construction and ventilation requirement for single-family house in each climate zone, which should also be satisfied by the local reference house. The IEA Annex 68 project developed a detailed procedure along with an example for defining a local reference building for both IAQ and energy performance evaluation (Zhenlei Liu et al. 2017; Qin and Zhang 2020). Baseline settings of public buildings in terms of airborne infection risk estimation and IAQ evaluation were also presented recently (Shen, Kong, Dong, et

al. 2021a). In this study, the DOE reference small office case was used as the reference case, which has been introduced in earlier sections.

For retrofitting projects, the existing conditions before the retrofitting can be selected as the baseline for comparison as in (Krietemeyer et al. 2020). This case was also discussed as an application example of the GDS in Chapter 2.

3.2.3 Database

A review was performed to collect these energy-efficiency and IAQ-improvement building technologies (Cao et al. 2016; Shen, Kong, Dong, et al. 2021a, 2021b; J. J. Zhang et al. 2022). Table 3-3 shows the major green building strategies collected from literature review. Table 3-4 provides more detailed information of airborne infection mitigation strategies.

Table 3-3. Typical strategies to improve building energy and IAQ improvements.

Category			**Strategy**
Energy efficiency	Passive technologies	Building envelope	Higher thermal insulation (e.g. vacuum insulation panel (VIP), prefabricated insulation panel)
			Ventilated/double-skin walls/roofs/floors to increase insulation or to enhance convective heat loss
			Passive solar thermal walls (e.g. Trombe wall)
			Daylight harvesting
			Energy-saving glazing technologies (e.g. double glazed window with argon gas, low-E coating)
			Passive shading technologies
			Low infiltration (airtightness enhancement)
			Solar-reflective/cool roofs

			Green roofs
			Evaporative roof cooling
		Passive heating, cooling and ventilation	Nighttime ventilation
			Earth-to-air heat exchange
			Natural ventilation
			Solar chimney (vented Trombe wall)
		Thermal storage	Phase-change materials (PCM)
			Thermal mass (e.g. concrete)
	Service systems	HVAC	Evaporative cooling
			Active thermal storage
			Heat recovery system
			Radiant heating/cooling

		VAV/VRF
		Demand-controlled ventilation (DCV)
		Optimized control of ventilation
	DHW	Solar water heater
		Solar-assisted heat pump system
		Combined cooling, heating and power
	Lighting	LEDs
		Energy efficient lighting
		Active shading technologies
		Demand response lighting
	Appliances	Energy-efficient appliances
		Demand response appliances

		Smart control strategies	Smart control algorithms to operate active systems in a more efficient way (e.g. MPC)
	Renewable energy generation	Solar energy	PV/building integrated PV
			Hybrid PV-thermal
		Wind energy	Wind turbine
		Geothermal energy	Ground source heat pump
		Bioenergy	Biomass heater
IAQ improvement	Source control	Outdoor pollutants	Reducing outdoor pollutants (traffic emissions)
			Greening
		Indoor pollutants	Low-emission building materials/furniture
			Local air exhaust
		Occupant pollutants	occupancy control/screening
			face covering

Ventilation	Passive ventilation	Natural ventilation
		Solar chimney
		Air infiltration
	HVAC system	Increasing outdoor air supply
		High-efficiency filters (e.g. HEPA)
	Optimized control of ventilation	Demand-controlled ventilation (DCV)
		MPC
		Other algorithms
	Advanced air distribution	Displacement ventilation
		Underfloor air distribution ventilation
		Personalized ventilation
	Partition	Partitions (semi-open spaces)

		Closing doors between rooms
		Cubicle workstation
		Enclosed/semi-enclosed modular office walls
Air cleaning	In-duct air cleaners	Filtration
		Upper-room UVGI system
	Portable air cleaners	Filtration
		UVGI
		Plasma
		Photocatalytic oxidation (PCO) or UV-PCO
		Sorption
		Plant-based air purifiers
	Other standalone air cleaners	Upper-room UVGI system

	Passive air cleaning technologies	Pollutant sorption materials
		Sunlight
	PPE	Mask
		Mask fitter/sealer/brace
		Face shield

Table 3-4. IAQ control strategies for mitigating the risk of airborne transmission.

Category	Strategy	Effectiveness	Effective scale	Capital cost[a]	Durability	Accessibility
PPE	Cloth mask	30% particle filtration efficiency for purchased masks (considering leakage from gaps caused by improper fit) (Konda et al. 2020); 20% particle filtration efficiency for homemade masks (cotton and nylon materials) (M. Zhao et al. 2020);	Breathing zone	US$3/count (purchased); US$0/count (homemade);	Reusable	Easy[b]; Homemade (using household materials like cotton and nylon (A. Davies et al. 2013)); Comfort should be considered;
	Surgical mask	50% particle filtration efficiency (considering	Breathing zone	US$0.2/count	Disposable[c]	Depending on supply capacity (including

	leakage from gaps caused by improper fit) (Konda et al. 2020; Rothamer et al. 2020);				conventional, contingency, and crisis situations (U.S. CDC 2021a)); Comfort should be considered;
N95 mask	95% particle filtration efficiency (without gaps)[d] (Konda et al. 2020)	Breathing zone	US$2/count	Disposable[c]	Depending on supply capacity (including conventional, contingency, and crisis situations (U.S. CDC 2021a)); Comfort should be considered;
Face shield	23% reduction on aerosol inhalation under long-	Breathing zone	US$2/count	Reusable	Easy;

		time use (more aerosol reduction under short-distance use) (William G. Lindsley et al. 2014)				Homemade (using plastic sheets and other materials);
	Mask fitter/sealer/brace[e]	Greatly improving the efficiency of masks by reducing the leakage through gaps (e.g. improve the particle filtration efficiency of surgical masks to over 90% (Rothamer et al. 2020))	Breathing zone	US$9/count (purchased (UW Madison 2020)); US$0/count (homemade);	Reusable	Easy; Homemade (using rubber or other materials (Fix The Mask 2020)); Increased discomfort;
Ventilation	Upgrading filters of building ventilation	99.9% removal efficiency for particles >0.3μm (HEPA filter)	Building	US$280/count (with an increase in	Replaced every 6-12 months	Easy

systems (e.g. HEPA)			fan power due to the increased pressure rise through higher-rating filters (Risbeck et al. 2021))		
Increasing outdoor air supply of building ventilation systems (e.g. 100% outdoor air)	Largely increasing the ventilation rate of the room (e.g. providing 60% more clean air compared to a reference system with	Building	US$5/m^2·year for extra energy consumption (central system);	Long-term use[f]	Easy (switching the damper to increase outdoor air supply)

	25% outdoor air and MERV 8 filter)		US$10/m^2·year for extra energy consumption (individual unit)[g] (U.S. EIA 2018);		
Personal ventilation (for fresh air supply)	Increasing clean air supply to the personal microenvironment with typical ventilation effectiveness of 1.7, depending on diffuser location and airflow rate (A. Melikov et al. 2007)	Personal environment	Varying greatly (depending on system scale)	Long-term use (filters need regular replacements)	Need professional design and installation

	Local air exhaust	Reducing the cross-contamination with typical ventilation effectiveness of 1.4 to 10, depending on the local partition configuration, exhaust location, and airflow rate (Dygert and Dang 2012)	Personal environment	Varying greatly (depending on system scale)	Long-term use	Need professional design and installation
	Displacement ventilation	Improving the clean air delivery efficiency with typical ventilation effectiveness of 1.2 to 2 (Q.Chen and Glicksman 2003)	Room	Varying greatly (depending on system scale)	Long-term use (filters need regular replacements)	Need professional design and installation

Natural ventilation	Providing more outdoor air to the room, e.g. >10h^{-1} air changes in some scenarios (H. Qian et al. 2010) (depending on window opening conditions, wind condition, and building geometry)[h]	Room	US$0	Long-term use	Depending on weather and outdoor air quality conditions
Closing doors between rooms (separating rooms and blocking air flow across rooms)	Reducing cross contamination across rooms (cross-contamination risk can be eliminated when the doors are fully closed)	Building/room	US$0	Long-term use	Easy (need to coordinate with occupant schedules)

Partition	Partition screens	Depending on airflow patterns in the room (well-designed partitions can reduce the risk of cross-contamination while bad designs may increase the risk in some locations) (Rooney et al. 2021)	Personal environment	US$100/m^2 material	Long-term use	Easy
	Cubicle workstation	Reducing cross-contamination between cubicles with typical ventilation effectiveness of 1.1 to 3.6 (require well-designed ventilation and air distribution) (Haghighat et al. 1996)	Personal environment	US$2000 for a 2×2m cubicle	Long-term use	Need professional design and installation (incorporating with ventilation)

	Enclosed/semi-enclosed modular office walls	Enclosed modular office walls can fully avoid cross-contamination between modular spaces (require sufficient ventilation supplied to each space)	Personal environment	US$3000 for a 2×2m seat	Long-term use	Need professional design and installation (incorporating with ventilation)
Air cleaning and disinfection	Upper-room UVGI system	Proper use can largely improve the inactivation rate of virus (e.g. 16h^{-1} for M. parafortuitum)[i]	Room	US$1200-2500 (US$40-90/m^2 floor area) (VirusLights 2021)	Long-term use	Need professional design and installation (incorporating with ventilation)
	Portable air cleaners	Typically supplying 361m^3/h CADR (median	Room	US$493/count (i.e.	Long-term use (filters	Easy;

	CADR from a market survey (B. Zhao et al. 2020b))		US$1.32 per m^3/h CADR, median price from a market survey (B. Zhao et al. 2020b)) (less than US$50/count for HEPA filter replacement)	need regular replacement)	Potential emissions should be considered (some air cleaners can generate hazardous emissions like ozone (C. Guo et al. 2019))
Sunlight	Increasing the natural inactivation of SARS-CoV-2 on aerosols (decay	Room	US$0[j]	Long-term use	Depending on weather conditions and building design[k]

		rate: <1h^{-1} without sunlight, >7h^{-1} with low-intensity sunlight, >18h^{-1} with high-intensity sunlight)				
Occupancy control	Occupancy density restriction (limiting occupant number and social distance in the building/room[m])	Reducing the potential emissions of pathogens to the air and reducing the risk of cross-contamination	Building/room	US$0[l]	Long-term use	Easy (need to coordinate with occupant schedules)
	Intermittent occupancy (A. K. Melikov et al. 2020) or	Reducing the potential emissions of pathogens to the air and decreasing the pathogen inhalation by the	Building/room	US$0	Long-term use	Easy (need to coordinate with occupant schedules)

	staggered scheduling (U.S. CDC 2021c)	susceptible people (e.g. asking students to leave the classroom during the 15min break after a 35min class can reduce 35% inhaled pathogen (A. K. Melikov et al. 2020))

[a] Capital costs are approximately estimated based on a brief market survey in the U.S. (data obtained from search results on Google). The actual costs may vary a lot in other countries or regions.

[b] The strategy can be accessed easily through in-store/online purchase or easy operation.

[c] Surgical and N95 masks are designed for disposable use but can be reused a couple of times after decontamination under certain conditions (U.S. CDC 2021b).

[d] N95 masks can generally fit better than cloth and surgical masks. Proper use of N95 masks can minimize air leakage through gaps.

[e] Other strategies that can maximize fit for surgical masks include 1) covering the surgical mask with a cloth mask, and 2) knotting ear loops of the surgical mask, which can improve the particle filtration efficiency to around 80% (Brooks et al. 2021).

[f] Long-term use indicates a duration of typically over one year.

[g] The annual average cost of air conditioning with central and individual units in the U.S. is US$0.31 and US$0.15 per square foot, respectively (U.S. EIA 2018). Assuming the outdoor air fraction of the HVAC system is 25%, applying 100% outdoor air will simply cost 3× more energy for pre-heating or pre-cooling the extra outdoor air.

[h] It can improve the natural ventilation efficiency and introduce more outdoor air to the room incorporating fans.

[i] The effectiveness of virus inactivation by the upper-room UVGI system also relies on room air distribution. Displacement ventilation may reduce the efficiency as it decreases the residence time of the virus in the irradiated zone (Kanaan and Abou Moughlbay 2018).

[j] Introducing more sunlight to the room may impact the heating and cooling energy consumption for the HVAC system.

[k] Building design like window/wall ratio and building geometry can impact the incident sunlight.

[l] The potential economic loss due to occupancy restriction is not considered.

[m] The safe social distance is recommended as 1.6-3.0m considering the aerosol transmission of exhaled large droplets from talking (Sun and Zhai 2020).

3.2.4 Selected green building technologies

The performance of building technologies is dependent on the design features of the technology. In earlier estimations, the design features of technologies were obtained from literature review. However, the information for many strategies, particularly more recent and novel technologies, is insufficient in literature. According to the review on green building technologies, some technologies have shown great potential for improving IAQ and reducing energy consumption. In this study, two novel IAQ control strategies, including needlepoint bipolar ionization technology and displacement ventilation integrated with partitions, that were thought to be effective for mitigating airborne infection risks were studied in detail through chamber experiments and CFD simulations. Because of the enhanced ventilation efficiency, energy use for providing the equivalent ventilation rate by these technologies is lower. Therefore, the energy performance of these technologies was also discussed. The results from this study can contribute to the proposed database, which can be used by more researchers who are interested in these novel technologies.

3.2.4.1 Needlepoint bipolar ionization technology

Ionization refers to the process of either removing or adding electrons from neutral atoms or molecules, resulting in the creation of ions carrying electric charge. Thus, it has the potential for eliminating particles and bioaerosols (Hyun et al. 2017; Nunayon et al. 2019; Pushpawela et al. 2017; U.S. EPA 2022d). However, the process may also result in the formation and destruction of some volatile organic compounds (VOCs) (Zeng et al. 2021) and other gaseous byproducts such as ozone and nitrogen oxides (NOx), particularly at higher ionization voltages (C. Guo et al. 2019). Earlier studies also observed adverse effects on cardiovascular health when people were exposed

to 13×10^3 #/cm^3 and 60×10^3 #/cm^3 level of airborne negative ions (W. Dong et al. 2019; W. Liu et al. 2021).

Needlepoint bipolar ionization technology is a technology using low ionization voltage to minimize the generation of ozone and ozone-associated secondary emissions but still compromise the pollutant removal capability (Waddell 2019). Some experts have recommended it as a possible mitigation strategy to against COVID-19 (Berry et al. 2022). However, recent studies (Zeng et al. 2021, 2022) indicated the research gap of adequate peer-reviewed evidence on the efficacy and safety of using air ionization technologies to address IAQ issues in practice. In the absence of peer-reviewed evidence, this technology was considered by some public agencies to be "emerging" with little available research outside of lab conditions (U.S. CDC 2020; U.S. EPA 2020).

Therefore, this study performed chamber experiments for two in-duct needlepoint bipolar ionization devices with different configurations in a full-scale office space built up inside the well-controlled environmental chamber. A thermal manikin wearing a pre-soiled shirt was used to mimic a real occupant in the office. Two different testing approaches were conducted, including decay tests and constant-source tests. Realistic room configurations and environmental settings were established during the tests. The performance of pollutant removal (size-speciated particles and VOCs), and potential secondary emissions such as ozone, VOCs, and negative ions were analyzed. The favourable configurations of in-duct ionizations for enhanced pollutant removal and minimal secondary emissions were discussed.

The ionizers were installed in a blower system that was used to simulate the realistic air handling unit (AHU). A regular MERV 8 filter was installed at the outlet of blower system. The operating airflow rate (Q_{AC}) of the blower in this study was controlled at 505 m^3/h (297 CFM, calibrated by the TSI AccuBalance Air Capture Hood 8380, see Supplementary Information). The two ionizers were installed inside the blower, one was a portable unit and installed 0.25 m upstream of the filter (Ionizer B or I-B), and another one was mounted on the MERV 8 filter (Ionizer A or I-A). The blower system and the ionizers are illustrated in Figure 3-2.

Full-scale chamber tests were performed in the Building Energy and Environmental System Laboratory (BEESL) at Syracuse University. A full-scale single office was built inside the full-scale environmental chamber with carpet floor, painted gypsum wallboards for walls and ceiling, a single workstation (a wooden table, a laptop, and partitions), a manikin wearing a pre-soiled T-shirt, and two mixing fans on the corners. The test room was originally built in November 2018 and all interior materials and facilities had been exposed to the laboratory condition for more than two years before the tests. The workstation, manikin, and mixing fans were set up before the presented study (October 2021). The test room has a dimension of 3.5 × 3.0 × 2.7 m (length × width × height) with a room volume of 29.1 m^3. The air cleaner (blower system) was placed inside the test room (behind the manikin). The environmental control system of the chamber was directly connected to the test room. The supply air entered the test room through a rectangular ceiling diffuser (0.9 × 0.017 m) and was exhausted through a circular outlet with a diameter of 0.1 m close to the floor. The environmental control system can provide a steady stream of fresh air to the test room when needed. The makeup air of the system originated from the outdoor air and filtered by a high-efficiency particulate absorbing (HEPA) filter and an activated carbon filter. The

recirculation damper of the system was completely closed during the test period, so no recirculated air was present.

Figure 3-2. Schematic of the test chamber and the air cleaner (blower system).

Two different test methods and procedures were used in this study, including pollutant decay (or "pull-down") testing for particles, and constant-source testing for particles and VOCs (Figure 3-3). In the decay tests, particle generation was stopped when the total particle concentration reached about 1000#/cm^3. A short period of natural decay was performed before turning on the air cleaner. The particle concentration variation was measured during the entire test period (i.e., both before and after turning on the air cleaner) in order to determine the decay rates due to natural deposition

and dilution by any possible infiltration airflow. The air handling unit (AHU) of the chamber system was completely off over the test period, with only natural infiltration presented. The method has been widely used in other studies and standards (ANSI/AHAM 2020).

The constant-source tests were designed to simulate realistic room scenarios with typical indoor particle and VOC levels under a constant ventilation rate. As shown in Figure 3-3, particles and/or VOCs were injected into the testing room continuously throughout the test period. When the background concentration reached a steady state, the blower fan was turned on to remove pollutants through the MERV 8 filter. When another steady state was reached, the ionizer (A or B) was turned on until the final stable state was reached. The steady-state pollutant concentrations at different states were used for estimating the removal efficiency of the air cleaner. The AHU was working continuously during the constant-source tests to provide constant outdoor/fresh air (purified by HEPA and carbon filters) to the indoor air. Two different outdoor airflow rates were provided in this study, including the low airflow (Q = 24.0 m^3/h) and the high airflow (Q = 55.6 m^3/h). The low airflow (Q = 24.0 m^3/h) just met the minimal ventilation required by the ASHRAE standard for office scenarios (i.e. 20.4 m^3/h, based on the area and occupant number of the test room (ASHRAE 2019a)). Thus, the constant-source tests with low ventilation rate can generally represent the worst-case scenario of an office space (high pollutant level and minimal ventilation). The high airflow (Q = 55.6 m^3/h) represented the scenarios with improved/enhanced ventilation systems (over 2× of the minimal requirement). CO2 decay tests were performed to confirm the ventilation airflow rate of the test room (see Supplementary Information).

A total of 11 tests were performed using different test methods between October 28th, 2021, and February 14th, 2022, including five decay tests and five constant-source tests (Table 3-5). Decay/pull-down tests were performed to estimate the natural decay rate, the removal rate by MERV 8 filter, the removal rate by ionizer A, and the removal rate by ionizer B. The MERV 8 filter was always utilized when the ionizer A was working because the ionizer was mounted on the filter. For the portable ionizer, ionizer B was tested under two different configurations, with and without MERV 8 filter installed, respectively. The constant-source tests were conducted for testing ionizer A. VOC injection was performed in a constant-source test only (Test 10).

Table 3-5. Test conditions of in-duct NPBI units.

Test method	Test ID	Test condition	Airflow condition	Injected pollutants	Test date
Decay test	Test 1	Natural decay	Infiltration[a]	Particles	Dec 1st, 2021
	Test 2	Blower w/ MERV 8 filter	Infiltration	Particles	Nov 29th, 2021
	Test 3	Ionizer A & filter	Infiltration	Particles	Nov 28th, 2021
	Test 4	Ionizer B & filter	Infiltration	Particles	Nov 30th, 2021
	Test 5	Ionizer B (w/t filter)	Infiltration	Particles	Dec 10th, 2021
Constant-source test	Test 6	Ionizer A & filter	Low airflow[b]	Particles	Oct 28th, 2021
	Test 7	Ionizer A & filter	Low airflow	Particles	Nov 24th, 2021
	Test 8	Ionizer A & filter	High airflow[c]	Particles	Feb 14th, 2022
	Test 9	Ionizer A & filter	High airflow	Particles	Feb 14th, 2022
	Test 10	Ionizer A & filter	Low airflow	VOCs	Nov 23rd, 2021

[a] Infiltration: Environmental system was fully closed. There was only natural infiltration existing in the room, λ_{inf} = 0.01h^{-1} (0.3 m^3/h).

[b] Low airflow: Q = 24.0 m^3/h.

[c] High airflow: Q = 55.6 m^3/h.

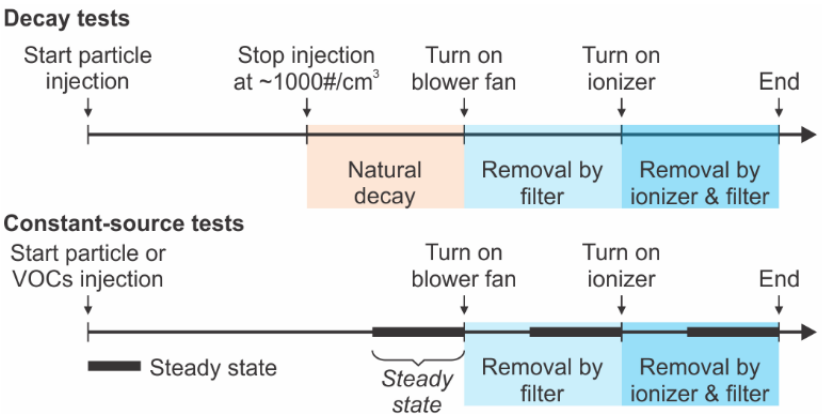

Figure 3-3. Procedures of different test methods.

Particles were disseminated using an 8-jets nebulizer (Blaustein Atomizing Modules (BLAM), CH Technologies Inc) driven by the purified/filtered clean air. The supply air was nominally provided at an airflow rate of 18 L/min with a liquid (salt solution) dissemination rate of approximately 0.14 mL/min. The salt solution was prepared and used for particle generation, which contains 0.05 mol sodium chloride (NaCl) and 0.004 mol anhydrous magnesium sulfate (MgSO4) in 0.5 L deionized (DI) water. The solution was injected into the nebulizer by a syringe pump (New Era Pump Systems Inc, Model NE-1000) at the rate of 0.3 mL/min. The generated particles were introduced into the tested room via a vinyl tube with a diameter of 1 cm (3/8 inch). The indoor particle concentrations measured in the presented study were generally within the typical indoor PM2.5 mass concentration range. In some worst-case scenarios, the indoor PM2.5 can reach the level of 90 $\mu g/m^3$ in offices or 180 $\mu g/m^3$ in schools (A. Zhang et al. 2021). The steady-state particle number concentrations monitored in the constant-source tests of this study were below 100 $\mu g/m^3$ (Kulkarni et al. 2011; TSI Inc 2012)), which is close to the worst-case indoor PM2.5 levels. The initial PM2.5 concentrations of the decay tests were approximately 200 $\mu g/m^3$ based on simple

conversions, which were also close to the indoor PM2.5 levels of the worst-case scenarios. Therefore, the particle generation in this study represented the worst-realistic case scenario of typical indoor particle levels.

In office spaces, over 100 different volatile organic compounds (VOCs) have been identified, although most are presented in relatively low concentrations. Formaldehyde (HCHO) and toluene are the two significant compounds of VOCs in offices. Toluene is often used as a reference compound to quantify the total volatile organic compounds (TVOC). Formaldehyde and Toluene are also the compounds selected to evaluate the performance of various sorbent media in the ASHRAE standard (ASHRAE 2015) and widely used as the target compounds for testing air cleaner performance in other studies (W. Chen et al. 2005; He et al. 2014; Pei et al. 2008; Zhiqiang Wang et al. 2012; X. Wu et al. 2011). They also represent water-soluble and water-insoluble compounds, respectively, representing different challenges faced by air cleaners.

Formaldehyde and toluene were selected as the target compounds to evaluate the removal performance of the tested air cleaning technologies. Constant emission was simulated by using pre-calibrated permeation tubes to achieve a slightly higher but realistic indoor concentration level for testing:

- Formaldehyde: target at a background level of 30+/-15 ppb (39.3 $\mu g/m^3$) with constant injection under the reference condition

- Toluene: target at a background level of 50+/-15 ppb (189.6 μg/m^3) with constant injection under the reference condition

In order to identify any potential secondary emission released through ozone-initiated reactions with human-related surfaces (e.g. skin or clothes), a soiled T-shirt was put on the thermal manikin as in a previous study (Rai et al. 2014). Prior to the testing day, a freshly cleaned T-shirt was worn by a volunteer overnight. The skin-oil-soiled T-shirt then was put on a heated anatomically correct 20-segment Newton thermal manikin made by Thermetrics (Measurement Technology Northwest Inc.) (Kong et al. 2019). The manikin has a total skin surface of 1.8 m^2 and height of 1.8 m, and was dressed in typical summer clothes, i.e. a T-shirt (soiled) and long trousers (clean), which has a total clothing insulation of 0.43 clo based on the ASHRAE standard (ASHRAE 2017b). The skin temperature was maintained at a set-point temperature of 33.9 °C by a computer-controlled feedback system (Khalifa et al. 2009).

A Dynacalibrator (VICI Metronics, Inc.) was used to supply constant VOC injections to the test room. The clean air ("carrier flow") went through a temperature-controlled glass chamber, where permeation tubes are located, to carry VOCs permeated from the permeation tubes. The VOC-carrying carrier flow then mixed with the rest part of the clean air ("dilution flow") to obtain the desired VOC concentration level at the outlet of the Dynacalibrator. The outlet VOC concentration was determined by the airflow rates of carrier flow and dilution flow, and VOC permeation rate from the permeation tube, which is highly dependent on the temperature. The permeation tubes of

formaldehyde and acetone (Dynacal permeation tubes from VICI Metronics, Inc.) were used as the VOC sources of interests in the present study. The Dynacal permeation tubes are small and inert capsules containing a pure chemical compound in a two-phase equilibrium between its gas phase and its liquid or solid phase. At a constant temperature, the device can emit the compound through its permeable portion at a constant rate, which was carried by the airflow over it.

During the experiments, particle concentrations were measured using the TSI Aerodynamic Particle Sizer (APS) 3321 spectrometer, which measures aerodynamic particle size from 0.5 to 20 μm. The total particle concentrations were calculated in the summing mode. Formaldehyde, acetone, and acetaldehyde were collected using 2,4-Dinitrophenylhydrazine (DNPH) sampling tubes connected to the sampling pumps (Alicat Scientific MC-2SLPM-D) with off-line analysis conducted via high-performance liquid chromatography (HPLC). Other VOCs were collected using sorbent tubes connected to the sampling pumps (Alicat Scientific MC-5SLPM-D) and analyzed on an Agilent 6890 gas chromatograph (GC) with an Agilent 5973 mass selective detector (MS). The sampling pumps were calibrated by a flow calibrator (SKC UltraFlo 709), and the total sampling volumes for sorbent and DNPH were 6L and 30L, respectively. The 2B Technologies Model 202 Ozone Monitor was used to measured ozone. Negative ions were monitored using an air ion counter (Alphalab Inc, Model AIC2) with an accuracy of ±20% of reading. A photoacoustic gas monitor (LumaSense Inc., Innova 1412i) and a CO2 logger (HOBO Inc., Onset MX1102) were used to monitor the CO2 concentration decay to determine the airflow rate and the infiltration rate of the room.

All samples were monitored at the exhaust of the room (return air). For decay tests and constant-source tests, particle, ozone, and ion concentrations were continuously monitored throughout the test period. For VOC sampling in Test 10, the sorbent and DNPH samples were collected during each steady state. One set of background samples was taken in the steady state before turning on the blower fan. Two sets of samples were collected in the steady state with the blower turned on, and two other sets were taken in the steady state with the ionizer working. For each set of sampling, two duplicated sorbent samples were collected to obtain duplicated results from GC/MS analyses. Since the DNPH samples can be analyzed repeatedly by HPLC, single sample was collected in each steady state. But each collected DNPH sample was analyzed repeatedly to get two sets of results as for the sorbent samples. A schematic of different test procedures was shown in Figure 3-3. Besides the pollutant samples, the electric energy powers of the tested ionizers were also monitored. A power line meter (Electronic Product Design, Inc.) was used to monitor the electric power when the ionizer was working.

The steady-state indoor pollutant concentration in a well-mixed space can be presented as a simplified single-zone model,

$$\lambda C_{in} = \lambda C_{out} - k_{dep} C_{in} + \frac{E'}{V} \tag{3-1}$$

where C_{in} is the steady-state indoor pollutant concentration, C_{out} is the concentration of the inlet air (outdoor air), λ is the total equivalent ventilation rate of the test room, k_{dep} is the

deposition/removal rate of the pollutant in the room, *E'* is the emission rate of the indoor source, and *V* is the room volume. For decay tests without any indoor emission sources, the indoor pollutant concentration at time *t* (C_t) depends on the initial concentration of the pollutant (C_0), the total equivalent ventilation rate λ of the room, and the decay time *t* (Eq. 3-2). Therefore, exponential regressions can be performed to time-sequential particle and CO2 concentrations to estimate the particle removal rates and the ventilation/infiltration rates of the room, respectively. For particle decay tests in this study, the estimated removal rate (λ) included the natural decay rate k_n (including infiltration λ_{inf} and deposition k_{dep}) and the removal rate of the air cleaning unit k_{AC} (including the removal by filter k_{filter} and the removal by ionizers $k_{ionizer}$) as Eq. 3-3. For CO2 decay tests, the estimated ventilation rate (λ) from exponential expressions can represent the infiltration rate of the room λ_{inf} (without any mechanical ventilation) or the combination of the infiltration rate and the ventilation rate by the control system λ_Q (Eq. 3-4).

$$C_t = C_0 \cdot e^{-\lambda t} \tag{3-2}$$

$$\lambda = k_n + k_{AC} = (\lambda_{inf} + k_{dep}) + k_{filter} + k_{ionizer} \tag{3-3}$$

$$\lambda = \lambda_{inf} + \lambda_Q = \lambda_{inf} + \frac{Q}{V} \tag{3-4}$$

The clean air delivery rate (CADR) is a factor widely used for evaluating the performance of air cleaning technologies. It represents the equivalent "clean" air supplied by the air cleaning

technology for a certain pollutant such as particle or formaldehyde. For decay tests in the present study, the CADR can be determined by the estimated pollutant removal rate (k_{AC}) and the room volume (V) as Eq. 3-5. For constant-source tests, the CADR of the air cleaner can be derived from Eqs. 3-1 and 3-6. It is dependent on the clean/outdoor air flow rate supplied to the test room by the control system (Q), and steady-state pollutant concentrations between the background (without air cleaner, C_1) and the stable concentration with air cleaner working (C_2), as well as the deposition rate of the pollutant k_{dep} (assuming a constant deposition rate) (Eq. 3-6). The equivalent single-pass pollutant removal efficiency (SPRE) can be determined by the estimated CADR for a certain pollutant and the airflow rate of the air cleaner (Q_{AC}) (Eq. 3-7). The SPRE estimated in this study represented the equivalent removal efficiency of the tested air cleaner for a specific pollutant, including the contributions from all possible removal mechanisms such as infiltration and deposition. It is different from the directly measured single-pass infiltration efficiency based on the concentration difference between downstream and upstream of the air cleaner.

$$CADR = k_{AC} \cdot V \tag{3-5}$$

$$CADR = (Q + k_{dep} \cdot V) \cdot (\frac{C_1}{C_2} - 1) \tag{3-6}$$

$$SPRE = \frac{CADR}{Q_{AC}} \tag{3-7}$$

The generation rates of certain compounds or byproducts in the room, e.g., ozone or VOCs, can be calculated through the single-zone model (Eq. 3-1). In this study, the generation rate of ozone was estimated. Indoor ozone originates from the outdoor air and the emission of the air cleaner and removed through deposition on material surfaces and reactions with some gaseous compounds. The overall ozone deposition rate in the test room was estimated in an earlier test performed on May 19th, 2021, which was used in this study (assuming constant deposition rate).

The infiltration rate of the test room was approximately 0.01h^{-1} through CO2 decay tests (R^2 > 0.99, see Appendix). All detected indoor particles were below 2 μm in size with a median diameter roughly between 0.7 and 0.8μm. The natural decay test (Test 1) illustrated that the natural decay rate of total particle concentrations (k_n), that is the combined effect of infiltration (λ_{inf}) and particle natural deposition (k_{dep}), was 0.22h^{-1} (R^2 > 0.99), which also revealed a particle natural deposition rate (k_{dep}) of 0.21h^{-1}. Table 3-6 showed the removal rate, CADR and SPRE for particulate matter (PM) removal of each decay test under the given experimental conditions. The regular MERV 8 filter illustrated a very low $SPRE_{PM}$ under current settings, around 1.7%, which was generally close to the lower bound of the particle removal efficiencies of MERV 8 filters tested by other studies (Alavy and Siegel 2020; Azimi et al. 2014; B. Shi et al. 2012; B. Shi and Ekberg 2015; Stephens and Siegel 2012; Zeng et al. 2022). The combined use of ionizers (A and B) and MERV 8 filter showed an absolute increase on $SPRE_{PM}$ by about 6-7.4%, which was 3.6 to 4.5 times higher than the efficiency of the tested filter. The ionizer B alone (i.e., without the MERV 8 filter) provided very limited particle removal efficiency (3.8%).

In this study, ionization can generally remove particulate matter from the indoor air through two approaches. One is the enhanced deposition of airborne particles to the indoor surfaces due to the aggregation of charged particles (increased particle size) and the attraction of charged particles by the surfaces. The other is the elevated particle filtration/capture by the charged filter as the generated ions attached on the filter. The aggregation of charged particles can also be filtered more readily attributed to the increased particle size. According to the collected ion concentrations (Section 3.2), most ions generated by the ionizer were trapped/captured by the filter when the filter was installed at the downstream of the ionizer. Therefore, the particle removal of using ionizer B individually ($CADR_{PM}$ of 19.4 m^3/h and $SPRE_{PM}$ of 3.8% in Test 5) was merely attribute to the enhanced deposition of charged particles to the indoor surfaces, which also represented the maximum particle removal contribution through enhanced deposition. Considering the notable drop of ion concentrations through the filter, the actual particle removal due to the enhanced deposition in the air may contribute less when the filter is installed and integrated with the ionizer. According to the test results, the integrated use of ionizer B and filter (Test 4) almost doubled the $CADR_{PM}$ and equivalent $SPRE_{PM}$ compared to ionizer B alone (Test 5). Based on the analysis above, the enhanced filtration/capture by the charged filter likely dominated the particle removal for the integrated use of ionizer and filter, while the enhanced deposition from the air to indoor surfaces had less effects.

Table 3-6. Performance of different units during chamber tests.

Tests	**Test 1**	**Test 2**	**Test 3**	**Test 4**	**Test 5**
Test conditions	**Natural decay**	**Filter (MERV 8)**	**I-A + filter**	**I-B + filter**	**I-B (w/t filter)**
Natural decay rate[a] [h^{-1}]	0.22	0.25	0.24	0.25	0.20
Removal rate [h^{-1}]	/	0.54	1.82	1.59	0.87
		0.29 (w/t decay)	**1.58** (w/t decay)	**1.34** (w/t decay)	**0.67** (w/t decay)
$CADR_{PM}$ [m^3/h]	/	15.7	53.0	46.3	25.3
		8.5 (w/t decay)	**46.0** (w/t decay)	**38.9** (w/t decay)	**19.4** (w/t decay)
$SPRE_{PM}$ [%]	/	3.1	10.5	9.2	5.0
		1.7 (w/t decay)	**9.1** (w/t decay)	**7.7** (w/t decay)	**3.8** (w/t decay)

[a] Natural decay rate (k_n): the combined effect of infiltration (λ_{inf}) and particle natural deposition (k_{dep}).

The results of decay tests were generally consistent with the results of constant-source tests. Figure 3-4 showed the steady-state total particle concentration before and after using the ionizer A in four constant-source tests. The 1-h stable data of the background, the state with only MERV 8 filter, and the state with the ionizer A on, were selected and calculated. The background concentrations in Tests 6 and 7 did not reach a steady state due to the large injection fluctuations during the tests, and thus, were not presented in this study. An example of time-sequential total particle concentration distribution during the test period (Test 9) was presented in Figure 3-4 (b). After the ionizer A was turned on, the total particle concentrations sharply declined. As shown in Table 3-7, the blower with the MERV 8 filter under the given conditions (Tests 8 and 9) provided 4.9-8.3 m^3/h $CADR_{PM}$, which resulted in $SPRE_{PM}$ between 1.0% and 1.6%, consistent with the results of decay tests. The particle natural deposition rate k_{dep} ($0.21h^{-1}$) measured in decay tests was applied in Eq. 3-6 for estimation (assuming constant particle natural deposition). The actual particle deposition rates (when the ionizers were working) were probably underestimated. They could be higher than the natural deposition rate estimated without the ionizers. In this case, the $CADR_{PM}$ and $SPRE_{PM}$ estimated through constant-source tests might be underestimated as well. The estimated $CADR_{PM}$ of the integrated uses of ionizer A and filter was 36.5-45.1 m^3/h and the $SPRE_{PM}$ was 7.2-8.1%. It is also consistent with the $CADR_{PM}$ and $SPRE_{PM}$ estimated through the decay test for ionizer A (Test 3). The steady-state particle concentration variations before and after using the ionizer also indicated the particle removal performance of ionizer A. The estimated $CADR_{PM}$ provided by the ionizer A individually were between 24.8 and 68.5 m^3/h, which is 1.3× to 3.4× of the minimal ventilation requirement per person (ASHRAE 2019a), and the estimated $SPRE_{PM}$ of the ionizer were around 4.9-13.5% under the given settings (Tests 6-9). During the constant-source test Test 8, a particle concentration decay test was also performed. The overall

decay rate estimated from the exponential regression was 3.86 h^{-1} (R^2 > 0.99, including natural deposition and dilution by the fresh air supplied by the control system Q). Then, the $CADR_{PM}$ supplied by the ionizer A and filter was 52.6 m^3/h (excluding particle deposition and dilution by the fresh air supply), assuming a constant particle deposition rate of 0.21 h^{-1}. The $SPRE_{PM}$ by the ionizer and filter was 10.4%.

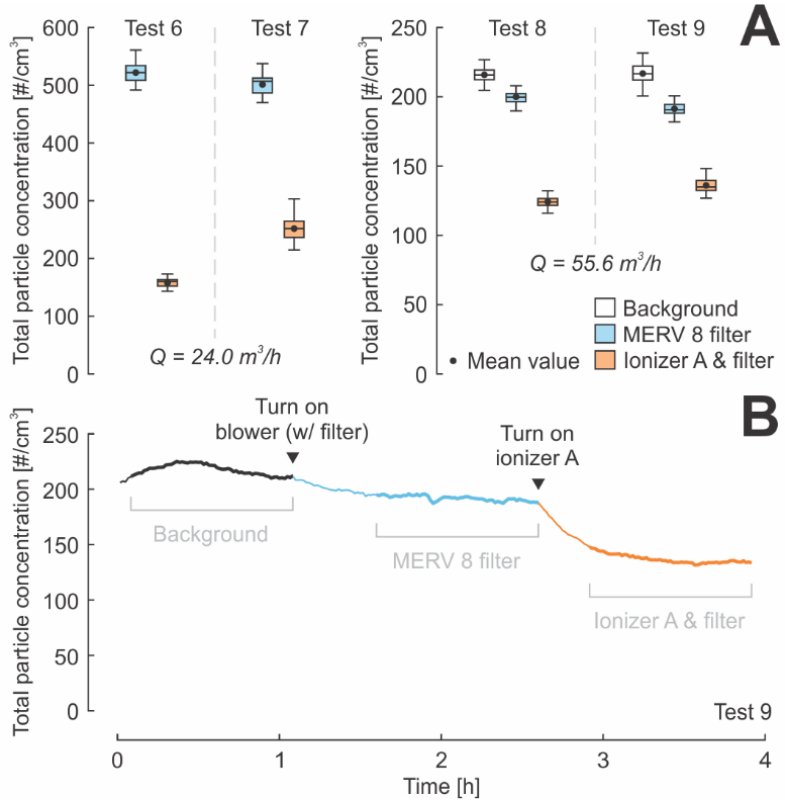

Figure 3-4. (a) Total particle concentration distributions of different states in constant-source tests; (b) An example (Test 9) of time-sequential total particle concentration distribution during the test period.

Table 3-7. Particle removal performance of constant-source tests.

Test	**Q [m^3/h]**	**$k_{dep} \cdot V^a$ [m^3/h]**	**Average total particle number level in each state [#/cm^3]**			**$CADR_{PM}$[b] [m^3/h]**			**$SPRE_{PM}$[b] [%]**		
			Bkg	**Blower on (w/ filter)**	**Ionizer A on**	**MERV 8 filter**	**Ionizer A & filter**	**Ionizer A[c]**	**MERV 8 filter**	**Ionizer A & filter**	**Ionizer A**
6	24.0	6.1	/	521.4	159.1	/	/	68.5	/	/	13.6
7	24.0	6.1	/	500.7	251.7	/	/	29.8	/	/	5.9
8	55.6	6.1	215.5	199.7	124.5	4.9	45.1	37.3	1.0	8.9	7.4
9	55.6	6.1	217.3	191.6	136.6	8.3	36.5	24.8	1.6	7.2	4.9
8[d]	55.6	6.1	/	/	/	/	52.6[e]	/	/	10.4[e]	/

[a] Assuming a constant particle deposition rate k_{dep} = 0.21 h^{-1}. The estimated $CADR_{PM}$ and $SPRE_{PM}$ for the scenario with ionizer A and filter, and the scenario with ionizer A individually, may be underestimated as the actual particle deposition rate was likely higher when the ionizer was working.

[b] Particle removal due to natural deposition were ruled out.

[c] The CADR of ionizer was calculated through Eq. 3-6, instead of subtracting the CADR of filter from the CADR of ionizer and filter.

[d] A decay test was performed along with the constant-source test of Test 8. The overall decay rate estimated from the exponential regression was 3.86 h^{-1} (including natural deposition and dilution by fresh air supplied by the control system Q).

[e] Excluding natural deposition and dilution by fresh air supply.

When the filter was installed at the downstream of the ionizer, a considerable number of produced ions were likely captured by the filter. The steady-state negative ion concentrations were only 1.1×10^3 #/cm^3 and 1.5×10^3 #/cm^3 for ionizer A and B of the decay tests, respectively. For constant-source tests, the indoor negative ion levels were around 0.9×10^3 to 1.4×10^3 #/cm^3 in the air for ionizer A. The measured negative ion concentrations were still close to the background level. However, if the filter was removed, most ions were introduced to the indoor air and the indoor negative ion level increased dramatically, i.e. approximately 16.1×10^3 #/cm^3 for ionizer B in the scenario without the filter, over 10 times higher than the level with the filter installed. The result indicated a significant reduction of around 91-94% through the filter. A previous study observed an almost 100% drop of air ions through higher-efficiency MERV 11-12 filters, although the downstream ion concentrations were measured at a longer distance after the filter, at which distance, many air ions were likely decomposed on the metal air duct (B. Shi and Ekberg 2015). Therefore, when a filter was installed at the downstream of the ionizer, most of the produced ions were captured by the filter, particularly for higher-efficiency filters.

In decay tests, ozone concentration increases were detected in the confined space after the ionizer was turned on due to zero outdoor ventilation airflow, though the amount of increase was less than 3 ppb in average. The background levels (Bkg) presented the steady-state concentrations over 60 min before the ionizers were turned on. The ionization levels showed the 60-min steady-state data of ozone concentrations when the ionizers were turned on. Significant ozone concentration increases were observed during the ionization periods (p-value < 0.001 for three tests), but the increases were fairly small. As carbon filters were used in HVAC systems of the chamber and the laboratory, the background ozone concentrations in the chamber were almost zero (0-0.1 ppb). The

negative values were within the detection errors. The mean steady-state ozone concentrations of the ionization periods in three tests (ionizer A, ionizer B, and ionizer B without filter) were 1.2, 2.0, and 2.9 ppb, respectively. Our earlier ozone decay test (in Appendix) illustrated that the ozone deposition rate in the same room setting was around 5.5 h^{-1} (most ozone deposition occurred on building surfaces and human-related surfaces (Nazaroff and Weschler 2021; Shen and Gao 2018; Yao and Zhao 2018)). Therefore, it can be estimated that the ozone generation rates during the ionization in three tests were 0.39, 0.63, and 0.92 mg/h for ionizer A (with filter), ionizer B (with filter), and ionizer B (without filter), respectively. Relative to other indoor air cleaning technologies that may generate ozone (C. Guo et al. 2019), the ozone emission rates of the tested ionizers were very low. Therefore, under scenarios with realistic room and ventilation settings, the ozone increases by ionization were likely negligible for the tested ionizers, which was closely consistent with the observations in the constant-source tests. No significant ozone increases were detected when certain ventilations were provided to the room (Tests 6-10). It was also observed by other studies and claimed by some needlepoint bipolar ionizer manufacturers (Carrier Global 2021; Waddell 2019; Zeng et al. 2021, 2022).

Indoor VOCs were collected and analyzed in Test 10. The background sampling set (two duplicated samples) were collected at time t = 0h. The background formaldehyde and toluene concentrations were around 20.6 and 138.7 $\mu g/m^3$, respectively, which were relatively lower than the target level (39.3 and 189.6 $\mu g/m^3$) but still within the typical indoor concentration range. Other detected VOCs, such as acetaldehyde, acetone, benzene, and other aldehydes, were relatively lower. Most VOCs were below the level of 2 $\mu g/m^3$ (see Appendix). After the blower was turned on and a steady state of indoor VOCs was reached, VOC samples were collected at t = 9h and t =

12h (for each set of sampling, two duplicated samples were collected). The mean values of two sets (four samples in total) were calculated. After a certain period since the ionizer (ionizer A) was turned on (t = 18h and t = 50h), another two sets of VOC sampling were performed (two duplicated samples for each sampling set were collected).

Reference background VOC levels were measured through a series of GC/MS analyses in the test room with same configurations, except the data of formaldehyde and toluene (injected compounds), which were collected through the real-time proton-transfer-reaction mass spectrometer (PTR-MS; Ionicon Analytik Ges.m.b.H., Austria) sampling in two tests with same injection procedure and test conditions (S. Zhou et al. 2020). Mean, standard deviation (SD), and relative standard deviation of reference background levels were calculated, representing the background fluctuations of VOCs of concern. A few compounds were not detected (n.d.) in some tests, in which case their concentrations were assumed to be zero for calculating mean and SD values. Another two injection tests were performed to study the injection fluctuations of formaldehyde and toluene with the same injection procedure and test settings (Q: 20.7-22.9 m^3/h).

The results showed that the VOC concentrations under the conditions with blower/filter and ionizer were very close, and both were close to the background level before using the blower. The concentration variations of all VOCs were within the 2 relative SD % of the background levels, which represented the range with about 95% of samples in the same group. Therefore, it is believed in this study that the measured VOC variations are all within background fluctuations or injection fluctuations under the given settings. The TVOC level increased 5% after turning on the ionizer,

which was also a slight variation. Thus, under the test conditions in this study, there were no significant chemical reactions with detected VOCs throughout the ionization process. No significant secondary VOC emissions were generated, and no specific VOCs were removed by the ionizer.

The electric powers of the tested ionizers were very stable when they were working. The average power of ionizer A was 0.4 W, and the average power of ionizer B was 1.0 W. They were significantly lower than the typical power of standalone air cleaners (median: 56 W (B. Zhao et al. 2020b)). Based on the results from decay tests and constant-source tests, the ionizer A can approximately provide an equivalent $CADR_{PM}$ of 24.8-68.5 m^3/h, while the ionizer B can roughly provide 19.4-30.4 m^3/h $CADR_{PM}$ without considering particle removal by the filter, under the settings of this study. Then the electric power per $CADR_{PM}$ was 0.006-0.016 $W/(m^3/h)$ and 0.033-0.052 $W/(m^3/h)$ for ionizer A and B, respectively. Therefore, the tested in-duct ionizers were effective for air cleaning/particle removal with low energy cost compared to typical standalone air cleaners with a median electric power per $CADR_{PM}$ of 0.15 $W/(m^3/h)$ (B. Zhao et al. 2020b). Therefore, the performance of the tested ionizers can be concluded in Table 3-8.

Table 3-8. Performance summary of studied ionizers.

Technology		In-duct needlepoint bipolar ionizer A	In-duct needlepoint bipolar ionizer B
Description		4 bars mounted on filter (34 +/- poles in total)	Portable unit with 6 pairs of +/- poles
Design features	$CADR_{PM}$ [m^3/h]	24.8 – 68.5	19.4 – 30.4
	$CADR_{VOC}$ [m^3/h]	0	0
	$CADR_{O3}$ [m^3/h]	0	0
	$SPRE_{PM}$ [%]	4.9 – 13.6	3.8 – 6
	$SPRE_{VOC}$ [%]	0	0
	$SPRE_{O3}$ [%]	0	0
	ER_{PM} [µg/h]	0	0
	ER_{VOC} [µg/h]	0	0
	ER_{O3} [µg/h]	390	630 - 920

Electric power [W]	0.4	1.0

3.2.4.2 Displacement ventilation integrated with partitions in offices

Displacement ventilation can typically improve the clean air delivery efficiency with a ventilation effectiveness of 1.2 to 2 comparing to mixing ventilation (Q.Chen and Glicksman 2003). Partitions have been widely used in office settings for creating private spaces. It has also been applied to reduce the transmission of SARS-CoV-2 through droplets during this pandemic when social distance cannot be maintained. Cubicle workstations (Haghighat et al. 1996), enclosed or semi-enclosed modular office wall assemblies (PoppinSpaces 2021), and portable partition screens (Rooney et al. 2021) are the major types of partitions used in office settings. Some studies suggested that the combination of displacement ventilation and partitions can effectively mitigate airborne transmission of respiratory diseases like COVID-19 and reduce cross contaminations (Shen, Kong, Dong, et al. 2021a; J. Zhang 2020). But the actual effectiveness of this strategy has not been tested yet. Therefore, the effectiveness of combined displacement ventilation and partitions in office settings for reducing airborne transmission of respiratory diseases like COVID-19 is investigated in this study. The best design for mitigating infection risk through airborne transmission is discussed when conducting displacement ventilation and partitions in offices. Experiments were conducted in the full-scale office space inside the environmental chamber in BEESL. CFD simulations were also performed to understand more details about the air distribution under certain ventilation settings.

The chamber experiment was performed in the same full-scale chamber with same office settings for testing the ionizers. But in this experiment, two identical tables (1.83×0.60 m with a height of 0.71 m) were placed in the middle of the tested room. Two full-scale manikins were sitting face to face. A semi-circular displacement diffuser (0.41 m in diameter, 0.81 m in height) was placed

attached to one lateral side of the room and delivered 208 m^3/h fresh air at around 15°C to the room. The displacement ventilation supply air settings were determined by the guidelines (Q.Chen and Glicksman 2003). The surface temperatures of manikins were set to 34°C with long-sleeve shirts and trousers on manikins. A laptop was placed in front of each manikin, while overhead ceiling lights were on during the tests. Two different respiratory conditions were tested, including breathing and coughing. The respiratory settings (pollutant injection settings) are presented in Table 3-11. Four different partition settings were studied (Figure 3-5), including no partition, single-panel partition (Partition A), semi-wrapped partitions (Partition B), and fully wrapped partitions (Partition C). There was a 0.30 m gap between the partition boards and the floor to introduce the supply air from the diffuser. TSI large particle generator was used to generate aerosols to and introduced to the room through the tube attached to the breathing zone of one manikin (i.e. the "virus carrier"). The other manikin was considered as the "susceptible subject". Airflow velocity and temperature were measured by the probes of the air distribution system. Particle number concentration and size distributions were sampled by the TSI aerodynamic particle sizer (APS) in multiple locations. Figure 3-6 shows the settings for the chamber tests and Figure 3-7 illustrates the sampling locations.

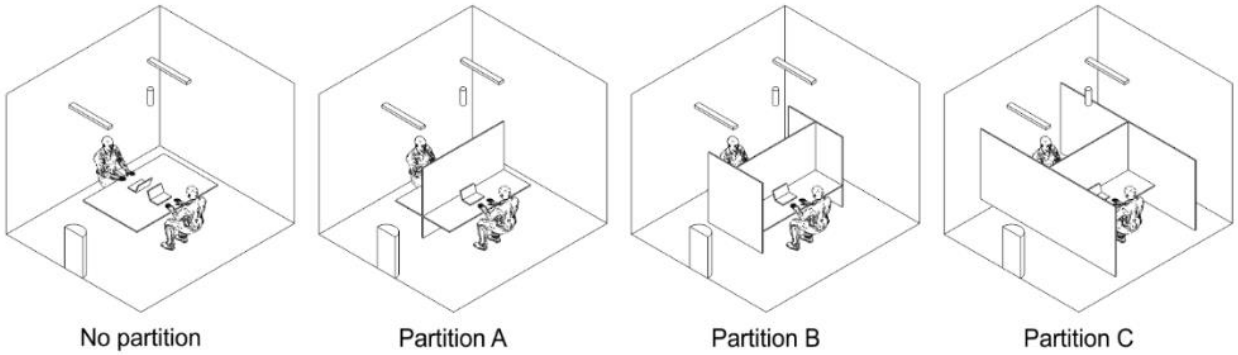

Figure 3-5. Indoor settings of the tested reference office room.

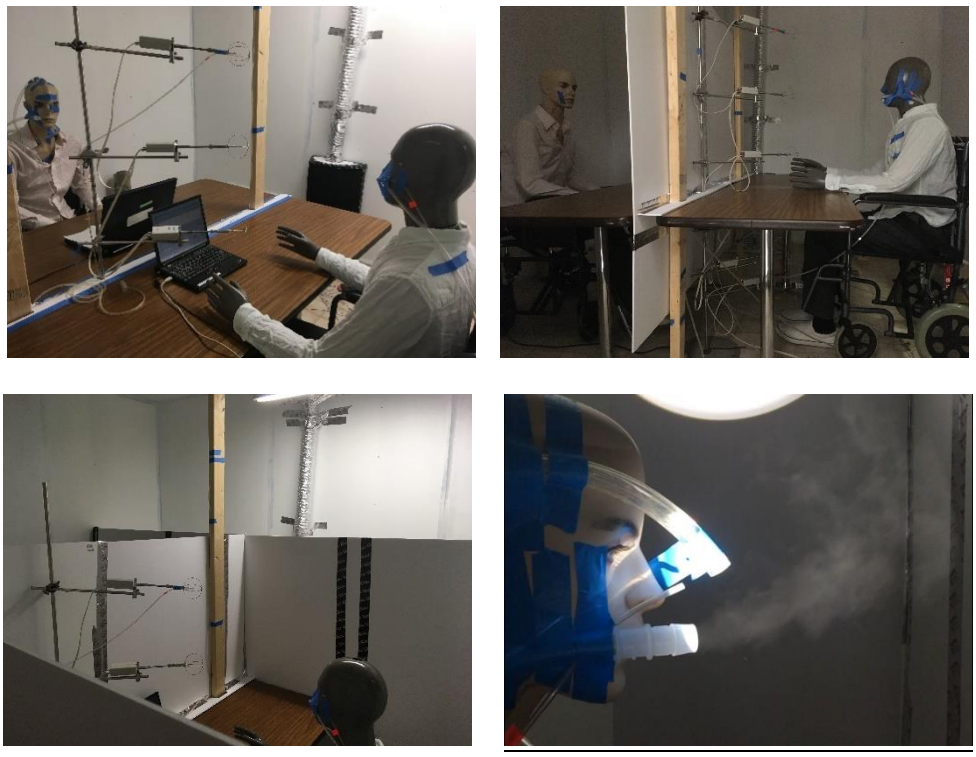

Figure 3-6. Experimental settings of the full-scale chamber tests.

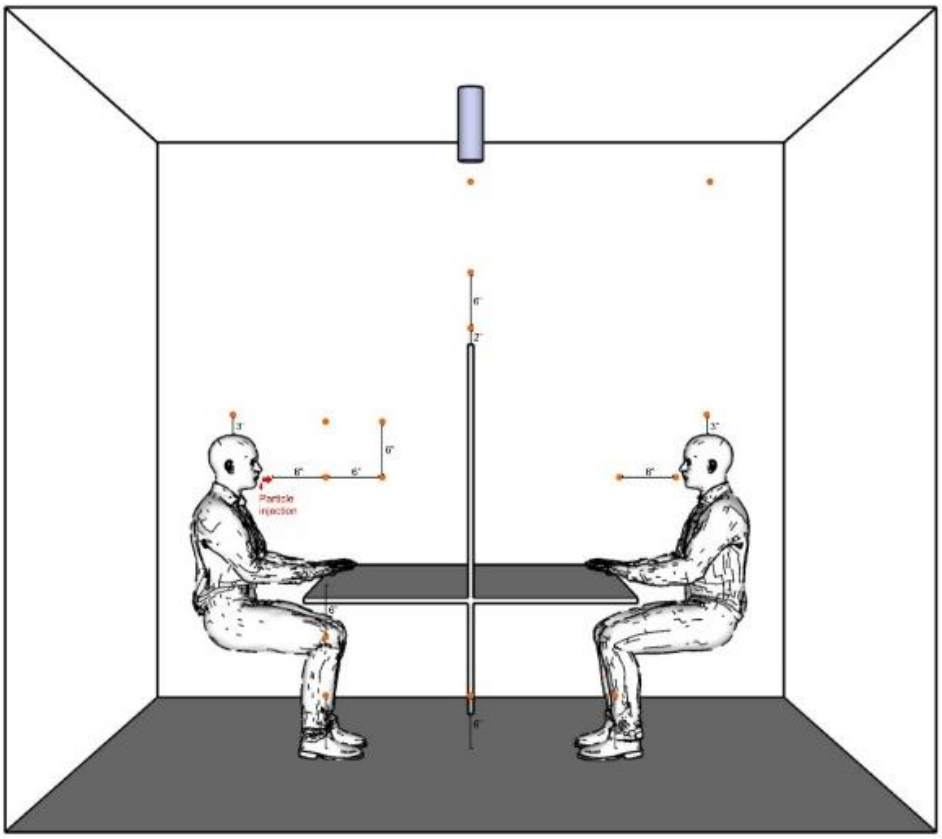

Figure 3-7. Sampling locations.

CFD simulation for the proposed 4 settings were conducted using ANSYS Fluent. Figure 3-8 shows an example of the geometry and mesh settings in CFD simulations. Based on a review on literature (Ahmadzadeh et al. 2021; Assaad et al. 2018; Katramiz et al. 2021; Lai and Cheng 2007; C. Wu and Ahmed 2012; Y. Yan et al. 2020), RNG K-epsilon was used with enhanced wall treatment as the meshes near surfaces are very fine (y+ <= 1). Full buoyancy effect was applied to study the thermal buoyancy and thermal plume with Boussinesq approximation. SIMPLE scheme was used with second-order accuracies. Discrete phase model (DPM) was used to simulate the particles exhaled by breathing and coughing. CFD settings were presented in Table 3-9.

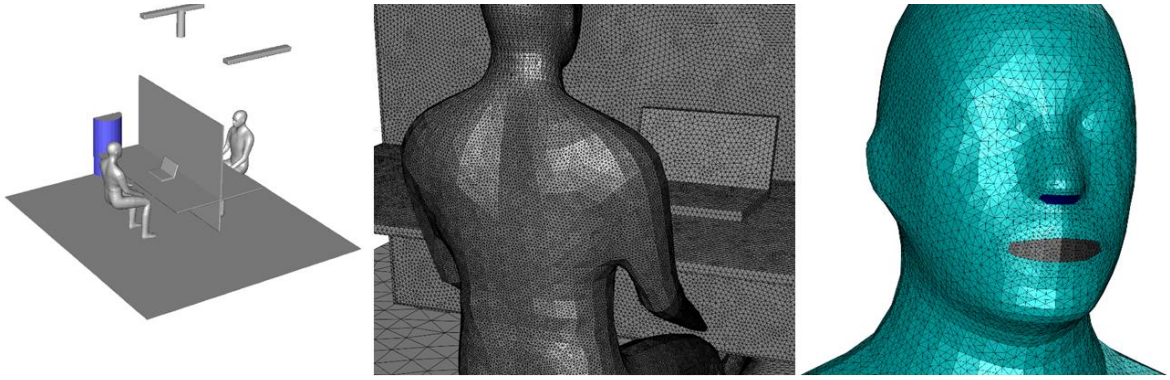

Figure 3-8. Preview of CFD grids.

Table 3-9. CFD settings of the studied displacement ventilation cases.

Facility	**Settings**
Diffuser (semi-circular diffuser):	Height: 32 in Diameter: 16 in Air flow rate: 0.049 m3/s (~104cfm)
Manikin:	Surface temperature: 33.89 °C Total area: 1.81 m2 Surface heat flux (steady-state, total): 70 W/m2 (we can assume 40% of total heat flux as convective heat flux, i.e. 28 W/m2)

Particle injection jet (through round tubes):	**Coughing/talking:** Tube diameter (circle): 5/8 in (0.015875 m) → area: 1.98 cm2 Injection velocity (uniform): 5.26 m/s Injection direction: horizontally forward
	Breathing: Tube diameter (circle): 3/8 in (0.009525 m) → area: 0.71 cm2 Injection velocity (uniform): 1.56 m/s Injection direction: vertically downward

Thermal stratification was observed in the tested room with testing settings. Thermal plume created uprising airflows around manikins and transported abundant quantities of expelled aerosols from the breathing zone of the virus carrier to the exhaust, while only few aerosols were transported to the breathing zone of the susceptible subject (Figure 3-9). Figure 3-10 shows the particle size distribution in the breathing zone of the susceptible subject (receiver).

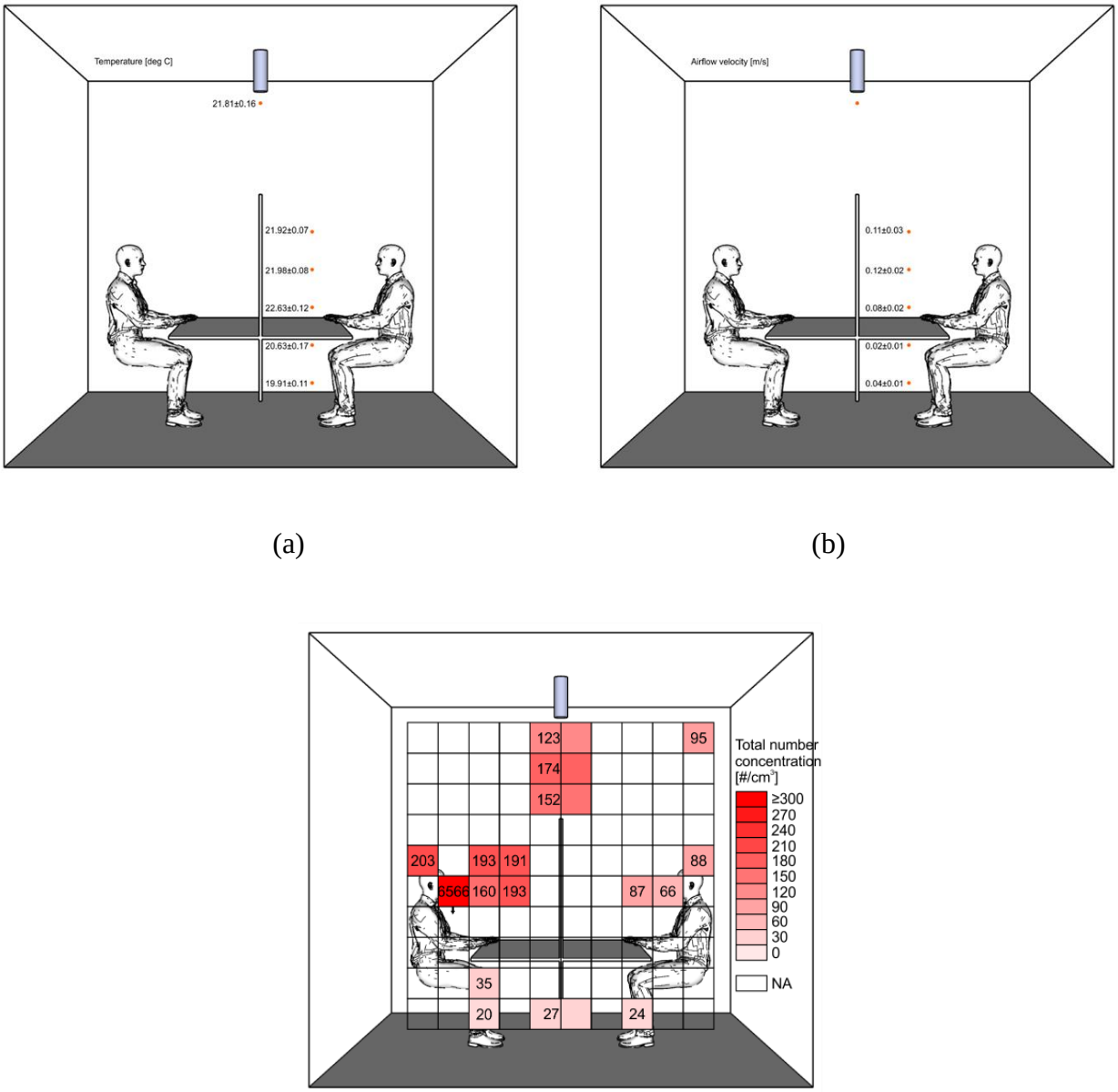

Figure 3-9. Measured total number concentration in the Partition-A scenario.

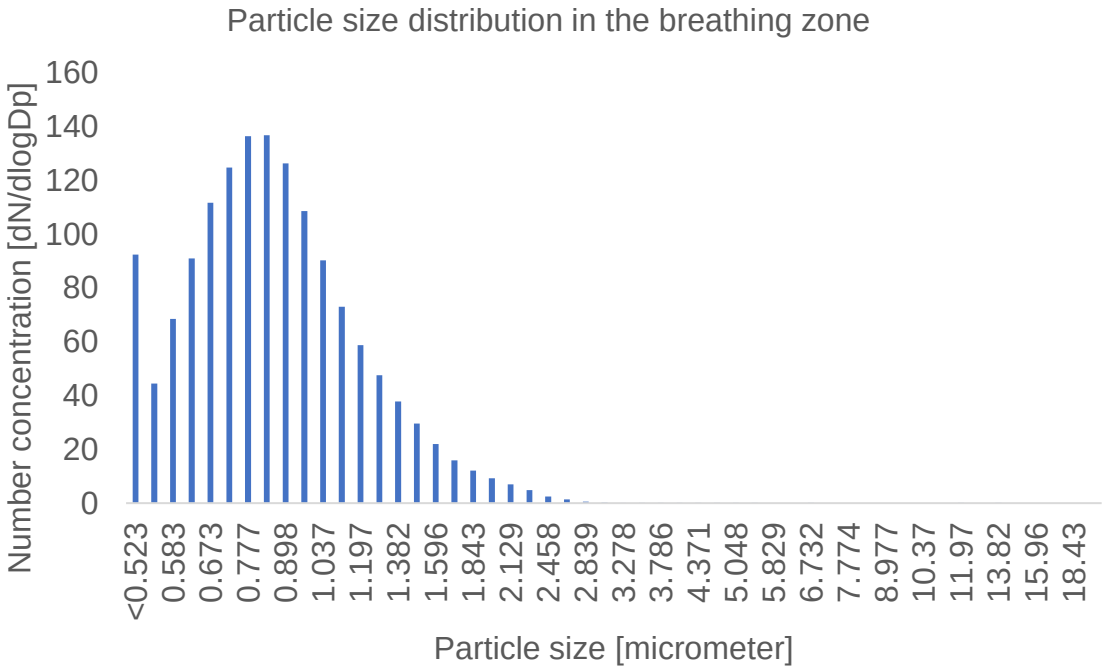

Figure 3-10. Particle size distribution.

The ratios of particle concentration in the breathing zone of the receiver and the particle concentration in the exhaust of the room indicate that displacement ventilation provided higher air distribution efficiency compared to the mixing ventilation (ratio < 1). Under the coughing scenario, adding partitions can further decrease the cross-contamination between the infector and the receiver. Under current settings, the Partition-B can provide highest air distribution efficiency (lowest breathing-zone/exhaust concentration ratio). Adding more partitions to form semi-open spaces does not further block the particle transmission. This may need further studies in future.

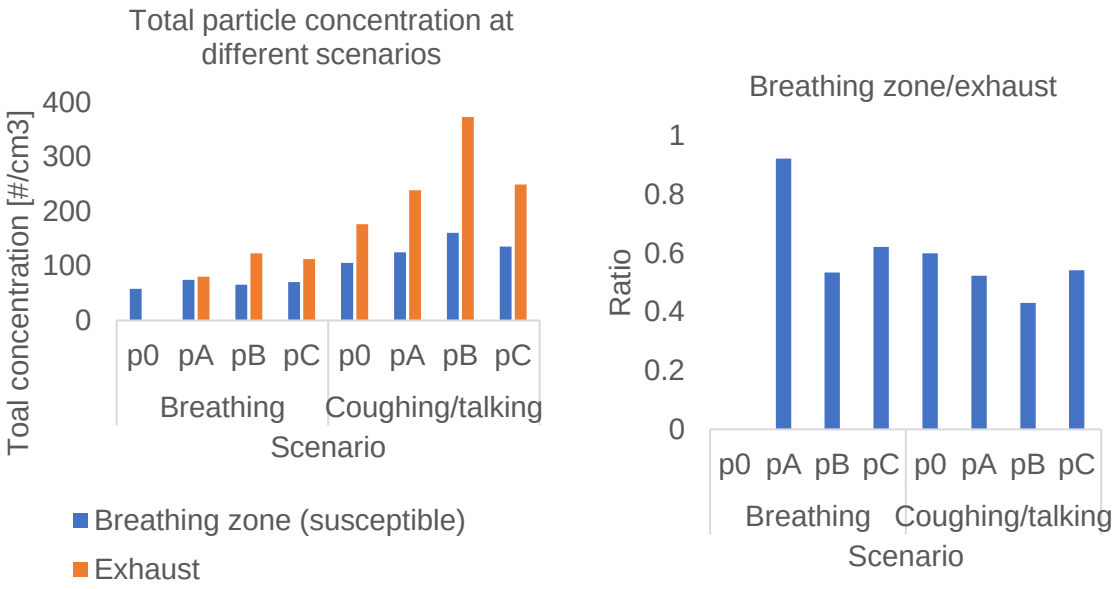

(a) (b)

Figure 3-11. Particle concentration at the breathing zone of the receiver and the exhaust of the room.

CFD simulations illustrate similar results. Under talking and coughing scenarios, if partitions were not installed, a huge amount of exhaled particles would be transmitted to the breathing zone of the receiver. However, if partitions were installed and used properly, most particles would be blocked by partitions and exhausted by the exhaust air. Results show that nearly 70% of exhaled particle were deposit on partitions and other surfaces, or removed by the exhaust air. However, adding more partitions does not further dramatically remove more particles, particularly from Partition-B to Partition-C, which is close to the experimental results. It's likely because the dominated airflow in the space the thermal plume surrounding the occupants. Particles were less likely to travel across the partitions and reach the receiver's breathing zone from lateral or behind directions. Therefore,

for workstations in the office scenario, Partitions that cover the workstation may be sufficient to mitigate the infection transmission between people who are sitting face to face. In the mixing ventilation scenario, because of the cross airflow between cubicles, semi-open space can be more effective in reducing cross-contamination.

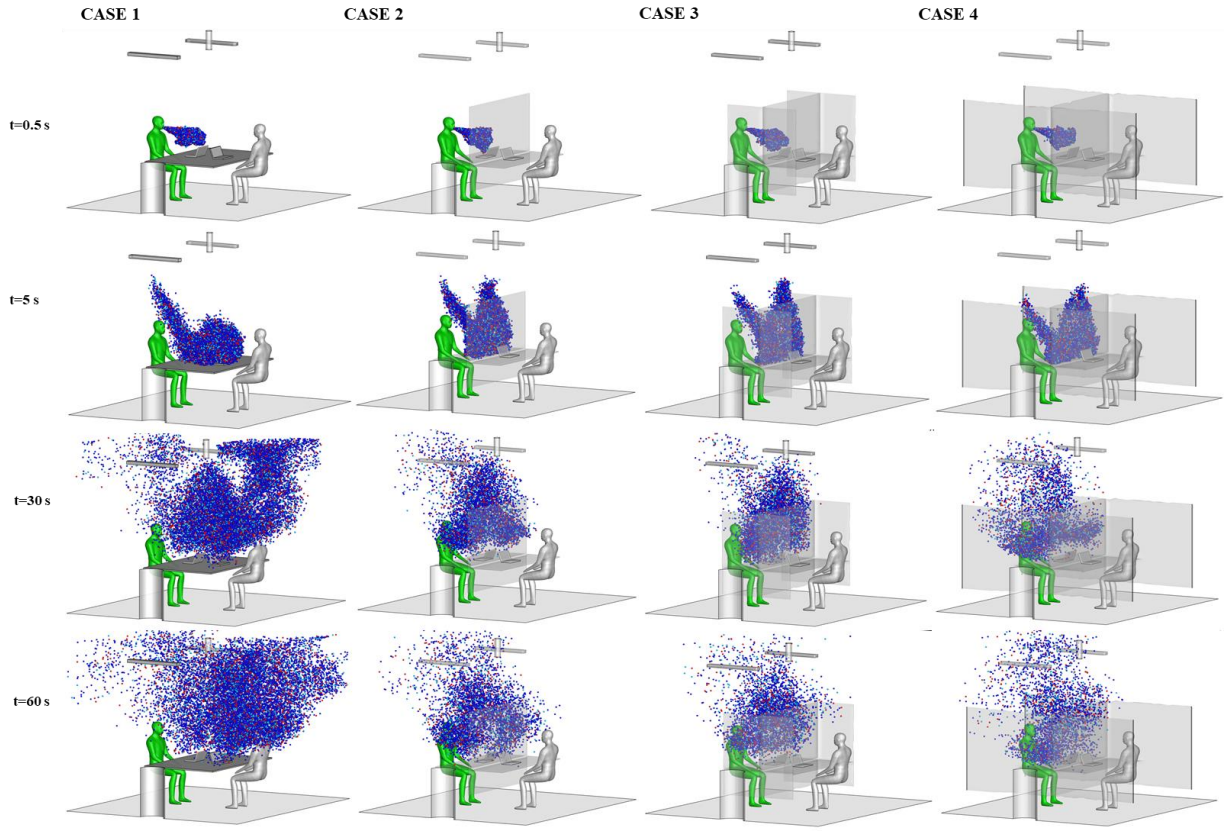

Figure 3-12. Particle distribution over time under coughing scenario.

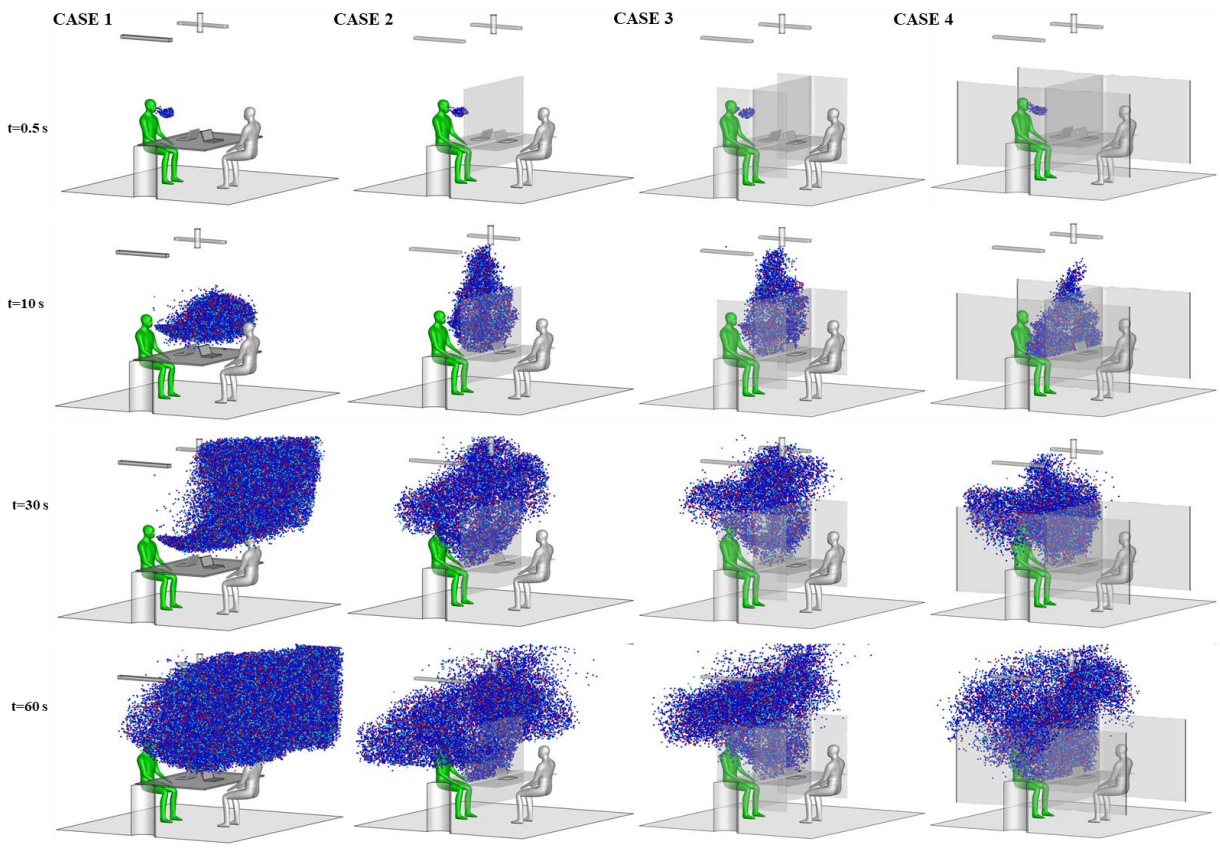

Figure 3-13. Particle distribution over time under talking scenario.

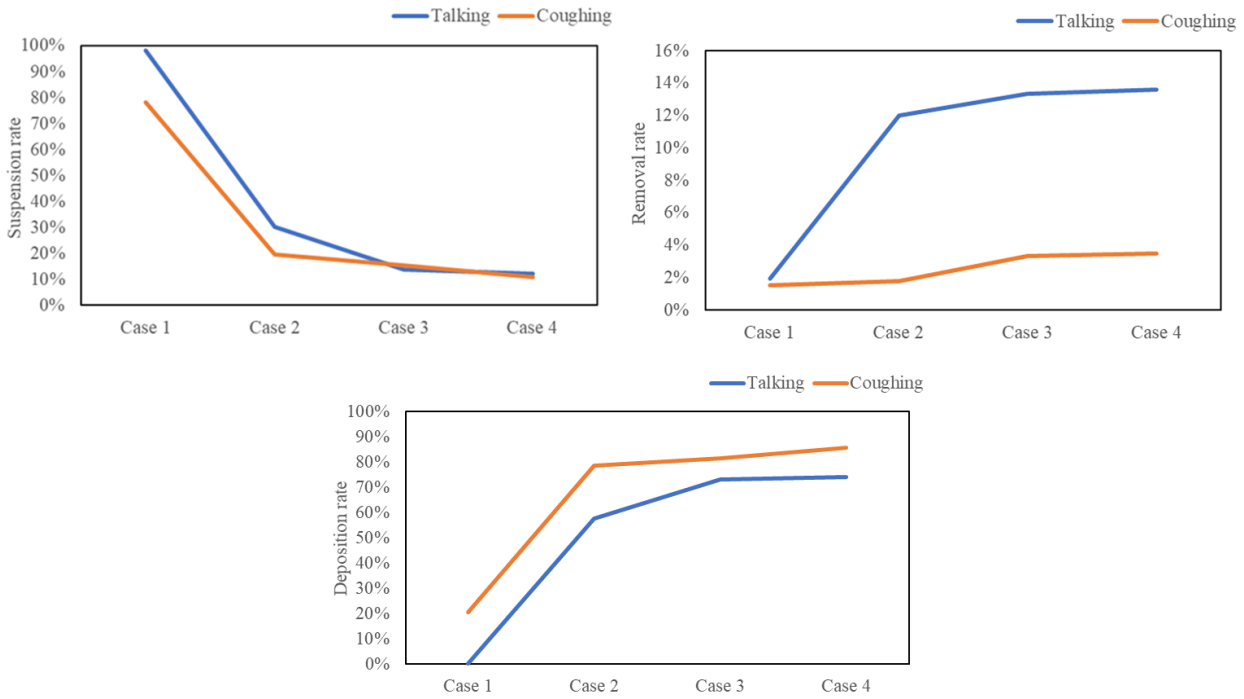

Figure 3-14. Effectiveness of particle removal in different scenarios.

3.3 Conclusions

This Chapter introduced a database of typical green building strategies on energy and IAQ improvement. Energy-efficiency strategies include passive technologies such as advanced envelope solutions, improved building service systems (e.g., HVAC, DHW, lighting, and other appliances), and renewable energy generation technologies. Major IAQ improvement strategies include source control, ventilation, and air cleaning. The performance of some strategies was estimated in Chapter 2. IAQ strategies were further discussed as they are directly related to people's health.

Two emerging IAQ technologies were selected and performed chamber experiments and/or CFD simulations, i.e., in-duct needlepoint bipolar ionization (NPBI) units, and the combined used of displacement ventilation and partitions. The in-duct NPBI system can provide an equivalent SPRE of 3.8-13.6% on particle removal without significant ozone and VOCs removal and generation. However, the technology consumes very minor energy consumption, which can result in considerable effectiveness on particle removal and infection risk mitigation with minimal energy use. The combined application of displacement ventilation and desk partitions can effectively mitigate the potential virus transmission between the infector and the receiver through coughing or talking. But adding additional partitions is less effective on mitigating infection risk through breathing as transmission due to breathing is less likely to occur with displacement ventilation. These experiments and CFD simulations provide abundant performance data for the studied technologies. The technologies and their performance metrics will be compiled into the database for green building technologies and systems.

4. Summary and conclusions

This dissertation developed a modular-based approach for designing buildings with improved performance at early design phase that can provide fast and reliable response. Reduced-order physics-based models were used to calculate thermal, air and mass balance equations and analyze building energy, thermal comfort, pollutant transfer, occupant exposure to pollutants and health impacts, and airborne infection risk. Green building technologies and systems from real and validated practices were collected and standardized as building modules. A Rhino Grasshopper plugin was developed to implement the proposed approach. Coupled simulation between IAQ and energy can be performed and multidiscipline building performance metrics (energy efficiency,

thermal comfort, IAQ, health impacts, and infection risk) were able to be analyzed. Optimization models can be used to find out the optimal design of building modules to achieve certain design goals. The DOE small office prototype, the Syracuse COE case, and the retrofitting case were studied using the developed tool through the proposed approach. Green building modules' performance on energy and IAQ improvement were analyzed. Simulation results suggested that many energy-saving technologies may have impacts on IAQ performance and IAQ strategies can affect energy performance as well. It is essential to comprehensively understand the performance of a certain building module in energy and IAQ performance to achieve the optimal design of a green building. Regarding the office prototype case, the optimal design can save up to 27.8% energy use while mitigating more than 99% infection risk compared to the reference case. Therefore, it reveals that the optimization of green building design using the proposed approach has high potential of energy and IAQ improvement.

A database of building technologies and systems was developed. The performance of IAQ strategies for mitigating infection risk were analyzed. Two emerging technologies were selected and performed chamber experiments and/or CFD simulations to further understand their practical effectiveness, i.e., in-duct needlepoint bipolar ionization (NPBI) units, and the combined used of displacement ventilation and partitions. The in-duct NPBI system can moderately elevate particle removal in the air, with an equivalent SPRE of 3.8-13.6% on particle removal. Ozone generation by the tested in-duct NPBI system can be neglected. No significant VOC removal or generation were observed either. Although its efficiency may sound moderate, its effectiveness on particle removal and infection risk mitigation is high considering its low energy consumption. The combined application of displacement ventilation and desk partitions can effectively mitigate the

potential virus transmission between the infector and the receiver through coughing or talking. However, under the current settings, adding more partitions to form semi-open spaces does not further dramatically increase the ventilation effectiveness. It's likely because of the dominated airflow in the space the thermal plume surrounding the occupants. Particles were less likely to travel across the partitions and reach the receiver's breathing zone from lateral or behind directions. Therefore, for workstations in the office scenario, Partitions that cover the workstation may be sufficient to mitigate the infection transmission between people who are sitting face to face. In the mixing ventilation scenario, because of the cross airflow between cubicles, semi-open space can be more effective in reducing cross-contamination. The abundant performance data from experiments and detailed simulations for the studied technologies will be used by the database of the green building technologies and systems. It will allow these two technologies to be applied through the Green Design Studio approach during the early-design stage for a high-performance building. This can potentially help to address IAQ issues, particularly the airborne transmission of respiratory diseases, while maintaining high energy efficiency.

Future works on this subject include:

a) Expanding the database of building technologies and introducing more quantitative analyses.

b) Expanding the use of data-driven building performance simulation models in the platform to further improve the analysis response speed and accuracy.

c) Applying the proposed tool to more realistic cases and using the measured data to further improve the simulation model with grey-box models.

5. Appendix

For the chamber experiments for the needlepoint bipolar ionizers, CO2 decay tests were performed to determine the infiltration and ventilation rates of the room. CO2 was injected into the room using the same procedure as the decay tests. Exponential regression was conducted to determine the CO2 decay rates. Figure A-1 exhibited a decay rate of $0.01h^{-1}$ in the room, indicating a filtration rate of $0.01h^{-1}$. Figure A-2 showed a decay rate of $1.92h^{-1}$, which revealed a ventilation rate of 55.6 m^3/h. Some datapoints in Figure A-2 were missing due to the CO2 monitor issues.

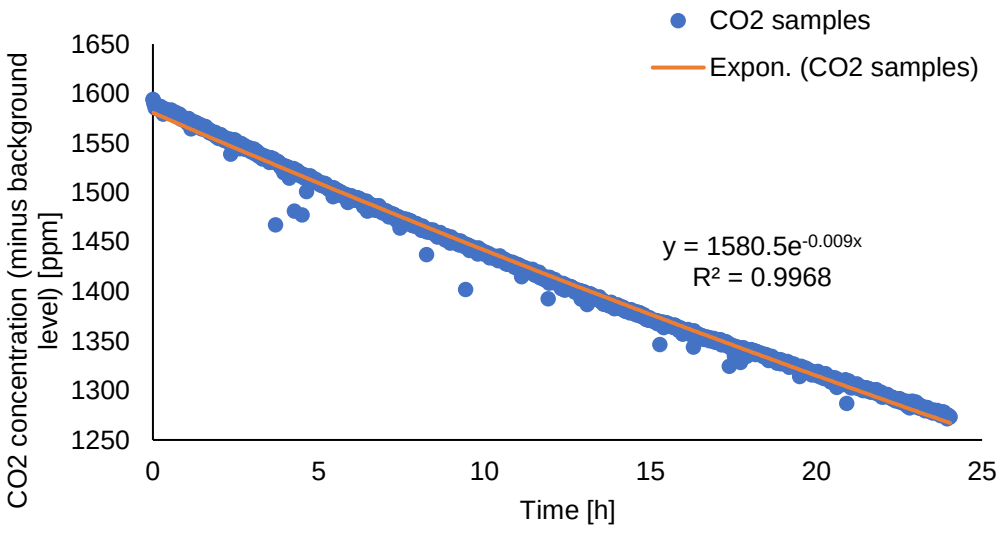

Figure A-1. CO2 decay test for the infiltration rate (Nov 28th, 2021).

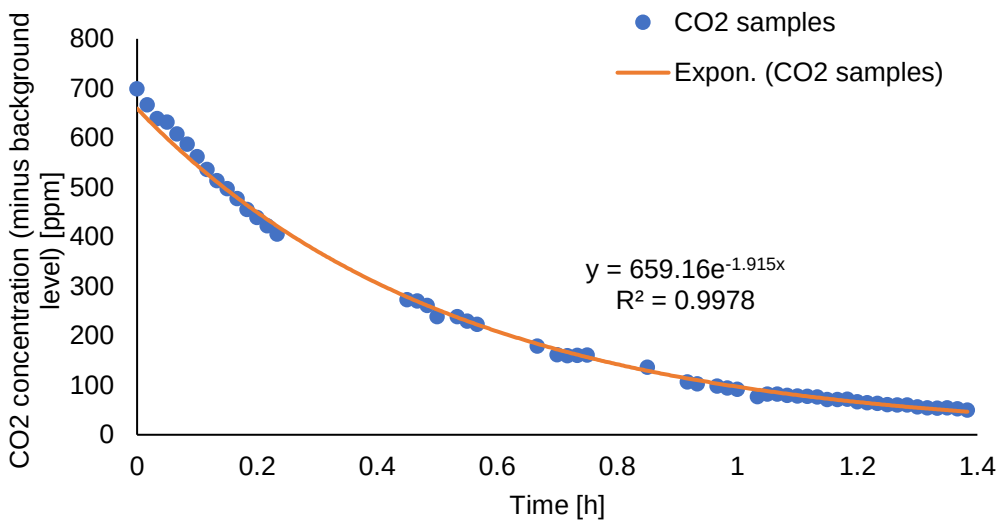

Figure A-2. CO2 decay test for the ventilation rate (Feb 14th, 2022).

The ozone decay test was performed by placing an air cleaner that can generate ozone in the test room on May 19th, 2021. The experiment was conducted with the same room settings (manikin settings, building materials, furniture etc.). The ventilation rate during the test was estimated through a CO2 test, indicating a ventilation rate of 22.9 m^3/h (i.e. 0.8 h^{-1}). The indoor ozone declined rapidly after the ozone generator (air cleaner) was turned off. The exponential regression of ozone concentration indicated an ozone decay rate of 6.3 h^{-1} (Figure A-3). Therefore, the ozone deposition rate on surfaces and by gaseous chemicals was around 5.5 h^{-1}.

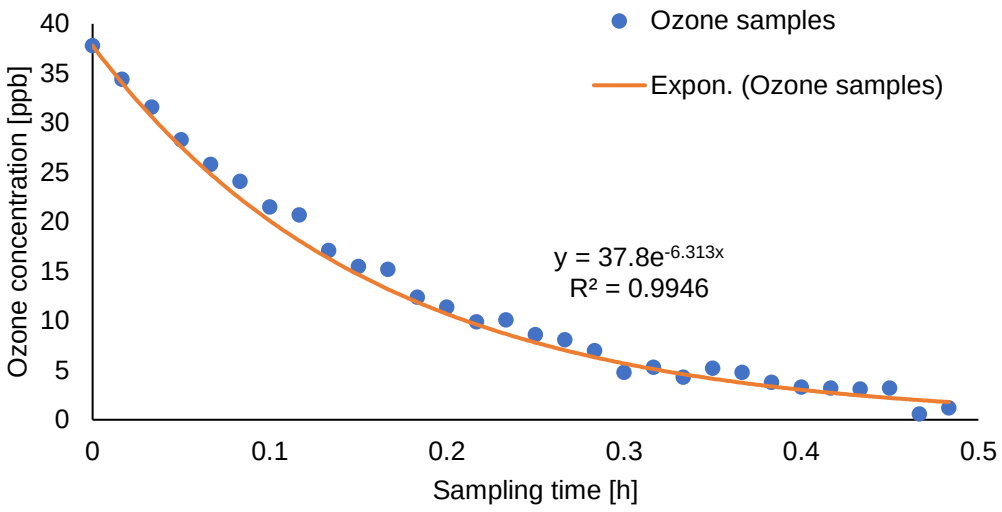

Figure A-3. Ozone decay test (May 19th, 2021).

VOC concentrations were measured during the chamber experiments for the ionizers, Table A-1 shows VOC concentrations at different test conditions before and after using the ionizers. Table A-2 shows VOC concentrations of the background level.

Table A-1. VOC concentrations at different test conditions (n.d. = not detected).

Compounds	Formula	VOC concentration at different test conditions [μg/m^3]							% change after using ionizer	Relative SD of reference bkg VOC levels[c] [%]
		Bkg	Blower on (with filter)			Ionizer A on				
			Set 1[b]	Set 2	Mean	Set 1	Set 2	Mean		
		t = 0h	t = 9h	t = 12h	/	t = 18h	t = 50h	/		
Formaldehyde[a]	CH2O	20.6	18.4	19.8	**19.1**	19.5	22.1	**20.8**	**+8.9%**	4.3%
Acetaldehyde	C2H4O	6.6	5.2	5.0	**5.1**	4.9	4.3	**4.6**	**-9.8%**	12.5%
Acetone	C3H6O	9.1	9.0	9.4	**9.2**	10.1	10.4	**10.3**	**+12.0%**	10.5%
Benzene	C6H6	1.8	1.8	1.7	**1.8**	1.8	1.8	**1.8**	**0.0%**	66.7%
Toluene[a]	C7H8	138.7	141.5	139.9	**140.7**	144.1	150.3	**147.2**	**+4.6%**	4.0%
Cyclotrisiloxane, hexamethyl-	C6H18O3Si3	3.8	3.1	3.2	**3.2**	3.2	3.6	**3.4**	**+6.2%**	25.0%
Hexanal	C6H12O	2.5	2.3	2.3	**2.3**	2.4	2.7	**2.6**	**+13.0%**	6.0%

Ethylbenzene	C8H10	n.d.	n.d.	n.d.	n.d.	1.1	1.2	**1.2**	+	n.d.
Cyclotetrasiloxane, octamethyl-	C8H24O4Si4	2.8	1.6	1.6	**1.6**	1.6	1.8	**1.7**	**+6.2%**	38.8%
Benzaldehyde	C7H6O	2.2	1.8	2.0	**1.9**	2.3	2.2	**2.2**	**+15.8%**	207.7%
2(5H)-Furanone, 3-methyl-	C5H6O2	2.2	1.8	n.d.	**1.8**	n.d.	n.d.	n.d.	-	n.d.
Phenol	C6H6O	1.0	0.8	0.9	**0.9**	0.9	0.9	**0.9**	**0.0%**	12.5%
Cyclopentasiloxane, decamethyl-	C10H30O5Si5	1.4	1.1	1.4	**1.3**	1.4	2.1	**1.7**	**+30.8%**	18.8%
Acetophenone	C8H8O	2.5	1.5	1.0	**1.2**	1.0	1.1	**1.1**	**-8.3%**	32.0%
Nonanal	C9H18O	1.3	1.1	1.1	**1.1**	1.5	1.8	**1.7**	**+54.5%**	47.8%
Naphthalene	C10H8	2.2	2.0	1.7	**1.9**	1.5	1.9	**1.7**	**-10.5%**	n.d.
Propanoic acid, 2-methyl-, 1-(1,1-	C16H30O4	4.1	5.3	5.6	**5.4**	5.7	5.4	**5.6**	**+3.7%**	27.6%

dimethylethyl)-2- methyl-1,3- propanediyl ester										
TVOC	/	202.8	198.3	196.6	**198.5**	203.0	213.6	**208.5**	**+5.0%**	/

[a] Injected compounds.

[b] Two duplicated samples were collected for each sampling set. The average of two duplicated samples was calculated and presented in the table.

[c] From Table A-2.

Table A-2. Reference background concentrations of VOCs concerned in this study.

Compounds	Formula	Reference background concentrations [μg/m^3]						
		Test R1	Test R2	Test R3	Test R4	Mean	SD	Relative SD [%]
Formaldehyde[a]	CH2O	/	/	/	/	57.8	2.5	4.3
Acetaldehyde	C2H4O	4.8	6.4	5.9	5.2	5.6	0.7	12.5
Acetone	C3H6O	4.8	6.0	6.3	5.7	5.7	0.6	10.5
Benzene	C6H6	2.0	n.d.	1.4	1.2	1.2	0.8	66.7
Toluene[a]	C7H8	/	/	/	/	107.3	4.3	4.0
Cyclotrisiloxane, hexamethyl-	C6H18O3Si3	3.2	6.0	6.1	5.4	5.2	1.3	25.0
Hexanal	C6H12O	5.4	4.7	5.2	4.7	5.0	0.3	6.0
Ethylbenzene	C8H10	n.d.	n.d.	n.d.	n.d.	n.d.	n.d.	n.d.
Cyclotetrasiloxane, octamethyl-	C8H24O4Si4	2.2	6.3	6.0	5.0	4.9	1.9	38.8

Benzaldehyde	C7H6O	0.53	n.d.	n.d.	n.d.	0.13	0.27	207.7
2(5H)-Furanone, 3-methyl-	C5H6O2	n.d.	n.d.	n.d.	n.d.	n.d.	n.d.	n.d.
Phenol	C6H6O	1.9	1.6	1.5	1.4	1.6	0.2	12.5
Cyclopentasiloxane, decamethyl-	C10H30O5Si5	1.3	1.9	1.8	1.4	1.6	0.3	18.8
Acetophenone	C8H8O	3.5	1.8	2.4	2.1	2.5	0.8	32.0
Nonanal	C9H18O	11.5	3.9	5.6	6.8	6.9	3.3	47.8
Naphthalene	C10H8	n.d.	n.d.	n.d.	n.d.	n.d.	n.d.	n.d.
Propanoic acid, 2-methyl-, 1-(1,1-dimethylethyl)-2-methyl-1,3-propanediyl ester	C16H30O4	3.6	2.4	2.0	3.5	2.9	0.8	27.6

[a] Injected compounds. The reference background concentrations were sampled through real-time PTR-MS sampling in two injection tests with same settings as Test 10.

6. Reference

Abadie, M., and P. Blondeau. 2011. Pandora database: A compilation of indoor air pollutant emissions. *HVAC and R Research*, *17*(4):602–613.

Abadie, M. O., and P. Wargocki. 2017. *Annex-68 subtask 1 final report: International Energy Agency Indoor Air Quality Design and Control in Low-energy Residential Buildings- Annex 68 | Subtask 1: Defining the metrics | In the search of indices to evaluate the Indoor Air Quality of low-energy* .

Abadie, M., P. Wargocki, C. Rode, and J. Zhang. 2019. Proposed metrics for IAQ in low-energy residential buildings.

ACEEE. 2022. ACEEE | Policy Database.

Ahmadzadeh, M., E. Farokhi, and M. Shams. 2021. Investigating the effect of air conditioning on the distribution and transmission of COVID-19 virus particles. *Journal of Cleaner Production*, *316*:128147.

Al-Janabi, A., and M. Kavgic. 2019. Application and sensitivity analysis of the phase change material hysteresis method in EnergyPlus: A case study. *Applied Thermal Engineering*, *162*:114222.

Alavy, M., and J. A. Siegel. 2020. In-situ effectiveness of residential HVAC filters. *Indoor Air*, *30*(1):156–166.

Allen, J. G., J. Cedeno-Laurent, and S. Miller. 2020. Harvard-CU Boulder Portable Air Cleaner Calculator for Schools.v1.2.

Amasyali, K., and N. El-Gohary. 2021. Machine learning for occupant-behavior-sensitive cooling

energy consumption prediction in office buildings. *Renewable and Sustainable Energy Reviews*, *142*:110714.

Amasyali, K., and N. M. El-Gohary. 2018. A review of data-driven building energy consumption prediction studies. *Renewable and Sustainable Energy Reviews*, *81*:1192–1205.

ANSI/AHAM. 2020. ANSI/AHAM AC-1-2020 (Portable Electric Room Air Cleaners). *ANSI/AHAM Standard*.

ANSI/BIFMA. 2007. *ANSI/BIFMA M7.1-2007 Standard Test Method For Determining VOC Emissions From Office Furniture Systems, Components And Seating*.

ANSYS. 2021. Ansys Fluent | Fluid Simulation Software.

ASHRAE. 2014. ASHRAE Guideline 14-2014 Measurement of Energy, Demand, and Water Savings. *ASHRAE Guideline 14-2014*, *4*:1–150.

ASHRAE. 2015. ASHRAE 145.1-2015. *ASHRAE Standard*.

ASHRAE. 2017a. ASHRAE Standard 140-2017 Standard method of test for the evaluation of building energy analysis computer programs.

ASHRAE. 2017b. ASHRAE Standard 55-2017, Thermal Environmental Conditions for Human Occupancy.

ASHRAE. 2017c. Standard 189.1-2017 Standard for the Design of High-Performance Green Buildings.

ASHRAE. 2018. ASHRAE Standard 90.2 - Energy-efficient design of low-rise residential buildings.

ASHRAE. 2019a. ASHRAE Standard 62.1-2019, Ventilation for Acceptable Indoor Air Quality.

ASHRAE. 2019b. ASHRAE Standard 62.2-2019, Ventilation and Acceptable Indoor Air Quality in Low-Rise Residential Buildings.

ASHRAE. 2019c. ASHRAE Standard 90.1-2019.

ASHRAE. 2020a. ASHRAE Standard 55-2020 Thermal environmental conditions for human occupancy.

ASHRAE. 2020b. Filtration / Disinfection.

ASHRAE. 2022. *ASHRAE Global Occupant Behavior Database*.

Assaad, D. Al, C. Habchi, K. Ghali, and N. Ghaddar. 2018. Effectiveness of intermittent personalized ventilation in protecting occupant from indoor particles. *Building and Environment*, *128*:22–32.

ATSDR. 2020. Sulfur Dioxide | Medical Management Guidelines | Toxic Substance Portal | ATSDR.

ATSDR. 2022. Minimal Risk Levels for Hazardous Substances (MRLs).

Attia, S., L. Beltrán, A. De Herde, and J. Hensen. 2009. "ARCHITECT FRIENDLY": A COMPARISON OF TEN DIFFERENT BUILDING PERFORMANCE SIMULATION TOOLS. In *Proceedings of 11th International Building Performance Simulation Association Conference and Exhibition*.

Attia, S., E. Gratia, A. De Herde, and J. L. M. Hensen. 2012. Simulation-based decision support tool for early stages of zero-energy building design. *Energy and Buildings*, *49*:2–15.

Azimi, P., D. Zhao, and B. Stephens. 2014. Estimates of HVAC filtration efficiency for fine and ultrafine particles of outdoor origin. *Atmospheric Environment*, *98*:337–346.

Bazant, M. Z. 2021. COVID-19 Indoor Safety Guideline.

Bazant, M. Z., and J. W. M. Bush. 2021. A guideline to limit indoor airborne transmission of COVID-19. *Proceedings of the National Academy of Sciences*, *118*(17):e2018995118.

Bell, M. L., A. McDermott, S. L. Zeger, J. M. Samet, and F. Dominici. 2004. Ozone and Short-term Mortality in 95 US Urban Communities, 1987-2000. *JAMA*, *292*(19):2372.

Berry, G., A. Parsons, M. Morgan, J. Rickert, and H. Cho. 2022. A review of methods to reduce the probability of the airborne spread of COVID-19 in ventilation systems and enclosed spaces. *Environmental Research*, *203*:111765.

BESTD. 2022. BEST Directory: Building Energy Software Tools.

Bogenstätter, U. 2010. Prediction and optimization of life-cycle costs in early design. *Https://Doi.Org/10.1080/096132100418528*, *28*(5–6):376–386.

Boodi, A., K. Beddiar, Y. Amirat, and M. Benbouzid. 2019. Model Predictive Control-based Thermal Comfort and Energy Optimization. In *IECON 2019 - 45th Annual Conference of the IEEE Industrial Electronics Society* (Vol. 2019-Octob, pp. 5801–5806). IEEE.

Braun, J. E., and N. Chaturvedi. 2002. An inverse gray-box model for transient building load prediction. *HVAC and R Research*, *8*(1):73–99.

BRE. 2018. BREEAM New Construction 2018.

BRE. 2019. BREEAM Projects.

Brooks, J. T., D. H. Beezhold, J. D. Noti, J. P. Coyle, R. C. Derk, F. M. Blachere, and W. G. Lindsley. 2021. Maximizing Fit for Cloth and Medical Procedure Masks to Improve Performance and Reduce SARS-CoV-2 Transmission and Exposure, 2021. *MMWR. Morbidity and Mortality Weekly Report*, *70*(7):254–257.

Bueno, A. M., A. A. de Paula Xavier, and E. E. Broday. 2021. Evaluating the Connection between Thermal Comfort and Productivity in Buildings: A Systematic Literature Review. *Buildings 2021, Vol. 11, Page 244*, *11*(6):244.

Buonanno, G., L. Morawska, and L. Stabile. 2020. Quantitative assessment of the risk of airborne transmission of SARS-CoV-2 infection: Prospective and retrospective applications. *Environment International*, *145*:106112.

Buonanno, G., L. Stabile, and L. Morawska. 2020. Estimation of airborne viral emission: Quanta emission rate of SARS-CoV-2 for infection risk assessment. *Environment International*, *141*:105794.

California Energy Commission. 2022. Building Energy Benchmarking Program | California Energy Commission.

Campagnolo, D., D. E. Saraga, A. Cattaneo, A. Spinazzè, C. Mandin, R. Mabilia, E. Perreca, I. Sakellaris, N. Canha, V. G. Mihucz, T. Szigeti, G. Ventura, J. Madureira, E. de Oliveira Fernandes, Y. de Kluizenaar, E. Cornelissen, O. Hänninen, P. Carrer, P. Wolkoff, D. M. Cavallo, and J. G. Bartzis. 2017. VOCs and aldehydes source identification in European office buildings - The OFFICAIR study. *Building and Environment*, *115*:18–24.

Cao, X., X. Dai, and J. Liu. 2016. Building energy-consumption status worldwide and the state-of-the-art technologies for zero-energy buildings during the past decade. *Energy and*

Buildings, *128*:198–213.

Cappucci, M., and M. Kornfield. 2022. U.S. heat wave: Over 100 million people under alerts in 28 states - The Washington Post.

Carrier Global. 2021. Needlepoint Bipolar Ionization.

CDPH. 2020. *THE ROLE OF BUILDING VENTILATION AND FILTRATION IN REDUCING RISK OF AIRBORNE VIRAL TRANSMISSION IN SCHOOLS, ILLUSTRATED WITH SARS-COV-2*.

CDPHE. 2020. Outbreak data | Colorado COVID-19 Updates.

Chegari, B., M. Tabaa, E. Simeu, F. Moutaouakkil, and H. Medromi. 2021. Multi-objective optimization of building energy performance and indoor thermal comfort by combining artificial neural networks and metaheuristic algorithms. *Energy and Buildings*, *239*:110839.

Chen, L., G. Ban, E. Long, G. Kalonji, Z. Cheng, L. Zhang, and S. Guo. 2021. Estimation of the SARS-CoV-2 transmission probability in confined traffic space and evaluation of the mitigation strategies. *Environmental Science and Pollution Research*, 1–13.

Chen, S. C., and C. M. Liao. 2008. Modelling control measures to reduce the impact of pandemic influenza among schoolchildren. *Epidemiology and Infection*, *136*(8):1035–1045.

Chen, W., J. S. Zhang, and Z. Zhang. 2005. Performance of air cleaners for removing multiple volatile organic compounds in indoor air. *ASHRAE Transactions*, *111 PART 1*:1101–1114.

Chen, X., Q. Wang, and J. Srebric. 2015. A data-driven state-space model of indoor thermal sensation using occupant feedback for low-energy buildings. *Energy and Buildings*, *91*:187–198.

Collins, K. J. 1986. LOW INDOOR TEMPERATURES AND MORBIDITY IN THE ELDERLY. *Age and Ageing*, *15*(4):212–220.

Corsi, R., K. Van Den Wymelenberg, and H. Parhizkar. 2020. Safeairspaces.

Craig, S., D. Harrison, A. Cripps, and D. Knott. 2008. BioTRIZ Suggests Radiative Cooling of Buildings Can Be Done Passively by Changing the Structure of Roof Insulation to Let Longwave Infrared Pass. *Journal of Bionic Engineering*, *5*(1):55–66.

Crowe, J. 2015. *2015 IECC-Whole Building Air Leakage Compliance*.

Dabisch, P., M. Schuit, A. Herzog, K. Beck, S. Wood, M. Krause, D. Miller, W. Weaver, D. Freeburger, I. Hooper, B. Green, G. Williams, B. Holland, J. Bohannon, V. Wahl, J. Yolitz, M. Hevey, and S. Ratnesar-Shumate. 2020. The influence of temperature, humidity, and simulated sunlight on the infectivity of SARS-CoV-2 in aerosols. *Aerosol Science and Technology*, 1–12.

Dai, H., and B. Zhao. 2020. Association of the infection probability of COVID-19 with ventilation rates in confined spaces. *Building Simulation*.

Davies, A., K.-A. Thompson, K. Giri, G. Kafatos, J. Walker, and A. Bennett. 2013. Testing the Efficacy of Homemade Masks: Would They Protect in an Influenza Pandemic?, *7*:413–418.

Davies, N., S. Abbott, R. Barnard, C. Jarvis, A. Kucharski, J. Munday, C. Pearson, T. Russell, D. Tully, A. Washburne, T. Wenseleers, A. Gimma, W. Waites, K. Wong, K. van Zandvoort, J. Silverman, K. Diaz-Ordaz, R. Keogh, R. Eggo, S. Funk, M. Jit, K. Atkins, and W. J. Edmunds. 2021. Estimated transmissibility and impact of SARS-CoV-2 lineage B.1.1.7 in England. *Science*.

Day, D. B., J. Xiang, J. Mo, F. Li, M. Chung, J. Gong, C. J. Weschler, P. A. Ohman-Strickland, J. Sundell, W. Weng, Y. Zhang, and J. (Jim) Zhang. 2017. Association of Ozone Exposure With Cardiorespiratory Pathophysiologic Mechanisms in Healthy Adults. *JAMA Internal Medicine*, *177*(9):1344.

Dbouk, T., and D. Drikakis. 2021. On airborne virus transmission in elevators and confined spaces. *Physics of Fluids*, *33*(1).

deCastro, B. R., S. N. Sax, S. N. Chillrud, P. L. Kinney, and J. D. Spengler. 2007. Modeling time-location patterns of inner-city high school students in New York and Los Angeles using a longitudinal approach with generalized estimating equations. *Journal of Exposure Science & Environmental Epidemiology*, *17*(3):233–247.

Deng, X., M. A. Garcia-Knight, M. M. Khalid, V. Servellita, C. Wang, M. Kate Morris, A. Sotomayor-González, K. R. Reyes, A. S. Gliwa, N. P. Reddy, C. Sanchez, S. Martin, S. Federman, J. Cheng, J. Balcerek, J. Taylor, A. Streithorst, S. Miller, G. Renuka Kumar, B. Sreekumar, P.-Y. Chen, U. Schulze-Gahmen, T. Y. Taha, J. Hayashi, S. McMahon, P. V Lidsky, Y. Xiao, P. Hemarajata, N. M. Green, A. Espinosa, C. Kath, M. Haw, J. Bell, C. Hanson, D. A. Wadford, C. Anaya, D. Ferguson, P. A. Frankino, H. Shivram, S. K. Wyman, R. Andino, and C. Y. Chiu. 2021. Transmission, infectivity, and antibody neutralization of an emerging SARS-CoV-1 2 variant in California carrying a L452R spike protein mutation 2. *MedRxiv*, 2021.03.07.21252647.

Department of Finance of New York City. 2022. NYC Energy Benchmarking Report.

Deru, M., K. Field, D. Studer, K. Benne, B. Griffith, P. Torcellini, B. Liu, M. Halverson, D. Winiarski, M. Rosenberg, M. Yazdanian, J. Huang, and D. Crawley. 2011. *U.S. Department*

of Energy Commercial Reference Building Models of the National Building Stock.

DesignBuilder Software Ltd. 2017a. Site Details - Ground.

DesignBuilder Software Ltd. 2017b. Solar Radiation Distribution.

Diakaki, C., E. Grigoroudis, and D. Kolokotsa. 2008. Towards a multi-objective optimization approach for improving energy efficiency in buildings. *Energy and Buildings*, *40*(9):1747–1754.

DLUHC. 2022. Energy Performance of Buildings Data England and Wales.

Doan, D. T., A. Ghaffarianhoseini, N. Naismith, T. Zhang, A. Ghaffarianhoseini, and J. Tookey. 2017, October 1. A critical comparison of green building rating systems. *Building and Environment*. Elsevier Ltd.

DOE. 2017. EnergyPlus | EnergyPlus.

Dols, W. S., C. W. Milando, L. Ng, S. J. Emmerich, and J. Teo. 2021. On the Benefits of Whole-building IAQ, Ventilation, Infiltration, and Energy Analysis Using Co-simulation between CONTAM and EnergyPlus. *Journal of Physics: Conference Series*, *2069*(1):012183.

Dols, W. S., B. J. Polidoro, D. Poppendieck, and S. J. Emmerich. 2020. *A Tool to Model the Fate and Transport of Indoor Microbiological Aerosols (FaTIMA)*.

Dong, B., Z. Li, S. M. M. Rahman, and R. Vega. 2016. A hybrid model approach for forecasting future residential electricity consumption. *Energy and Buildings*, *117*:341–351.

Dong, B., Y. Liu, W. Mu, Z. Jiang, P. Pandey, T. Hong, B. Olesen, T. Lawrence, Z. O'Neil, C. Andrews, E. Azar, K. Bandurski, R. Bardhan, M. Bavaresco, C. Berger, J. Burry, S. Carlucci, K. Chvatal, M. De Simone, S. Erba, N. Gao, L. T. Graham, C. Grassi, R. Jain, S. Kumar, M.

Kjærgaard, S. Korsavi, J. Langevin, Z. Li, A. Lipczynska, A. Mahdavi, J. Malik, M. Marschall, Z. Nagy, L. Neves, W. O'Brien, S. Pan, J. Y. Park, I. Pigliautile, C. Piselli, A. L. Pisello, H. N. Rafsanjani, R. F. Rupp, F. Salim, S. Schiavon, J. Schwee, A. Sonta, M. Touchie, A. Wagner, S. Walsh, Z. Wang, D. M. Webber, D. Yan, P. Zangheri, J. Zhang, X. Zhou, and X. Zhou. 2022. A Global Building Occupant Behavior Database. *Scientific Data 2022 9:1*, *9*(1):1–15.

Dong, W., S. Liu, M. Chu, B. Zhao, D. Yang, C. Chen, M. R. Miller, M. Loh, J. Xu, R. Chi, X. Yang, X. Guo, and F. Deng. 2019. Different cardiorespiratory effects of indoor air pollution intervention with ionization air purifier: Findings from a randomized, double-blind crossover study among school children in Beijing. *Environmental Pollution*, *254*:113054.

Dubert, M., B. Visseaux, V. Isernia, L. Bouadma, L. Deconinck, J. Patrier, P. H. Wicky, D. Le Pluart, L. Kramer, C. Rioux, Q. Le Hingrat, N. Houhou-Fidouh, Y. Yazdanpanah, J. Ghosn, and F. X. Lescure. 2020. Case report study of the first five COVID-19 patients treated with remdesivir in France. *International Journal of Infectious Diseases*, *98*:290–293.

Dygert, R. K., and T. Q. Dang. 2012. Experimental validation of local exhaust strategies for improved IAQ in aircraft cabins. *Building and Environment*, *47*(1):76–88.

Energy Saving Trust. 2022. Guide to Energy Performance Certificates - Energy Saving Trust.

EnergyPlus. 2022a. Climate Calculations: Engineering Reference — EnergyPlus 22.1.

EnergyPlus. 2022b. Outside Surface Heat Balance: Engineering Reference.

EnergyPlus. 2022c. Performance Curves: Engineering Reference — EnergyPlus 22.2.

EnergyPlus. 2022d. Shading Module: Engineering Reference — EnergyPlus 8.0.

EnergyPlus. 2022e. Window Calculation Module: Engineering Reference — EnergyPlus 8.9.

EnergyPlus. 2022f. Zone Internal Gains: Engineering Reference — EnergyPlus 22.2.

ESRU. 2018. ESP-r.

European Parliament. 2021. What is carbon neutrality and how can it be achieved by 2050? | News | European Parliament.

Fajnzylber, J., J. Regan, K. Coxen, H. Corry, C. Wong, A. Rosenthal, D. Worrall, F. Giguel, A. Piechocka-Trocha, C. Atyeo, S. Fischinger, A. Chan, K. T. Flaherty, K. Hall, M. Dougan, E. T. Ryan, E. Gillespie, R. Chishti, Y. Li, N. Jilg, D. Hanidziar, R. M. Baron, L. Baden, A. M. Tsibris, K. A. Armstrong, D. R. Kuritzkes, G. Alter, B. D. Walker, X. Yu, J. Z. Li, B. A. (Betty. Abayneh, P. Allen, D. Antille, A. Balazs, J. Bals, M. Barbash, Y. Bartsch, J. Boucau, S. Boyce, J. Braley, K. Branch, K. Broderick, J. Carney, J. Chevalier, M. C. Choudhary, N. Chowdhury, T. Cordwell, G. Daley, S. Davidson, M. Desjardins, L. Donahue, D. Drew, K. Einkauf, S. Elizabeth, A. Elliman, B. Etemad, J. Fallon, L. Fedirko, K. Finn, J. Flannery, P. Forde, P. Garcia-Broncano, E. Gettings, D. Golan, K. Goodman, A. Griffin, S. Grimmel, K. Grinke, C. A. Hartana, M. Healy, H. Heller, D. Henault, G. Holland, C. Jiang, H. Jordan, P. Kaplonek, E. W. Karlson, M. Karpell, C. Kayitesi, E. C. Lam, V. LaValle, K. Lefteri, X. Lian, M. Lichterfeld, D. Lingwood, H. Liu, J. Liu, K. Lopez, Y. Lu, S. Luthern, N. L. Ly, M. MacGowan, K. Magispoc, J. Marchewka, B. Martino, R. McNamara, A. Michell, I. Millstrom, N. Miranda, C. Nambu, S. Nelson, M. Noone, L. Novack, C. O'Callaghan, C. Ommerborn, M. Osborn, L. C. Pacheco, N. Phan, S. Pillai, F. A. Porto, Y. Rassadkina, A. Reissis, F. Ruzicka, K. Seiger, K. Selleck, L. Sessa, A. Sharpe, C. Sharr, S. Shin, N. Singh, S. Slaughenhaupt, K. S. Sheppard, W. Sun, X. Sun, E. (Lizzie) Suschana, O. Talabi, H. Ticheli,

S. T. Weiss, V. Wilson, and A. Zhu. 2020. SARS-CoV-2 viral load is associated with increased disease severity and mortality. *Nature Communications*, *11*(1):1–9.

Fazli, T., and B. Stephens. 2018. Development of a nationally representative set of combined building energy and indoor air quality models for U.S. residences. *Building and Environment*, *136*:198–212.

Fears, A., W. Klimstra, P. Duprex, A. Hartman, S. Weaver, K. Plante, D. Mirchandani, J. Plante, P. Aguilar, D. Fernandez, A. Nalca, A. Totura, D. Dyer, B. Kearney, M. Lackemeyer, J. K. Bohannon, R. Johnson, R. Garry, D. Reed, and C. Roy. 2020. Comparative dynamic aerosol efficiencies of three emergent coronaviruses and the unusual persistence of SARS-CoV-2 in aerosol suspensions. *MedRxiv : The Preprint Server for Health Sciences*, 2020.04.13.20063784.

Feng, W., J. Grunewald, A. Nicolai, C. Zhang, and J. S. Zhang. 2012. CHAMPS-MultizoneA combined heat, air, moisture and pollutant simulation environment for whole-building performance analysis. In *HVAC and R Research* (Vol. 18, pp. 233–251).

Fix The Mask. 2020. DIY Mask Brace from Rubber Sheet Downloadable Template – Fix The Mask.

FMI-standard. 2022. Functional Mock-up Interface.

Földváry Ličina, V., T. Cheung, H. Zhang, R. de Dear, T. Parkinson, E. Arens, C. Chun, S. Schiavon, M. Luo, G. Brager, P. Li, S. Kaam, M. A. Adebamowo, M. M. Andamon, F. Babich, C. Bouden, H. Bukovianska, C. Candido, B. Cao, S. Carlucci, D. K. W. Cheong, J. H. Choi, M. Cook, P. Cropper, M. Deuble, S. Heidari, M. Indraganti, Q. Jin, H. Kim, J. Kim, K. Konis, M. K. Singh, A. Kwok, R. Lamberts, D. Loveday, J. Langevin, S. Manu, C. Moosmann, F.

Nicol, R. Ooka, N. A. Oseland, L. Pagliano, D. Petráš, R. Rawal, R. Romero, H. B. Rijal, C. Sekhar, M. Schweiker, F. Tartarini, S. ichi Tanabe, K. W. Tham, D. Teli, J. Toftum, L. Toledo, K. Tsuzuki, R. De Vecchi, A. Wagner, Z. Wang, H. Wallbaum, L. Webb, L. Yang, Y. Zhu, Y. Zhai, Y. Zhang, and X. Zhou. 2018. Development of the ASHRAE Global Thermal Comfort Database II. *Building and Environment*, *142*:502–512.

Fontenot, H., K. S. Ayyagari, B. Dong, N. Gatsis, and A. Taha. 2021. Buildings-to-distribution-network integration for coordinated voltage regulation and building energy management via distributed resource flexibility. *Sustainable Cities and Society*, *69*:102832.

Foucquier, A., S. Robert, F. Suard, L. Stéphan, and A. Jay. 2013. State of the art in building modelling and energy performances prediction: A review. *Renewable and Sustainable Energy Reviews*, *23*:272–288.

Fowler, K. M., E. M. Rauch, J. W. Henderson, and A. R. Kora. 2010. *Re-Assessing Green Building Performance: A Post Occupancy Evaluation of 22 GSA Buildings*.

Fry, E., and N. Rapp. 2021. The COVID-19 Delta variant is now dominant in the U.S. See the states where it's most prevalent | Fortune.

Fumo, N. 2014. A review on the basics of building energy estimation. *Renewable and Sustainable Energy Reviews*, *31*:53–60.

Gammaitoni, L., and M. C. Nucci. 1997. Using a Mathematical Model to Evaluate the Efficacy of TB Control Measures. *Emerging Infectious Diseases*, *3*(3):335–342.

Gan, W. Q., M. Koehoorn, H. W. Davies, P. A. Demers, L. Tamburic, and M. Brauer. 2011. Long-term exposure to traffic-related air pollution and the risk of coronary heart disease

hospitalization and mortality. *Environmental Health Perspectives*.

Gao, N. P., J. L. Niu, M. Perino, and P. Heiselberg. 2008. The airborne transmission of infection between flats in high-rise residential buildings: Tracer gas simulation. *Building and Environment*, *43*(11):1805–1817.

Gao, T., X. C. Wang, R. Chen, H. Hao Ngo, and W. Guo. 2014. Disability adjusted life year (DALY): A useful tool for quantitative assessment of environmental pollution.

Ghaderian, M., and F. Veysi. 2021. Multi-objective optimization of energy efficiency and thermal comfort in an existing office building using NSGA-II with fitness approximation: A case study. *Journal of Building Engineering*, *41*:102440.

Grunewald, J., and A. Nicolai. 2005. *User Manual - CHAMPS-BES Program for Coupled Heat, Air, Moisture and Pollutant Simulation in Building Envelope Systems*.

Guo, C., Z. Gao, and J. Shen. 2019. Emission rates of indoor ozone emission devices: A literature review. *Building and Environment*, *158*:302–318.

Guo, W., S. Liang, W. Li, B. Xiong, and H. Wen. 2022. Combining EnergyPlus and CFD to predict and optimize the passive ventilation mode of medium-sized gymnasium in subtropical regions. *Building and Environment*, *207*:108420.

Guo, Y., H. Qian, Z. Sun, J. Cao, F. Liu, X. Luo, R. Ling, L. B. Weschler, J. Mo, and Y. Zhang. 2021. Assessing and controlling infection risk with Wells-Riley model and spatial flow impact factor (SFIF). *Sustainable Cities and Society*, *67*:102719.

Haghighat, F., Y. Huo, J. Zhang, and C. Shaw. 1996. The Influence of Office Furniture, Workstation Layouts, Diffuser Types and Location on Indoor Air Quality and Thermal

Comfort Conditions at Workstations. *Indoor Air*, *6*(3):188–203.

Han, M. S., M.-W. Seong, E. Y. Heo, J. H. Park, N. Kim, S. Shin, S. I. Cho, S. S. Park, and E. H. Choi. 2020. Sequential Analysis of Viral Load in a Neonate and Her Mother Infected With Severe Acute Respiratory Syndrome Coronavirus 2. *Clinical Infectious Diseases*, *71*(16):2236–2239.

Hao, Z. 2019. *Model-Based Estimation on Building Envelope Infiltration*. The University of Alabama.

Harrichandra, A., A. M. Ierardi, and B. Pavilonis. 2020. An estimation of airborne SARS-CoV-2 infection transmission risk in New York City nail salons. *Toxicology and Industrial Health*, 074823372096465.

He, C., W. Chen, K. Han, B. Guo, J. Pei, and J. S. Zhang. 2014. Evaluation of filter media performance: Correlation between high and low challenge concentration tests for toluene and formaldehyde (ASHRAE RP-1557). *Http://Dx.Doi.Org/10.1080/10789669.2014.907096*, *20*(5):508–521.

Health Canada. 2018. Indoor Air Reference Levels.

Health Canada. 2022. Indoor air quality resources for professionals.

Hester Allen, A., A. Vusirikala, J. Flannagan, K. A. Twohig, A. Zaidi, R. Harris, A. Charlett, G. Dabrera, M. Kall, and M. Author affiliations. 2021. Increased household transmission of COVID-19 cases associated with SARS-CoV-2 Variant of Concern B.1.617.2: a national case-control study.

Hirsch, J. 2016. DOE2.com Home Page.

Hoffman, A. 2022. As UK Temperatures Soar, UN Warns of Worsening Heat Waves to at Least 2060 - Bloomberg.

Hu, M., B. Zhao, Suhendri, X. Ao, J. Cao, Q. Wang, S. Riffat, Y. Su, and G. Pei. 2022. Applications of radiative sky cooling in solar energy systems: Progress, challenges, and prospects. *Renewable and Sustainable Energy Reviews*, *160*:112304.

Huijbregts, M. A. J., L. J. A. Rombouts, A. M. Ragas, and D. van de Meent. 2005. Human-toxicological effect and damage factors of carcinogenic and noncarcinogenic chemicals for life cycle impact assessment. *Integrated Environmental Assessment and Management*, *1*(3):181–244.

Hygh, J. S., J. F. DeCarolis, D. B. Hill, and S. Ranji Ranjithan. 2012. Multivariate regression as an energy assessment tool in early building design. *Building and Environment*, *57*:165–175.

Hyun, J., S. G. Lee, and J. Hwang. 2017. Application of corona discharge-generated air ions for filtration of aerosolized virus and inactivation of filtered virus. *Journal of Aerosol Science*, *107*:31–40.

ICC. 2009. International Energy Conservation Code.

ICC, and ASHRAE. 2021. *2021 International Green Construction Code (IgCC)*.

IESNA. 2011. *The Lighting Handbook 10th Edition - Reference and Application*. New York: Illuminating Engineering Society.

Imai, N., A. Cori, I. Dorigatti, M. Baguelin, C. A. Donnelly, S. Riley, and N. M. Ferguson. 2020. *Transmissibility of 2019-nCoV*. London, UK.

International Code Council (ICC). 2021. *CHAPTER 4 [CE] COMMERCIAL ENERGY*

EFFICIENCY, 2021 International Energy Conservation Code (IECC) | ICC Digital Codes.

IPCC. 2018. *Summary for Policymakers of IPCC Special Report on Global Warming of 1.5°C approved by governments — IPCC*.

ISO. 2005. ISO 7730: Ergonomics of the thermal environment Analytical determination and interpretation of thermal comfort using calculation of the PMV and PPD indices and local thermal comfort criteria.

IWBI. 2018. WELL Building Standard.

IWBI. 2019. WELL Building Porjects.

Jiang, J., D. Wang, Y. Liu, Y. Xu, and J. Liu. 2018. A study on pupils' learning performance and thermal comfort of primary schools in China. *Building and Environment*, *134*:102–113.

Jimenez, J. L., and Z. Peng. 2020. 2020_COVID-19_Aerosol_Transmission_Estimator - Google Sheets.

JJH. 2018. eQUEST.

Jones, E. R., J. G. Cedeño Laurent, A. S. Young, P. MacNaughton, B. A. Coull, J. D. Spengler, and J. G. Allen. 2021. The effects of ventilation and filtration on indoor PM2.5 in office buildings in four countries. *Building and Environment*, *200*:107975.

Justo Alonso, M., W. S. Dols, and H. M. Mathisen. 2022. Using Co-simulation between EnergyPlus and CONTAM to evaluate recirculation-based, demand-controlled ventilation strategies in an office building. *Building and Environment*, *211*:108737.

Kanaan, M., and A. Abou Moughlbay. 2018. *Comparative CFD Investigation of Upper Room UVGI Efficacy with Three Different Ventilation Systems*. *International Journal of Applied*

Engineering Research (Vol. 13).

Kasibhatla, P., J. Jimenez, J. Fay, E. Albright, and W. Pan. 2020. COVID exposure modeler.

Katramiz, E., N. Ghaddar, K. Ghali, D. Al-Assaad, and S. Ghani. 2021. Effect of individually controlled personalized ventilation on cross-contamination due to respiratory activities. *Building and Environment*, *194*:107719.

Kaushik, A., M. Arif, P. Tumula, and O. J. Ebohon. 2020. Effect of thermal comfort on occupant productivity in office buildings: Response surface analysis. *Building and Environment*, *180*:107021.

Khalifa, H. E., M. I. Janos, and J. F. Dannenhoffer. 2009. Experimental investigation of reduced-mixing personal ventilation jets. *Building and Environment*, *44*(8):1551–1558.

Khalili, A., E. Petersen, M. Koopmans, U. Go, D. H. Hamer, N. Petrosillo, F. Castelli, M. Storgaard, and S. Al Khalili. 2020. Personal View Comparing SARS-CoV-2 with SARS-CoV and influenza pandemics. *The Lancet Infectious Diseases*, *20*:e238–e244.

Kheiri, F. 2018. A review on optimization methods applied in energy-efficient building geometry and envelope design. *Renewable and Sustainable Energy Reviews*, *92*:897–920.

Kim, D. W., C. S. Park, and I. H. Kim. 2013. Use of kalman filter for estimating unknown internal loads. *Proceedings of BS 2013: 13th Conference of the International Building Performance Simulation Association*, 1239–1246.

Kim, J. Y., J.-H. Ko, Y. Kim, Y.-J. Kim, J.-M. Kim, Y.-S. Chung, H. M. Kim, M.-G. Han, S. Y. Kim, and B. S. Chin. 2020. Viral Load Kinetics of SARS-CoV-2 Infection in First Two Patients in Korea. *Journal of Korean Medical Science*, *35*(7).

Klepeis, N. E., W. C. NELSON, W. R. OTT, J. P. ROBINSON, A. M. TSANG, P. SWITZER, J. V BEHAR, S. C. HERN, and W. H. ENGELMANN. 2001. The National Human Activity Pattern Survey (NHAPS): a resource for assessing exposure to environmental pollutants. *Journal of Exposure Science & Environmental Epidemiology*, *11*(3):231–252.

Ko, G., H. A. Burge, E. A. Nardell, and K. M. Thompson. 2001. Estimation of Tuberculosis Risk and Incidence under Upper Room Ultraviolet Germicidal Irradiation in a Waiting Room in a Hypothetical Scenario. *Risk Analysis*, *21*(4):657–674.

Ko, G., K. M. Thompson, and E. A. Nardell. 2004. Estimation of Tuberculosis Risk on a Commercial Airliner. *Risk Analysis*, *24*(2):379–388.

Konda, A., A. Prakash, G. A. Moss, M. Schmoldt, G. D. Grant, and S. Guha. 2020. Aerosol Filtration Efficiency of Common Fabrics Used in Respiratory Cloth Masks. *ACS Nano*, *14*(5):6339–6347.

Kong, M., J. Zhang, T. Q. Dang, A. Hedge, T. Teng, B. Carter, C. Chianese, and H. Ezzat Khalifa. 2019. Micro-environmental control for efficient local cooling: Results from manikin and human participant tests. *Building and Environment*, *160*:106198.

Kong, M., J. Zhang, and J. Wang. 2015. Air and air contaminant flows in office cubicles with and without personal ventilation: A CFD modeling and simulation study. *Building Simulation*, *8*(4):381–392.

Konis, K., A. Gamas, and K. Kensek. 2016. Passive performance and building form: An optimization framework for early-stage design support. *Solar Energy*, *125*:161–179.

Krietemeyer, B., M. Knapp, T. King, J. Zhang, A. Bartosh, E. Bogucz, T. Rosanio, I. Shapiro, and

R. Zhang. 2020. Integrated Whole-Building Energy Efficiency Retrofit Solution for Residences in Cold/Very Cold Climates | Department of Energy.

Kulkarni, P., P. A. Baron, and K. Willeke. 2011. Aerosol Measurement: Principles, Techniques, and Applications: Third Edition. *Aerosol Measurement: Principles, Techniques, and Applications: Third Edition*.

Lai, A. C. K., and Y. C. Cheng. 2007. Study of expiratory droplet dispersion and transport using a new Eulerian modeling approach. *Atmospheric Environment*, *41*(35):7473–7484.

Larsson, N. 2009. *The Integrated Design Process; History and Analysis The C-2000 Program*.

LBNL. 2011. Building Performance Database (BPD).

LBNL. 2016. bcvtb.

LBNL. 2017. Radiance.

LBNL. 2021. EnergyPlusToFMU | Simulation Research.

LBNL. 2022. Modelica Buildings library.

LEB. 2010. Low Energy Building Database.

Lednicky, J. A., M. Lauzard, Z. H. Fan, A. Jutla, T. B. Tilly, M. Gangwar, M. Usmani, S. N. Shankar, K. Mohamed, A. Eiguren-Fernandez, C. J. Stephenson, M. M. Alam, M. A. Elbadry, J. C. Loeb, K. Subramaniam, T. B. Waltzek, K. Cherabuddi, J. G. Morris, and C. Y. Wu. 2020. Viable SARS-CoV-2 in the air of a hospital room with COVID-19 patients. *International Journal of Infectious Diseases*, *100*:476–482.

Lee, K. K., R. Bing, J. Kiang, S. Bashir, N. Spath, D. Stelzle, K. Mortimer, A. Bularga, D.

Doudesis, S. S. Joshi, F. Strachan, S. Gumy, H. Adair-Rohani, E. F. Attia, M. H. Chung, M. R. Miller, D. E. Newby, N. L. Mills, D. A. McAllister, and A. S. V. Shah. 2020. Adverse health effects associated with household air pollution: a systematic review, meta-analysis, and burden estimation study. *The Lancet Global Health*, *8*(11):e1427–e1434.

Lee, M., E. Carter, L. Yan, Q. Chan, P. Elliott, M. Ezzati, F. Kelly, J. J. Schauer, Y. Wu, X. Yang, L. Zhao, and J. Baumgartner. 2021. Determinants of personal exposure to PM2.5 and black carbon in Chinese adults: A repeated-measures study in villages using solid fuel energy. *Environment International*, *146*:106297.

Li, B., A. Deng, K. Li, Y. Hu, Z. Li, Q. Xiong, Z. Liu, Q. Guo, L. Zou, H. Zhang, M. Zhang, F. Ouyang, J. Su, W. Su, J. Xu, H. Lin, J. Sun, J. Peng, H. Jiang, P. Zhou, T. Hu, M. Luo, Y. Zhang, H. Zheng, J. Xiao, T. Liu, R. Che, H. Zeng, Z. Zheng, Y. Huang, J. Yu, L. Yi, J. Wu, J. Chen, H. Zhong, X. Deng, M. Kang, O. G. Pybus, M. Hall, K. A. Lythgoe, Y. Li, J. Yuan, J. He, and J. Lu. 2021. Viral infection and transmission in a large, well-traced outbreak caused by the SARS-CoV-2 Delta variant. *MedRxiv*, 2021.07.07.21260122.

Li, J., Z. Cheng, Y. Zhang, N. Mao, S. Guo, Q. Wang, L. Zhao, and E. Long. 2021. Evaluation of infection risk for SARS-CoV-2 transmission on university campuses. *Science and Technology for the Built Environment*, *27*(9):1165–1180.

Li, M., G. Bekö, N. Zannoni, G. Pugliese, M. Carrito, N. Cera, C. Moura, P. Wargocki, P. Vasconcelos, P. Nobre, N. Wang, L. Ernle, and J. Williams. 2022. Human metabolic emissions of carbon dioxide and methane and their implications for carbon emissions. *Science of The Total Environment*, *833*:155241.

Li, Q., X. Guan, P. Wu, X. Wang, L. Zhou, Y. Tong, R. Ren, K. S. M. Leung, E. H. Y. Lau, J. Y.

Wong, X. Xing, N. Xiang, Y. Wu, C. Li, Q. Chen, D. Li, T. Liu, J. Zhao, M. Liu, W. Tu, C. Chen, L. Jin, R. Yang, Q. Wang, S. Zhou, R. Wang, H. Liu, Y. Luo, Y. Liu, G. Shao, H. Li, Z. Tao, Y. Yang, Z. Deng, B. Liu, Z. Ma, Y. Zhang, G. Shi, T. T. Y. Lam, J. T. Wu, G. F. Gao, B. J. Cowling, B. Yang, G. M. Leung, and Z. Feng. 2020. Early Transmission Dynamics in Wuhan, China, of Novel Coronavirus–Infected Pneumonia. *New England Journal of Medicine*, *382*(13):1199–1207.

Li, W., S. Wang, and C. Koo. 2021. A real-time optimal control strategy for multi-zone VAV air-conditioning systems adopting a multi-agent based distributed optimization method. *Applied Energy*, *287*:116605.

Li, X., C. Shen, and C. W. F. Yu. 2017. Building energy efficiency: Passive technology or active technology?: *Http://Dx.Doi.Org/10.1177/1420326X17719157*, *26*(6):729–732.

Li, Y., H. Qian, J. Hang, X. Chen, L. Hong, P. Liang, J. Li, S. Xiao, J. Wei, L. Liu, and M. Kang. 2020. Evidence for probable aerosol transmission of SARS-CoV-2 in a poorly ventilated restaurant. *MedRxiv*, 2020.04.16.20067728.

Li, Z., T. Ming, T. Shi, H. Zhang, C.-Y. Wen, X. Lu, X. Dong, Y. Wu, R. de Richter, W. Li, and C. Peng. 2021. Review on pollutant dispersion in urban areas-part B: Local mitigation strategies, optimization framework, and evaluation theory. *Building and Environment*, *198*:107890.

Licina, D., and S. Langer. 2021. Indoor air quality investigation before and after relocation to WELL-certified office buildings. *Building and Environment*, *204*:108182.

Lim, S., E. Bassey, B. Bos, L. Makacha, D. Varaden, R. E. Arku, J. Baumgartner, M. Brauer, M. Ezzati, F. J. Kelly, and B. Barratt. 2022. Comparing human exposure to fine particulate matter

in low and high-income countries: A systematic review of studies measuring personal PM2.5 exposure. *Science of The Total Environment*, *833*:155207.

Lindsley, W G, F. M. Blachere, R. E. Thewlis, A. Vishnu, and K. A. Davis. 2010. Measurements of Airborne Influenza Virus in Aerosol Particles from Human Coughs. *PLoS ONE*, *5*(11):15100.

Lindsley, William G., J. D. Noti, F. M. Blachere, J. V. Szalajda, and D. H. Beezhold. 2014. Efficacy of face shields against cough aerosol droplets from a cough simulator. *Journal of Occupational and Environmental Hygiene*, *11*(8):509–518.

Liu, Han, S. He, L. Shen, and J. Hong. 2021. Simulation-based study of COVID-19 outbreak associated with air-conditioning in a restaurant. *Physics of Fluids*, *33*(2):23301.

Liu, Hongbin, S. Lee, M. Kim, H. Shi, J. T. Kim, K. L. Wasewar, and C. Yoo. 2013. Multi-objective optimization of indoor air quality control and energy consumption minimization in a subway ventilation system. *Energy and Buildings*, *66*:553–561.

Liu, W., J. Huang, Y. Lin, C. Cai, Y. Zhao, Y. Teng, J. Mo, L. Xue, L. Liu, W. Xu, X. Guo, Y. Zhang, and J. Zhang. 2021. Negative ions offset cardiorespiratory benefits of PM2.5 reduction from residential use of negative ion air purifiers. *Indoor Air*, *31*(1):220–228.

Liu, Zhenlei, R. Zhang, T. Stenson, A. Rais, W. Chen, and J. Zhang. 2017. Definition of a Reference Residential Building Prototype for Evaluating IAQ and Energy Efficiency Strategies. In *Healthy Building 2017 Asia*.

Liu, Zhijian, D. Wu, Y. Liu, Z. Han, L. Lun, J. Gao, G. Jin, and G. Cao. 2019. Accuracy analyses and model comparison of machine learning adopted in building energy consumption

prediction: *Energy Exploration & Exploitation*, *37*(4):1426–1451.

Logue, J. M., P. N. Price, M. H. Sherman, and B. C. Singer. 2012. A Method to Estimate the Chronic Health Impact of Air Pollutants in U.S. Residences. *Environmental Health Perspectives*, *120*(2):216.

Long, Q., C. Wu, X. Wang, L. Jiang, and J. Li. 2015. A Multiobjective Genetic Algorithm Based on a Discrete Selection Procedure. *Mathematical Problems in Engineering*, *2015*.

Lvovsky, K., G. Hughes, D. Maddison, B. Ostro, and D. Pearce. 2000. Environmental Costs of Fossil Fuels : A Rapid Assessment Method with Application to Six Cities.

Majumder, M., and K. D. Mandl. 2020. Early Transmissibility Assessment of a Novel Coronavirus in Wuhan, China. *SSRN Electronic Journal*.

Masrour, M. M., M. Abbasi, and H. M. Hallaj. 2012. Study Of Windcatchers: The Mass Flow Rate And Inlet Air To The Building In Traditional Windcatchers. *Australian Journal of Basic and Applied Sciences*, *6*(10):159–165.

Mathai, V., A. Das, J. A. Bailey, and K. Breuer. 2021. Airflows inside passenger cars and implications for airborne disease transmission. *Science Advances*, *7*(1):eabe0166.

Mathew, P. A., L. N. Dunn, M. D. Sohn, A. Mercado, C. Custudio, and T. Walter. 2015. Big-data for building energy performance: Lessons from assembling a very large national database of building energy use. *Applied Energy*, *140*:85–93.

Max Roser, and Hannah Ritchie. 2022. Indoor Air Pollution - Our World in Data.

McCabe, K., M. Gleason, T. Reber, and K. R. Young. 2016. Characterizing U.S. Heat Demand for Potential Application of Geothermal Direct Use: Preprint.

Melikov, A., H. Grønbaek, and J. B. Nielsen. 2007. *Personal Ventilation: from research to practical use*.

Melikov, A. K., Z. T. Ai, and D. G. Markov. 2020. Intermittent occupancy combined with ventilation: An efficient strategy for the reduction of airborne transmission indoors. *Science of The Total Environment*, *744*:140908.

Miller, C., A. Kathirgamanathan, B. Picchetti, P. Arjunan, J. Y. Park, Z. Nagy, P. Raftery, B. W. Hobson, Z. Shi, and F. Meggers. 2020. The Building Data Genome Project 2, energy meter data from the ASHRAE Great Energy Predictor III competition. *Scientific Data*, *7*(1):1–13.

Miller, S. L., W. W. Nazaroff, J. L. Jimenez, A. Boerstra, G. Buonanno, S. J. Dancer, J. Kurnitski, L. C. Marr, L. Morawska, and C. Noakes. 2020. Transmission of SARS-CoV-2 by inhalation of respiratory aerosol in the Skagit Valley Chorale superspreading event. *MedRxiv*, (June):2020.06.15.20132027.

Minnesota Pollution Control Agency. 2022. Ozone | Minnesota Pollution Control Agency.

Mirakhorli, A., and B. Dong. 2016, October 1. Occupancy behavior based model predictive control for building indoor climate—A critical review. *Energy and Buildings*. Elsevier Ltd.

Montazeri, H., F. Montazeri, R. Azizian, and S. Mostafavi. 2010. Two-sided wind catcher performance evaluation using experimental, numerical and analytical modeling. *Renewable Energy*, *35*(7):1424–1435.

Mueller, A., M. Eden, J. Oakes, C. Bellini, and L. Fernandez. 2020. Quantitative Method for Comparative Assessment of Particle Removal Efficiency of Fabric Masks as Alternatives to Standard Surgical Masks for PPE. *Matter*.

Murakami, S., S. Kato, and J. Zeng. 2000. Combined simulation of airflow, radiation and moisture transport for heat release from a human body. *Building and Environment*, *35*(6):489–500.

NASA. 2022. Heatwaves and Fires Scorch Europe, Africa, and Asia.

Nazari, A., M. Jafari, N. Rezaei, F. Taghizadeh-Hesary, and F. Taghizadeh-Hesary. 2021. Jet fans in the underground car parking areas and virus transmission. *Physics of Fluids*, *33*(1):13603.

Nazaroff, W. W., and C. J. Weschler. 2021. Indoor ozone: Concentrations and influencing factors. *Indoor Air*.

New Jersey Department of Health. 2015. Hazardous Substance Fact Sheet - Acetone. *New Jersey Department of Health*.

New Jersey Department of Health. 2017. Hazardous Substance Fact Sheet - Benzo[a]pyrene. *New Jersey Department of Health*.

Newsham, G. R., S. Mancini, and B. J. Birt. 2009. Do LEED-certified buildings save energy? Yes, but... *Energy and Buildings*, *41*(8):897–905.

Ng, L. C., W. S. Dols, and S. J. Emmerich. 2021. Evaluating potential benefits of air barriers in commercial buildings using NIST infiltration correlations in EnergyPlus. *Building and Environment*, *196*:107783.

Ng, L. C., A. Musser, A. K. Persily, and S. J. Emmerich. 2013. Multizone airflow models for calculating infiltration rates in commercial reference buildings. *Energy and Buildings*, *58*:11–18.

Nguyen, A. T., S. Reiter, and P. Rigo. 2014. A review on simulation-based optimization methods applied to building performance analysis. *Applied Energy*, *113*:1043–1058.

Nicas, M., W. W. Nazaroff, and A. Hubbard. 2005. Toward understanding the risk of secondary airborne infection: Emission of respirable pathogens. *Journal of Occupational and Environmental Hygiene*, *2*(3):143–154.

NIST. 2018. Contam | Nist.

NIST. 2022. CONTAM 3D Exporter | NIST.

Noakes, C. J., and P. A. Sleigh. 2009. Mathematical models for assessing the role of airflow on the risk of airborne infection in hospital wards. *Journal of The Royal Society Interface*, *6*(suppl_6).

NRCan. 2021. National Energy Use Database | Natural Resources Canada.

NREL. 2021. Building Component Library.

Nunayon, S. S., H. H. Zhang, X. Jin, and A. C. Lai. 2019. Experimental evaluation of positive and negative air ions disinfection efficacy under different ventilation duct conditions. *Building and Environment*, *158*:295–301.

Nurchis, M. C., D. Pascucci, M. Sapienza, L. Villani, F. D'ambrosio, F. Castrini, M. L. Specchia, P. Laurenti, and G. Damiani. 2022. Impact of the Burden of COVID-19 in Italy: Results of Disability-Adjusted Life Years (DALYs) and Productivity Loss.

O'Neill, Z., and S. Narayanan. 2014. Model-based estimation of cold room temperatures in a supermarket refrigeration system. *Applied Thermal Engineering*, *73*(1):819–830.

O'Neill, Z., S. Narayanan, and R. Brahme. 2010. Model-based thermal load estimation in buildings. *Proceedings of Simbuild 4.1*, 474–481.

OEHHA. 2019. OEHHA Acute, 8-hour and Chronic Reference Exposure Level (REL) Summary

- OEHHA.

OEHHA. 2022. Chemicals - OEHHA.

Office of Climate Change and Health Equity. 2022. *Climate and Health Outlook: Extreme Heat*. *Climate and Health Outlook.*

Office of Sustainability & Environment of Seattle. 2022. Data and Reports - Environment | seattle.gov.

Ogunsola, O. T., L. Song, and G. Wang. 2014. Development and validation of a time-series model for real-time thermal load estimation. *Energy and Buildings*, *76*:440–449.

Okoronkwo, C. A., K. N. Nwigwe, N. V. Ogueke, E. E. Anyanwu, D. C. Onyejekwe, and P. E. Ugwuoke. 2014. An Experimental Investigation of the Passive Cooling of a Building Using Nighttime Radiant Cooling. *Https://Doi.Org/10.1080/15435075.2013.829775*, *11*(10):1072–1083.

Ong, S. W. X., C. J. Chiew, L. W. Ang, T.-M. Mak, L. Cui, M. P. H. Toh, Y. D. Lim, P. H. Lee, T. H. Lee, P. Y. Chia, S. Maurer-Stroh, R. T. P. Lin, Y.-S. Leo, V. J. Lee, D. C. Lye, and B. E. Young. 2021. Clinical and Virological Features of SARS-CoV-2 Variants of Concern: A Retrospective Cohort Study Comparing B.1.1.7 (Alpha), B.1.315 (Beta), and B.1.617.2 (Delta). *SSRN Electronic Journal*.

OpenFOAM Ltd. 2023. OpenFOAM.

Ormandy, D., and V. Ezratty. 2012. Health and thermal comfort: From WHO guidance to housing strategies. *Energy Policy*, *49*:116–121.

Østergård, T., R. L. Jensen, and S. E. Maagaard. 2016. Building simulations supporting decision

making in early design – A review. *Renewable and Sustainable Energy Reviews*, *61*:187–201.

Ouaret, R., A. Ionescu, V. Petrehus, Y. Candau, and O. Ramalho. 2018. Spectral band decomposition combined with nonlinear models: application to indoor formaldehyde concentration forecasting. *Stochastic Environmental Research and Risk Assessment*, *32*(4):985–997.

Pan, Y., D. Zhang, P. Yang, L. L. M. Poon, and Q. Wang. 2020, April 1. Viral load of SARS-CoV-2 in clinical samples. *The Lancet Infectious Diseases*. Lancet Publishing Group.

Parkinson, T., F. Tartarini, V. Földváry Ličina, T. Cheung, H. Zhang, R. de Dear, P. Li, E. Arens, C. Chun, S. Schiavon, M. Luo, and G. Brager. 2022. ASHRAE global database of thermal comfort field measurements.

Passivhaus Institute. 2023. Passive House Database.

Pavilonis, B., A. M. Ierardi, L. Levine, F. Mirer, and E. A. Kelvin. 2021. Estimating aerosol transmission risk of SARS-CoV-2 in New York City public schools during reopening. *Environmental Research*, *195*:110805.

Pearson, C. A., T. W. Russell, N. G. Davis, A. J. Kucharski, CMMID COVID-19 working group, W. J. Edmunds, and R. M. Eggo. 2020. *Estimates of severity and transmissibility of novel South Africa SARS-CoV-2 variant 501Y.V2*.

Pei, J., W. Chen, J. Zhang, B. Guo, S. Nair, and J. Wong. 2008. VOC removal performance of pellet/granular type sorbent media--from testing to predictions. *ASHRAE Transactions*, *114*(2):462–472.

Peng, Z., and J. L. Jimenez. 2021. Exhaled CO2 as a COVID-19 Infection Risk Proxy for Different

Indoor Environments and Activities. *Environmental Science & Technology Letters*, *8*(5):392–397.

Persily, A., and L. de Jonge. 2017. Carbon dioxide generation rates for building occupants. *Indoor Air*, *27*(5):868–879.

Persily, A., A. Musser, and S. J. Emmerich. 2010. Modeled infiltration rate distributions for U.S. housing. *Indoor Air*, *20*(6):473–485.

Pétigny, N., J. Zhang, E. Horner, S. Steady, M. Chenal, G. Mialon, and V. Goletto. 2021. Indoor air depolluting material: Combining sorption testing and modeling to predict product's service life in real conditions. *Building and Environment*, *202*:107838.

PoppinSpaces. 2021. PoppinSpaces | Free-Standing Rooms + Office Walls.

Practice, B. on P. H. and P. H., H. and M. Division, and E. and M. National Academies of Sciences. 2016. Sources of Indoor Particulate Matter.

Pushpawela, B., R. Jayaratne, A. Nguy, and L. Morawska. 2017. Efficiency of ionizers in removing airborne particles in indoor environments. *Journal of Electrostatics*, *90*:79–84.

Puttaswamy, N., S. Natarajan, S. R. Saidam, K. Mukhopadhyay, S. Sadasivam, S. Sambandam, and K. Balakrishnan. 2021. Evaluation of health risks associated with exposure to volatile organic compounds from household fuel combustion in southern India. *Environmental Advances*, *4*:100043.

Q.Chen, and Glicksman. 2003. System performance evaluation and design guidelines for displacement ventilation.

Qian, H., Y. Li, P. V. Nielsen, and X. Huang. 2009. Spatial distribution of infection risk of SARS

transmission in a hospital ward. *Building and Environment*, *44*(8):1651–1658.

Qian, H., Y. Li, W. H. Seto, P. Ching, W. H. Ching, and H. Q. Sun. 2010. Natural ventilation for reducing airborne infection in hospitals. *Building and Environment*, *45*(3):559–565.

Qian, H., T. Miao, L. Liu, X. Zheng, D. Luo, and Y. Li. 2020. Indoor transmission of SARS-CoV-2. *Indoor Air*, ina.12766.

Qian, J., J. Peccia, and A. R. Ferro. 2014, June 1. Walking-induced particle resuspension in indoor environments. *Atmospheric Environment*. Elsevier Ltd.

Qin, M., and J. Zhang. 2020. *Annex 68 Subtask 2 Final Report: Indoor pollution loads*.

Qin, M., J. Zhang, Z. Liu, L. Weihui, Y. Xudong, J. Grunewald, A. Nicolai, and M. Abadie. 2020. Indoor Air Quality Design and Control in Low-Energy Residential Buildings Subtask 2: Pollutant loads in residential buildings Energy in Buildings and Communities Technology Collaboration Programme.

Rahman, S. M. M. 2019. Simplified 3R2C Building Thermal Network Model: A Case Study. *International Journal of Structural and Construction Engineering*, *13*(6).

Rai, A. C., B. Guo, C. H. Lin, J. Zhang, J. Pei, and Q. Chen. 2014. Ozone reaction with clothing and its initiated VOC emissions in an environmental chamber. *Indoor Air*, *24*(1):49–58.

Read, J., J. R. Bridgen, D. A. Cummings, A. Ho, and C. Jewell. 2020. Novel coronavirus 2019-nCoV: early estimation of epidemiological parameters and epidemic predictions. *MedRxiv*, 2020.01.23.20018549.

REHVA. 2020. COVID-19 Ventilation Calculator.

Riediker, M., and C. Monn. 2020. Simulation of SARS-CoV-2 Aerosol Emissions in the Infected

Population and Resulting Airborne Exposures in Different Indoor Scenarios. *Aerosol and Air Quality Research*, *20*.

Riether, G., and T. Butler. 2008. Simulation Space. *Proceedings of the 26th International Conference on Education and Research in Computer Aided Architectural Design in Europe (ECAADe)*, 133–142.

Riley, E. C., G. Murphy, and R. L. Riley. 1978. Airborne spread of measles in a suburban elementary school. *American Journal of Epidemiology*, *107*(5):421–432.

RILEY, E. C., G. MURPHY, and R. L. RILEY. 1978. AIRBORNE SPREAD OF MEASLES IN A SUBURBAN ELEMENTARY SCHOOL. *American Journal of Epidemiology*, *107*(5):421–432.

Risbeck, M. J., M. Z. Bazant, Z. Jiang, Y. M. Lee, K. H. Drees, and J. D. Douglas. 2021. Quantifying the Tradeoff Between Energy Consumption and the Risk of Airborne Disease Transmission for Building HVAC Systems. *MedRxiv*, 2021.06.21.21259287.

Robert McNeel & Associates. 2022a. Food4Rhino.

Robert McNeel & Associates. 2022b. Rhino - RhinoCommon Guides.

Robert McNeel and Associates. 2009. Grasshopper SDK.

Rooney, C. M., J. McIntyre, L. Ritchie, and M. H. Wilcox. 2021. Evidence review of physical distancing and partition screens to reduce healthcare acquired SARS-CoV-2. *Infection Prevention in Practice*, *3*(2):100144.

Rothamer, D. A., S. Sanders, D. Reindl, T. H. Bertram, and D. Rothamer. 2020. Strategies to minimize SARS-CoV-2 transmission in classroom settings: Combined impacts of ventilation

and mask effective filtration efficiency. *MedRxiv*, 2020.12.31.20249101.

Rothe, C., M. Schunk, P. Sothmann, G. Bretzel, G. Froeschl, C. Wallrauch, T. Zimmer, V. Thiel, C. Janke, W. Guggemos, M. Seilmaier, C. Drosten, P. Vollmar, K. Zwirglmaier, S. Zange, R. Wölfel, and M. Hoelscher. 2020. Transmission of 2019-nCoV Infection from an Asymptomatic Contact in Germany. *New England Journal of Medicine*, *382*(10):970–971.

Rupp, R. F., N. G. Vásquez, and R. Lamberts. 2015. A review of human thermal comfort in the built environment. *Energy and Buildings*, *105*:178–205.

Sadineni, S. B., S. Madala, and R. F. Boehm. 2011. Passive building energy savings: A review of building envelope components. *Renewable and Sustainable Energy Reviews*, *15*(8):3617–3631.

Salonen, H., T. Salthammer, and L. Morawska. 2019. Human exposure to NO2 in school and office indoor environments. *Environment International*, *130*:104887.

Salonvaara, M., A. Karagiozis, and O. Corning. 2015. *Acceptable Air Tightness of Walls in Passive Houses*.

Santarpia, J. L., D. N. Rivera, V. L. Herrera, M. J. Morwitzer, H. M. Creager, G. W. Santarpia, K. K. Crown, D. M. Brett-Major, E. R. Schnaubelt, M. J. Broadhurst, J. V. Lawler, S. P. Reid, and J. J. Lowe. 2020. Aerosol and surface contamination of SARS-CoV-2 observed in quarantine and isolation care. *Scientific Reports*, *10*(1):12732.

Schuit, M., S. Ratnesar-Shumate, J. Yolitz, G. Williams, W. Weaver, B. Green, D. Miller, M. Krause, K. Beck, S. Wood, B. Holland, J. Bohannon, D. Freeburger, I. Hooper, J. Biryukov, L. A. Altamura, V. Wahl, M. Hevey, and P. Dabisch. 2020. Airborne SARS-CoV-2 Is Rapidly

Inactivated by Simulated Sunlight. *The Journal of Infectious Diseases*, *222*(4):564–571.

Schweizer, C., R. D. Edwards, L. Bayer-Oglesby, W. J. Gauderman, V. Ilacqua, M. Juhani Jantunen, H. K. Lai, M. Nieuwenhuijsen, and N. Künzli. 2007. Indoor time–microenvironment–activity patterns in seven regions of Europe. *Journal of Exposure Science & Environmental Epidemiology*, *17*(2):170–181.

Scofield, J. H., and J. Doane. 2018. Energy performance of LEED-certified buildings from 2015 Chicago benchmarking data. *Energy and Buildings*, *174*:402–413.

Seyedzadeh, S., F. P. Rahimian, I. Glesk, and M. Roper. 2018. Machine learning for estimation of building energy consumption and performance: a review. *Visualization in Engineering 2018 6:1*, *6*(1):1–20.

Shaikh, P. H., N. B. M. Nor, P. Nallagownden, and I. Elamvazuthi. 2018. Intelligent multi-objective optimization for building energy and comfort management. *Journal of King Saud University - Engineering Sciences*, *30*(2):195–204.

Shao, S., D. Zhou, R. He, J. Li, S. Zou, K. Mallery, S. Kumar, S. Yang, and J. Hong. 2021. Risk assessment of airborne transmission of COVID-19 by asymptomatic individuals under different practical settings. *Journal of Aerosol Science*, *151*:105661.

Shen, J. 2022. DALYs in Indoor Air - Google Sheets.

Shen, J., J. Chen, X. Zhang, S. Zou, and Z. Gao. 2017. Outdoor and Indoor Ozone Concentration Estimation Based on Artificial Neural Network and Single Zone Mass Balance Model. In *Procedia Engineering* (Vol. 205, pp. 1835–1842). Elsevier Ltd.

Shen, J., and Z. Gao. 2018. Ozone removal on building material surface: A literature review.

Building and Environment, *134*:205–217.

Shen, J., M. Kong, M. J. Birnkrant, P. J. McKinney, B. Dong, and J. Zhang. 2021. Indoor Airborne Risk COVID-19 Estimator - Google Sheets.

Shen, J., M. Kong, B. Dong, M. J. Birnkrant, and J. Zhang. 2021a. A systematic approach to estimating the effectiveness of multi-scale IAQ strategies for reducing the risk of airborne infection of SARS-CoV-2. *Building and Environment*, 107926.

Shen, J., M. Kong, B. Dong, M. J. Birnkrant, and J. Zhang. 2021b. Airborne transmission of SARS-CoV-2 in indoor environments: A comprehensive review. *Science and Technology for the Built Environment*, 1–60.

Shen, J., B. Krietemeyer, A. Bartosh, Z. Gao, and J. Zhang. 2020. Green Design Studio: A modular-based approach for high-performance building design Article History. *Building Simulation*.

Shen, J., and J. Zhang. 2019. An approach to develop a green building technology database for residential buildings. *IOP Conference Series: Materials Science and Engineering*, *609*.

Shi, B., and L. Ekberg. 2015. Ionizer assisted air filtration for collection of submicron and ultrafine particles-evaluation of long-term performance and influencing factors. *Environmental Science and Technology*, *49*(11):6891–6898.

Shi, B., L. E. Ekberg, A. Truschel, and J. Gusten. 2012. Influence of Filter Fiber Material on Removal of Ultrafine and Submicron Particles Using Carbon Fiber Ionizer-Assisted Intermediate Air Filters | Techstreet Enterprise. *ASHRAE Transactions*, *118*.

Shi, S., C. Chen, and B. Zhao. 2015. Air infiltration rate distributions of residences in Beijing.

Building and Environment, *92*:528–537.

Shupler, M., K. Balakrishnan, S. Ghosh, G. Thangavel, S. Stroud-Drinkwater, H. Adair-Rohani, J. Lewis, S. Mehta, and M. Brauer. 2018. Global household air pollution database: Kitchen concentrations and personal exposures of particulate matter and carbon monoxide. *Data in Brief*, *21*:1292–1295.

Shupler, M., P. Hystad, A. Birch, Y. L. Chu, M. Jeronimo, D. Miller-Lionberg, P. Gustafson, S. Rangarajan, M. Mustaha, L. Heenan, P. Seron, F. Lanas, F. Cazor, M. Jose Oliveros, P. Lopez-Jaramillo, P. A. Camacho, J. Otero, M. Perez, K. Yeates, N. West, T. Ncube, B. Ncube, J. Chifamba, R. Yusuf, A. Khan, Z. Liu, S. Wu, L. Wei, L. A. Tse, D. Mohan, P. Kumar, R. Gupta, I. Mohan, K. G. Jayachitra, P. K. Mony, K. Rammohan, S. Nair, P. V. M. Lakshmi, V. Sagar, R. Khawaja, R. Iqbal, K. Kazmi, S. Yusuf, and M. Brauer. 2022. Multinational prediction of household and personal exposure to fine particulate matter (PM2.5) in the PURE cohort study. *Environment International*, *159*:107021.

Shupler, M., P. Hystad, A. Birch, D. Miller-Lionberg, M. Jeronimo, R. E. Arku, Y. L. Chu, M. Mushtaha, L. Heenan, S. Rangarajan, P. Seron, F. Lanas, F. Cazor, P. Lopez-Jaramillo, P. A. Camacho, M. Perez, K. Yeates, N. West, T. Ncube, B. Ncube, J. Chifamba, R. Yusuf, A. Khan, B. Hu, X. Liu, L. Wei, L. A. Tse, D. Mohan, P. Kumar, R. Gupta, I. Mohan, K. G. Jayachitra, P. K. Mony, K. Rammohan, S. Nair, P. V. M. Lakshmi, V. Sagar, R. Khawaja, R. Iqbal, K. Kazmi, S. Yusuf, and M. Brauer. 2020. Household and personal air pollution exposure measurements from 120 communities in eight countries: results from the PURE-AIR study. *The Lancet Planetary Health*, *4*(10):e451–e462.

Smither, S. J., L. S. Eastaugh, J. S. Findlay, and M. S. Lever. 2020, January 1. Experimental aerosol

survival of SARS-CoV-2 in artificial saliva and tissue culture media at medium and high humidity. *Emerging Microbes and Infections*. Taylor and Francis Ltd.

Soares, N., A. R. Gaspar, P. Santos, and J. J. Costa. 2014. Multi-dimensional optimization of the incorporation of PCM-drywalls in lightweight steel-framed residential buildings in different climates. *Energy and Buildings*, *70*:411–421.

Stabile, L., A. Pacitto, A. Mikszewski, L. Morawska, and G. Buonanno. 2021. Ventilation procedures to minimize the airborne transmission of viruses at schools. *MedRxiv*, 2021.03.23.21254179.

Steinemann, A., P. Wargocki, and B. Rismanchi. 2017. Ten questions concerning green buildings and indoor air quality. *Building and Environment*, *112*:351–358.

Stephens, B. 2012. *Wells-Riley & HVAC Filtration for infectious airborne aerosols NAFA Foundation Report HVAC filtration and the Wells-Riley approach to assessing risks of infectious airborne diseases Final Report Prepared for: The National Air Filtration Association (NAFA)*.

Stephens, B. 2013. HVAC filtration and the Wells-Riley approach to assessing risks of infectious airborne diseases. *NAFA Foundation Report*, (March):44.

Stephens, B., and J. A. Siegel. 2012. Comparison of test methods for determining the particle removal efficiency of filters in residential and light-commercial central HVAC systems. *Aerosol Science and Technology*, *46*(5):504–513.

Stine, D. 2022. Early Energy Modeling and Comparing Tools to Validate Results | Lake Flato.

Sun, C., and Z. Zhai. 2020. The efficacy of social distance and ventilation effectiveness in

preventing COVID-19 transmission. *Sustainable Cities and Society*, *62*:102390.

Sze To, G. N., and C. Y. H. Chao. 2010, February. Review and comparison between the Wells-Riley and dose-response approaches to risk assessment of infectious respiratory diseases. *Indoor Air*. Wiley-Blackwell.

Tagiyeva, N., and A. Sheikh. 2014. Domestic exposure to volatile organic compounds in relation to asthma and allergy in children and adults. *Expert Review of Clinical Immunology*.

Tang, R., and S. Wang. 2019. Model predictive control for thermal energy storage and thermal comfort optimization of building demand response in smart grids. *Applied Energy*, *242*:873–882.

Tartarini, F., S. Schiavon, T. Cheung, and T. Hoyt. 2020. CBE Thermal Comfort Tool: Online tool for thermal comfort calculations and visualizations. *SoftwareX*, *12*.

Tham, S., R. Thompson, O. Landeg, K. A. Murray, and T. Waite. 2020. Indoor temperature and health: a global systematic review. *Public Health*, *179*:9–17.

To, K. K. W., O. T. Y. Tsang, W. S. Leung, A. R. Tam, T. C. Wu, D. C. Lung, C. C. Y. Yip, J. P. Cai, J. M. C. Chan, T. S. H. Chik, D. P. L. Lau, C. Y. C. Choi, L. L. Chen, W. M. Chan, K. H. Chan, J. D. Ip, A. C. K. Ng, R. W. S. Poon, C. T. Luo, V. C. C. Cheng, J. F. W. Chan, I. F. N. Hung, Z. Chen, H. Chen, and K. Y. Yuen. 2020. Temporal profiles of viral load in posterior oropharyngeal saliva samples and serum antibody responses during infection by SARS-CoV-2: an observational cohort study. *The Lancet Infectious Diseases*, *20*(5):565–574.

Tomson, M., P. Kumar, Y. Barwise, P. Perez, H. Forehead, K. French, L. Morawska, and J. F. Watts. 2021. Green infrastructure for air quality improvement in street canyons. *Environment*

International.

Townsend, C. L., and R. L. Maynard. 2002. Effects on health of prolonged exposure to low concentrations of carbon monoxide. *Occupational and Environmental Medicine, 59*(10):708–711.

TRNSYS. 2019. Welcome | TRNSYS : Transient System Simulation Tool.

TSI Inc. 2012. Estimation of Mass with the Model 3321 APS Spectrometer.

Tung, Y. C., and S. C. Hu. 2008. Infection risk of indoor airborne transmission of diseases in multiple spaces. *Architectural Science Review, 51*(1):14–20.

Turner, C., S. Analyst, and M. Frankel. 2008. *Energy Performance of LEED ® for New Construction Buildings*.

U.S. CDC. 2020. Ventilation in Buildings | CDC.

U.S. CDC. 2021a. COVID-19: Strategies for Optimizing the Supply of PPE | CDC.

U.S. CDC. 2021b. COVID-19 Decontamination and Reuse of Filtering Facepiece Respirators | CDC.

U.S. CDC. 2021c. Operational Strategy for K-12 Schools through Phased Prevention | CDC.

U.S. CDC. 2021d. SARS-CoV-2 Variant Classifications and Definitions.

U.S. Census Burean. 2021. 2021 California wildfires.

U.S. DOE. 2013. Commercial Prototype Building Models | Building Energy Codes Program.

U.S. DOE. 2020. Commercial Reference Buildings | Department of Energy.

U.S. EIA. 2018. Air conditioning accounts for about 12% of U.S. home energy expenditures - Today in Energy - U.S. Energy Information Administration (EIA).

U.S. EIA. 2020a. 2015 Residential Energy Consumption Survey (RECS).

U.S. EIA. 2020b. 2018 Commercial buildings energy consumption survey data.

U.S. EPA. 2005. *Supplemental Guidance for Assessing Cancer Susceptibility from Early-Life Exposure to Carcinogens*. *U.S. Environmental Protection Agency*.

U.S. EPA. 2020. Can air cleaning devices that use bipolar ionization, including portable air cleaners and in-duct air cleaners used in HVAC systems, protect me from COVID-19? | US EPA.

U.S. EPA. 2021a. Basic Information about Carbon Monoxide (CO) Outdoor Air Pollution | US EPA.

U.S. EPA. 2021b. Basic Information about NO2 | US EPA.

U.S. EPA. 2022a. Health and Environmental Effects of Particulate Matter (PM) | US EPA.

U.S. EPA. 2022b. Health Risk of Radon | US EPA.

U.S. EPA. 2022c. Nitrogen Oxides Control Regulations | Ozone Control Strategies | Ground-level Ozone | New England | US EPA.

U.S. EPA. 2022d. What are ionizers and other ozone generating air cleaners? | US EPA.

U.S. EPA. 2023. AQS API | AirData | US EPA.

U.S. Green Building Council. 2022. Top 10 Countries and Regions for LEED in 2021 | U.S. Green Building Council.

United Nations Environment Programme. 2020. *2020 Global Status Report for buildings and construction - Towards a zero-emissions, efficient and resilient buildings and construction sector*. *United Nations Environment Programme*.

USGBC. 2013. LEED rating system.

USGBC. 2022. Projects | U.S. Green Building Council.

UW Madison. 2020. Badger Seal (Mask Fitter, Mask Sealer, Mask Brace).

van Doremalen, N., T. Bushmaker, D. H. Morris, M. G. Holbrook, A. Gamble, B. N. Williamson, A. Tamin, J. L. Harcourt, N. J. Thornburg, S. I. Gerber, J. O. Lloyd-Smith, E. de Wit, and V. J. Munster. 2020. Aerosol and Surface Stability of SARS-CoV-2 as Compared with SARS-CoV-1. *New England Journal of Medicine*, *382*(16):1564–1567.

Vierra, S. 2018. *Green building standards and certification systems*.

Virginia Department of Health. 2022. Radon Health Effects – Radiological Health.

VirusLights. 2021. LIGHTDIS Upper Air Fixtures – VirusLights.

Waddell, C. 2019. An Overview of Needlepoint Bipolar Ionization.

Walton, G. N. 1983. Thermal Analysis Research Program Reference Manual. | National Technical Reports Library - NTIS.

Wang, N., F. Fang, and M. Feng. 2014. Multi-objective optimal analysis of comfort and energy management for intelligent buildings. *26th Chinese Control and Decision Conference, CCDC 2014*, 2783–2788.

Wang, S., and X. Xu. 2006. Parameter estimation of internal thermal mass of building dynamic

models using genetic algorithm. *Energy Conversion and Management*, *47*(13–14):1927–1941.

Wang, Z, T. Wu, X. Duan, S. Wang, W. Zhang, X. Wu, and Y. Yu. 2009. Research on inhalation rate exposure factors of Chinese residents in environmental health risk assessment (in Chinese). *Research of Environmental Sciences*, *10*:1171–05.

Wang, Zhiqiang, J. Pei, and J. S. Zhang. 2012. Modeling and simulation of an activated carbon-based botanical air filtration system for improving indoor air quality. *Building and Environment*, *54*:109–115.

Wei, W., O. Ramalho, L. Malingre, S. Sivanantham, J. C. Little, and C. Mandin. 2019. Machine learning and statistical models for predicting indoor air quality. *Indoor Air*, *29*(5):704–726.

Wei, X., A. Kusiak, M. Li, F. Tang, and Y. Zeng. 2015. Multi-objective optimization of the HVAC (heating, ventilation, and air conditioning) system performance. *Energy*, *83*:294–306.

Wells, W. F. 1955. Airborne Contagion and Air Hygiene. An Ecological Study of Droplet Infections. *Airborne Contagion and Air Hygiene. An Ecological Study of Droplet Infections.*

Weschler, C. J., H. C. Shields, and D. V. Naik. 1994. Ozone-removal efficiencies of activated carbon filters after more than three years of continuous service. *ASHRAE Transactions*, *100*(2):1121–1129.

White House. 2021a. FACT SHEET: President Biden Sets 2030 Greenhouse Gas Pollution Reduction Target Aimed at Creating Good-Paying Union Jobs and Securing U.S. Leadership on Clean Energy Technologies | The White House.

White House. 2021b. *The Long-Term Strategy of the United States, Pathways to Net-Zero Greenhouse Gas Emissions by 2050*.

WHO. 2005. *WHO Air quality guidelines for particulate matter, ozone, nitrogen dioxide and sulfur dioxide. WHO Air quality guidelines for particulate matter, ozone, nitrogen dioxide and sulfur dioxide*. Geneva, Switzerland.

WHO. 2010. WHO Guidelines for Indoor Air Quality: Selected Pollutants. *WHO Guidelines for Indoor Air Quality: Selected Pollutants*.

WHO. 2020a. Global Health Estimates: Leading Causes of DALYs.

WHO. 2020b. Mortality and global health estimates.

WHO. 2022a. Household air pollution and health.

WHO. 2022b. List of Classifications – IARC Monographs on the Identification of Carcinogenic Hazards to Humans.

William S. Dols, B. J. Polidoro, D. G. Poppendieck, and S. J. Emmerich. 2020. Fate and Transport of Indoor Microbiological Aerosols (FaTIMA).

Wilson, E., C. E. Metzger, S. Horowitz, and R. Hendron. 2014. 2014 Building America House Simulation Protocols. *National Renewable Energy Laboratory*.

Wölfel, R., V. M. Corman, W. Guggemos, M. Seilmaier, S. Zange, M. A. Müller, D. Niemeyer, T. C. Jones, P. Vollmar, C. Rothe, M. Hoelscher, T. Bleicker, S. Brünink, J. Schneider, R. Ehmann, K. Zwirglmaier, C. Drosten, and C. Wendtner. 2020. Virological assessment of hospitalized patients with COVID-2019. *Nature*.

Wu, B., W. Cai, and H. Chen. 2021. A model-based multi-objective optimization of energy consumption and thermal comfort for active chilled beam systems. *Applied Energy*, *287*:116531.

Wu, C., and N. A. Ahmed. 2012. Numerical Study of Transient Aircraft Cabin Flowfield with Unsteady Air Supply. *Https://Doi.Org/10.2514/1.C031415*, *48*(6):1994–2001.

Wu, P., C. Mao, J. Wang, Y. Song, and X. Wang. 2016. A decade review of the credits obtained by LEED v2.2 certified green building projects. *Building and Environment*, *102*:167–178.

Wu, X., M. G. Apte, R. Maddalena, and D. H. Bennett. 2011. Volatile organic compounds in small- and medium-sized commercial buildings in California. *Environmental Science and Technology*, *45*(20):9075–9083.

Wysocka, M. 2018. DALY indicator as an assessment tool for indoor air quality impact on human health. *E3S Web of Conferences*, *49*.

Xiang, J., C. J. Weschler, J. Zhang, L. Zhang, Z. Sun, X. Duan, and Y. Zhang. 2019. Ozone in urban China: Impact on mortalities and approaches for establishing indoor guideline concentrations. *Indoor Air*, *29*(4):604–615.

Xiong, Y., and H. Chen. 2021. Impacts of uneven surface heating of an ideal street canyon on airflows and indoor ventilation: Numerical study using OpenFOAM coupled with EnergyPlus. *Building Simulation 2021 15:2*, *15*(2):265–280.

Xu, X., and S. Wang. 2007. Optimal simplified thermal models of building envelope based on frequency domain regression using genetic algorithm. *Energy and Buildings*, *39*(5):525–536.

Yan, S., N. Liu, M. Chen, Y. Liu, and S. Han. 2020. The thermal effect of the tandem kang model for rural houses in Northern China: a case study in Tangshan. *Https://Doi.Org/10.1080/13467581.2020.1839468*, *21*(2):187–196.

Yan, Y., X. Li, L. Yang, and J. Tu. 2016. Evaluation of manikin simplification methods for CFD

simulations in occupied indoor environments. *Energy and Buildings*, *127*:611–626.

Yan, Y., X. Li, L. Yang, P. Yan, and J. Tu. 2020. Evaluation of cough-jet effects on the transport characteristics of respiratory-induced contaminants in airline passengers' local environments. *Building and Environment*, *183*:107206.

Yang, X., C. Ou, H. Yang, L. Liu, T. Song, M. Kang, H. Lin, and J. Hang. 2020. Transmission of pathogen-laden expiratory droplets in a coach bus. *Journal of Hazardous Materials*, *397*:122609.

Yang, Z., J. Shen, and Z. Gao. 2018. Ventilation and Air Quality in Student Dormitories in China: A Case Study during Summer in Nanjing. *International Journal of Environmental Research and Public Health*.

Yao, M., and B. Zhao. 2018. Surface removal rate of ozone in residences in China. *Building and Environment*, *142*(June):101–106.

Yates, T. A., P. Y. Khan, G. M. Knight, J. G. Taylor, T. D. McHugh, M. Lipman, R. G. White, T. Cohen, F. G. Cobelens, R. Wood, D. A. J. Moore, and I. Abubakar. 2016, February 1. The transmission of Mycobacterium tuberculosis in high burden settings. *The Lancet Infectious Diseases*. Lancet Publishing Group.

Yoon, J. G., J. Yoon, J. Y. Song, S. Y. Yoon, C. S. Lim, H. Seong, J. Y. Noh, H. J. Cheong, and W. J. Kim. 2020. Clinical significance of a high SARS-CoV-2 viral load in the Saliva. *Journal of Korean Medical Science*, *35*(20).

Zemouri, C., S. F. Awad, C. M. C. Volgenant, W. Crielaard, A. M. G. A. Laheij, and J. J. de Soet. 2020. Modeling of the Transmission of Coronaviruses, Measles Virus, Influenza Virus,

Mycobacterium tuberculosis, and Legionella pneumophila in Dental Clinics. *Journal of Dental Research*, *99*(10):1192–1198.

Zeng, Y., M. Heidarinejad, and B. Stephens. 2022. Evaluation of an in-duct bipolar ionization device on particulate matter and gas-phase constituents in a large test chamber. *Building and Environment*, *213*:108858.

Zeng, Y., P. Manwatkar, A. Laguerre, M. Beke, I. Kang, A. S. Ali, D. K. Farmer, E. T. Gall, M. Heidarinejad, and B. Stephens. 2021. Evaluating a commercially available in-duct bipolar ionization device for pollutant removal and potential byproduct formation. *Building and Environment*, *195*:107750.

Zhang, A., Y. Liu, B. Zhao, Y. Zhang, H. Kan, Z. Zhao, F. Deng, C. Huang, X. Zeng, Y. Sun, H. Qian, W. Liu, J. Mo, C. Sun, and X. Zheng. 2021. Indoor PM2.5 concentrations in China: A concise review of the literature published in the past 40 years. *Building and Environment*, *198*:107898.

Zhang, J. 2020. Integrating IAQ control strategies to reduce the risk of asymptomatic SARS CoV-2 infections in classrooms and open plan offices. *Science and Technology for the Built Environment*, *26*(8):1013–1018.

Zhang, J. J., J. Shen, and Z. Gao. 2022. Managing IAQ at Multiple Scales: From Urban to Personal Microenvironments. *Handbook of Indoor Air Quality*, 1–42.

Zhang, S., and Z. Lin. 2020. Dilution-based Evaluation of Airborne Infection Risk-Thorough Expansion of Wells-Riley Model 2 Running Head: Thorough Expansion of Wells-Riley Model. *MedRxiv*, 2020.10.03.20206391.

Zhang, Z., T. Han, K. H. Yoo, J. Capecelatro, A. L. Boehman, and K. Maki. 2021. Disease transmission through expiratory aerosols on an urban bus. *Physics of Fluids*, *33*(1):15116.

Zhao, B., Y. Liu, and C. Chen. 2020a. Air purifiers: A supplementary measure to remove airborne SARS-CoV-2. *Building and Environment*, *177*.

Zhao, B., Y. Liu, and C. Chen. 2020b, June 15. Air purifiers: A supplementary measure to remove airborne SARS-CoV-2. *Building and Environment*. Elsevier Ltd.

Zhao, L., Y. Qi, P. Luzzatto-Fegiz, Y. Cui, and Y. Zhu. 2020. COVID-19: Effects of Environmental Conditions on the Propagation of Respiratory Droplets. *Nano Letters*, *20*(10):7744–7750.

Zhao, M., L. Liao, W. Xiao, X. Yu, H. Wang, Q. Wang, Y. L. Lin, F. S. Kilinc-Balci, A. Price, L. Chu, M. C. Chu, S. Chu, and Y. Cui. 2020. Household Materials Selection for Homemade Cloth Face Coverings and Their Filtration Efficiency Enhancement with Triboelectric Charging. *Nano Letters*, *20*(7):5544–5552.

Zhao, S., Q. Lin, J. Ran, S. S. Musa, G. Yang, W. Wang, Y. Lou, D. Gao, L. Yang, D. He, and M. H. Wang. 2020. Preliminary estimation of the basic reproduction number of novel coronavirus (2019-nCoV) in China, from 2019 to 2020: A data-driven analysis in the early phase of the outbreak. *International Journal of Infectious Diseases*, *92*:214–217.

Zheng, K., Y. K. Cho, A. M. Asce, ; Chao Wang, and H. Li. 2016. Noninvasive Residential Building Envelope R-Value Measurement Method Based on Interfacial Thermal Resistance. *Journal of Architectural Engineering*, *22*(4):A4015002.

Zheng, S., J. Fan, F. Yu, B. Feng, B. Lou, Q. Zou, G. Xie, S. Lin, R. Wang, X. Yang, W. Chen, Q.

Wang, D. Zhang, Y. Liu, R. Gong, Z. Ma, S. Lu, Y. Xiao, Y. Gu, J. Zhang, H. Yao, K. Xu, X. Lu, G. Wei, J. Zhou, Q. Fang, H. Cai, Y. Qiu, J. Sheng, Y. Chen, and T. Liang. 2020. Viral load dynamics and disease severity in patients infected with SARS-CoV-2 in Zhejiang province, China, January-March 2020: Retrospective cohort study. *The BMJ*, *369*.

Zhou, S., Z. Liu, Z. Wang, C. J. Young, T. C. Vandenboer, B. B. Guo, J. Zhang, N. Carslaw, and T. F. Kahan. 2020. Hydrogen Peroxide Emission and Fate Indoors during Non-bleach Cleaning: A Chamber and Modeling Study. *Environmental Science and Technology*, *54*(24):15643–15651.

Zhou, Z., Y. Liu, J. Yuan, J. Zuo, G. Chen, L. Xu, and R. Rameezdeen. 2016, October 1. Indoor PM2.5 concentrations in residential buildings during a severely polluted winter: A case study in Tianjin, China. *Renewable and Sustainable Energy Reviews*. Elsevier Ltd.

Zhu, D., T. Hong, D. Yan, and C. Wang. 2013. A detailed loads comparison of three building energy modeling programs: EnergyPlus, DeST and DOE-2.1E. *Building Simulation*, *6*(3):323–335.

Zhuang, Z., Y. Li, B. Chen, and J. Guo. 2009. Chinese kang as a domestic heating system in rural northern China—A review. *Energy and Buildings*, *41*(1):111–119.

Zomorodian, Z. S., M. Tahsildoost, and M. Hafezi. 2016. Thermal comfort in educational buildings: A review article. *Renewable and Sustainable Energy Reviews*, *59*:895–906.

7. Index

A	Envelope area
A_{PV}	Net area of PV surface
c_i	Conversion factor of virus quanta emission rate
c_v	Viral load in the sputum
C_0	Initial pollutant concentration
$C_{adj,j}$	Pollutant concentration of the adjacent room j
C_{es}	Thermal capacity on exterior envelope node
$C_{exhaust}$	Concentration in the exhaust air
$C_{exposure}$	Exposure-related concentration
$C_{hvac,r}$	Pollutant concentration of the return air of the HVAC system
$C_{hvac,s}$	Pollutant concentration of the supply air of the HVAC system
C_i	Indoor concentration of the specific pollutant in room i
C_{in}	Thermal capacity on indoor air node
C_{is}	Thermal capacity on interior envelope node
C_{out}	Outdoor concentration of the specific pollutant
$C_{p,air}$	Specific heat of indoor air
$C_{p,w}$	Specific heat of wall material

C_t	Indoor pollutant concentration at time t
C_{vir}	Concentration of viral particles
d_p	Particle diameter
E'	Emission rate of indoor pollutant source
E_{clg}	Energy use by cooling coils in HVAC system
E_{eqm}	Energy use by equipment
E_{fac}	Energy use by facilities
E_{fan}	Energy use by fan in HVAC system
E_{htg}	Energy use by heating coils in HVAC system
E_{lgt}	Energy use by lighting system
E_{net}	Net energy use for building needs
E_{pro}	Energy production by renewable or sustainable energy generation system
E_i	Total concentration-independent emission rate of the pollutant in room i
ER	Emission rate of infectious quanta per infector
f_{activ}	Fraction of surface area with active solar cells
f_{cl}	Clothing area factor and dimensionless
$f_{recirculated}$	Fraction of recirculated air in the supply air of HVAC system
f_{UV}	Fraction of UVGI operation time

F_{air}	View factor of wall surface to air temperature
F_{gnd}	View factor of wall surface to ground surface temperature
F_{sky}	View factor of wall surface to sky temperature
G_T	Total solar radiation incident on PV array
h	Heat transfer coefficient
h_c	Overall convective heat transfer coefficient between body (including clothing) and the surrounding air
h_{es}	Convective heat transfer coefficient on the exterior surface
h_{is}	Convective heat transfer coefficient on the interior surface
$h_{r,gnd}$	Equivalent radiative heat transfer coefficient between envelope surface and ground
$h_{r,sky}$	Equivalent radiative heat transfer coefficient between envelope surface and sky
$h_{r,air}$	Equivalent radiative heat transfer coefficient between envelope surface and air
H	Room height
I	Number of infectors
IR	Inhalation rate
I_{cl}	Clothing vapor permeation efficiency ratio of actual evaporative heat flow capability through clothing to sensible heat flow capability
IR_H	Horizontal infrared radiation intensity
k	Thermal conductivity

k_{AC}	Pollutant removal rate by air cleaning units
$k_{AirCleaner}$	Fresh air supply rate by standalone portable air cleaners
$k_{a,i}$	First-order reaction rate of the pollutant with other gaseous compounds in room i
$k_{b,i}$	First-order generation rate of the pollutant due to reactions in room i
k_{dep}	Deposition/removal rate of the pollutant in the room
$k_{deposition}$	Infectious particle deposition rate
$k_{d,i}$	Deposition rate of the pollutant in room i
k_{filter}	Pollutant removal by filtration
$k_{inactivation}$	Pathogen natural inactivation rate in the air
$k_{ionizer}$	Pollutant removal by ionization
k_n	Natural decay rate of pollutant
k_{UV}	Pathogen inactivation rate by UVGI system
K_{filter}	Filter pressure drop coefficient
L	Thickness of envelope
$m'_{adj,j}$	Air flow rate between room i and the adjacent room j
$m'_{hvac,i}$	Supply and return air flow rate of the HVAC system to room i
m'_{inf}	Air infiltration rate
$m'_{inf,i}$	Air flow rate of air infiltration or natural ventilation between the outdoor air and the indoor air of room i

$m'_{PAC,i}$	Air flow rate of portable air cleaners in room i
N_C	New infection case number
N_D	Particle number
N_S	Susceptible case number
p_a	Water vapor pressure of indoor air
P	Infection possibility
P_i	Penetration factor of the pollutant through infiltration or natural ventilation
P_{PV}	Electrical power produced by PV
$q'_{DHI,ext}$	Heat flow due to incident DHI on the exterior side of envelope
$q'_{DNI,ext}$	Heat flow due to incident DNI on the exterior side of envelope
$q'_{HL,1}$	Heat loss through skin
$q'_{HL,2}$	Heat loss through sweating
$q'_{HL,3}$	Latent respiratory heat loss
$q'_{HL,4}$	Dry respiratory heat loss
$q'_{HL,5}$	Heat loss by radiation
$q'_{HL,6}$	Heat loss by convection
$q'_{infiltration}$	Heat flow from air infiltration on indoor air
$q'_{internal}$	Internal heat gain/loss of indoor air

$q'_{LWR,ext}$	Longwave radiative heat flow on exterior envelope
$q'_{LWR,s\text{-}air}$	Longwave radiative heat flow on exterior envelope due to radiation exchange with outdoor air
$q'_{LWR,s\text{-}gnd}$	Longwave radiative heat flow on exterior envelope due to radiation exchange with ground
$q'_{LWR,s\text{-}sky}$	Longwave radiative heat flow on exterior envelope due to radiation exchange with sky
q'_{MW}	Heat generation by individuals
$q'_{rad,in}$	Radiative heat flow on interior surface of envelope
$q'_{rad,out}$	Radiative heat flow on exterior surface of envelope
$q'_{sol\text{-}reflected,ext}$	Heat flow due to ground-reflected solar radiation on the exterior side of envelope
$q'_{sol,in}$	Solar heat flow on interior surface of envelope
$q'_{sol,out}$	Solar heat flow on exterior surface of envelope
q'_{system}	Heat flow from HVAC system on indoor air
q'_{WME}	Heat flow from external work
Q	Air flow rate
Q_{AC}	Air flow rate of air cleaner
Q_{inhale}	Inhalation rate
Q_{intake}	Volume rate of air intake

R_{es}	Resistance between external surface and exterior air
R_i	Total concentration-independent removal rate of the pollutant in room *i*
R_{is}	Resistance between internal surface and interior air
$R_{is,adj,1}$	Resistance between internal surface of the adjacent zone and interior air
R_w	Resistance of envelope
t	Time
t_s	Sampling time
ts	Thermal sensation transfer coefficient
T_{cl}	Surface temperature of clothes
T_{es}	Surface temperature of envelope exterior side
T_{gnd}	Ground surface temperature
$T_{hvac,s}$	Supply air temperature of HVAC system
T_{in}	Indoor air temperature
T_{is}	Surface temperature of envelope interior side
$T_{is,adj,1}$	Surface temperature of envelope interior side of the adjacent zone
T_{mrt}	Mean radiant temperature
T_{out}	Outdoor air temperature
T_{sky}	Sky temperature

u	Input vector of SSM (input variables)
v	Control vector of SSM (control variables)
V	Room volume
V_D	Particle volume
V_i	Volume of room i
V'_{CO2}	Volumetric emission rate of CO2
w	Input vector of SSM (input variables)
x	State vector of SSM (state variables)
v_{met}	Wind speed measured at the meteorological station
v_z	Wind speed at altitude z
y	Output vector of SSM (output variables)
y_0	Baseline prevalence of illness per year
z	Altitude or height above ground
z_{met}	Height above ground of the wind speed sensor at the meteorological station
α	Absorptance of envelope
β	Factor to split the view factor between surface and sky
β_{exp}	Coefficient of concentration change associated with exposure
α_{wind}	Wind speed profile exponent at the site

α_{met}	Wind speed profile exponent at the meteorological station
δ	Wind speed profile boundary layer thickness at the site
δ_{met}	Wind speed profile boundary layer thickness at the meteorological station
ΔP_{coil}	Pressure drops by heating/cooling coils in HVAC system
$\Delta P_{diffuser}$	Pressure drops by air diffuser in HVAC system
ΔP_{filter}	Pressure drops by filter in HVAC system
ΔP_{hvac}	Total pressure drops in HVAC system
$\Delta P_{return\ duct}$	Pressure drops by return ducts in HVAC system
$\Delta P_{return\ grille}$	Pressure drops by return grille in HVAC system
$\Delta P_{supply\ duct}$	Pressure drops by supply ducts in HVAC system
Δt	Exposure time
ε	Longwave emittance of surface
$\varepsilon_{hvac,rec}$	recirculated air ratio of HVAC system
ε_{vent}	Ventilation effectiveness
$\eta_{AirCleaner}$	Particle removal efficiency by air cleaner
η_{cell}	Module conversion efficiency of PV
η_{coil}	Conversion factor of HVAC coils
η_{filter}	Particles filtration efficiency by filter

η_{invert}	DC to AC conversion efficiency of PV
$\eta_{PAC,i}$	Pollutant removal efficiency of portable air cleaners in room *i*
η'_{mask}	Equivalent fraction of infectious particle penetration through the face mask
θ_{in}	Angle of incidence
$\theta_{s\text{-}sky}$	Angle between surface and sky
θ_z	Sun's zenith angle
λ_{HVAC}	Fresh air supply rate by the HVAC system
λ_{inf}	Air infiltration rate
λ_Q	Ventilation rate by the control system
$\lambda_{recirculated}$	Recirculated airflow rate
λ_{vent}	Equivalent ventilation air change rate
Λ	Equivalent room air change rate
ρ	Reflectance of envelope
ρ_{air}	Air density
ρ_{gnd}	Ground reflectance
ρ_w	Density of wall material
σ	Stefan-Boltzmann constant
τ	Transmittance of envelope

Φ	Tilt angle of the surface
ACD	Air cleaning device
ACH	Air change per hour
ADAF	Age-dependent adjustment factor
AHU	Air handling unit
ANN	Artificial neural network
API	Application programming interface
AQI	Air quality index
BCVTB	Building Controls Virtual Test Bed
BMR	Basal metabolic rate
BPO	Building performance optimization
BPS	Building performance simulation
BREP	Boundary representation
CADR	Clean air delivery rate
CFD	Computational fluid dynamics
CO	Carbon monoxide
CO2	Carbon dioxide
COP	Coefficient of performance

C-R	Concentration-response
CV	Coefficient of variation
DALYs	Disability-adjusted life years
DCV	Demand-controlled ventilation
DHI	Diffuse horizontal irradiation
DHW	Domestic hot water
DPM	Discrete phase model
DNI	Direct normal irradiation
DNPH	2,4-Dinitrophenylhydrazine
EPS	Expanded polystyrene
EPW	Energyplus weather file
ERV	Energy recovery ventilator
EUI	Energy use intensity
FMI	Functional Mock-up Interface
FMU	Functional Mock-up Unit
GA	Genetic algorithm
GC	Gas chromatograph
GDS	Green Design Studio

HCHO	Formaldehyde
HEPA	High efficiency particulate air (filter)
HPB	High-performance building
HPLC	High-performance liquid chromatography
HVAC	Heating, ventilation, and air conditioning
IAQ	Indoor air quality
ID	Intake-DALY
IDF	Input data file of EnergyPlus
IEQ	Indoor environmental quality
IND	Intake-incidence-DALY
IOT	Internet of thing
M	Metabolic rate
MERV	Minimum efficiency reporting value
ML	Machine learning
MLR	Multiple linear regression
MOGA	Multi-objective genetic algorithm
MOO	Multi-objective optimization
MPC	Model predictive control

MS	Mass selective detector
NO2	Nitrogen dioxide
NOx	Nitrogen oxides
NPBI	Needlepoint bipolar ionization
O3	Ozone
OLS	Ordinary least squares regression
OSM	OpenStudio model file
PAC	Portable air cleaner
PCM	Phase-change material
PCO	Photocatalytic oxidation
PM	Particulate matter
PM2.5	Particulate matters with a diameter of 2.5 micrometers or less
PM10	Particulate matters with a diameter of 10 micrometers or less
PMV	Predicted mean vote
ppb	Part per billion
ppm	Part per million
PPD	Predicted percentage of dissatisfied
PPE	Personal protective equipment

PTR-MS	Proton transfer reaction - Mass spectrometry
PV	Photovoltaics
RC	Resistance-capacitance
RH	Relative humidity
SET	Standard effective temperature
SHGC	Solar heat gain coefficient
SIMPLE	Semi-implicit method for pressure-linked equations
SO2	Sulfur dioxide
SPRE	Single-pass pollutant removal efficiency
SSM	State-space matrices/models
SVM	Support vector machine
SVOC	Semi-volatile organic compound
TVOC	Total volatile organic compound
UV	Ultraviolet
UVGI	Ultraviolet germicidal irradiation
VAV	Variable air volume
VIP	Vacuum insulation panel
VOC	Volatile organic compound

YLD	Years of life disability
YLL	Years of life lost

8. Vita

Jialei Shen

National Institute of Standards and Technology, Gaithersburg, MD 20899, USA

jshen20@syr.edu | jialei.shen@nist.gov

Research Objectives & Interests

Indoor air quality (IAQ) and ventilation

Building energy and environmental performance simulation and optimization

Urban morphology, greening, transportation, and urban microclimate

Evaluation and mitigation of infection risk through airborne transmission

Education

2018 – 2023	Syracuse University	Ph.D.	Mechanical & Aerospace Engineering
2015 – 2018	Nanjing University	M.S.	Architectural Engineering
2011 – 2015	Xi'an Jiaotong University	B.S.	Mechanical Engineering

Experience

<u>After graduation</u>			
2022 – 2023	NIST & University of Maryland	Research Associate	Infection risk estimation in CONTAM; ANT: CONTAM on Rhino Grasshopper (funded by NIST)
<u>Before graduation</u>			
2022 Summer	Syracuse University	RA	IAQ Sensor testing and evaluation (Industrial project)
2021 – 2022	Syracuse University	RA	Effectiveness of Building Systems Strategies for Mitigation of Airborne Transmission of SARS-CoV-2 (Industrial project)
2020 Summer	Syracuse University	RA	Integrated Whole-Building Energy Efficiency Retrofit Solution for Residences in Cold/Very Cold Climates (DOE ABC project)
2020 Spring	Syracuse University	TA	ECS104: Engineering Computational Tools
2019 Fall	Syracuse University	TA	MEE416: Mechanical Engineering Lab

2019 Summer	Syracuse University	RA	Green building design for high-performance buildings (funded by Syracuse Center of Excellence)
2017 – 2018	Nanjing University	RA	Research on Residential Building Ventilation and IAQ Strategies (NSFC project)
2016 – 2017	Nanjing University	RA	Urban Form-Microclimate Coupling Mechanism and Control (NSFC project)

Publications (total citations: 550, based on Google Scholar)

Book chapters

2022

1. Zhang, J., **Shen, J.**, Gao, Z., 2022. Managing IAQ at Multiple Scales - from Urban to Personal Microenvironments. *Handbook of Indoor Air Quality*, 1-42.

Journal articles

2023

16. Xu, F., **Shen, J.**, Gao, Z., 2023. A field measurement study of the effects of outdoor pollutants and room volumes on indoor fine particle and ozone concentrations in residential buildings in Nanjing. *Journal of Building Engineering*. (*co-first author*)

2022

15. Guo, X., Buccolieri, R., Gao, Z., Zhang, M., Lyu, T., Rui, L., **Shen, J.**, 2022. On the effects of urban-like intersections on ventilation and pollutant dispersion. *Building Simulation* 15 (3), 419-433.

2021

14. **Shen, J.**, Kong, M., Dong, B., Birnkrant, M.J., Zhang, J., 2021. Airborne transmission of SARS-CoV-2 in indoor environments: A comprehensive review. *Science and Technology for the Built Environment* 27 (10), 1331-1367.
13. Guo, X., Gao, Z., Buccolieri, R., Zhang, M., **Shen, J.**, 2021. Effect of greening on pollutant dispersion and ventilation at urban street intersections. *Building and Environment* 203, 108075.
12. **Shen, J.**, Kong, M., Dong, B., Birnkrant, M.J., Zhang, J., 2021. A systematic approach to estimating the effectiveness of multi-scale IAQ strategies for reducing the risk of airborne infection of SARS-CoV-2. *Building and Environment* 200, 107926.
11. Peng, Y., Gao, Z., Buccolieri, R., **Shen, J.**, Ding, W., 2021. Urban ventilation of typical residential streets and impact of building form variation. *Sustainable Cities and Society* 67, 102735.
10. Zhang, M., Gao, Z., Guo, X., **Shen, J.**, 2021. Ventilation and pollutant concentration for the pedestrian zone, the near-wall zone, and the canopy layer at urban intersections. *International Journal of Environmental Research and Public Health* 18 (21), 11080.

2020

9. **Shen, J.**, Krietemeyer, B., Bartosh, A., Gao, Z., Zhang, J., 2020. Green Design Studio: A modular-based approach for high-performance building design. *Building Simulation* 14, 241–268.

2019

8. Guo, C., Gao, Z., **Shen, J.**, 2019. Emission Rates of Indoor Ozone Emission Devices: A Literature Review. *Building and Environment* 158, 302–318.
7. **Shen, J.**, Gao, Z., 2019. Commuter Exposure to Particulate Matters in Four Common Transportation Modes in Nanjing. *Building and Environment* 156, 156–170.
6. Huang, Y., Rui, L., Gao, Z., **Shen, J.**, 2019. Research progress on reaction between ozone and human occupants. *Journal of Environment and Health* 36(02), 182–187. (*in Chinese language*)

2018

5. You, W., **Shen, J.**, Ding, W., 2018. Improving residential building arrangement design by assessing outdoor ventilation efficiency in different regional spaces. *Architectural Science Review*.
4. Yang, Z., **Shen, J.**, Gao, Z., 2018. Ventilation and Air Quality in Student Dormitory in China: A Case Study during Summer in Nanjing. *International Journal of Environmental Research and Public Health* 15(7), 1328.
3. Rui, L., Buccolieri, R., Gao, Z., Ding, W., **Shen, J.**, 2018. The Impact of Green Space Layouts on Microclimate and Air Quality in Residential Districts of Nanjing, China. *Forests* 9, 224.
2. **Shen, J.**, Gao, Z., 2018. Ozone removal on building material surface: A literature review. *Building and Environment* 134, 205–217.

2017

1. **Shen, J.**, Gao, Z., Ding, W., Yu, Y., 2017. An investigation on the effect of street morphology to ambient air quality using six real-world cases. *Atmospheric Environment* 164, 85–101.

Conference articles and presentations

2023

17. Hu, Y., **Shen, J.**, Zhang, J., Gao, Z., 2023. A CFD approach to reduce the risk of Covid-19 airborne transmission in a typical office. *IAQVEC 2023*, Tokyo, Japan.

2022

16. **Shen, J.**, Nabutola, K., Birnkrant, M.J., McKinney, P.J., Dong, B., Zhang, J., 2022. Estimation of infection risk through airborne transmission in large open spaces with different air distributions. *RoomVent 2022*, Xi'an, China. (*Best Paper Award*)
15. Liu, Z., **Shen, J.**, Guo, B., Zhang, J., 2022. Modeling Secondary Emissions from Indoor Chemical Reactions Initiated by Ozone and Hydroxyl Radicals. *Indoor Air 2022*, Kuopio, Finland.
14. Liu, Z., Parry-Nweye, E., Dhaouadi, Y., Wang, X., **Shen, J.**, Guo, B., Ramirez, M., Gupta, B., Ren, D., Dong, B., Zhang, J., 2022. A Comprehensive Approach to Testing Air Cleaning Devices Under Realistic Room Conditions. *Indoor Air 2022*, Kuopio, Finland.
13. **Shen, J.**, Liu, Z., Guo, B., Love, D., Dekold, M., Birnkrant, M.J., Dong, B., Zhang, J., 2022. Performance of in-duct bipolar ionization devices on pollutant removal and potential byproduct formation in indoor environments. *Indoor Air 2022*, Kuopio, Finland.

2021

12. **Shen, J.**, Liu, Z., Hu, Y., Birnkrant, M.J., Gao, Z., Dong, B., Zhang, J., 2021. Effectiveness of combined displacement ventilation and partitions for reducing airborne transmission of respiratory diseases in office settings. *Healthy Buildings 2021 America*, Honolulu, United States (online).
11. **Shen, J.**, Kong, M., Dong, B., Birnkrant, M.J., Zhang, J., 2021. Effectiveness of IAQ strategies for mitigating the airborne infection risk of SARS-CoV-2. *IBPC 2021*, Copenhagen, Denmark (online).

10. **Shen, J.**, 2021. Ozone Emission Sources and Surface Removal in Indoor Environments. *ASHRAE Virtual Annual Conference 2021* - Seminar 14: Reducing Ozone: A Critical Factor in Improving IAQ (online).

2019

9. **Shen, J.**, Zhang, J., 2019. An approach to develop a green technology database for residential buildings. *IAQVEC 2019*, Bari, Italy.

8. Zhang, J., **Shen, J.**, Krietemeyer, E., Bartosh, A., Gu, R., 2019. Green Design Studio for Healthy and Sustainable Buildings and Communities: Exploration of an Innovative Approach. *17th New York State Green Building Conference*, Syracuse, United States.

7. **Shen, J.**, Gu, R., Bartosh, A., Krietemeyer, E., Zhang, J., 2019. Modular-based Green Design Studio for Sustainable Building. *17th New York State Green Building Conference*, Syracuse, United States.

2017

6. **Shen, J.**, Chen, J., Zhang, X., Zou, S., Gao, Z., 2017. Outdoor and Indoor Ozone Concentration Estimation Based on Artificial Neural Network and Single Zone Mass Balance Model. *10th International Symposium on Heating, Ventilation and Air Conditioning (ISHVAC 2017)*, Jinan, China.

5. **Shen, J.**, Gao, Z., 2017. Commuter Exposure to Particulate Matter of Different Transportation Modes in Nanjing. *10th International Symposium on Heating, Ventilation and Air Conditioning (ISHVAC 2017)*, Jinan, China.

4. **Shen, J.**, Gao, Z., 2017. Steady State and Dynamic Indoor Ozone Estimation Model with Indoor Ozone Source. *Healthy Buildings 2017 Europe*, Lublin, Poland.

3. **Shen, J.**, Gao, Z., Ding, W., You, W., 2017. Study on Relationship of Residential Building Form Variations to Pollutant Dispersion in Streets. *Healthy Buildings 2017 Europe*, Lublin, Poland.

2. You, W., **Shen, J.**, Ding, W., 2017. Improving Wind Environment of Residential Neighborhoods by Understanding the Relationship between Building Layouts and Ventilation Efficiency. *8th International Conference on Applied Energy (ICAE 2016)*, Beijing, China.

1. You, W., **Shen, J.**, Ding, W., 2017. Improving wind environment design based on assessing spatial distribution of ventilation efficiency in regional space. *9th International Conference on Applied Energy (ICAE 2017)*, Cardiff, United Kingdom.

Grants & Fellowships

2018, 2020	Graduate Fellowship	Syracuse University

Honors & Awards

2022	Best Paper Award	RoomVent 2022 Conference
2019	Excellent Master's Degree Dissertation of Jiangsu Province	Ministry of Education of Jiangsu Province, China
2018	Excellent Postgraduate Honor	Nanjing University
2017	National Scholarship	Ministry of Education of China

2017	ISIAQ Student Conference Support Award	International Society of Indoor Air Quality and Climate (ISIAQ)
2017	Excellent Graduate Student Honor	Nanjing University
2014	Excellent Social Activist Honor	Xi'an Jiaotong University
2013	Excellent Undergraduate Student Honor	Xi'an Jiaotong University
2012 – 2014	Siyuan Scholarship	Xi'an Jiaotong University

Services

2020 – Now	Serving as a reviewer for journals including 1) *Building and Environment*, 2) *Building Simulation*, 3) *Science and Technology for the Built Environment*, 4) *International Journal of Ventilation*, etc.

Memberships & Affiliations

2020 – Now	*Science and Technology for the Built Environment* journal	Reviewer Board
2018 – Now	American Society of Heating, Refrigerating and Air-Conditioning Engineers (ASHRAE)	Associate Member
2022 – Now	International Building Performance Simulation Association (IBPSA)	Associate Member
2019 – 2022	ASHRAE Syracuse University Student Branch	Vice President
2021 – 2023	International Society of Indoor Air Quality and Climate (ISIAQ)	Student Member